MAGNETIC AND STRUCTURAL PROPERTIES OF CHEMICALLY SYNTHESIZED Fe(Co)-Pt(Ni, Bi) NANOPARTICLES

by

Vimal Deepchand

A dissertation submitted to the Faculty of the University of Delaware in partial fulfillment of the requirements for the degree of Doctor of Philosophy in Physics

Spring 2021

MAGNETIC AND STRUCTURAL PROPERTIES OF CHEMICALLY SYNTHESIZED Fe(Co)-Pt(Ni, Bi) NANOPARTICLES

by

Vimal Deepchand

Approved: _____
Edmund R. Nowak, Ph.D.
Chair of the Department of Physics and Astronomy

Approved: _____
John A. Pelesko, Ph.D.
Dean of the College of Arts and Science

Approved: _____
Louis F. Rossi, Ph.D.
Dean of the Graduate College and Vice Provost for Graduate and Professional Education

I certify that I have read this dissertation and that in my opinion it meets the academic and professional standard required by the University as a dissertation for the degree of Doctor of Philosophy.

Signed: _____

George C. Hadjipanayis, Ph.D.
Professor in charge of dissertation

I certify that I have read this dissertation and that in my opinion it meets the academic and professional standard required by the University as a dissertation for the degree of Doctor of Philosophy.

Signed: _____

M. Benjamin Jungfleisch, Ph.D.
Member of dissertation committee

I certify that I have read this dissertation and that in my opinion it meets the academic and professional standard required by the University as a dissertation for the degree of Doctor of Philosophy.

Signed: _____

James MacDonald, Ph.D.
Member of dissertation committee

I certify that I have read this dissertation and that in my opinion it meets the academic and professional standard required by the University as a dissertation for the degree of Doctor of Philosophy.

Signed: _____

Chaoying Ni, Ph.D.
Member of dissertation committee

ACKNOWLEDGMENTS

My first and foremost words of gratitude and appreciation go to Professor Hadipanayis for accepting me in his group and providing many research ideas. His guidance and flexibility in giving me free rein to try out ideas independently has been an important part in a journey of discovery for me in becoming a better scientist.

I am also grateful to all my committee members for being part of the process and being flexible, sometimes under short notice. Special thanks also go to Dr Aleksandr Gabay for in-lab assistance and providing feedback on my research and Dr Vasileios Tzitzios for his collaboration in my published work and supplying some research ideas that made it into this work.

My current and former groupmates, as well as visiting scholars, have my appreciation for teaching me new things or simply enjoying time together. I especially thank Dr Frank Abel for training me in the various chemical synthesis techniques crucial to my work as well as pointing me in new directions to carry my research work to the next level.

TABLE OF CONTENTS

LIST OF TABLES

LIST OF FIGURES

ABSTRACT

This work is focused on the study of FePt and CoPt nanoparticles synthesized by a chemical route, and their ternary alloys made with small substitutions with Ni and Bi. Chemically ordered $L1_0$ FePt and CoPt nanoparticles, with face-centered tetragonal (fct) phase structure have attracted extensive attention for potential applications in ultrahigh-density magnetic recording media, magnetic energy storage, and electrocatalysis because of their large anisotropy constant ($K_u \sim 5-7$ Merg/cc). In the first part of the work, Fe-Pt-Ni nanoparticle were synthesized by the co-reduction of iron(iii) acetylacetonate ($Fe(acac)_3$), platinum(ii) acetylacetonate ($Pt(acac)_2$) and nickel(ii) acetylacetonate ($Ni(acac)_2$) in a standard solution synthesis. Structural analysis showed that Ni replaces Pt in the lattice to form $FePt_{1-x}Ni_x$. For low Ni content, high chemical ordering was obtained after annealing at 700°C for at least 15 minutes, with a coercivity of 10.7 kOe, compared to 14.9 kOe for L1o FePt. At higher Ni content the $L1_0$ chemical ordering decreased, and this correlated with a decrease in coercivity. However it was found that when Bi was used in the synthesis, it improved the chemical ordering the $L1_0$ ordering to the point that the coercivity in the $x = 0.4$ nanoparticles increased from 1.1 kOe to 2.8 kOe in one of the heat treated sample. Ni substitution led to an increased saturation magnetization and a decrease in magnetocrystalline anisotropy consistent with the decrease of coercivity. This study demonstrated the possibility of creating ternary $L1_0$ structure derived from FePt through Ni substitution of Pt and still retain the desired hard magnetic properties. The Ni and Bi substitutions

were performed with CoPt, where in one part, Ni was used to form $CoPt_xNi_{1-x}$ and in another part, Bi was used in the synthesis to attempt to obtain the $L1_0$ structure. However, it was found that Ni substitution does not work in the same way with CoPt, resulting in a significant loss of the hard magnetic properties of CoPt.

In the second part of the thesis, $FePt_3$ nanoparticles were synthesized using iodine as an intermediary in our reaction We found that iodine helped the formation of the $L1_2$ $FePt_3$ phase in the as-synthesized particles, and that the $L1_2$ ordering was further improved by heat treatment at 700°C. $L1_2$ $FePt_3$ is antiferromagnetic below 160K and, whereas the disordered state is ferromagnetic at room temperature. The degree of ordering of the $L1_2$ phase in the as-synthesized nanoparticles could be controlled by modifying the reaction parameters. The structural and magnetic properties, including antiferromagnetic and ferromagnetic phase transitions, of the various nanoparticles were studied.

In the final part of this work, different stages of the fcc to $L1_0$ phase transformation of FePt nanoparticles were studied, along with their effect on the magnetic properties. Their properties were compared to those of $L1_0$ CoPt nanoaparticles. A ternary alloy of PtFeCo was synthesized and annealed, and its transformation to the L1o stage and the resulting changes in magnetic properties compared to those of CoPt and FePt. The dependence of coercivity, anisotropy and saturation magnetizations with temperature of samples of FePt, CoPt and PtFeCo at various stages of the $L1_0$ transformation were also investigated and compared with theoretical models.

Chapter 1

INTRODUCTION

1.1 Scientific and Technological Importance of Magnetic Nanostructures

Magnetic nanoparticles forms an area of study that is of high interest due to their applications in various fields such as biomedicine, catalysis and ultra-high density storage [1–11]. The size of magnetic nanoparticles can be controlled to range from a few nanometers to tens of nanometers, which is comparable to the size of cells and proteins. For biomedicine applications, this means that the magnetic nanoparticles can be brought close to the biological entities of interest and/or tag them there. Furthermore, since the nanoparticles can be controlled by magnetic field which can go through human tissues, the magnetic nanoparticles can be transported and/or immobilized near magnetically tagged biological entities. This forms the basis of targeted drug delivery inside the body [1,2]. Another growing biomedical application of magnetic nanoparticles is magnetic hyperthermia, which is a technique where the nanoparticles are heated when subjected to an alternating magnetic field, which may then be used in targeted selective tumor killing in the treatment of cancer [4,5].

Catalysts are used to increase reaction rates, improve reaction yields and reduce reaction temperatures. Using nanoparticle catalysts offer the added benefit of providing an increased surface area which allows for increased reaction rates [8,12]. Magnetic nanoparticles can be useful in this field since magnetic catalysts can be immobilized and recovered for later reuse with the application of a magnetic field [13]. There is a

large interest in nanoscale platinum-based catalyst for oxygen reduction reaction (ORR) and hydrogen evolution reaction (HER) to improve the efficiency of fuel cells. Using Pt based alloys, rather than pure Pt, such as FePt and CoPt which are stable in acids will also lead to a reduction of cost [14–16].

Another important application of magnetic nanoparticles is magnetic storage media. Over recent years, the aerial density of hard disks have increased from 1 Tb/in^2 to 3-4 Tb/in^2 with the help of heat assisted magnetic recording (HAMR) where the magnetic media is heated close to its Curie temperature to read/write on it. The smallest unit of storage in a media, the bit, is made up of multiple magnetic grains/particles. The storage of one bit may require up to 100 grains which represent a grain diameter of about 8 nm. To achieve a higher storage density, the size of the grains/particles needs to be reduced. This increases the likelihood of the reversal of the magnetic orientation of the microscopic grains by the ambient temperature (the superparamagnetic effect). To avoid this possibility, the magnetic materials need to have a high magnetocrystalline anisotropy. This may be seen from the equation for the lifetime of the recorded data per particle:

$$\tau = \tau_0 \exp\left(\frac{K_u V}{k_B T}\right) \tag{1.1}$$

τ is the relaxation time, τ_0 is the time for the attempted reversal, K_u is the magnetocrystalline anisotropy, V is the particle volume, k_B the Boltzmann constant and T the temperature. $K_u V$ represents the energy barrier between the two magnetic orientations.

FePt in the $L1_0$ phase is a good candidate for recording media. It has a magnetocrystalline anisotropy of 70 Merg/cc, resulting in a particle size of 3 nm [10,17–19]. Other ongoing aspects are involved in creating and improving new types of magnetic storage, which may include lowering of the Curie temperature in HAMR or doping the FePt structure with a third element such as Cu [20–22].

Permanent magnets form another application-driven aspect of magnetic nanoparticles. High performance permanent magnets are in high demand in environmentally friendly technologies such as wind turbines and electric vehicles [23]. The best performing permanent magnets like NdFeB or SmCo magnets are made up of rare earth elements such as Nd and Sm [24], and have high coercivities H_c and remanence. Because of the limited availability/distribution of rare-earth elements [25–27], there is an increasing need to develop rare-earth free alternatives.

1.2 Research Objectives

Our main goal in this work is to study FePt, CoPt and rare earth-free alloys derived from them. The main objectives are:

- Synthesize and characterize $FePt_{1-x}Ni_x$ nanoparticles and observe the effect of Ni substitution of Pt on structural and magnetic properties.
- Use of a small amount of Bi in $FePt_{1-x}Ni_x$ synthesis to improve chemical ordering, and the corresponding effect on magnetic properties.
- Study $CoPt_{1-x}Ni_x$ alloys, and how Ni substitution of Pt affects the magnetic properties.
- Synthesis of $FePt_3$ nanoparticles using an iodine-mediated method, and characterization of the properties of the resulting nanoparticles.

- Study the effects of processing FePt and CoPt and $PtFe_{0.5}Co_{0.5}$ nanoparticles at different temperatures on their structural transformation (fcc to $L1_0$) and their resulting magnetic properties.

1.3 Outline of Thesis Chapters

In Chapter 2, a brief description of types of magnetism, magnetic terms, anisotropy and determing anisotropy is discussed. Chapter 3 covers the experimental methods used to chemically synthesize the nanoparticles as well as the characterization techniques such as X-ray diffraction, vibrating sample magnetometry (VSM) and physical property measurement system (PPMS). Chapter 4 is focused on Fe-Pt-Ni and Co-Pt-Ni nanoparticles. It starts with the description of the synthesis and characterization of nanoparticles created by substituting Pt in FePt with Ni to form Fe-Pt-Ni ternary alloy nanoparticles. The effect of Bi addition to this ternary alloy on the chemical ordering is also discussed next. Ni substitution of Pt in CoPt is also discussed in this chapter and comparisons are drawn with the Fe-Pt-Ni and Fe-Pt-Ni-Bi alloy nanoparticles. Chapter 5 is focused on the use of iodine in the chemical synthesis of $Fe-Pt_3$ alloy nanoparticles and the study of their structural and magnetic properties. Chapter 6 discusses the effect of the structural transformation from fcc to $L1_0$ on the magnetic properties of FePt, CoPt and $PtFe_{0.5}Co_{0.5}$ when processed/annealed at different temperatures. The intrinsic properties including the saturation magnetization, magnetocrystalline anisotropy and Curie temperature of these nanoparticles have been determined. The temperature dependence of coercivity and its relation to anisotropy and particle size is discussed in selected samples of FePt, CoPt and $PtFe_{0.5}Co_{0.5}$. Chapter 7 gives a summary of the findings of this work and proposes suggestions for future work.

REFERENCES

[1] Q. A. Pankhurst, J. Connolly, S. K. Jones, and J. Dobson, *Applications of Magnetic Nanoparticles in Biomedicine*, J. Phys. Appl. Phys. **36**, R167 (2003).

[2] Q. A. Pankhurst, N. T. K. Thanh, S. K. Jones, and J. Dobson, *Progress in Applications of Magnetic Nanoparticles in Biomedicine*, J. Phys. Appl. Phys. **42**, 224001 (2009).

[3] C. C. Berry and A. S. G. Curtis, *Functionalisation of Magnetic Nanoparticles for Applications in Biomedicine*, J. Phys. Appl. Phys. **36**, R198 (2003).

[4] X. Liu, Y. Zhang, Y. Wang, W. Zhu, G. Li, X. Ma, Y. Zhang, S. Chen, S. Tiwari, K. Shi, S. Zhang, H. M. Fan, Y. X. Zhao, and X.-J. Liang, *Comprehensive Understanding of Magnetic Hyperthermia for Improving Antitumor Therapeutic Efficacy*, Theranostics **10**, 3793 (2020).

[5] A. J. Giustini, A. A. Petryk, S. M. Cassim, J. A. Tate, I. Baker, and P. J. Hoopes, *Magnetic Nanoparticle Hyperthermia in Cancer Treatment*, Nano LIFE **1**, (2010).

[6] J. Kim, Y. Lee, and S. Sun, *Structurally Ordered FePt Nanoparticles and Their Enhanced Catalysis for Oxygen Reduction Reaction*, J. Am. Chem. Soc. **132**, 4996 (2010).

[7] B. Arumugam, B. A. Kakade, T. Tamaki, M. Arao, H. Imai, and T. Yamaguchi, *Enhanced Activity and Durability for the Electroreduction of Oxygen at a Chemically Ordered Intermetallic PtFeCo Catalyst*, RSC Adv. **4**, 27510 (2014).

[8] J. Govan and Y. K. Gun'ko, *Recent Advances in the Application of Magnetic Nanoparticles as a Support for Homogeneous Catalysts*, Nanomaterials **4**, 2 (2014).

[9] J. Feng, L. Su, Y. Ma, C. Ren, Q. Guo, and X. Chen, *$CuFe_2O_4$ Magnetic Nanoparticles: A Simple and Efficient Catalyst for the Reduction of Nitrophenol*, Chem. Eng. J. **221**, 16 (2013).

[10] D. Weller and M. F. Doerner, *Extremely High-Density Longitudinal Magnetic Recording Media*, Annu. Rev. Mater. Sci. **30**, 611 (2000).

[11] D. Weller, A. Moser, L. Folks, M. E. Best, Wen Lee, M. F. Toney, M. Schwickert, J.- Thiele, and M. F. Doerner, *High K_u Materials Approach to 100 Gbits/in^2*, IEEE Trans. Magn. **36**, 10 (2000).

[12] L. L. Chng, N. Erathodiyil, and J. Y. Ying, *Nanostructured Catalysts for Organic Transformations*, Acc. Chem. Res. **46**, 1825 (2013).

[13] R. B. Nasir Baig and R. S. Varma, *Magnetically Retrievable Catalysts for Organic Synthesis*, Chem. Commun. **49**, 752 (2013).

[14] M. K. Debe, *Electrocatalyst Approaches and Challenges for Automotive Fuel Cells*, Nature **486**, 7401 (2012).

[15] Q. Li, L. Wu, G. Wu, D. Su, H. Lv, S. Zhang, W. Zhu, A. Casimir, H. Zhu, A. Mendoza-Garcia, and S. Sun, *New Approach to Fully Ordered Fct-FePt Nanoparticles for Much Enhanced Electrocatalysis in Acid*, Nano Lett. **15**, 2468 (2015).

[16] R. M. Arán-Ais, F. Dionigi, T. Merzdorf, M. Gocyla, M. Heggen, R. E. Dunin-Borkowski, M. Gliech, J. Solla-Gullón, E. Herrero, J. M. Feliu, and P. Strasser, *Elemental Anisotropic Growth and Atomic-Scale Structure of Shape-Controlled Octahedral Pt–Ni–Co Alloy Nanocatalysts*, Nano Lett. **15**, 7473 (2015).

[17] D. Weller, G. Parker, O. Mosendz, A. Lyberatos, D. Mitin, N. Y. Safonova, and M. Albrecht, *Review Article: FePt Heat Assisted Magnetic Recording Media*, J. Vac. Sci. Technol. B **34**, 060801 (2016).

[18] A. Q. Wu, Y. Kubota, T. Klemmer, T. Rausch, C. Peng, Y. Peng, D. Karns, X. Zhu, Y. Ding, E. K. C. Chang, Y. Zhao, H. Zhou, K. Gao, J. Thiele, M. Seigler,

G. Ju, and E. Gage, *HAMR Areal Density Demonstration of 1+ Tbpsi on Spinstand*, IEEE Trans. Magn. **49**, 779 (2013).

[19] C. Rong, N. Poudyal, G. S. Chaubey, V. Nandwana, R. Skomski, Y. Q. Wu, M. J. Kramer, and J. P. Liu, *Structural Phase Transition and Ferromagnetism in Monodisperse 3 Nm FePt Particles*, J. Appl. Phys. **102**, 043913 (2007).

[20] D. A. Gilbert, L.-W. Wang, T. J. Klemmer, J.-U. Thiele, C.-H. Lai, and K. Liu, *Tuning Magnetic Anisotropy in (001) Oriented $L1_0$ $(Fe_{1-x}Cu_x)_{55}Pt_{45}$ Films*, Appl. Phys. Lett. **102**, 132406 (2013).

[21] C. Brombacher, M. Grobis, J. Lee, J. Fidler, T. Eriksson, T. Werner, O. Hellwig, and M. Albrecht, *$L1_0$ FePtCu Bit Patterned Media*, Nanotechnology **23**, 025301 (2011).

[22] T. Maeda, A. Kikitsu, T. Kai, T. Nagase, H. Aikawa, and J. Akiyama, *Effect of Added Cu on Disorder-Order Transformation of $L1_0$-FePt*, IEEE Trans. Magn. **38**, 2796 (2002).

[23] P. Shankhari, O. Janka, R. Pöttgen, and B. P. T. Fokwa, *Rare-Earth-Free Magnets: Enhancing Magnetic Anisotropy and Spin Exchange Toward High-T_C $Hf_2MIr_5B_2$ (M = Mn, Fe)*, J. Am. Chem. Soc. **143**, 4205 (2021).

[24] O. Gutfleisch, M. A. Willard, E. Brück, C. H. Chen, S. G. Sankar, and J. P. Liu, *Magnetic Materials and Devices for the 21st Century: Stronger, Lighter, and More Energy Efficient*, Adv. Mater. **23**, 821 (2011).

[25] S. Hoenderdaal, L. Tercero Espinoza, F. Marscheider-Weidemann, and W. Graus, *Can a Dysprosium Shortage Threaten Green Energy Technologies?*, Energy **49**, 344 (2013).

[26] N. A. Mancheri, *World Trade in Rare Earths, Chinese Export Restrictions, and Implications*, Resour. Policy **46**, 262 (2015).

[27] D. Bauer, D. Diamond, J. Li, D. Sandalow, P. Telleen, and B. Wanner, *U.S. Department of Energy Critical Materials Strategy*, (2010).

Chapter 2

THEORETICAL BACKGROUND

2.1 Atomic Origin of Magnetism

Moving charges generate magnetic fields. In solids, magnetic fields are produced due to the intrinsic spin and orbital motion of electrons about atomic nuclei. The magnetic moment of an electron orbiting around a nucleus in terms of the quantized angular moment *L* is given by

$$\mu_L = -\frac{e}{2m_e}L = -\frac{e}{2m_e}\sqrt{l(l+1)}\hbar \tag{2.1}$$

Similarly, the magnetic moment due to the intrinsic spin in terms of the quantized spin number *S* is given by

$$\mu_S = -\frac{e}{m_e}S = -\frac{e}{m_e}\sqrt{s(s+1)}\hbar \tag{2.2}$$

The total magnetic moment of an atom for both orbital and spin moments can be written as

$$\mu_{total} = -\frac{e\hbar}{2m_e}\frac{1}{\hbar}(L+2S) \tag{2.3}$$

In the first Bohr orbit, the magnetic moment due to spin and due to orbital motion are equal. The total magnetic moment in that case is

$$\mu_B = \frac{e\hbar}{2m_e} \tag{2.4}$$

μ_B is called the Bohr magneton, a natural unit of magnetic moment [1–3]. For example, the magnetic moment μ_B per atom is 2.2 for iron, 0.6 for nickel and 1.7 for cobalt. If the total magnetic moments of all the electrons are oriented such that they cancel one another, the atom will have no net magnetic moment. This leads to diamagnetism. On the other hand, if the cancellation of the electron moments is partial, the atom will be left with a net magnetic moment. Substances composed of atoms of this kind are para-, ferro-, antiferro- or ferrimagnetic.

2.2 Types of Magnetism

2.2.1 Diamagnetism

Diamagnetism is exhibited in a substance with filled electronic shells in the presence of an externally applied magnetic field, giving it a negative moment. Diamagnetism results from changes in the orbital motion of electrons, which orient themselves such that a magnetic moment antiparallel to the applied field is produced. Examples of diamagnetic materials are substances with closed electronic shells such as the monoatomic rare gases and ionic solids

2.2.2 Paramagnetism

Paramagnetic materials have permanent magnetic moments. In the absence of an externally applied field, the moments are oriented randomly due to thermal effects, resulting in a net zero magnetic moment. When an external field is applied, the atomic moments tend to orient in the direction of the applied field. In a paramagnetic material, the susceptibility $\chi = M/H$ is inversely proportional to the temperature:

$$\chi = \frac{C}{T} \tag{2.5}$$

C is known as the Curie constant. Equation 2.5 is the Curie's law.

2.2.3 Ferromagnetism

Ferromagnetism is a type of magnetism that occurs even in the absence of any external magnetic field due to the existence of spontaneous magnetization below a temperature known as the Curie temperature. Ferromagnetic materials show parallel alignment of moments which results a large net magnetization even in the absence of a magnetic field. Above the Curie temperature, the thermal fluctuations overcome the exchange interactions which results in no net moment. The presence of spontaneous moments suggests that electron spins and magnetic moments become aligned parallel to each other. Weiss explained this phenomenon in terms of an internal molecular field, which is proportional to the magnetization of the material [3]. The origin of this internal field is the exchange interaction, which reflects the electrostatic Coulomb repulsion of electrons on neighboring atoms, and the Pauli principle, and it is described by Heisenberg in the form of the following Hamiltonian

$$H = -\sum_{i \neq j} J_{ij}\, \boldsymbol{S_i} \cdot \boldsymbol{S_j} \tag{2.6}$$

J_{ij} is the exchange constant. It is positive for ferromagnets and negative for antiferromagnets. S_i is a unit vector of the local spin moment and S_j is the corresponding spin of an adjacent atom. The susceptibility of a ferromagnetic materials as a function of temperature is given by the Curie-Weiss law

$$\chi = \frac{C}{T - \theta} \tag{2.7}$$

where C is the Curie constant. θ is nonzero where neighboring magnetic moments interact with each other. $\theta > 0$ for ferromagnetic material and corresponds to the Curie temperature T_C. At this temperature, the saturation magnetization of the material goes to zero. For $T > T_C$, the sample effectively shows paramagnetic behavior (Figure 2.1).

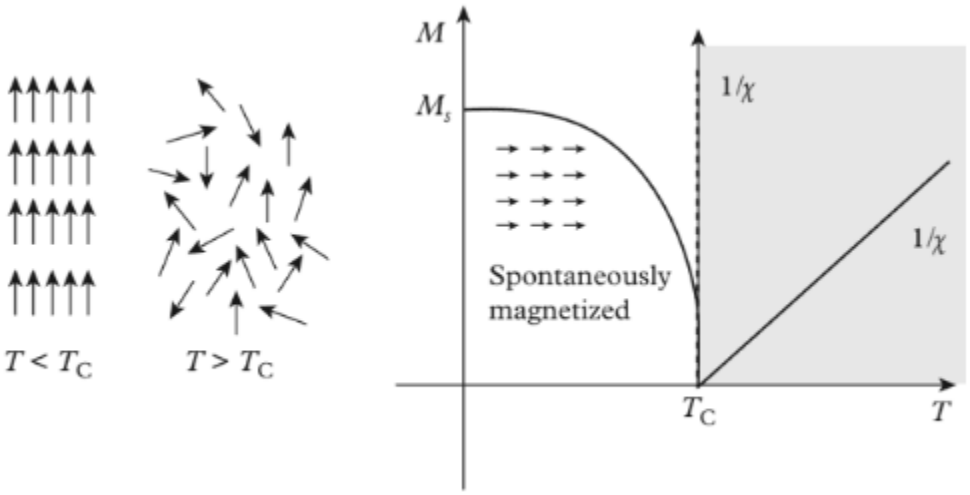

Figure 2.1: Magnetization of a ferromagnet as a function of temperature. Above the Curie temperature T_C, it behaves like a paramagnet [adapted from Fundamentals and Applications of Magnetic Materials KM Krishnan [4]].

2.2.4 Antiferromagnetism

The atoms in such materials have permanent magnetic moments but with a strong, negative interaction between them, resulting in neighboring magnetic moments preferring an antiparallel arrangement. Many of these materials are observed to be paramagnetic at room temperature. Below a critical temperature T_N, the Néel temperature, they show an abrupt change in susceptibility. Moreover, below T_N, the susceptibility is orientation dependent: it varies depending on whether the field is applied parallel, $\boldsymbol{H}_{\parallel}$, or perpendicular, $\boldsymbol{H}_{\perp}$, to the preferred direction of the spin lattice in this material (Figure 2.2). Curie-Weiss law for these kinds of materials is

$$\chi = \frac{C}{T-\theta} = \frac{C}{T+T_N} \tag{2.7}$$

where $\theta = -T_N$.

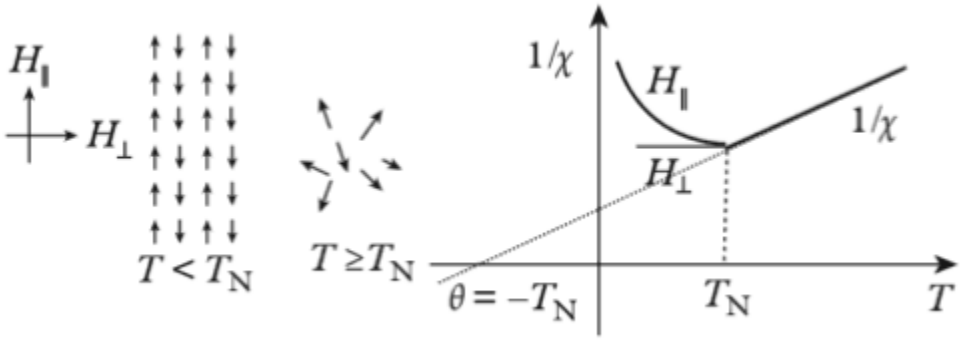

Figure 2.2: Magnetization behavior of an antiferromagnetic material as a function of temperature [adapted from Fundamentals and Applications of Magnetic Materials KM Krishnan [4]].

2.2.5 Ferrimagnetism

Ferrimagnetism is normally observed in materials with two or more magnetic species occupying positions on different sublattices and possessing different magnetic moments. A strong and negative interaction between the two sub-lattices leads to an anti-parallel arrangement. Unlike antiferromagnets, ferrimagnets exhibit spontaneous magnetization below the Curie temperature, when the two sub-lattices are ordered (Figure 2.3).

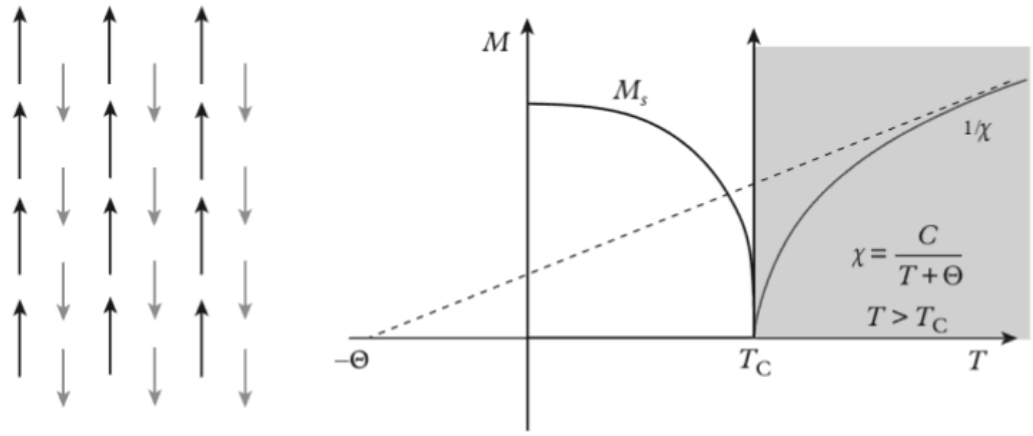

Figure 2.3: Magnetization of a ferrimagnet as a function of temperature [adapted from Fundamentals and Applications of Magnetic Materials KM Krishnan [4]].

2.3 Magnetization Curve and Hysteresis Loop

Hysteresis describes the field-response of the magnetization in ferromagnetic and ferrimagnetic materials. Figure 2.4 shows an example of a hysteresis loop for a ferromagnetic material. Although ferromagnets can be spontaneously magnetized, a portion of a ferromagnetic material can be demagnetized because of the different alignments of its magnetic domains. If a field is applied and then reduced, in general the magnetization will not return to its original value.

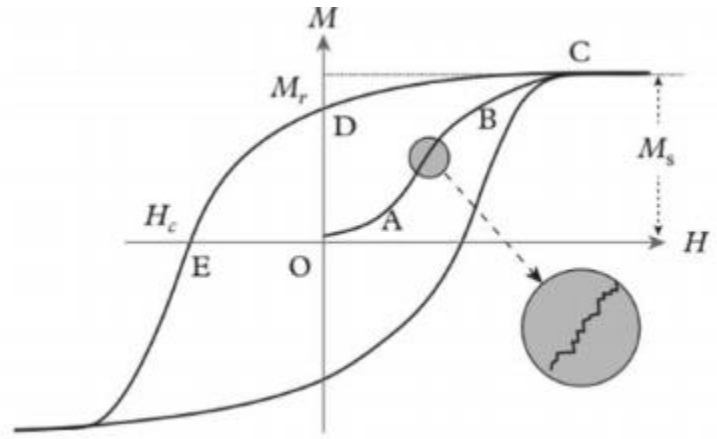

Figure 2.4: Typical hysteresis loop for a ferromagnetic material, showing the points of interest.

In the typical hysteresis loop shown in Figure 2.4, OA which represents the initial magnetization curve is reversible. In the region AB, there is significant and irreversible domain wall motion. In the region BC, the domains rotate and align themselves in the direction of the applied field direction, leading to complete saturation magnetization M_s. After the applied field is removed, the magnetization does not decrease to zero. The magnetization at $H = 0$ is known as the remanence or remanent magnetization M_r. To reduce the magnetization to zero, a negative field must be applied. Segment DE in the second quadrant is known as a demagnetizing curve. The negative value of the applied field for which $M = 0$ is called the intrinsic coercivity of the material, H_c. Magnetically hard materials, which can be used for permanent magnets and recording media, usually have a large remanence and high coercivity and magnetically soft materials usually have a small coercivity.

2.4 Magnetic Anisotropy

Magnetic anisotropy is the dependence of the internal energy of a magnetic material on the direction of spontaneous magnetization. As a result, the shape of the hysteresis loop is affected by magnetic anisotropy. The magnetic anisotropy can be related to the sample shape, crystal symmetry, stress, or symmetry breaking. In ferromagnets, antiferromagnets and ferrimagnets, the magnetization prefers to lie along certain crystallographic directions. This effect is known as magnetocrystalline anisotropy. Only magnetocrystalline anisotropy is intrinsic to the material.

2.4.1 Magnetocrytalline Anisotropy

For a single crystal, the direction in which saturation can be easily achieved is called the easy direction or easy axis of the magnetization. The easy direction of magnetization is the direction of spontaneous magnetization in the demagnetized state. Conversely, the directions along which it is hardest to magnetize the crystal are called the hard directions. For example, in a single crystal of nickel (with face centered cubic structure), <111> is the easy direction of magnetization and <100> is the hard direction [3]. Figure 2.5 shows the magnetization curves for fields applied along different crystallographic directions for (a) iron (bcc), (b) nickel (face centered cubic) and (c) cobalt (hexagonal close packed).

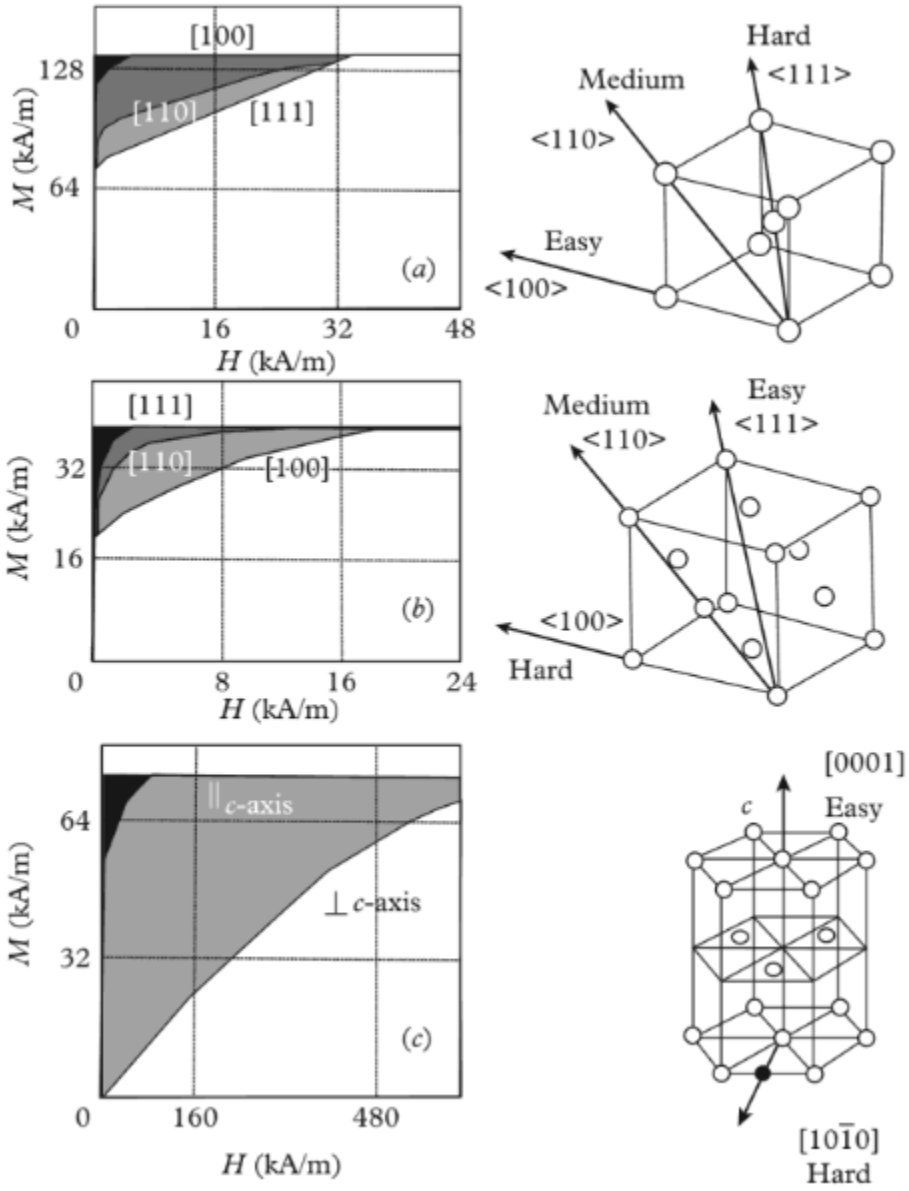

Figure 2.5: The magnetization curves for fields applied along different crystallographic directions for (a) Fe (bcc), (b) Ni (fcc) and (c) Co (hcp) [adapted from Fundamentals and Applications of Magnetic Materials KM Krishnan [4]].

The magnetocrystalline anisotropy energy is the energy stored in the crystal resulting from the work done by an external field in magnetizing the crystal at constant temperature. It is the energy required to move the magnetization vector away from the easy direction to the hard direction and is determined by integrating the area between the hard magnet magnetization curve and the easy magnetization curve:

$$E_{mc} = \int_0^{M_s} \mu_0 \mathbf{H} \cdot d\mathbf{M} \tag{2.8}$$

The origin of magnetocrystalline anisotropy is the spin-orbit coupling. The orbits are coupled to the crystal lattice and prefer certain directions due to the influence of the electrostatic fields which are shaped by the symmetries of the crystal. Thus, if an applied field tries to reorient the spin of an electron, its orbit resists this change and work is required to break this spin-orbit coupling to magnetize the material.

Magnetocrystalline anisotropy may be further subcategorized into uniaxial anisotropy (one axis of symmetry only) such as in Co (hcp) and cubic anisotropy like in Fe (bcc) and Ni (fcc). Cubic anisotropy has three axes of symmetry instead of just one. The magnetocrytalline anisotropy energy density for cubic crystals is written as

$$E_{mc} = K_0 + K_1(\alpha_1^2\alpha_2^2 + \alpha_2^2\alpha_3^2 + \alpha_3^2\alpha_1^2) + K_2\alpha_1^2\alpha_2^2\alpha_3^2 + \cdots \tag{2.9}$$

where $\alpha_i = \cos\theta_i$ and θ_i is the angle between the magnetization vector and the i^{th} axis. The anisotropy coeffficients K_0, K_1, K_2… are constants at a given temperature. Higher order terms may be neglected as they contribute little to E_{mc}. K_2 is in fact sometimes neglected for the same reason. Typical room temperature values for Fe and Ni are [5]

Fe: $K_1 \sim 4.8 \times 10^4$ J/m^3 (4.8×10^5 erg/cc) and $K_2 \sim 5.0 \times 10^3$ J/m^3

Ni: $K_1 \sim -4.5 \times 10\text{^}3$ J/m^3 and $K_2 \sim -2.3 \times 10^3$ J/m^3.

For hexagonal materials, the anisotropy energy density is given by

$$E_{mc} = K_0 + K_1 \sin^2\theta + K_2 \sin^4\theta + \cdots \tag{2.10}$$

where θ is the angle between the c axis and the magnetization.

For tetragonal materials, the anisotropy energy density is given by

$$E_{mc} = K_1 \sin^2\theta + K_2 \sin^4\theta + K_3 \sin^4\theta \sin^2\phi \cos^2\phi + \cdots \tag{2.11}$$

2.4.2 Experimental Determination of Anisotropy Constants

There are few ways of measuring the anisotropy constants K_1 and K_2 which appear in the expression for the anisotropy energy.

Sucksmith-Thompson Method

By minimizing the anisotropy energy of a single crystal with respect to the angle between the magnetization $\vec{\boldsymbol{M}}$ and the easy axis, and correcting for the demagnetizing field $H_D = -N_D M$, one may obtain an expression for $\frac{H}{M}$, where H is the effective field:

$$\frac{H}{M} = \frac{2K_1}{M_s^2} + \frac{4K_2 M^2}{M_s^4} \tag{2.12}$$

M_s is the saturation magnetization. The above equation forms the basis for the Sucksmith-Thompson method: a plot of $\frac{H}{M}$ versus M^2 will be a straight line, from which one can find the anisotropy constants K_1 and K_2 from the intercept and slope respectively [6].

Law of saturation method

In this technique, one measures the magnetization M as a function of the applied field H [7]. Close to saturation, one may write

$$M = M_s \left(1 - \frac{A}{H} - \frac{B}{H^2}\right) + \chi H \tag{2.13}$$

For our purposes, we will use

$$M = M_s \left(1 - \frac{B}{H^2}\right) + \chi H \tag{2.14}$$

where $B = \frac{4}{15}\frac{K_1^2}{M_S^2}$ [8]. A plot of M versus $1/H^2$ for high field values will therefore be a straight line with the saturation magnetization equal to the intercept. K_1 may be determined from the slope.

2.4.3 Magnetocrystalline Anisotropy in $L1_0$ Binary Alloys

In the face-centered cubic (fcc or A1) structure, all faces and corner sites of unit cell are occupied by the same atom. In the case of an alloy, each site atom of the alloy has an equal likelihood of occupying one site. The $L1_0$ phase is a CuAu prototype structure in the P4/mmm spacegroup with a Pearson symbol tP2 and has a tetragonal

crystal structure. The $L1_0$ structure is a crystallographic derivative of the fcc structure where atoms of one type occupy two of the faces and atoms of the other type occupy the other remaining faces, such that the two types of atoms are arranged in alternate layers. The face-centered cubic (fcc) and $L1_0$ phases of FePt are shown in Figure 2.6.

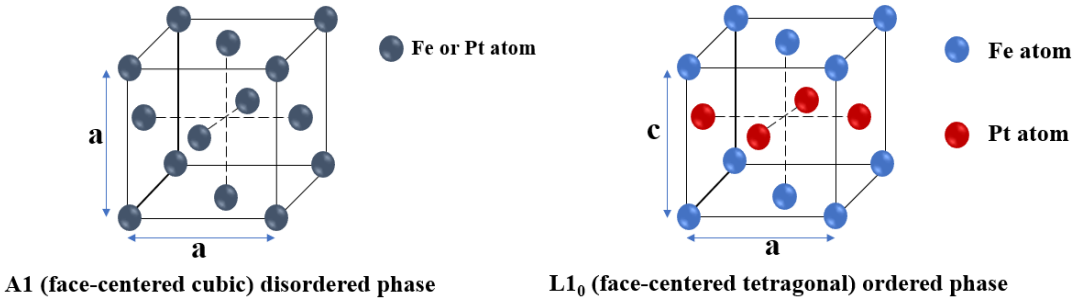

Figure 2.6: Cubic (A1) disordered structure and tetragonal ($L1_0$) ordered structure of FePt binary alloy. The lattice parameters a and c are shown.

$L1_0$ magnetic alloys have large magnetocrystalline anisotropy energies. Because of this, $L1_0$ magnetic alloys may play an important role in magnetic recording media [9]. Table 2.1 lists typical bulk properties of some alloys in the $L1_0$ structure.

Table 2.1: Typical magnetic and structural properties of some bulk $L1_0$ ordered alloys [10–12].

$L1_0$ alloy	K_u (10^7 erg/cm^3)	M_s (emu/cm^3)	T_c (K)	a (Å)	c(Å)
FePt	7.0	1140	750	3.85	3.71
FePd	1.8	1100	760	3.85	3.72
FeNi	1.3	1270	820	3.58	3.61
CoPt	4.9	800	840	3.80	3.70
MnAl	1.7	560	650	3.94	3.58

The chemical ordering S can be estimated based on the experimentally determined lattice parameters. The following equation may be used estimate the chemical ordering in $L1_0$ structures such as FePt:

$$S = \left[\frac{1-\left(\frac{c}{a}\right)_{exp}}{1-\left(\frac{c}{a}\right)_{ref}}\right]^{1/2} \tag{2.15}$$

$(c/a)_{exp}$ is the experimentally determined lattice ratio from X-ray diffraction data and $(c/a)_{ref}$ corresponds to the expected fully ordered ratio (0.964 for FePt $L1_0$).

2.5 Superparamagnetism

For a single domain ferromagnetic nanoparticle, the anisotropy energy is proportional to the volume. Below a critical size of the nanoparticles, the thermal energy is large enough to overcome the magnetocrystalline energy and reverse the

magnetization. Therefore, the moments of these particles fluctuate with time. This effect is referred to as superparamagnetism. The time for the magnetization reversal is known as the relaxation time and is given by

$$\tau = \tau_0 \exp\left(\frac{\Delta E}{k_B T}\right) = \tau_0 \exp\left(\frac{K_u V}{k_B T}\right) \tag{2.16}$$

where τ_0^{-1} is the attempt frequency on the order of 1 GHz [3]. Below a critical temperature, the blocking temperature T_B, there is a rapid reduction in the magnetic relaxation time. Superparamagnetic behavior can be experimentally determined by performing zero field cooled (ZFC) and field cooled (FC) measurements to determine the blocking temperature. The sample of fine particles is cooled from its superparamagnetic state without applying any filed to a temperature that is low enough to freeze the magnetic moments of the particles in random orientations. The sample is then warmed up in the presence of a small magnetic field, typically 100 Oe to 500 Oe, to room temperature or some other temperature. As the sample is warmed up, some of the moments of the nanoparticles align along the applied field and there is an increase in the magnetization. At a certain temperature, the thermal energy starts to overcome the anisotropy energy barrier, causing the moments of the particles to be randomly oriented again and leading to a drop in the magnetization. The nanoparticles are then cooled in the same applied field. As the temperature decreases, the thermal fluctuation becomes less important and the particles get aligned in the direction of the applied field as they get blocked. This causes an increase in the magnetization with cooling until it reaches its saturation temperature. The blocking temperature is defined as the point at which the ZFC curve deviates from the FC curve.

REFERENCES

[1] S. Blundell, *Magnetism in Condensed Matter* (American Association of Physics Teachers, 2003).

[2] N. A. Spaldin, *Magnetic Materials: Fundamentals and Applications* (Cambridge university press, 2010).

[3] J. M. Coey, *Magnetism and Magnetic Materials* (Cambridge university press, 2010).

[4] K. M. Krishnan, *Fundamentals and Applications of Magnetic Materials* (Oxford University Press, 2016).

[5] V. Sechovský, *Magnetism in Solids: General Introduction*, in *Encyclopedia of Materials: Science and Technology*, edited by K. H. J. Buschow, R. W. Cahn, M. C. Flemings, B. Ilschner, E. J. Kramer, S. Mahajan, and P. Veyssière (Elsevier, Oxford, 2001), pp. 5018–5032.

[6] W. Sucksmith and J. E. Thompson, *The Magnetic Anisotropy of Cobalt*, Proc. R. Soc. Lond. Ser. Math. Phys. Sci. **225**, 362 (1954).

[7] B. D. Cullity and C. D. Graham, *Introduction to Magnetic Materials* (John Wiley & Sons, 2011).

[8] N. S. Akulov, *Über Den Verlauf Der Magnetisierungskurve in Starken Feldern*, Z. Für Phys. **69**, 822 (1931).

[9] D. E. Laughlin, K. Srinivasan, M. Tanase, and L. Wang, *Crystallographic Aspects of $L1_0$ Magnetic Materials*, Scr. Mater. **53**, 383 (2005).

[10] D. Weller, O. Mosendz, G. Parker, S. Pisana, and T. S. Santos, *$L1_0$ Fe P t X–Y Media for Heat-assisted Magnetic Recording*, Phys. Status Solidi A **210**, 1245 (2013).

[11] R. A. Lukaszew, *Handbook of Nanomagnetism: Applications and Tools* (CRC Press, 2015).

[12] M. Kotsugi, H. Maruyama, N. Ishimatsu, N. Kawamura, M. Suzuki, M. Mizumaki, K. Osaka, T. Matsumoto, T. Ohkochi, and T. Ohtsuki, *Structural, Magnetic and Electronic State Characterization of $L1_0$-Type Ordered FeNi Alloy Extracted from a Natural Meteorite*, J. Phys. Condens. Matter **26**, 064206 (2014).

Chapter 3

EXPERIMENTAL TECHNIQUES

3.1 Introduction

In this work, the nanoparticles were prepared using a solution based chemical synthesis. Some samples were subjected to additional heat treatment. The nanomaterials were characterized using the following tools: X-ray diffraction (XRD), magnetometry using a vibrating sample magnetometry (VSM) and the physical property measurement systems (PPMS), Mössbauer spectroscopy, and transmission electron microscopy (TEM). In this chapter, the synthesis procedure and characterization methods are discussed.

3.2 Synthesis of Magnetic Nanoparticles

Figure 3.1 shows the typical setup used. A three-neck round bottom flask is connected to a condenser. One side of the flask is connected to a source of forming gas (95% Ar – 5 % H_2). The chemicals and solvents are fed through the other end, which is then sealed with a glass stopper during reaction. A glass-coated magnetic stir bar is used to continuously mix the solvent and precursor before and throughout the reaction. The flask is placed on a heating mantle connected to a temperature controller used to set the reaction temperature.

The details of the various synthesis are described in Chapters 4, 5 and 6. In general, pre-determined amounts of the precursors were added along with the surfactant and the reducing agent, followed by the solvents. The mixture was mixed and purged under forming gas before and throughout the reaction to reduce/eliminate oxygen presence. The mixture was heated until the selected reaction temperature was reached. After the reaction has proceeded for a specified duration, the heating was turned off and the mixture allowed to cool to room temperature. Afterwards, the solution was washed in ethanol and/or hexane to precipitate and separate the magnetic material from the remaining organics magnetically. In some reactions, centrifuging was also necessary to improve the reaction yield. Further washing with ethanol and hexane, and ultrasonicating at 50% amplitude for 20 seconds, were carried out to remove the organics as much as possible.

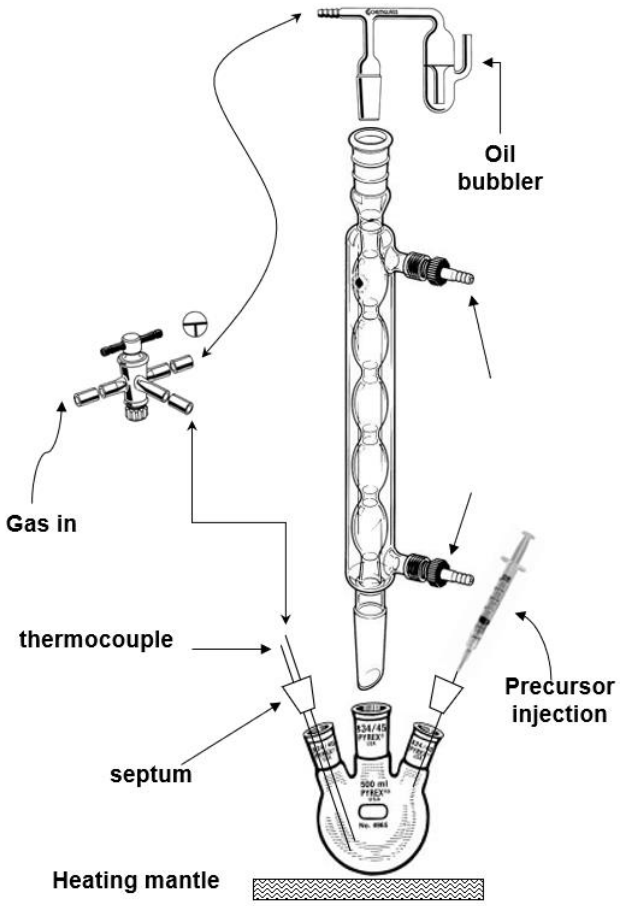

Figure 3.1: Schematic diagram of the experimental setup used in the chemical synthesis of the nanoparticles.

The resulting powder was then dried in a desiccator. This unprocessed powder is referred to as the as-made or as-synthesized sample. Most of the times, a portion of the as-made sample was heat-treated (annealed) to study the structure transformation resulting from heat treatment. To anneal the as-made powder, it was placed in a quartz tube and connected to a rough pump and diffusion system to create a vacuum inside the tube. After some time, usually around 25 minutes, the tube was filled with forming gas

(95% Ar – 5% H_2) to further inhibit oxidation, sealed and placed in a pre-heated furnace for the heat treatment of the powder.

The materials used in the synthesis are commercially available at a nominal purity. The metal precursors used in this work are as follows: iron(iii) acetylacetonate (97%) [$Fe(acac)_3$], platinum(ii) acetylacetonate [$Pt(acac)_2$], cobalt(ii) acetylacetonate (97%) [$Co(acac)_2$] and bismuth(ii) acetate (99.99%) [$(CH_3CO_2)_3Bi$], all purchased from Sigma Aldrich. The reducing agent 1,2-hexadecanediol (98%) was purchased from Fischer Scientific. The surfactants palmitic acid (99%) and oleic acid (99%) were purchased from Sigma Aldrich. In our studies on iodine-mediated synthesis of $FePt_3$ discussed in Chapter 5, we also used elemental iodine and ammonium tetracholoro-platinate(ii) [$(NH_4)_2PtCl_4$].

3.3 X-ray Crystallography

X-ray diffraction (XRD) is a measurement technique that can reveal information such as crystallographic structure, crystallite size, chemical composition, stress, strain, lattice spacing and lattice parameters about a sample. A typical X-ray diffractometer consists of an X-ray source, a sample holder, and an X-ray detector to collect the diffracted rays. A cathode ray tube is used to produce X-rays which are filtered to produce monochromatic X-rays and collimated to produce a narrow beam which is directed towards the sample under study. A spherical wave is radiated when X-rays are diffracted by atoms from internal crystal planes of the sample. Spherical waves from different scattering centers interfere constructively or destructively. Diffraction of X-rays for a particular sample occurs according to Bragg's law, which enables the identification of unique crystal structures [1,2]:

$$2d \sin\theta = n\lambda \tag{3.1}$$

A visual representation of Bragg's law is shown in Figure 3.2.

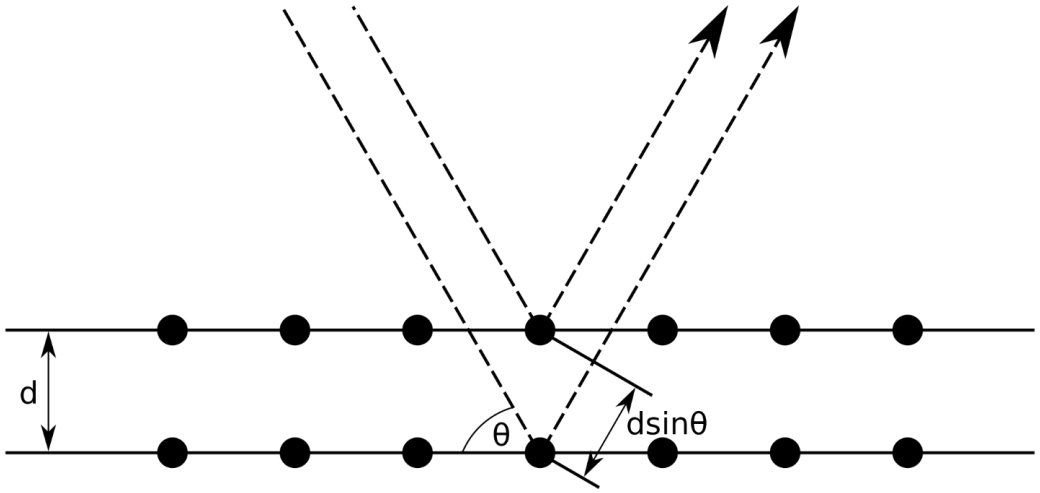

Figure 3.2: Illustration of Bragg diffraction from crystalline planes with a spacing d.

In equation 3.1, λ is the wavelength of the X-rays, d the interplanar distance, n the diffraction order and θ the angle between the incident beam and the crystal plane. By scanning the sample through a range of 2θ angles, all possible diffraction directions of the lattice can be obtained from the random orientations of the powder material (Figure 3.3).

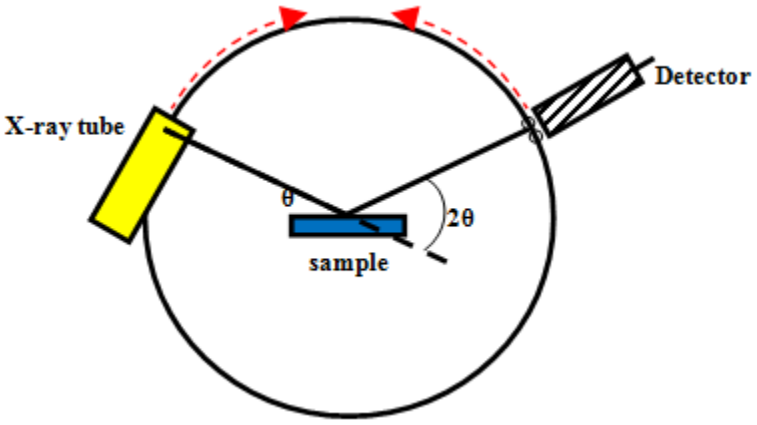

Figure 3.3: Detection of reflected X-rays in an X-ray diffractometer.

The Scherrer equation is used to approximate the crystallite size by relating the width of the diffraction peaks to the size of the crystals in the sample [3,4]. It is written as

$$\tau = \frac{K\lambda}{(\beta - \alpha)\cos\theta} \tag{3.2}$$

τ is the calculated crystallite size, K a dimensionless shape factor which is approximately 0.9 for spherical particles, β is the full width half maximum of a diffraction peak and α is a correction factor for instrumental broadening. The Scherrer equation has a few limitations. In a polycrystalline sample, the relative intensities due to the larger particles dominate the signal and the Scherrer equation would be slanted towards the larger sizes. In the case of smaller particles sintered together from annealing, the Scherrer equation may again overestimate the size if the aggregates form coherent planes. The Scherrer formula gives a good estimate mostly in the case of a

sample made of uniform, monodisperse single crystal nanoparticles. For these reasons, the Scherrer size should be considered as an approximate method to qualitatively compare samples.

In this work, a Rigaku Ultima IV diffractometer using Cu-K_α radiation ($\lambda = 1.5418$ Å) was used to characterize the samples.

3.4 Transmission Electron Microscopy

The transmission electron microscope (TEM) is used to study the structure and microstructure of nanomaterials and bulk materials. Compared to optical microscopes which can reach a resolution of 300 nm, electron microscopes can attain resolutions as low as 2 Å. Transmission electron microscopes can be used to determine the size and morphology of nanometer scale materials. A TEM can also be used to directly determine the crystal lattice spacing through selected area diffraction, in which case, the atomic spacing act as diffraction gratings for the electron interacting with the sample. The image formed in this case can either be spots or a series of rings, depending on whether the sample is a single crystal or numerous single crystals with different orientations. The rings or spots can be related to a specific atomic spacing in the crystal lattice, which allows for the identification of the crystal phase [5]. High resolution electron microscopy (HREM) can also be used to directly image the lattice planes.

The main parts of the TEM are: (1) an electron gun, which generates a stream of electrons, and a system of condenser lenses which focus the electrons on the sample, (2) the image-producing system, consisting of the objective lens, a movable sample holder, and intermediate and projector lenses, which focus the electrons passing through the specimen to form a real, highly magnified image, and (3) the image-

recording system consisting of a fluorescent screen for viewing and focusing the image and a digital camera for recording the image. In addition, a vacuum system is required for the electrons to travel without any scattering from the source to the sample [6,7].

In this work, a JEOL 3010 ultrahigh resolution analytical electron microscope was used to study the particle morphology and to perform phase analysis of select samples.

3.5 Magnetomery Measurements

A **vibrating sample magnetometer** (VSM) was used to measure the magnetic and thermomagnetic properties of the samples. The VSM used in this work is a Quantum Design VersaLab with a maximum 3 Tesla applied field, with low temperature capacities down to 50 K. The VSM is also equipped with a high temperature oven attachment, which allows for magnetic measurements up to 950 K to investigate high temperature properties of the samples.

The VSM is based on Faraday's law. It operates by applying a constant magnetic field within the sample chamber. The sample is placed within sensing coils, and then vibrated in a sinusoidal motion which introduces perturbations in the external magnetic field. This change in flux causes a current in the sensing coil that is proportional to the magnetic moment of the sample, allowing for measurements of magnetization versus applied magnetic field, or measurements of magnetization versus temperature in a constant magnetic field [8].

In a typical measurement, dried powder is placed in a Teflon holder, and covered with melted wax, ensuring there are no air bubbles which could cause the rotation of the powder in the magnetic field. After the wax has cooled and solidified to seal the powder

in place, the Teflon sample holder is placed in the VSM and the measurement is performed. For high temperature measurements, the powdered sample is mixed in zirconium cement, and the mixture is placed on the high temperature stick. The cement is dried using hot air and wrapped around with copper foil to ensure uniform heating during measurement. The measurement temperature is controlled by a thermocouple. Based on nickel calibration measurements, the error in VSM measurements is taken to be approximately 1%.

A Quantum Design **Physical Property Measurement System** (PPMS) was also used to study magnetic phase transitions in select samples. The PPMS used can perform high magnetic field measurements with an applied maximum field of 9 Tesla and at temperatures as low as 4.2 K. In a few of our $FePt_3$ samples (Chapter 5), we measured the AC susceptibility, which involves measuring the magnetic moment of sample exposed to an oscillating external magnetic field.

3.6 Mössbauer Spectroscopy

Mössbauer spectroscopy is based on the recoilless, resonant absorption and emission of gamma rays in solids. The most common nucleus used in this technique is Fe^{57}. In a typical setup, the gamma rays are emitted by the source that moves towards and away from a sample at velocities in the mm/s range [9]. The isotopes in the source emitting the gamma rays are the same as the isotopes in the sample absorbing them. The gamma rays that pass through the sample are detected by a radiation detector. The relative motion between source and sample results in an energy shift, due to the Doppler effect. In the resulting spectrum, the gamma ray intensity is plotted as a function of source velocity. At velocities corresponding to the resonant energy levels of the sample,

some of the gamma rays are absorbed, and a drop (also known as a peak) is observed in the spectrum. The minimum peaks produced in the spectrum are used to characterize the material.

Because of the high sensitivity of the measurements in this technique, Mössbauer spectroscopy permits the distinction between compounds usually not possible by other means such as X-ray diffraction. For example, Fe_3O_4 and Fe_2O_4, which typically cannot be distinguished by X-ray diffraction measurements, can be identified, and have their phase percentages quantified using Mössbauer spectroscopy. In this work, Mössbauer spectroscopy was used to characterize some samples of FePtNiBi alloys to identify the iron-based phases (such as the oxides) present in in these samples.

REFERENCES

[1] L. V. Azaroff, *X-Ray Diffraction: [By] Leonid V. Azaroff [And Others]* (McGraw-Hill, New York, 1974).

[2] B. D. (Bernard D. Cullity, *Elements of X-Ray Diffraction* (Addison-Wesley Pub. Co., Reading, Mass., 1956).

[3] A. L. Patterson, *The Scherrer Formula for X-Ray Particle Size Determination*, Phys. Rev. **56**, 978 (1939).

[4] P. Scherrer, *Bestimmung der inneren Struktur und der Größe von Kolloidteilchen mittels Röntgenstrahlen*, in *Kolloidchemie Ein Lehrbuch*, edited by R. Zsigmondy (Springer, Berlin, Heidelberg, 1912), pp. 387–409.

[5] D. B. 1949- Williams and C. B. Carter, *Transmission Electron Microscopy a Textbook for Materials Science 3 Imaging*, 2. ed., [pbk-ed.] (Plenum Press, New York, NY [u.a.], 2009).

[6] R. F. Egerton, *Physical Principles of Electron Microscopy*, Vol. 56 (Springer, 2005).

[7] H. H. Rose, *Optics of High-Performance Electron Microscopes*, Sci. Technol. Adv. Mater. (2016).

[8] S. Foner, *Versatile and Sensitive Vibrating-sample Magnetometer*, Rev. Sci. Instrum. **30**, 548 (1959).

[9] *Introduction to Mössbauer Spectroscopy*, https://www.rsc.org/membership-and-community/connect-with-others/through-interests/interest-groups/mossbauer/.

Chapter 4

STRUCTURAL AND MAGNETIC PROPERTIES OF $L1_0$ FePtNi ALLOYS AND CoPtNi ALLOYS

4.1 Introduction

$L1_0$ FePt nanoparticles have been chosen as the ideal candidate for the future of ultra-high density recording media due to its high magnetocrystalline anisotropy energy of 70 Merg/cc [1,2]. However, the media must be heated close to the Curie temperature for the writing and reading of bits. Producing $L1_0$ alloys with high thermal stability, while reducing the Curie temperature is critical for the development of heat assisted magnetic recording media, and has led to the exploration of third element doping into $L1_0$ FePt [1]. Additionally, substituting platinum with nickel while retaining the desired magnetic properties would lead to an overall reduction of recording media cost.

A plethora of techniques exist for the synthesis of FePt nanoparticles including coreduction of precursors, single source molecular precursors, and solid-state reactions [3–12]. However, few have considered ternary alloys with Fe and Pt. Most reports focus on the addition of a third element dopant keeping the stoichiometry between Fe and Pt fixed with the purpose of reducing ordering the ordering temperature [13–19].

FeNi prepared in the $L1_0$ phase has been suggested as a potential candidate for a rare earth free permanent magnet with theoretical energy product predictions of up to 42 MGOe comparable to some of the commercially available sintered NdFeB

magnets [20]. The phase transformation to the $L1_0$ structure in FeNi is significantly more sluggish compared to its FePt counterpart which until recently has only been found naturally occurring in meteorites formed over millions of years [21,22]. The first report of bulk $L1_0$ FeNi was fabricated by producing an amorphous alloy which was then crystallized at a temperature close to the ordering temperature of $L1_0$ FeNi of about 320°C [23].

To our knowledge only one other study considered the chemical synthesis of an Fe-Pt-Ni alloy, in which $(FePt)_{1-x}Ni_x$ nanoparticles were obtained. It was shown that the addition of Ni in an FePt phase suppresses the transformation from the disordered fcc to the ordered fct $L1_0$ phase, up to a certain Ni content, beyond which nanoparticles in the $L1_2$ phase are obtained [24].

In this study, we report the effect of Ni substitution of Pt on the development of $L1_0$ structure of FePt nanoparticles synthesized chemically. We study samples with nominal Ni compositions of x = 0.2, 0.3, 0.4 in $FePt_{1-x}Ni_x$ nanoparticles. We also report the effect of annealing at 700°C on degree of ordering and magnetic properties of the $FePt_{1-x}Ni_x$ nanoparticles. In another project of this study, we introduce a small amount of Bi to the $FePt_{1-x}Ni_x$ structure and investigate the effect Bi addition has on chemical ordering and magnetic properties, most notably, the coercivity and Curie temperature.

In the final part of this chapter, we discuss the effect of Ni substitution of Pt and Bi addition to a CoPt lattice, to form $CoPt_{1-x}Ni_x$ and $CoPt_{1-x}Ni_x$ (+10% Bi), and highlight the differences in properties of the CoPt-based nanoparticles and the FePt-based nanoparticles.

4.2 FePtNi Alloys

4.2.1 Sample Preparation

Fe-Pt-Ni ternary nanoparticles of different compositions were synthesized by the chemical reduction of $Fe(acac)_3$, $Pt(acac)_2$ and $Ni(acac)_2$. 0.25 mmol of $Fe(acac)_3$ were mixed with pre-determined amounts of $Pt(acac)_2$ and $Ni(acac)_2$ to obtain $FePt_{1-x}Ni_x$ alloys with x = 0.2, 0.3, 0.4. The precursors were mixed in a 3-stopper flask with 1 mmol of 1,2-hexadecanediol, the reducing agent, 200 mg of palmitic acid, the surfactant, and 20 ml of trioctylamine, as solvent. To avoid oxygen contamination, the flask was constantly purged with forming gas (5% H_2 – 95% Ar) before and throughout the whole reaction. The refluxing temperature was set to be 330°C for 1 hour. After the solution was cooled to room temperature, the resulting solution was washed with ethanol and hexane. The black resulting material was isolated from the solution magnetically before being dried in a desiccator at room temperature. The as-synthesized particles were annealed at 700°C for different times. The samples were sealed in quartz tubes using a rough pump and a diffusion pump, filled with forming gas (5% H2 – 95% Ar), and then subjected to heat treatment.

The crystal structure of the as-synthesized and annealed $FePt_{1-x}Ni_x$ samples was analyzed using X-ray diffraction (XRD) and the magnetic properties were measured using a vibrating sample magnetometer (VSM). Two of the compositions (x = 0.2, 0.4) were also analyzed using a JEOL 3010 transmission electron microscope (TEM). Crystal size was also calculated for the as-synthesized nanoparticles from the X-ray diffraction data using the Scherrer's formula.

4.2.2 Characterization of $FePt_{1-x}Ni_x$ Nanoparticles

Figure 4.1(a) shows the X-ray diffraction data for the as-synthesized equiatomic $Fe_{0.5}Pt_{0.5}$, $FePt_{1-x}Ni_x$, and $Fe_{1.4}Pt_{0.6}$ alloys along with the reference peaks of $L1_0$ FePt. The $Fe_{1.4}Pt_{0.6}$ composition was chosen as comparison to the $FePt_{0.6}Ni_{0.4}$ since both alloys have the same percentage of transition metal relative to Pt. The purpose of this was to determine whether Ni is being substituted for Pt in the lattice, or if the ternary alloys with Ni are just increasing the relative percentage of the magnetic transition metal.

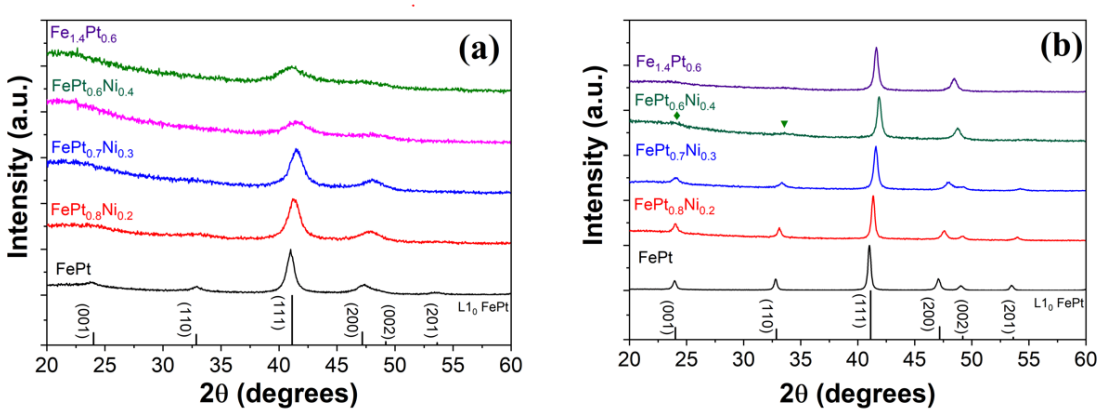

Figure 4.1: X-ray diffraction of (a) as-synthesized FePt and FePtNi alloys, and (b) after annealing at 700°C for 15 minutes. The ♦ and ▼ on the XRD pattern of the annealed $FePt_{0.6}Ni_{0.4}$ indicates the low intensity (001) and (100) peaks.

The as-synthesized $Fe_{0.5}Pt_{0.5}$ alloy shows the presence of $L1_0$ structure but with a low degree of $L1_0$ ordering, as evident by the low intensity (001) and (110) superlattice peaks. In the as-synthesized ternary nanoparticles the degree of ordering decreases with increasing Ni content, with the $FePt_{0.7}Ni_{0.3}$ and $FePt_{0.6}Ni_{0.4}$ alloys having a nearly pure

fcc cubic structure. Additionally, increasing the overall percent of Fe has a similar effect with the $Fe_{1.4}Pt_{0.6}$ alloy being purely fcc cubic as well. Figure 4.1(b) shows the alloys after 15-minute annealing at 700°C. After the heat treatment, the $Fe_{0.5}Pt_{0.5}$ alloy converts to a highly ordered L10 structure, as is evident by the observed splitting of the (200) and (002) fundamental peaks and the increase in superlattice peak intensities, respectively. The low nickel content samples $x = 0.3$ and $x = 0.2$ show a similar transformation with differentiation between (200) and (002) peaks being evident but less intense relative to the pure $Fe_{0.5}Pt_{0.5}$ alloy. In the case of the annealed $FePt_{0.6}Ni_{0.4}$ alloy low intensity (001) and (110) peaks are present suggesting that the structure has transformed to an $L1_0$ structure. Comparison with the $Fe_{1.4}Pt_{0.6}$ alloy shows that it has remained mostly cubic.

The degree of ordering S was calculated for alloys to better quantify the structural transformation after annealing. The following formula is used for S [25]:

$$S^2 = \frac{I_s/I_f}{I_s^o/I_f^o} = \frac{I_{001}/I_{111}}{I_{001}^s/I_{111}^s} \tag{4.1}$$

I_s and I_f are the measured peak intensities of the experimental superlattice and corresponding fundamental peaks respectively, and I_s^o and I_s^o are the corresponding intensities for the ordered phase. We used the ratio of the I_{001}/I_{111} peak intensities from our XRD signals after correcting for the background signal and performing a fit on the data. Figure 4.2 shows detailed X-ray diffraction data of the $FePt_{0.6}Ni_{0.4}$ sample, with fit allowing for quantification of chemical ordering.

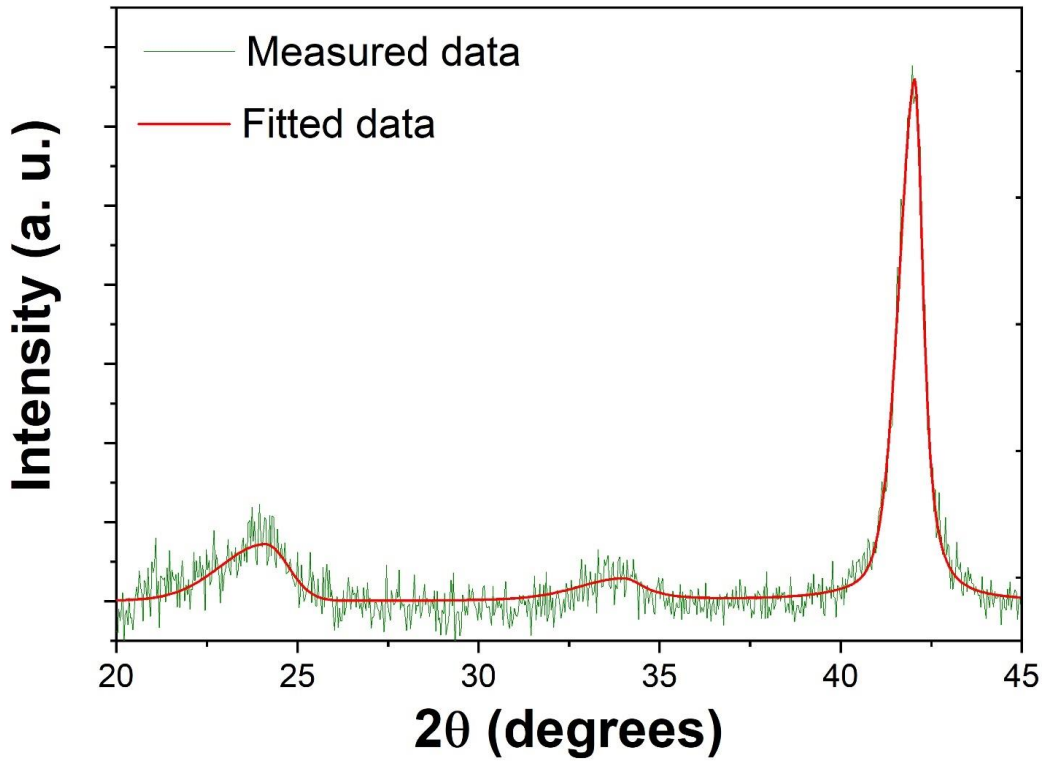

Figure 4.2: Measured and fitting of X-ray diffraction data of annealed $FePt_{0.6}Ni_{0.4}$ after background subtraction.

For our reference sample, we used I_{001}/I_{111} for $L1_0$-FePt [26]. $S = 1$ for complete ordering and $S = 0$ for the disordered cubic structure.

Figure 4.3 shows the degree of ordering S as a function of Ni content, ranging from $Fe_{0.5}Pt_{0.5}$ to $FePt_{0.6}Ni_{0.4}$ compositions. The $Fe_{1.4}Pt_{0.6}$ composition is excluded due to being mostly cubic, which leads to difficulties in properly quantifying S when the value approaches 0. The degree of chemical ordering S decreases with increasing Ni content, as qualitatively observed.

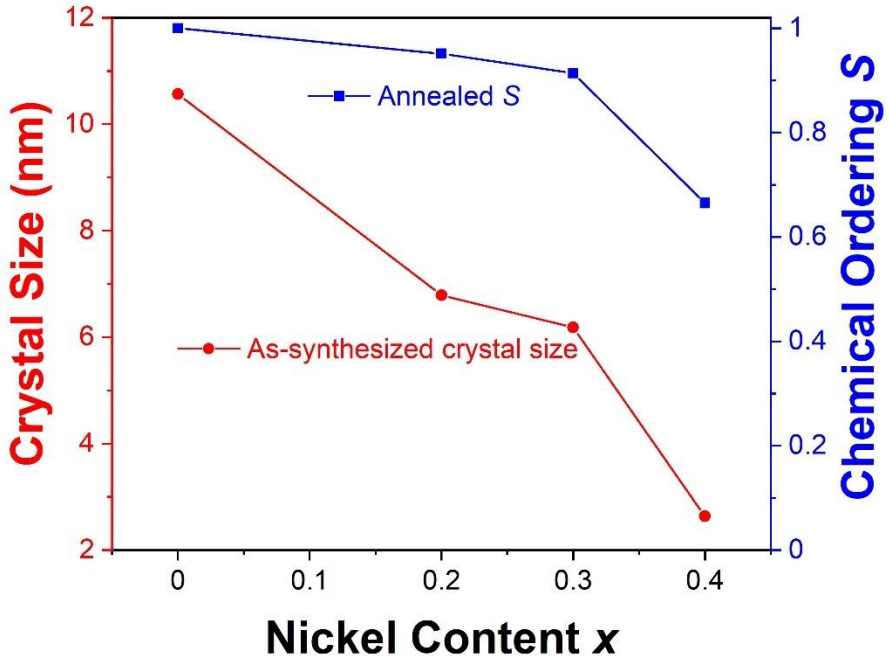

Figure 4.3: Crystal size and chemical ordering *S* as a function of *x*, for as-synthesized $FePt_{1-x}Ni_x$ alloys (red circles) and for 15-minute annealed at 700°C $FePt_{1-x}Ni_x$ alloys (blue squares).

The crystal size of the nanoparticles, also shown in Figure 4.3,was determined by the Scherrer equation and was found to decrease with increasing nickel content. Figure 4.4 shows the TEM images for the as-synthesized samples with $x = 0.2$ and $x = 0.4$. The nanoparticles appear as clustered aggregates when deposited on TEM grids, and the particle size decreases with increasing Ni content, in agreement with the crystal size calculated from the Scherrer equation.

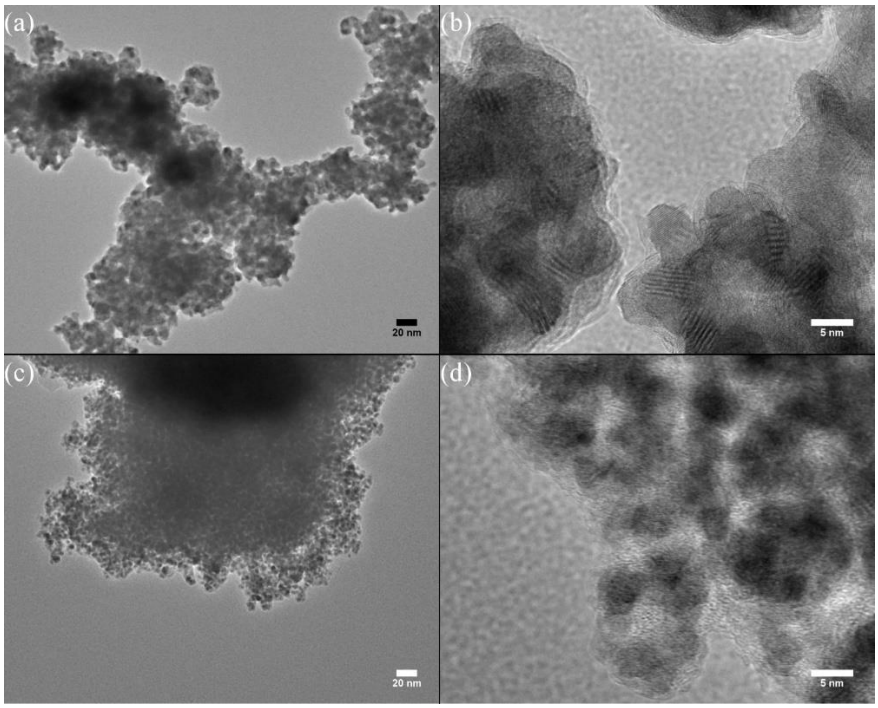

Figure 4.4: TEM images for the as-synthesized (a), (b) $FePt_{0.8}Ni_{0.2}$ and (c), (d) $FePt_{0.6}Ni_{0.4}$ alloys.

The structural transformation of the alloys with annealing time was also investigated for an annealing temperature of 700°C. Figure 4.5 shows the XRD data for the $FePt_{0.8}Ni_{0.2}$ sample.

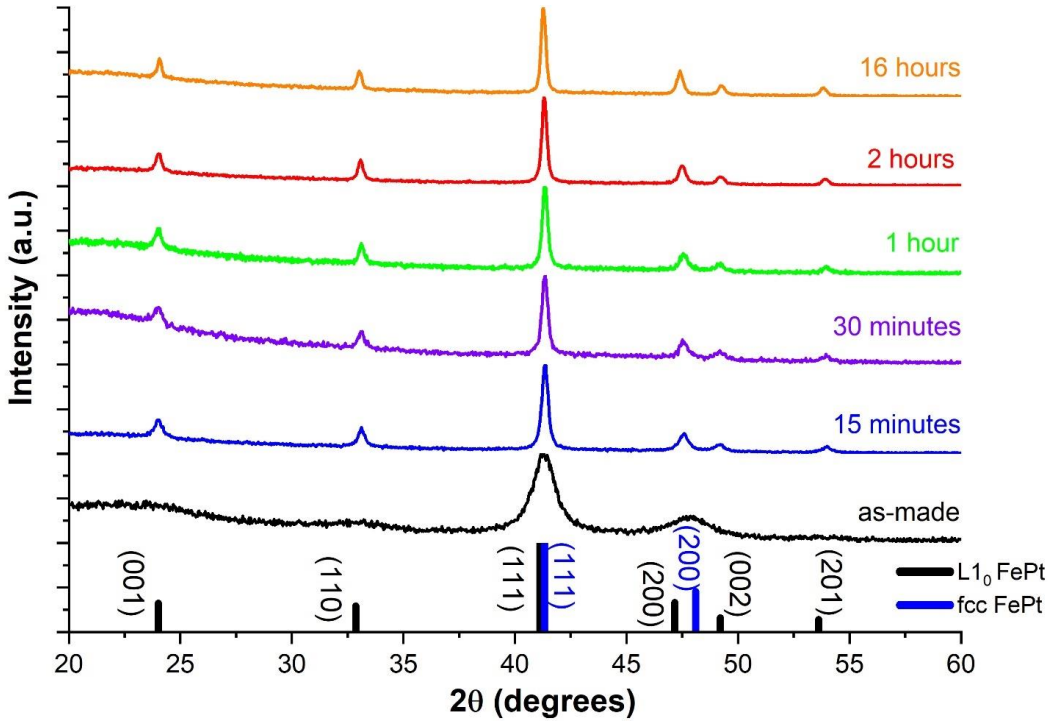

Figure 4.5: XRD data of $FePt_{0.8}Ni_{0.2}$ nanoparticles annealed at 700°C for different durations. The as-made data is included for comparison.

The XRD pattern shows that the splitting of the (200) and (002) peaks generally increases with annealing duration, indicating an increasing transformation towards the ordered $L1_0$ phase. Annealing for a much longer time than 2 hours did not bring in a noticeably larger separation. The $FePt_{0.7}Ni_{0.3}$ and $FePt_{0.6}Ni_{0.4}$ samples were also annealed at 700°C for up to 2 hours, and X-ray diffraction measurements were performed on them.

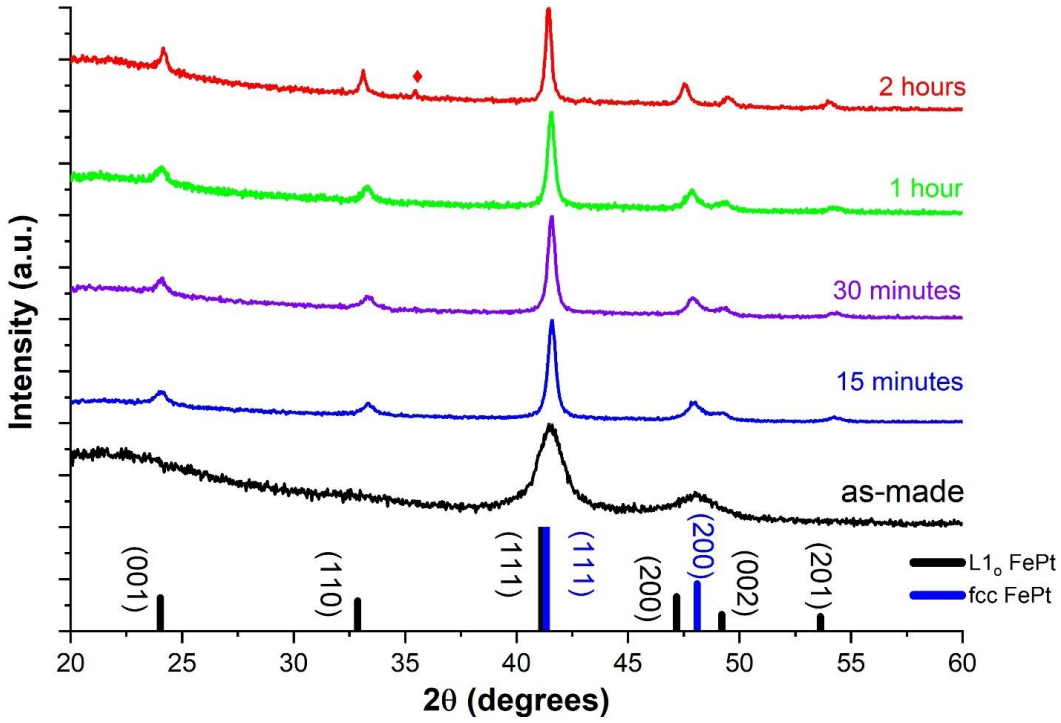

Figure 4.6: XRD data for $FePt_{0.7}Ni_{0.3}$ annealed at 700°C for different durations. The peak marked by a ♦ on the 2-hour pattern represents (311) peak of Fe_3O_4, its main peak in the plotted range of 2θ values.

From the XRD data in Figure 4.6, annealing for longer time increases the $L1_0$ ordering in the $FePt_{0.7}Ni_{0.3}$ sample. A 2-hour annealing time was sufficient to create a complete separation of the (200) and (002) peaks. On the other hand, the XRD data for $FePt_{0.6}Ni_{0.4}$ (Figure 4.7) shows more sluggish transformation towards the fully ordered $L1_0$ phase. Annealing at 700°C for any duration produced the lower angle peaks (001) and (110) indicating the onset of the $L1_0$ phase transformation. Our data suggests that a combination of longer annealing time and higher temperature may be required to transform the FePtNi alloys with higher Ni content into the $L1_0$ phase.

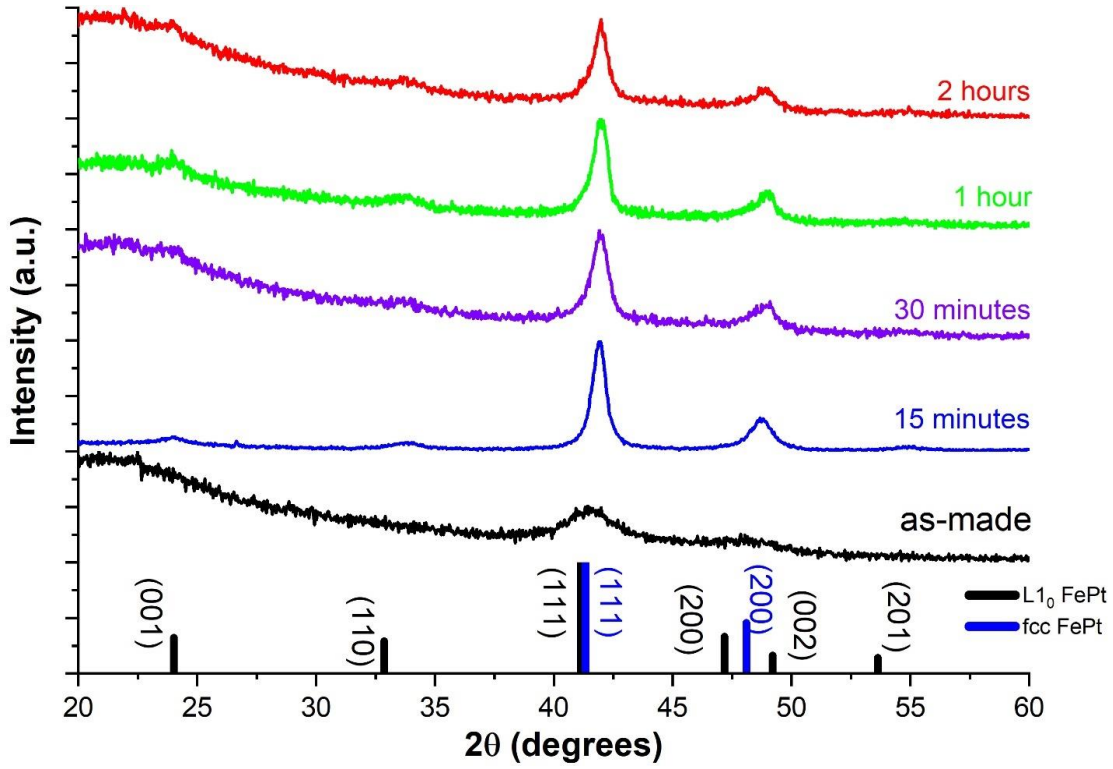

Figure 4.7: XRD data for $FePt_{0.6}Ni_{0.4}$ annealed at 700°C for different durations.

The transformation to the tetragonal structure was also investigated by calculating the lattice parameters *a* and *c* from the XRD data. The following equation was used [27]:

$$\frac{1}{d_{hkl}^2} = \frac{h^2 + k^2}{a^2} + \frac{l^2}{c^2} \tag{4.2}$$

d_{hkl} is the plane separation matching the Miller indices *(hkl)* and is found from the Bragg condition $2d_{hkl} \sin\theta = \lambda$. The following equation can also be used to quantify the chemical ordering in a tetragonal structure [28]:

$$S^2 = \frac{1 - \frac{c}{a}}{1 - \left(\frac{c}{a}\right)_o} \tag{4.3}$$

$\left(\frac{c}{a}\right)_o$ is the ratio for perfect ordering. As a reference, the *c*/a ratio of the perfectly ordered $L1_o$ FePt structure is 0.964 [26]. Table 4.1 lists the sizes estimated using the Scherrer equation, lattice parameters *a* and *c*, and the *c/a* ratio of the different samples annealed under different conditions.

Table 4.1: Estimated size, lattice parameters a and c, and c/a ratio of different samples.

Sample	**Annealing duration**	**Estimated size (nm)**	a **(Å)**	c **(Å)**	c/a
$FePt_{0.8}Ni_{0.2}$	As-made	7	3.814	3.756	0.985
	15 minutes	31	3.824	3.705	0.969
	30 minutes	34	3.822	3.697	0.967
	1 hour	37	3.821	3.705	0.970
	2 hours	42	3.830	3.702	0.967
	16 hours	44	3.833	3.699	0.965
$FePt_{0.7}Ni_{0.3}$	As-made	7	3.792	3.706	0.977
	15 minutes	24	3.797	3.690	0.972
	30 minutes	25	3.808	3.692	0.970
	1 hour	27	3.795	3.690	0.972
	2 hours	35	3.826	3.675	0.961
$FePt_{0.6}Ni_{0.4}$	As-made	3	3.752	3.779	1.000
	15 minutes	13	3.730	3.742	0.997
	30 minutes	14	3.738	3.709	0.992
	1 hour	12	3.723	3.709	0.996
	2 hours	14	3.742	3.711	0.992

For each alloy, the reference sample should be the alloy itself annealed at least a high enough temperature and long enough duration to obtain a complete splitting of the (200) and (002) peaks in their XRD data (near perfect ordering). We are comparing

the change in ordering qualitatively for the samples with the same Ni content annealed under different times, instead of comparing samples of different Ni content. From equation (4.3), a lower *c/a* ratio indicates a higher degree of ordering. For all alloys, Table 4.1 shows that generally, annealing for longer time increases the degree of ordering. In the case of the $FePt_{0.6}Ni_{0.4}$, the chemical ordering is found to change by very little with annealing time of up to 2 hours, again suggesting higher temperatures and/or longer annealing time may be required to get the ordered $L1_0$ structure when the Ni content is high.

4.2.3 Magnetic Properties of $FePt_{1-x}Ni_x$

The room temperature hysteresis loops for the as-synthesized alloys are shown in Figure 4.8(a). The $FePt_{0.8}Ni_{0.2}$ shows a high magnetization with a coercivity of 1.4 kOe, consistent with the low $L1_0$ ordering. The $FePt_{0.7}Ni_{0.3}$, $FePt_{0.6}Ni_{0.4,}$ and $Fe_{1.4}Pt_{0.6}$ alloys show a smaller magnetization with no significant coercivity. We believe the reduction in magnetization of the as-synthesized $FePt_{0.6}Ni_{0.4}$ nanoparticles at 3 T is due to both a smaller particle size and to nonmagnetic organic material left on the particle surfaces from the synthesis. Figure 4.8(b) shows that such an effect is not observed in the annealed sample due to decomposition of organics and increase in particle size because of the high temperature heat treatment.

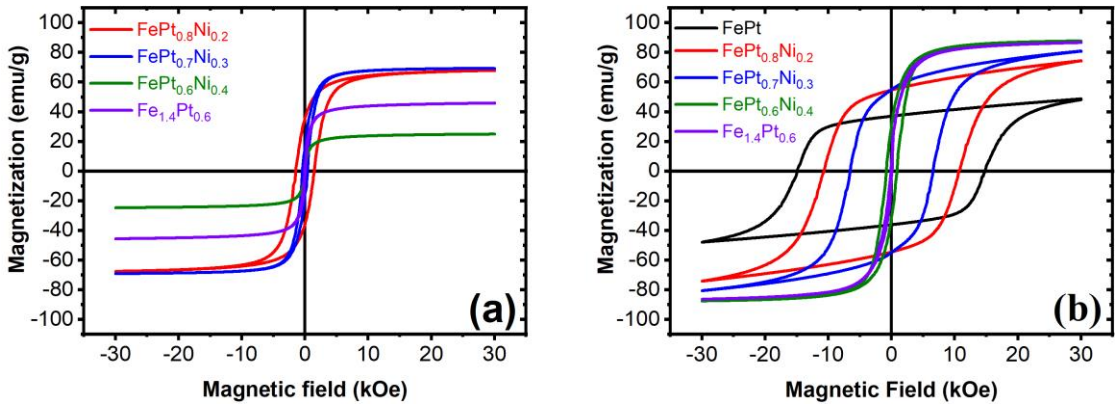

Figure 4.8: Room temperature hysteresis loops of (a) as-synthesized FePt and Fe-Pt-Ni alloys, and (b) after annealing at 700°C for 15 minutes.

Field cooled (FC) and zero field cooled (ZFC) experiments were performed on the as-synthesized $FePt_{0.6}Ni_{0.4}$ sample to verify size effect reduction of magnetization at room temperature due to superparamagnetism. Figure 4.9 shows a blocking temperature at approximately 240 K, estimated from the bifuraction point on the ZFC/FC curves, suggesting superparamagnetic behavior at room temperature leading in part to the lower magnetization observed in the sample.

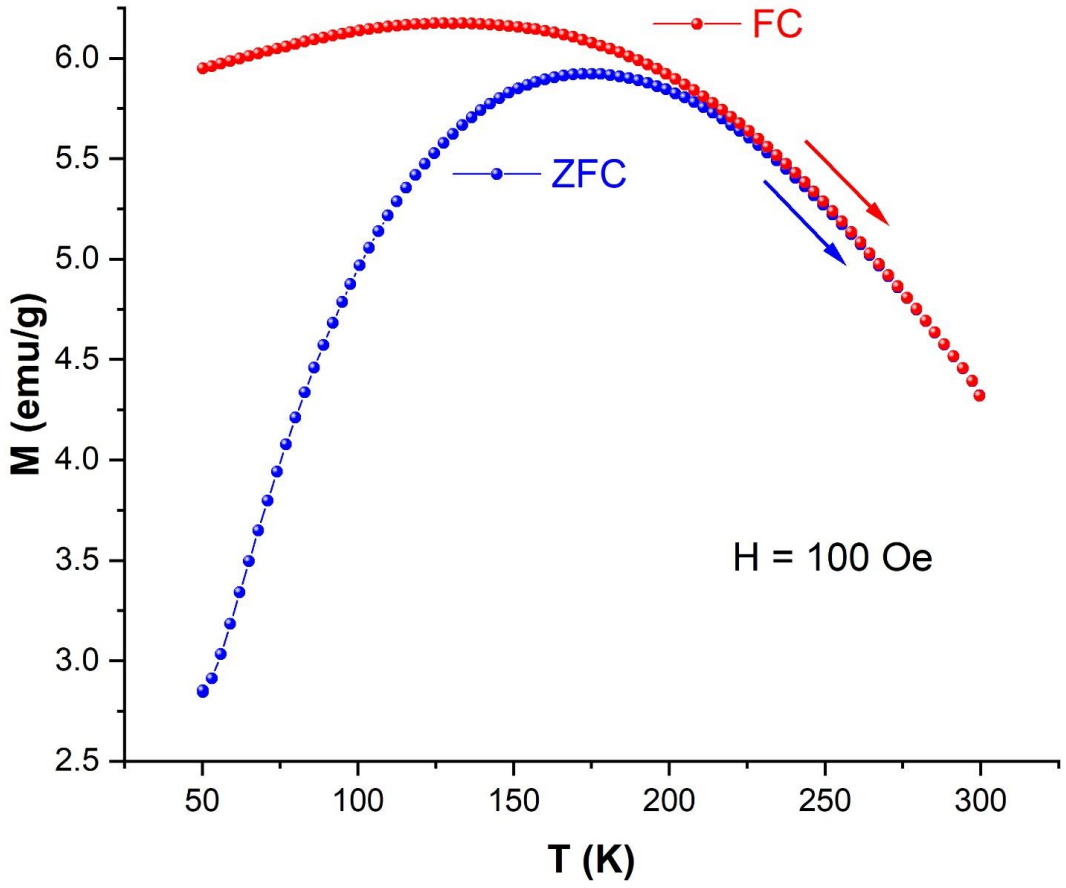

Figure 4.9: Field cooled and zero field cooled measurements on the as-synthesized $FePt_{0.6}Ni_{0.4}$ at 100 Oe applied field.

Figure 4.8(b) shows the room temperature hysteresis loops after 15-minute annealing at 700°C, with all the alloys apart from the $Fe_{1.4}Pt_{0.6}$ composition showing a ferromagnetic behavior with significant increase in coercivity from the as-synthesized alloys. Coercivity decreased from 14.9 kOe in FePt to 0.85 kOe in $FePt_{0.6}Ni_{0.4}$ with increasing nickel content. The magnetization at 3 T increases with increasing Ni content, from 48 emu/g in FePt to 88 emu/g with the $FePt_{0.6}Ni_{0.4}$ alloy. The decrease in coercivity is consistent with the percentage of $L1_0$ structure quantified in Figure 4.2 with the

chemical ordering *S*. The result clearly shows that the partial Pt substitution by Ni in the FePt alloys can lead to a ternary material that keeps a strong magnetically hard behavior up to an alloy composition of $FePt_{0.7}Ni_{0.3}$ with a simultaneous increase in the magnetization value.

At higher percentage of Pt substitution, the result of primary interest is the difference in magnetic properties observed between the $FePt_{0.6}Ni_{0.4}$ and $Fe_{1.4}Pt_{0.6}$ alloys suggesting that Ni substituted for Pt in the lattice leads to a different behavior than simply increasing the overall percentage of magnetic transition metal. Both $FePt_{0.6}Ni_{0.4}$ and $Fe_{1.4}Pt_{0.6}$ alloys after annealing result in similarly high values of magnetization at 3 T, however, only with Ni substitution does the alloy retain hard magnetic properties.

We also investigated the effect of Ni content on the saturation magnetization M_s and anisotropy constant K_1 on the samples annealed at 700°C for 15 minutes. The law of approach to saturation was used (Chapter 2). The magnetization *M* was converted from emu/g to emu/cm^3 by first estimating the densities of the alloys and multiplying the densities by the values of magnetic moments per gram. The volume of the conventional unit cell was found using the lattice parameters *a* and *c*. The mass of a conventional unit cell was estimated by multiplying the mass of each atom type (Fe, Pt, Ni) by the number of atoms in that cell. M was then plotted vs $1/H^2$ using high field values which would produce an accurate linear fit (typically $H \geq 25$ kOe values were chosen). Figure 4.10 shows one example of such a plot with the linear fitting, for the $FePt_{0.8}Ni_{0.2}$ sample. The slope of the straight line is used to determine the anisotropy constant and the extrapolation to zero $1/H^2$ gives the magnetization M_s. These values for $FePt_{0.8}Ni_{0.2}$ are 1090 emu/cm^3 and 1.64×10^7 erg/cm^3. For comparison, the room temperature value of K_1 for $L1_0$ FePt is about 70 Merg/cm^3 [1,2,29].

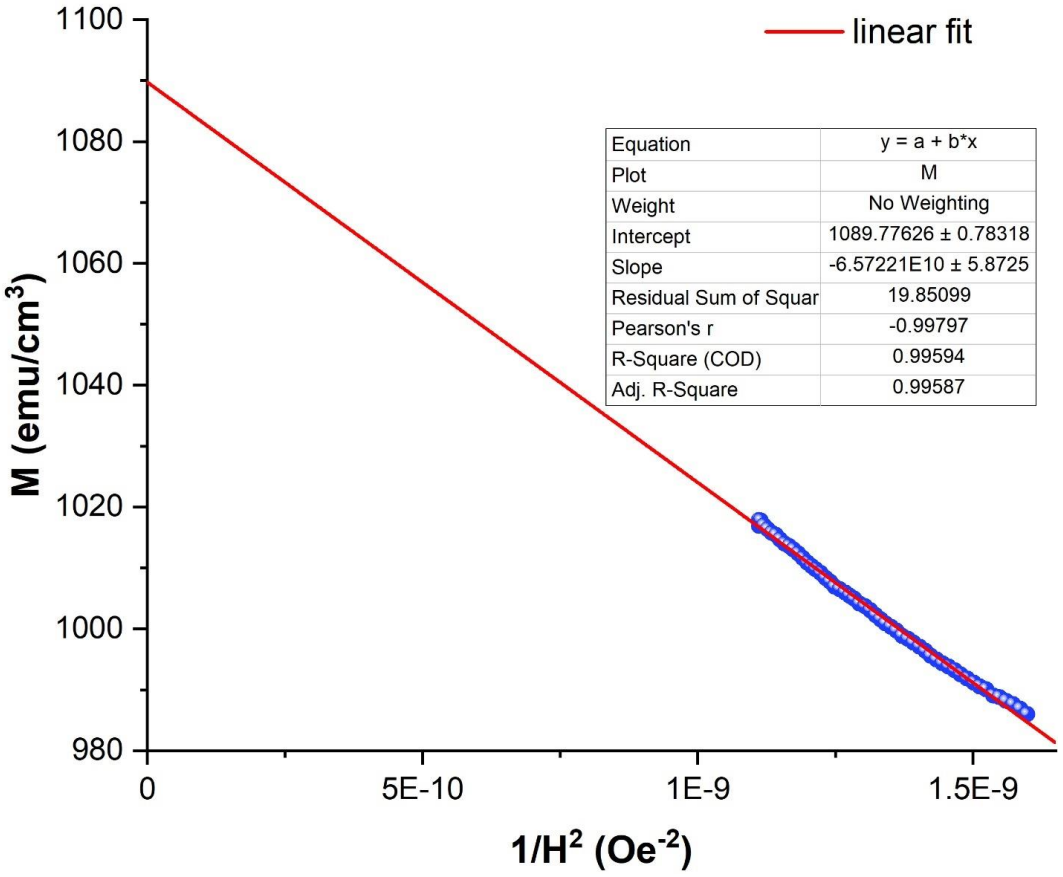

Figure 4.10: Example of M versus $1/H^2$ graph for $FePt_{0.8}Ni_{0.2}$ annealed at 700°C for 15 minutes.

In general, alloys with larger Ni content have higher M_s values but lower K_1 as seen in Figure 4.11. This again correlates with a higher degree of chemical ordering at low Ni content.

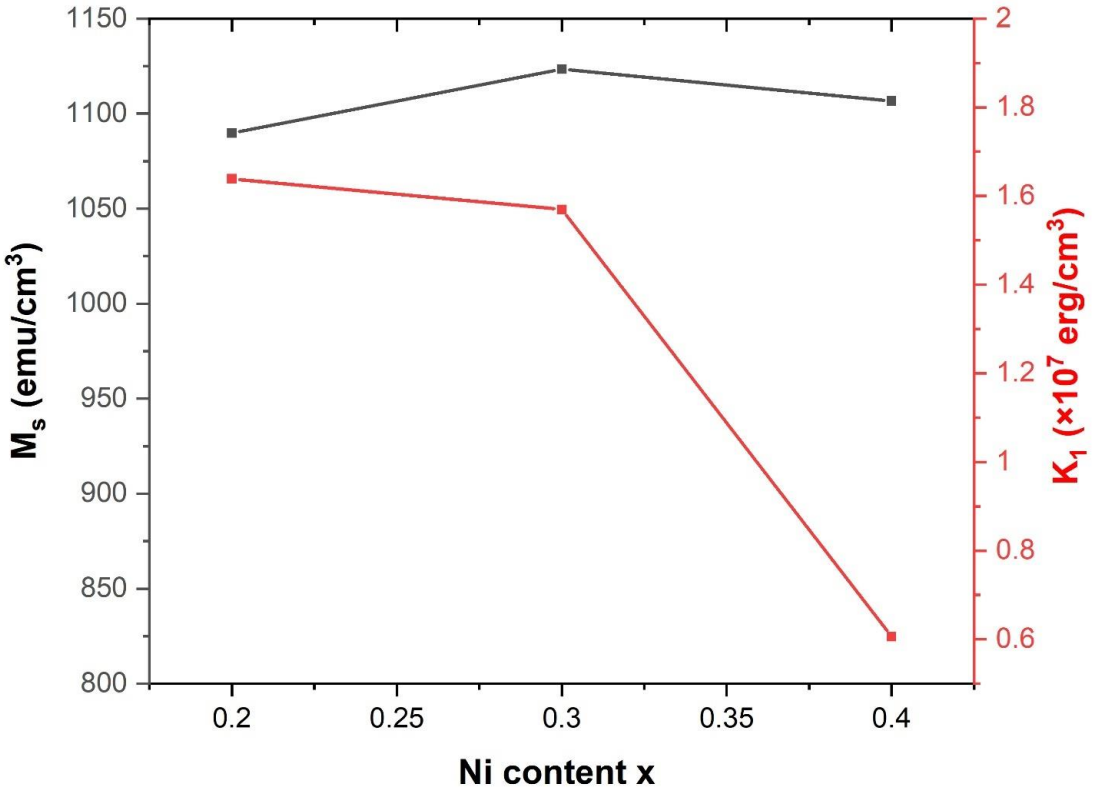

Figure 4.11: Variation of saturation magnetization M_s and anisotropy constant K_1 with nickel content for samples annealed at 700°C for 15 minutes.

The variation of coercivity with annealing time was also investigated for each alloy. The hysteresis loops for $FePt_{1-x}Ni_x$ with $x = 0.2, 0.3, 0.4$ are shown in Figures 4.12-4.14.

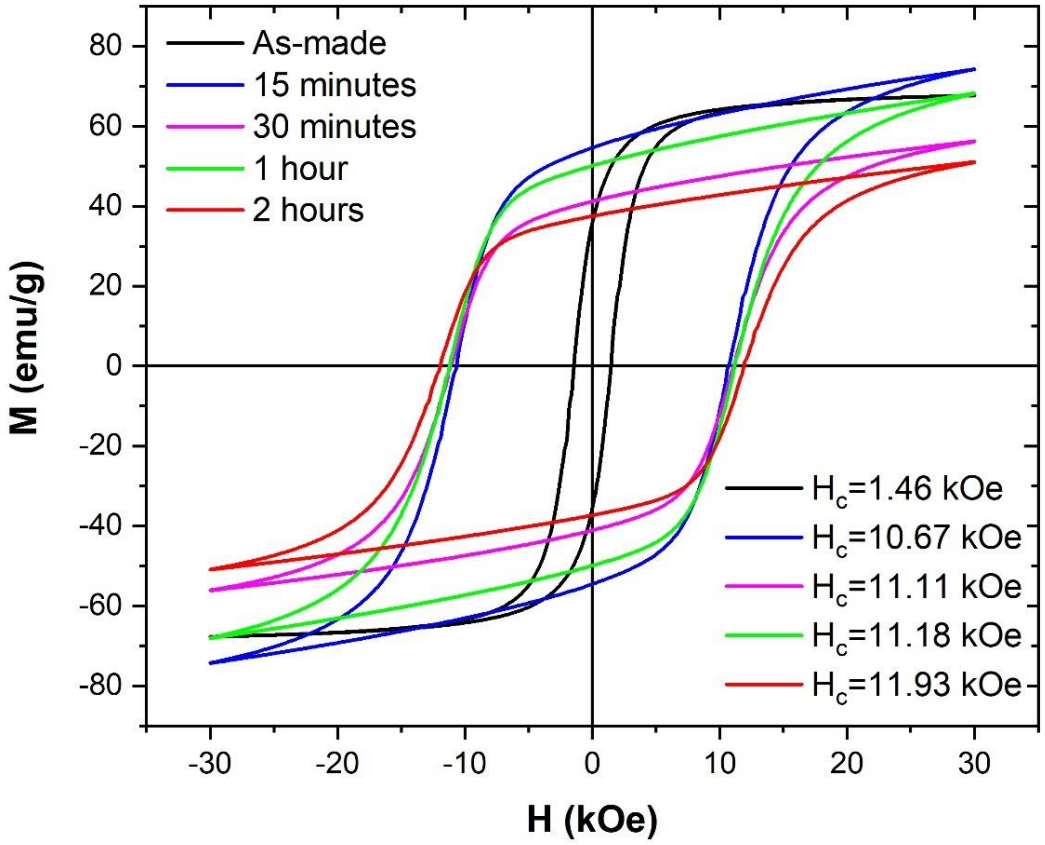

Figure 4.12: Room temperature hysteresis loops on as-synthesized $FePt_{0.8}Ni_{0.2}$ and $FePt_{0.8}Ni_{0.2}$ annealed at 700°C for different durations.

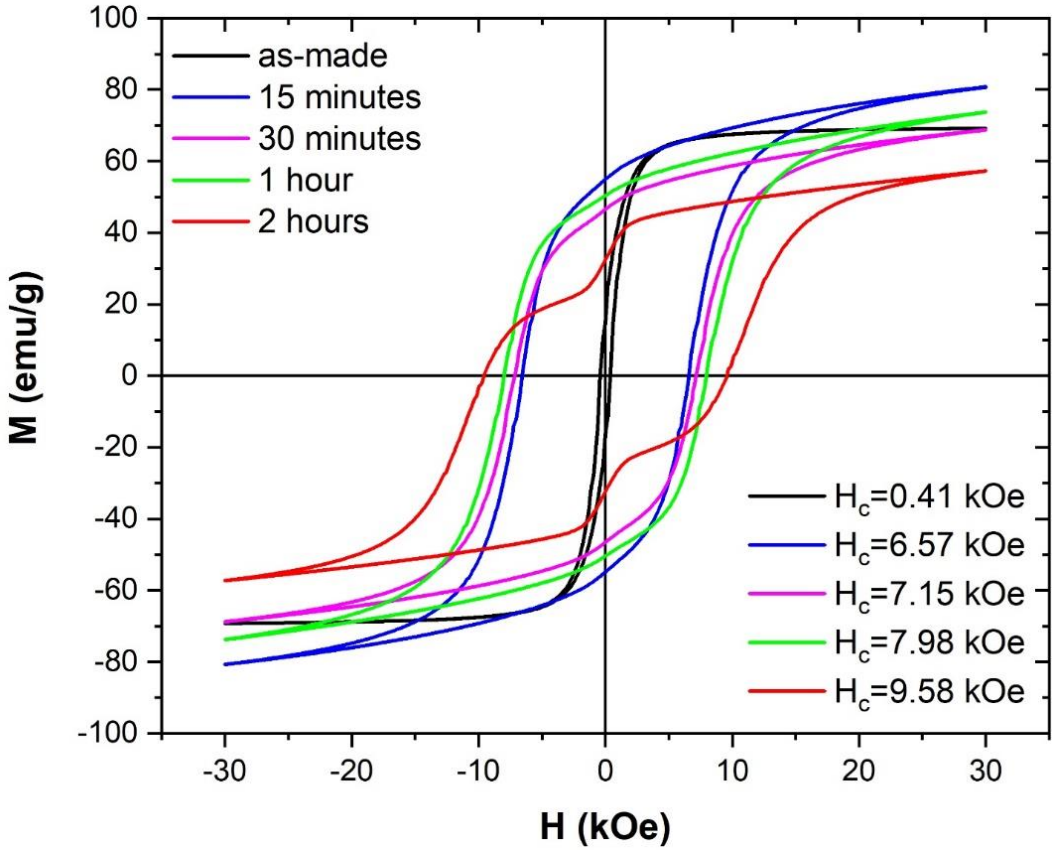

Figure 4.13: Room temperature hysteresis loops on as-synthesized $FePt_{0.7}Ni_{0.3}$ and $FePt_{0.7}Ni_{0.3}$ annealed at 700°C for different durations. The shoulder for the 2-hour data is due to the presence of the magnetically soft Fe_3O_4 phase.

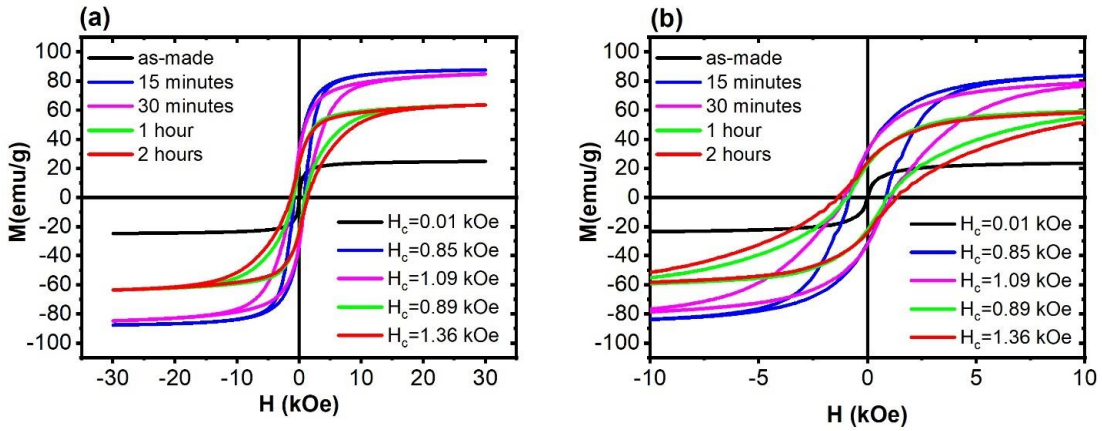

Figure 4.14: (a) Room temperature hysteresis loops on as-synthesized $FePt_{0.6}Ni_{0.4}$ and $FePt_{0.6}Ni_{0.4}$ annealed at 700°C for different durations. (b) Expanded view to better show variation of coercivity with annealing temperature.

In general, the coercivity increased with annealing time, which is again indicative of an ongoing transformation to the $L1_0$ phase. A plot of coercivity versus annealing time further reveals that at an annealing temperature of 700°C, the transformation towards a fully ordered $L1_0$ phase is less complete for higher Ni content for annealing times up to 2 hours (Figure 4.15).

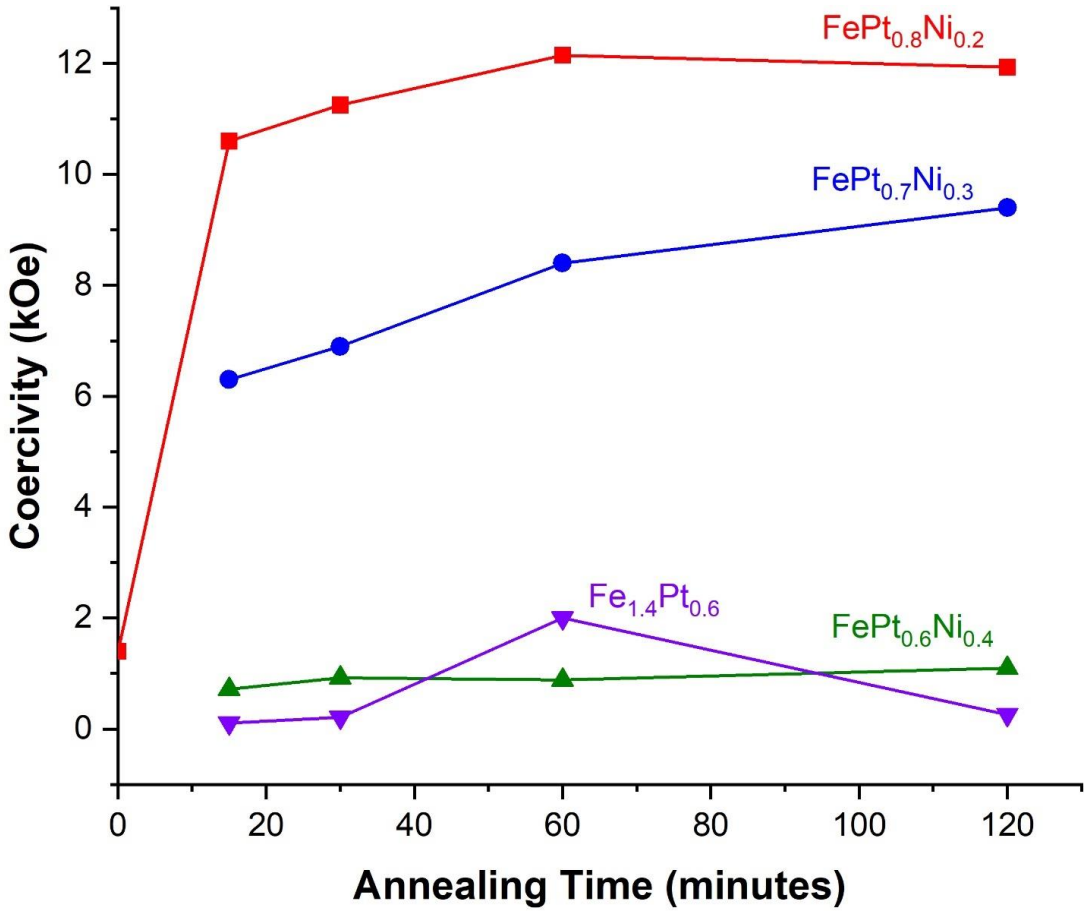

Figure 4.15: Variation of coercivity with annealing temperature of the different FePtNi alloys.

Thermomagnetic measurements were performed at high temperatures to investigate the effect the Ni content has on the temperature of the phase transformation from ferromagnetic to paramagnetic state (the Curie temperature). All alloys were annealed at 700°C for 30 minutes. The measurements were done at an applied field of 500 Oe. The samples were heated from 300 K to 900 K, and then then cooled back to 300 K. Figure 4.16(a) shows the thermomagnetic measurements on the $FePt_{0.8}Ni_{0.2}$

nanoparticles. Figure 14.16(b) shows the corresponding plot of magnetization squared as a function of temperature which shows how the Curie temperature was determined.

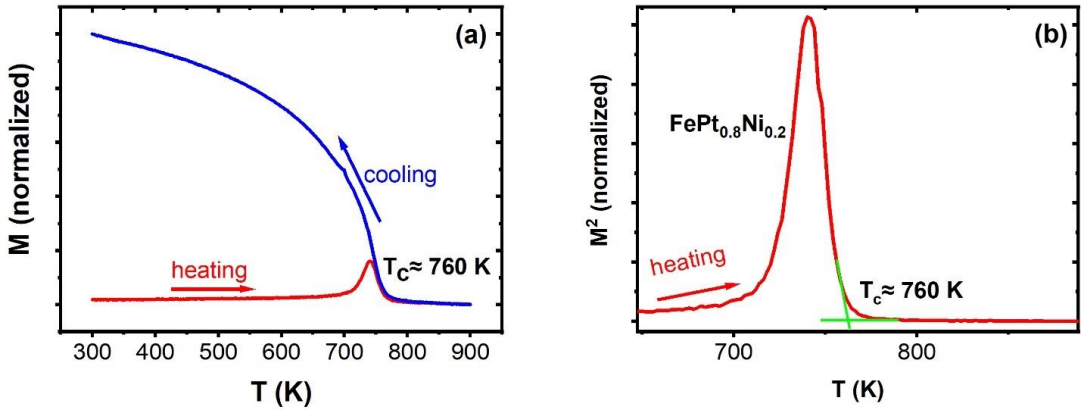

Figure 4.16: (a) Thermomagnetic measurements of $FePt_{0.8}Ni_{0.2}$ annealed at 700°C for 30 minutes and (b) the corresponding magnetization squared versus temperature showing how the Curie temperature was determined.

For alloys with a higher Ni to Pt ratio, the Curie temperature decreased as shown in Figure 4.17.

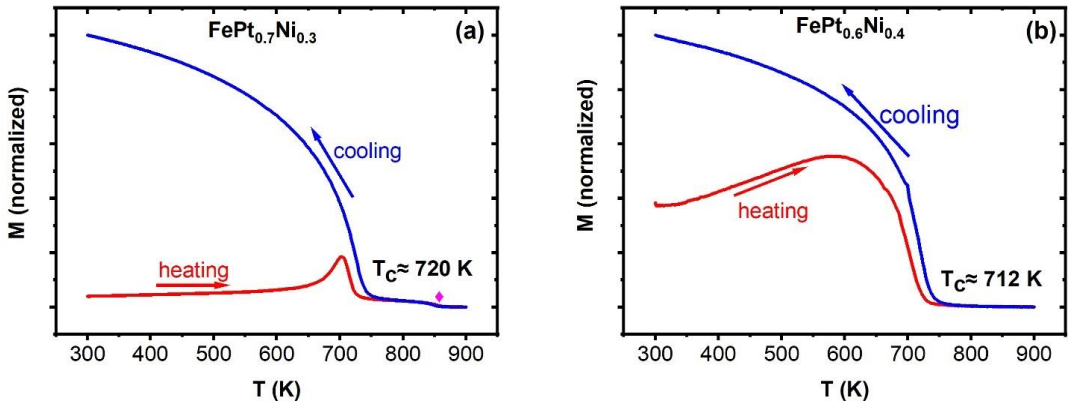

Figure 4.17: Thermomagnetic measurements of (a) $FePt_{0.7}Ni_{0.3}$ and (b) $FePt_{0.6}Ni_{0.4}$. Both samples are annealed at 700°C for 30 minutes. The ♦ in the thermomagnetic data for $FePt_{0.7}Ni_{0.3}$ indicates the presence of Fe_3O_4.

In our $FePt_{0.7}Ni_{0.3}$ sample, the presence of an Fe_3O_4 phase was indicated by the presence of a secondary Curie temperature above 850 K in the thermomagnetic data. The presence of the Fe_3O_4 phase was especially visible in the $FePt_{0.7}Ni_{0.3}$ nanoparticles annealed for 2 hours. Its XRD data in Figure 4.6 has a peak around 36°, which coincides with the location of the main peak of Fe_3O_4 in this range of 2θ values, the (311) peak. The shape of its hysteresis loops in Figure 4.13 also shows the presence of a soft magnetic phase.

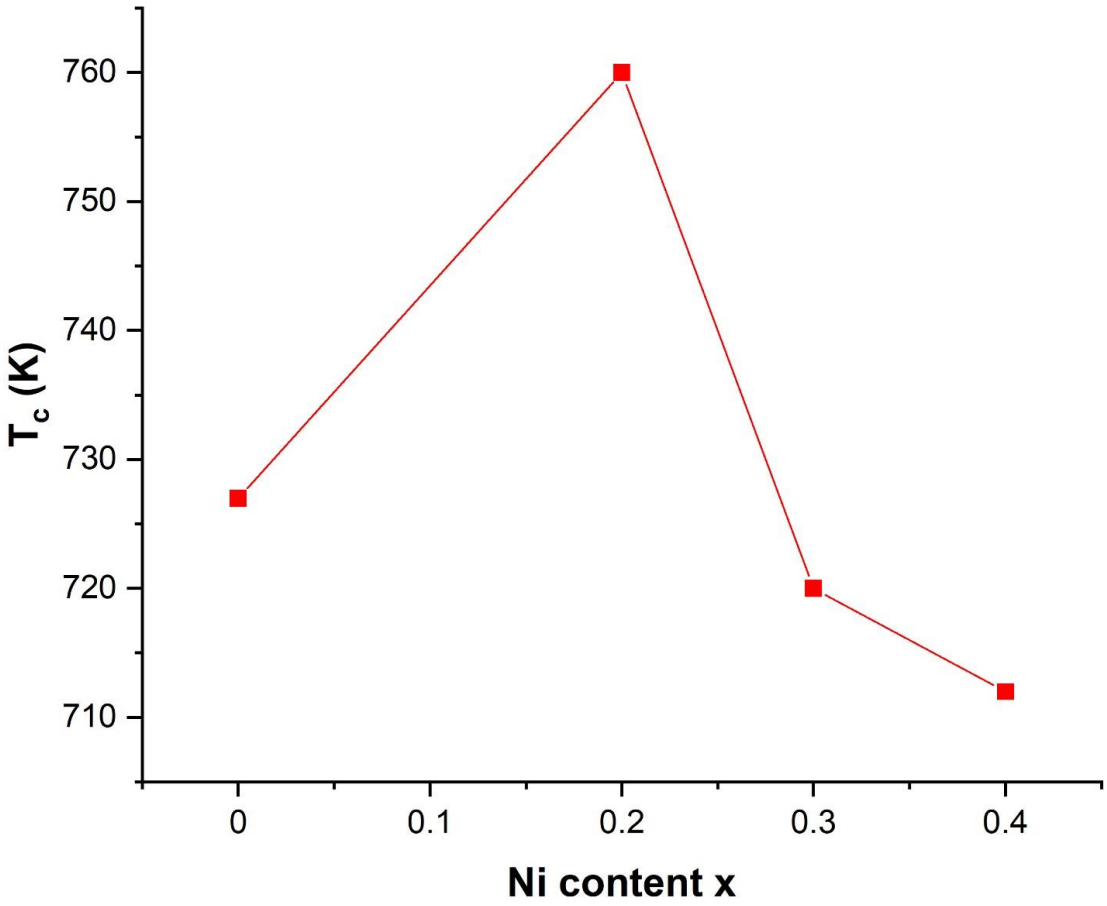

Figure 4.18: Curie temperature vs Ni content for x = 0 (FePt), 0.2, 0.3 and 0.4. All samples were annealed at 700°C for 1 hour.

For comparison, we chemically synthesized $L1_0$ FePt nanoparticles and annealed them at 700°C for 1 hour. Their Curie temperature was found be around 727 K. Figure 4.18 shows that adding a small amount of Ni in the lattice to form the $FePt_{0.8}Ni_{0.2}$ drastically increases the Curie temperature. However, subsequent Pt substitution by Ni decreases the Curie temperature (x = 0.3 and 0.4).

4.3 FePtNiBi Alloys

4.3.1 Structural Properties of FePtNiBi Alloys

Our earlier studies showed that the addition of a small amount of Bi assists the ordering to the $L1_0$ structure in FePt nanoparticles [30]. Therefore, we decided to investigate this effect on the FePtNi particles we synthesized. The procedure used to obtain FePtNiBi nanoparticles was similar to the one used to produce FePtNi alloys, with the modification that 0.025 mmol of bismuth(ii) acetate added to the mixture. XRD data in Figure 4.19 of the as-made nanoparticles shows that Bi addition to 10% the molar amount of Fe does not produce the $L1_o$ phase in the as-made state. The main Fe_3O_4 peak appeared around 36° and was most prominent in the $FePt_{0.7}Ni_{0.3}$ (+10% Bi) and $FePt_{0.6}Ni_{0.4}$(+10% Bi) particles.

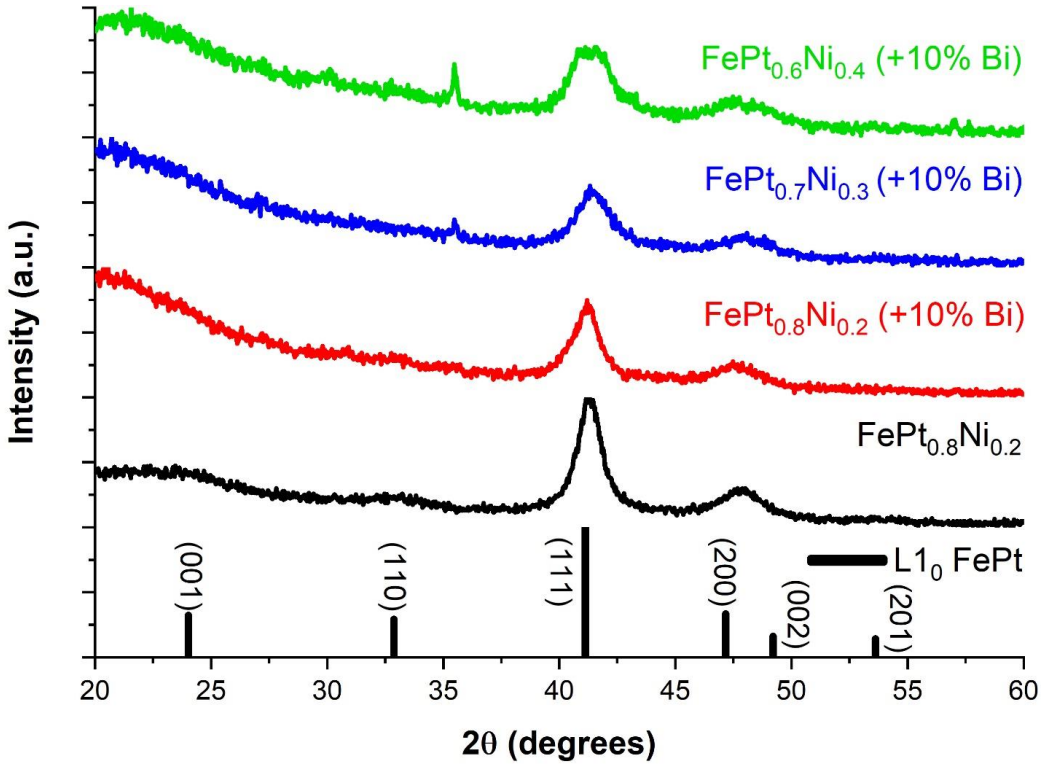

Figure 4.19: XRD data of as-made $FePt_{1-x}Ni_x$ (+10% Bi) particles. The XRD of as-synthesized $FePt_{0.8}Ni_{0.2}$ is included for comparison.

Upon annealing at 700°C for 30 minutes, the $L1_0$ phase was formed, as shown by the XRD pattern in Figure 4.20. Bi also introduced additional phases, as seen by the presence of additional peaks.

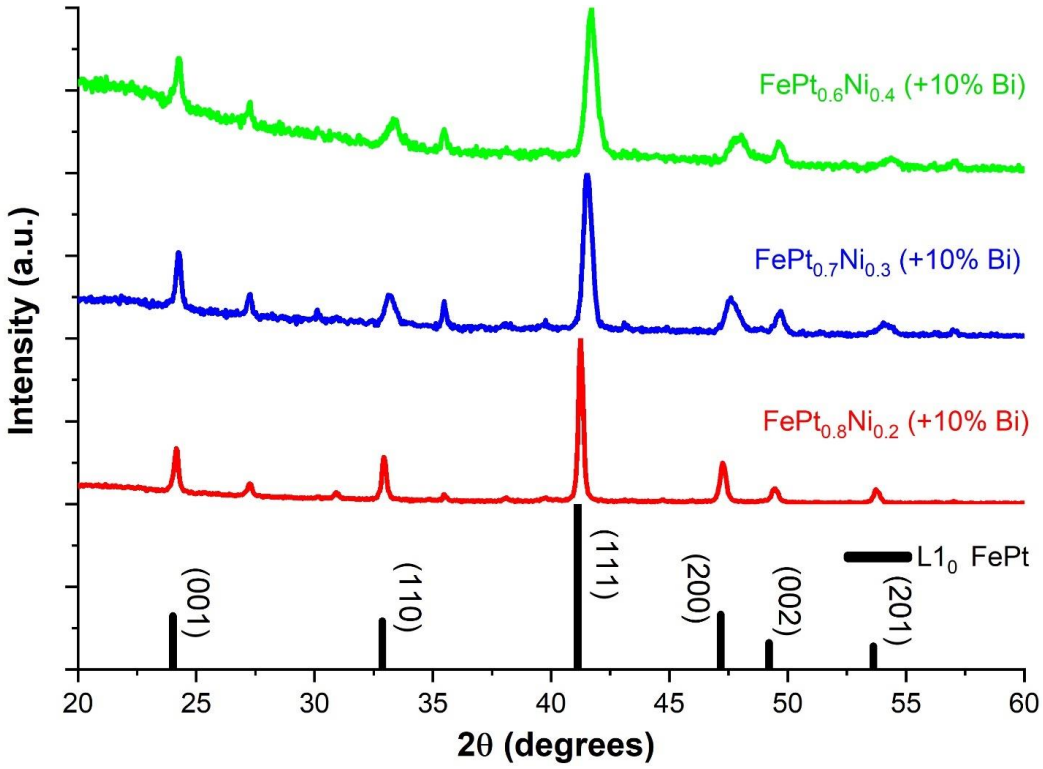

Figure 4.20: XRD data for $FePt_{1-x}Ni_x$ (+10% Bi) annealed at 700°C for 30 minutes.

The introduction of Bi in the structure has a noticeable effect on the ordering parameter. The addition of a small amount of Bi increases the chemical ordering. This is seen by a bigger splitting of the (200) and (002) peak and also by the larger I_{001}/I_{111} peak intensity ratio, compared to when no Bi was used previously. To better quantify the $L1_0$ ordering, the c/a ratio of $FePt_{1-x}Ni_x$ (+10% Bi) nanoparticles were found and compared to the corresponding c/a ratio of the corresponding $FePt_{1-x}Ni_x$ samples for the same *x*, for the case of samples annealed at 700°C for 30 minutes. The results are listed in Table 4.2. The change in lattice parameters is mainly due to the higher degree of ordering caused using Bi because Bi does not enter the unit cell.

Table 4.2: Lattice parameters, c/a ratio, and estimated sized of samples annealed at 700°C for 30 minutes. The sizes were estimated using the Scherrer equation.

Sample	**Estimated size (nm)**	***a* (Å)**	***c* (Å)**	c/a
$FePt_{0.8}Ni_{0.2}$	34	3.822	3.697	0.967
$FePt_{0.8}Ni_{0.2}$ (+10% Bi)	45	3.844	3.688	0.959
$FePt_{0.7}Ni_{0.3}$	25	3.808	3.692	0.970
$FePt_{0.7}Ni_{0.3}$ (+10% Bi)	23	3.823	3.673	0.961
$FePt_{0.6}Ni_{0.4}$	14	3.738	3.709	0.992
$FePt_{0.6}Ni_{0.4}$ (+10% Bi)	18	3.803	3.668	0.964

From equation (4.3) for ordering parameter S,

$$S^2 = \frac{1 - \frac{c}{a}}{1 - \left(\frac{c}{a}\right)_o} \tag{4.3}$$

the ordering parameter is higher when c/a is lower. The actual values of S were not computed owing to the difficulty to comparing the ordering parameter across samples with different x using a unified reference sample with lattice parameter ratio $(c/a)_o$. Like in the case of $FePt_{1-x}Ni_x$ previously described, the reference sample should be one with the same value of *x*, which has been heat treated under the correct temperature and time conditions that give a fully ordered structure. Usually this signifies annealing at high temperatures (at least 700°C for $FePt_{0.8}Ni_{0.2}$ and possibly higher for the higher Ni content) for long periods of time. From Table 4.2, the calculated c/a values support the fact that that for the same Ni composition *x*, Bi enhances the $L1_0$ ordering.

The XRD patterns of both the as-made and annealed nanoparticles also reveals that the 10% Bi addition introduces other phases in the samples, which we will demonstrate to have an effect on their magnetic properties. Based on the XRD pattern of the $FePt_{0.7}Ni_{0.3}$ heat treated at 700°C for 2 hours where it is clear that there was Fe_3O_4 present, the (311) peak around 35° is suspected – and eventually confirmed – to be that of Fe_3O_4. To verify this, we prepared a sample using 30% less Fe precursor to produce an alloy with a lower concentration of Fe, $Fe_{0.7}Pt_{0.7}Ni_{0.3}$ (+10% Bi) and its XRD pattern was compared to that of a $FePt_{0.7}Ni_{0.3}$ (+10% Bi) sample annealed under the same conditions (Figure 4.21).

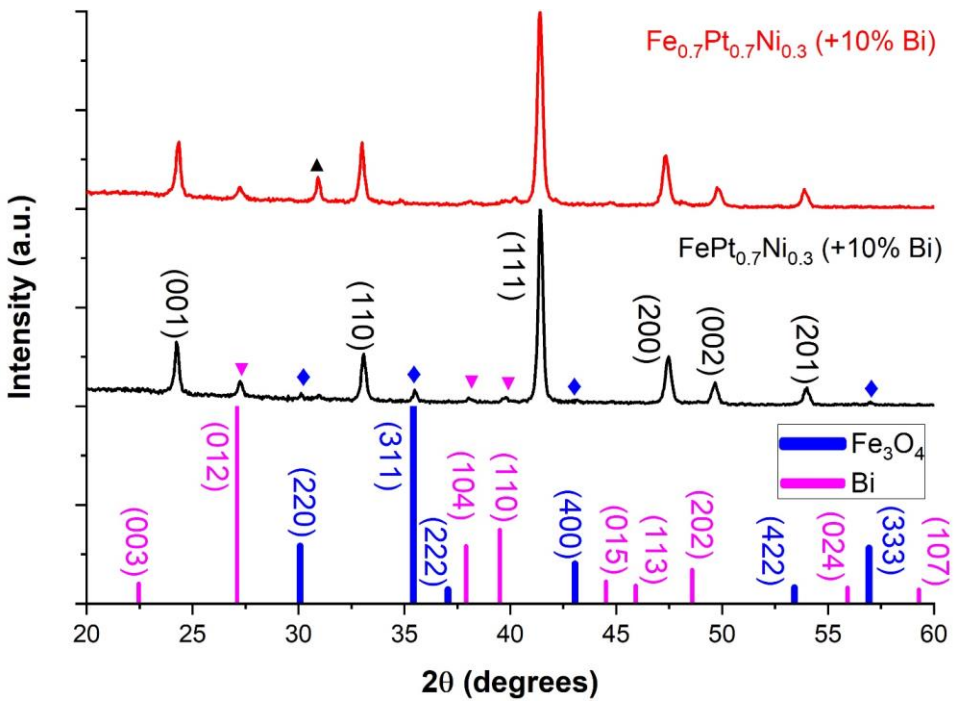

Figure 4.21: Comparison of XRD patterns of $FePt_{0.7}Ni_{0.3}$ (+10% Bi) and $Fe_{0.7}Pt_{0.7}Ni_{0.3}$ (+10% Bi). Both samples are annealed at 700°C for 30 minutes. The stronger peaks of Fe_3O_4 are marked by ♦ and those of Bi by ▼. The peak marked by ▲ is the strongest peak of $PtBi_2$ in this range of 2θ. The $L1_0$ peaks are also indexed in black in the $FePt_{0.7}Ni_{0.3}$ pattern.

The main (311) Fe_3O_4 peak is not visible in the XRD pattern of the $Fe_{0.7}Pt_{0.7}Ni_{0.3}$ (+10% Bi), suggesting less Fe was available to be oxidized to Fe_3O_4 in this sample. In contrast, the more intense peaks of Fe_3O_4 are seen in the XRD pattern of $FePt_{0.7}Ni_{0.3}$ (+10% Bi) sample. These XRD data suggest that it may be possible to reduce the Fe_3O_4 content formed in the FePtNi samples synthesized with Bi addition by controlling the Fe precursor amount. More studies are needed to find the right precursor ratios required to decrease as much as possible the amount of Fe_3O_4 in our samples.

To identify other Fe related phases present, we performed Mössbauer studies on these two samples, both in the as-made and the annealed states. The Mössbauer spectra of the $Fe_{0.7}Pt_{0.7}Ni_{0.3}$ (+10% Bi) and $FePt_{0.7}Ni_{0.3}$ (+10% Bi) are shown in Figures 4.22 and 4.23.

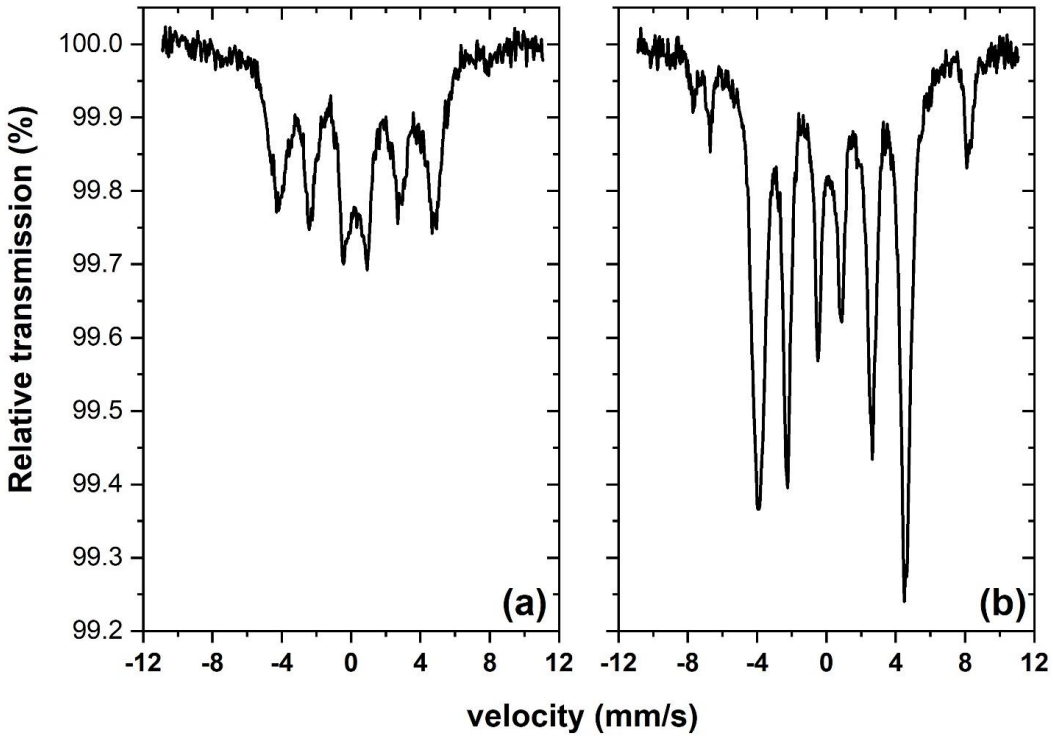

Figure 4.22: Mössbauer spectra of (a) as-made and (b) annealed $Fe_{0.7}Pt_{0.7}Ni_{0.3}$ (+10% Bi) nanoparticles.

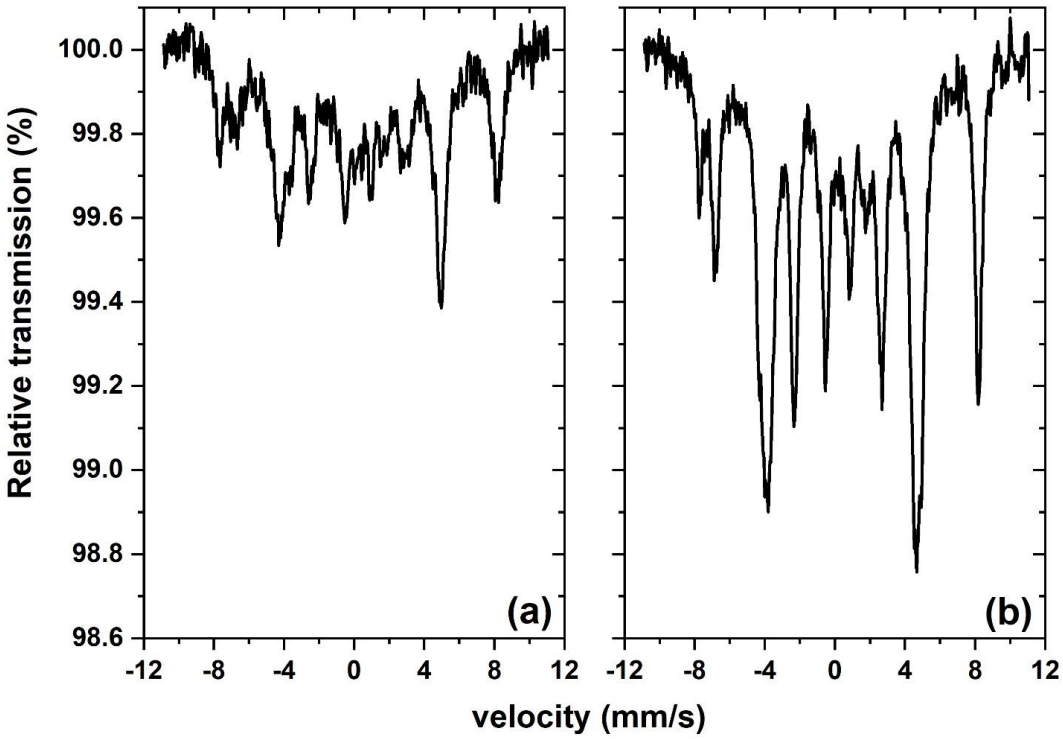

Figure 4.23: Mössbauer spectra of (a) as-made and (b) annealed $FePt_{0.7}Ni_{0.3}$ (+10% Bi) nanoparticles.

A detailed analysis reveals that no iron oxide is detectable in the as-made sample of $Fe_{0.7}Pt_{0.7}Ni_{0.3}$ (+10% Bi). The annealed samples have approximately 10% Fe_3O_4 and 3% Fe_2O_3. In the case of $FePt_{0.7}Ni_{0.3}$ (+10% Bi), the approximate Fe_3O_4/Fe_2O_3 oxide ratio in the as made sample is 27%: 9% and 28%:3% in the annealed sample. It is to be noted that these ratios are approximate, and one source of uncertainty in quantifying the oxide content arises from the relatively low mass of samples used in those measurements. The main qualitative results of the Mössbauer studies are that the $Fe_{0.7}Pt_{0.7}Ni_{0.3}$ (+10% Bi) sample have less oxides than its Fe-rich counterpart, again suggesting the possibility of controlling the amount of oxides formed in the sample by tuning the Fe:Pt precursor ratio used in the synthesis.

To further investigate the origin of Fe_3O_4 in our FePtNiBi samples, we synthesized another sample using the same procedure as before, but without any Pt, Ni and Bi precursor, which we will label as $FePt_0Ni_0$ (+0% Bi). The XRD patterns of $FePt_0Ni_0$ (+0% Bi) in both as-made and annealed (at 700°C for 30 minutes) states in Figure 4.24 show that Fe_3O_4 is present. We conclude that Fe_3O_4 is formed by the reduction of the $Fe(acac)_3$ precursor by 1,2-hexadecanediol, the reducing agent used in the synthesis.

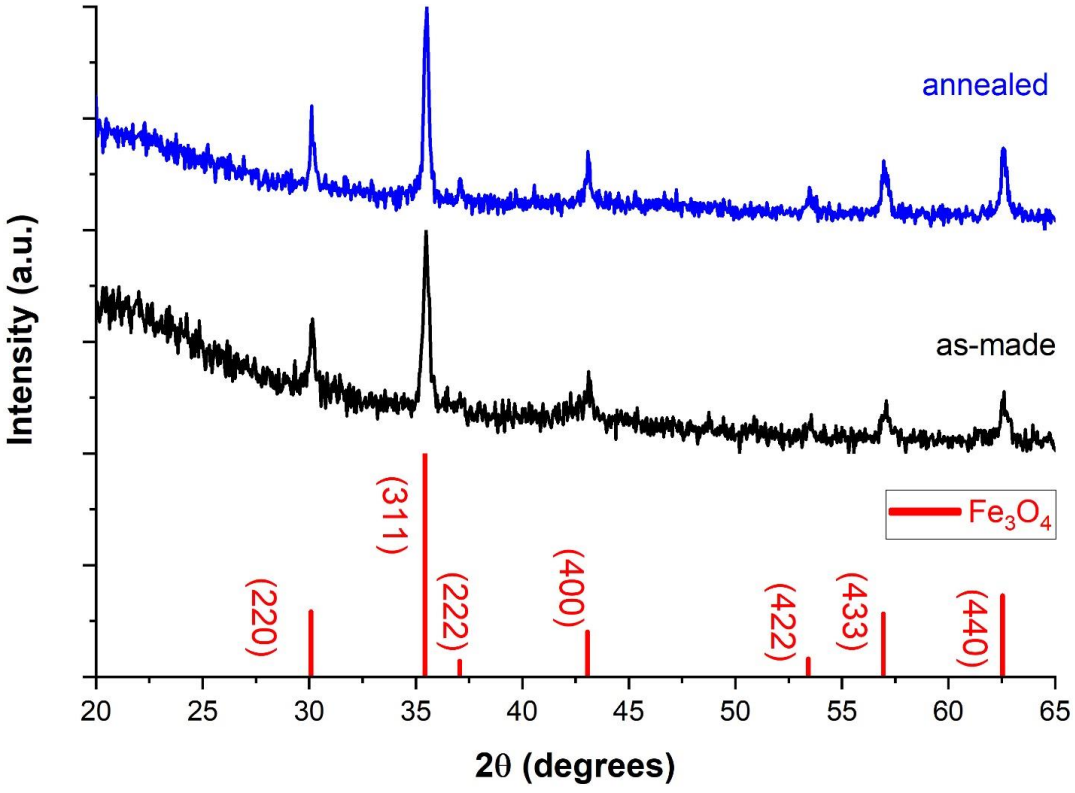

Figure 4.24: XRD pattern of as-made and annealed $FePt_0Ni_0$ (+0% Bi), revealing the presence of Fe_3O_4 as a by-product of the synthesis.

4.3.2 Magnetic Properties of FePtNiBi Alloys

The effect of Bi addition on coercivity was investigated by measuring magnetization as a function of applied field at room temperature on the $FePt_{1-x}Ni_x$ (+10% Bi) nanoparticles annealed at 700°C for 30 minutes. The hysteresis loops are shown in Figures 4.25 – 4.27 and include the corresponding data for the $FePt_{1-x}Ni_x$ with the same Ni content annealed under the same condition for comparison.

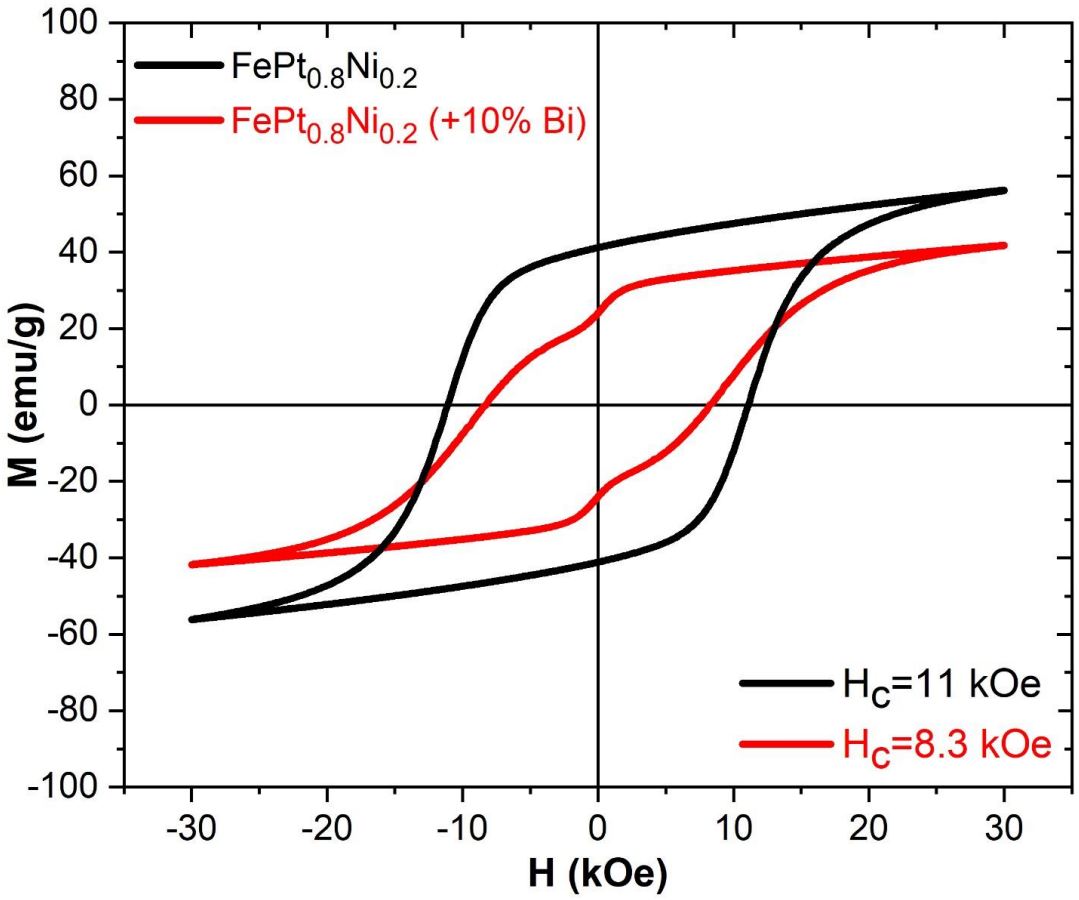

Figure 4.25: Room temperature hysteresis data of the $FePt_{0.8}Ni_{0.2}$ (+10% Bi) and $FePt_{0.8}Ni_{0.2}$ nanoparticles annealed at 700°C for 30 minutes.

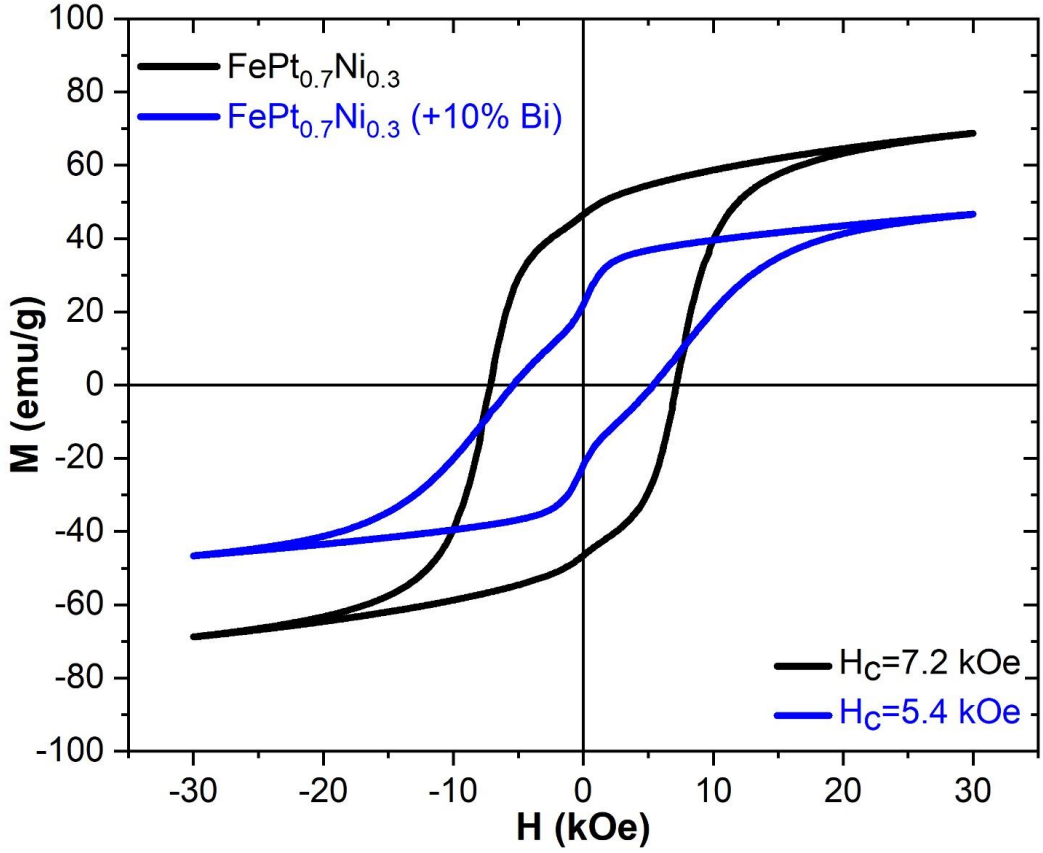

Figure 4.26: Room temperature hysteresis data of the $FePt_{0.7}Ni_{0.3}$ (+10% Bi) and $FePt_{0.7}Ni_{0.3}$ nanoparticles annealed at 700°C for 30 minutes.

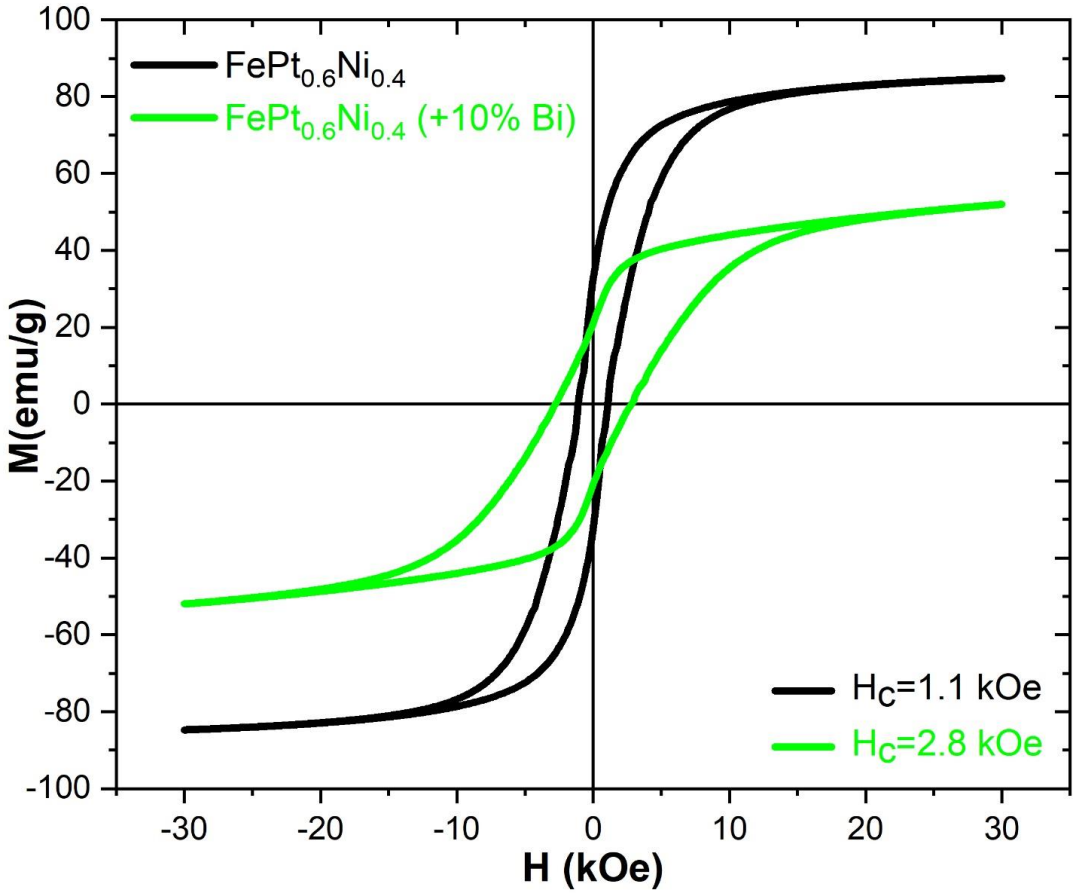

Figure 4.27: Room temperature hysteresis data of the $FePt_{0.6}Ni_{0.4}$ (+10% Bi) and $FePt_{0.6}Ni_{0.4}$ nanoparticles annealed at 700°C for 30 minutes.

For $x = 0.2$ and $x = 0.3$, Bi addition leads to a decrease in coercivity in these samples despite the improvement in their $L1_0$ ordering as discussed earlier. The shapes of their hysteresis loops in Figures 4.25 and 4.26 suggest the presence of soft phases. As discussed earlier, one of these phases is Fe_3O_4 which is ferrimagnetic and magnetically soft. The XRD pattern in Figure 4.21 also shows that minority phases such as Bi and $PtBi_2$ also emerge when Bi is used in the nanoparticle synthesis. These soft phases cause an overall decrease in the coercivity, as compared to the $FePt_{1-x}Ni_x$ samples synthesized without using Bi for up to $x = 0.3$.

In contrast, an increase in coercivity is observed for $x = 0.4$. This may be explained by two competing effects. Firstly, the replacement of Pt by Ni in FePt decreases the chemical ordering as previously described. Bi addition on the other hand improves the chemical ordering. For $x = 0.4$, the XRD data in Figure 4.20 for the annealed $FePt_{0.6}Ni_{0.4}$ (+10% Bi) shows a more complete splitting of the (200) and (002) peaks, compared to the corresponding data for $FePt_{0.6}Ni_{0.4}$ in Figure 4.7, where the two peaks are not yet resolved. For this sample, the enhancement of the $L1_0$ structure from Bi addition is more important than the decrease in ordering from a higher Ni content, leading to an overall increase in coercivity.

We also studied the effect of Bi addition on Curie temperature. The magnetic moment of the annealed samples (700°C, 30 minutes) was measured at an applied field of 500 Oe. Only the heating curves are shown in Figures 4.28 and 4.29. The Curie temperature was determined as explained before, from a plot of the magnetization squared versus temperature (see Figure 4.16).

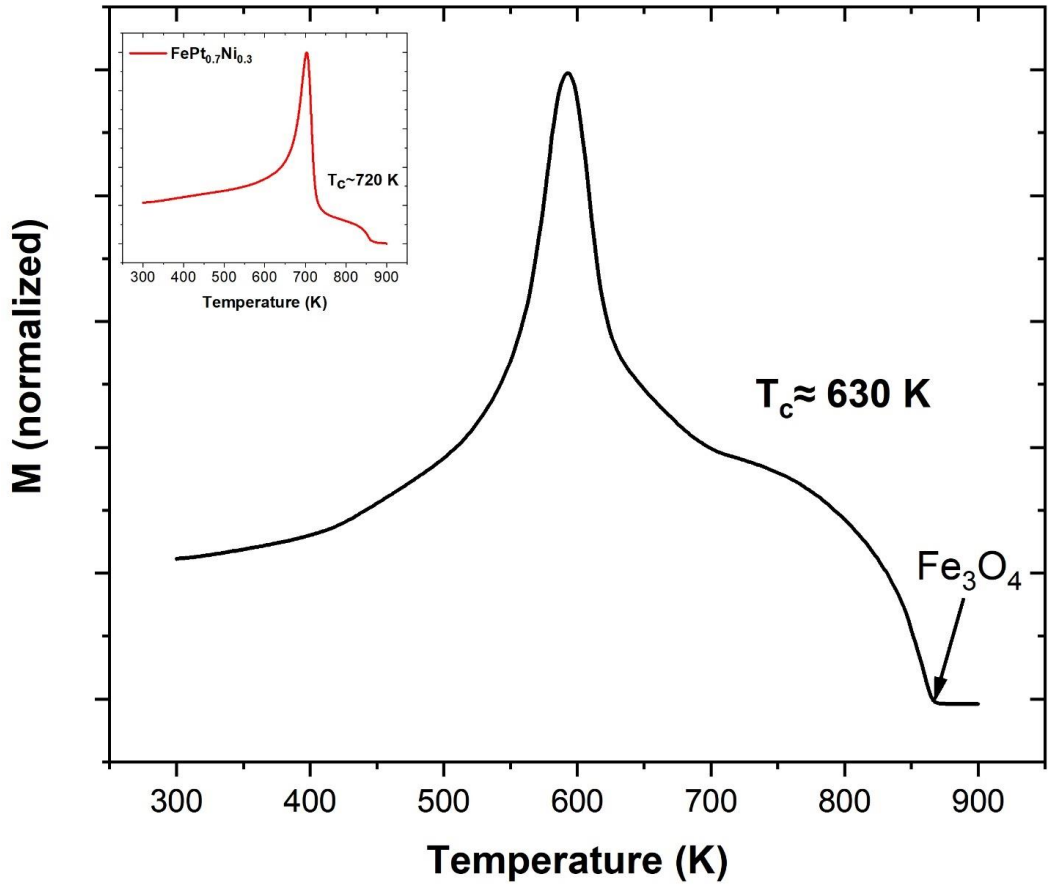

Figure 4.28: Thermomagnetic measurement on $FePt_{0.7}Ni_{0.3}$ (+10% Bi). The inset shows the corresponding data for $FePt_{0.7}Ni_{0.3}$.

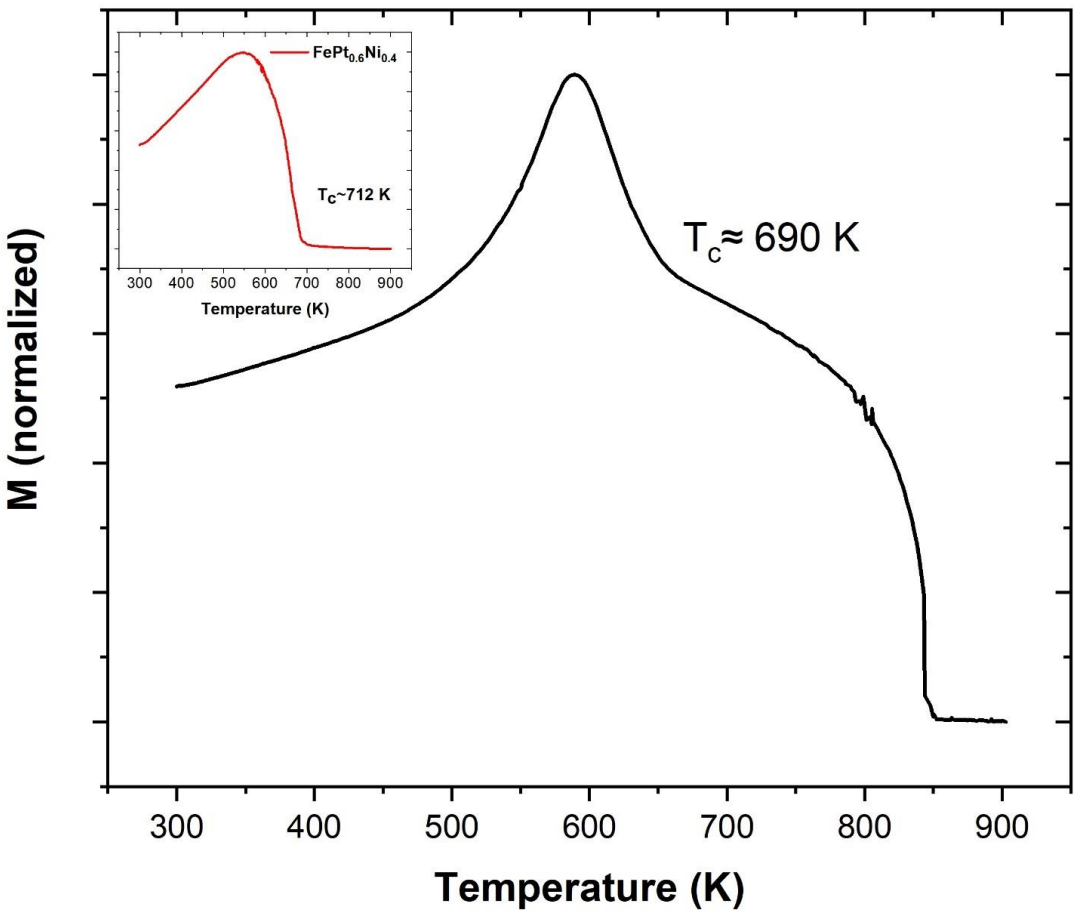

Figure 4.29: Thermomagnetic measurement on $FePt_{0.6}Ni_{0.4}$ (+10% Bi). The inset shows the corresponding data for $FePt_{0.6}Ni_{0.4}$.

The presence of Fe_3O_4 is again seen from a transition around 850 K in both Figures 4.28 and 4.29. As far as the importance of the presence of Bi is concerned, the addition of Bi to $FePt_{1-x}Ni_x$ considerably decreases the Curie temperature in the case of $x = 0.3$ (by about 90 K). The decrease is smaller for $x = 0.4$.

4.3.3 Effect of Modifying The Bi Content on Structural and Magnetic Properties of $FePt_{0.7}Ni_{0.3}$

Since Bi clearly enhances the formation of the $L1_0$ phase, we also explored the effect of varying the amount of Bi inserted in the $FePt_{1-x}$ alloys on the magnetic properties of the $FePt_{1-x}Ni_x$ alloys. We prepared samples with twice and three times the amount of Bi used previously (20% Bi and 30% Bi), for $x = 0.3$. These samples were annealed at 700°C for 30 minutes. Figure 4.30 shows the XRD patterns of the as-made samples.

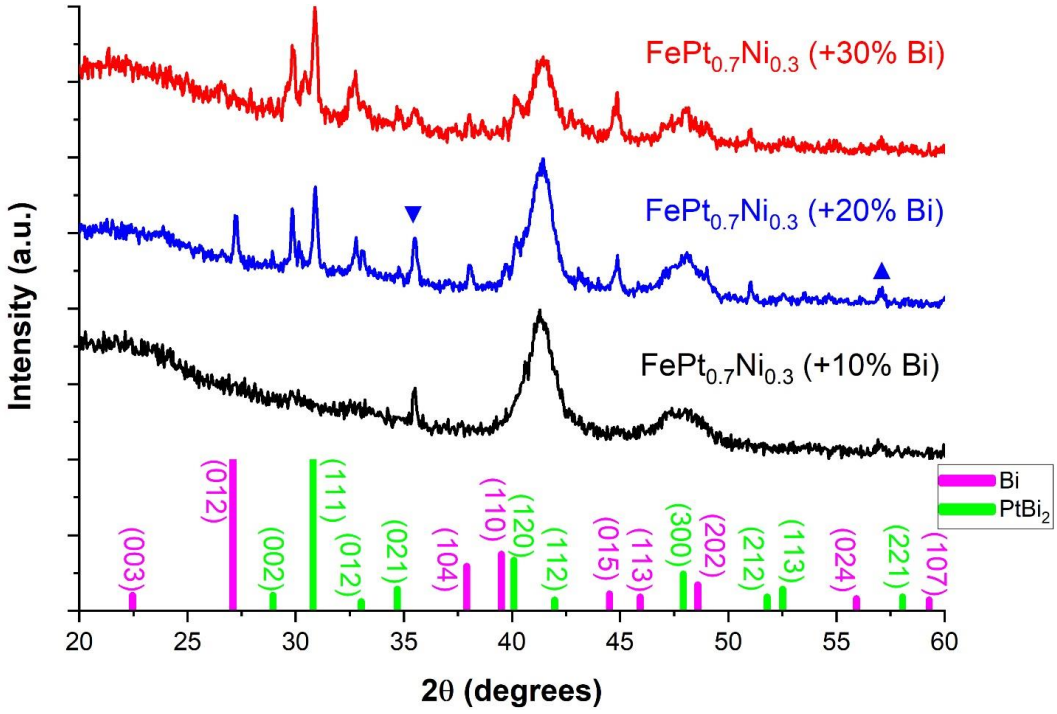

Figure 4.30: XRD data of $FePt_{0.7}Ni_{0.3}$ (+z% Bi), for $z = 10,20,30$. For clarity, the 2 strongest peaks of Fe_3O_4 which do not appreciably overlap with other phases in the samples are shown on the 20% Bi sample (blue curve, ▼ and ▲ representing the (311) and (333) peaks respectively.

Increasing the amount of Bi did not introduce splitting of the (200) and (002) peaks, the broad peaks indicating a small particle size. This indicates that increasing Bi content alone will not form as-made nanoparticles in the $L1_0$ structure. The XRD data in Figure 4.30 also shows that increasing the amount of Bi enhanced the presence of the Bi and $PtBi_2$ phases, as seen by more intense peaks of these phases in the $FePt_{0.7}Ni_{0.3}$ (+20%) and $FePt_{0.7}Ni_{0.3}$ (+30%) samples. Figure 4.31 shows the XRD data of the annealed samples.

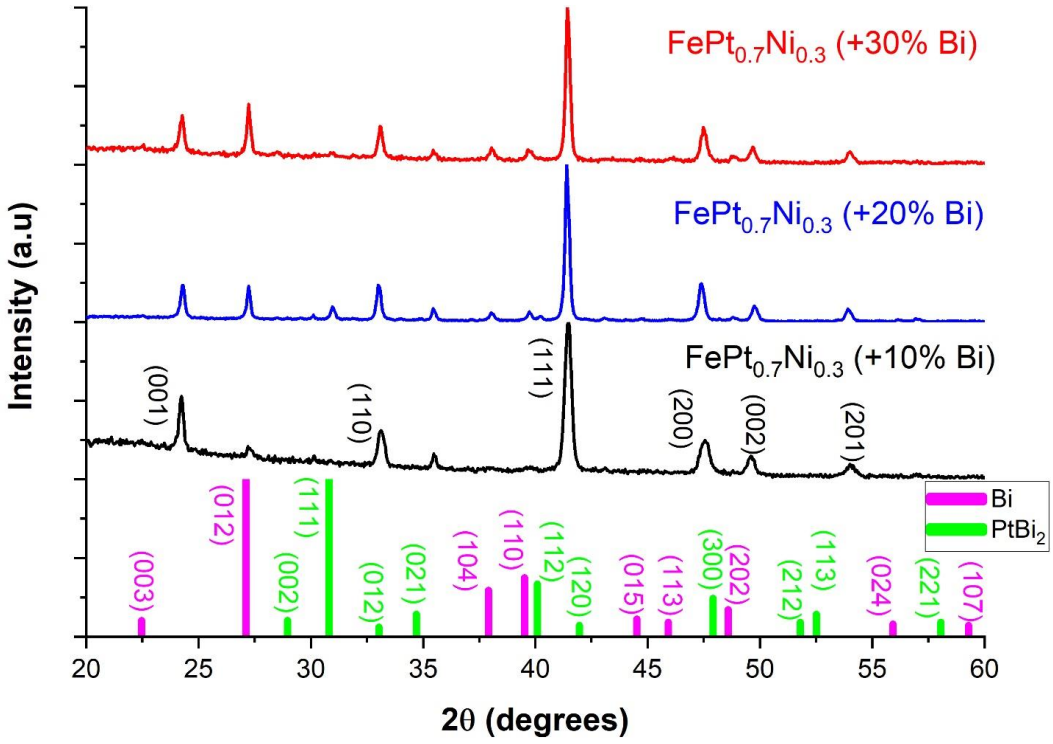

Figure 4.31: XRD data of $FePt_{0.7}Ni_{0.3}$ (+z% Bi), for $z = 10,20,30$ for the samples annealed at 700°C for 30 minutes. The peaks of the $L1_0$ phase are indexed on the XRD pattern of $FePt_{0.7}Ni_{0.3}$ (+10%).

When more Bi is used in the synthesis, the elemental Bi (012) peak becomes more intense, indicating a higher elemental Bi content in these annealed samples. The $PtBi_2$ phase increases for the 20% Bi case, but decreases for the 30% Bi sample. This means that the minority Bi-related phases in the annealed samples are mostly elemental Bi. In the $FePt_{0.7}Ni_{0.3}$ (+10% Bi), a non-negligible amount Bi is present as seen from XRD in relation to the $L1_0$ phase. Even when more Bi is used in the synthesis, there was no visible improvement in the $L1_0$ ordering, as characterized by the unchanged splitting of the (200) and (002) peaks. Since the chemical ordering in $FePt_{0.7}Ni_{0.3}$ improves considerably when as little as 10% Bi is used, compared to the chemical ordering in $FePt_{0.7}Ni_{0.3}$ nanoparticles, the XRD data in Figure 4.31 suggest that it may be possible to obtain $L1_0$ ordering with even a smaller quantity Bi used in the synthesis. Finding the optimum amount of Bi which reduces the amount of secondary phase while still producing a highly ordered $L1_0$ phase is the subject of future work.

Table 4.3: Lattice parameters, c/a ratio, and estimated size of samples annealed at 700°C for 30 minutes.

Sample	**Estimated size (nm)**	***a* (Å)**	***c* (Å)**	$\boldsymbol{c/a}$
$FePt_{0.7}Ni_{0.3}$ (+10% Bi)	40	3.823	3.668	0.958
$FePt_{0.7}Ni_{0.3}$ (+20% Bi)	49	3.834	3.663	0.955
$FePt_{0.7}Ni_{0.3}$ (+30% Bi)	43	3.823	3.673	0.961

Table 4.3 shows the lattice parameters and the particle size found using the XRD data using the Scherrer equation. Quantifying the chemical ordering is difficult because

we do not have a common reference sample for these samples. From the c/a ratios being close to each other, we estimate the chemical ordering of the samples with different Bi percentage to be about the same. Any change in the magnetic properties described below would therefore be mostly due to the additional phases introduced by Bi.

We estimated the percentage composition of Fe_3O_4 and the other known phases in the annealed $FePt_{0.7}Ni_{0.3}$ ($+z\%$ Bi) from our XRD pattern using a computational method requiring the software Powder Cell [31]. The known phases that were input were Fe_3O_4, Bi, $PtBi_2$ and $L1_0$ FePt to represent the $L1_0$ structure, which is an approximation. The lattice parameters were adjusted in the simulation to get a good fit as much as possible. It must be noted that while this method of finding composition may be approximate, it still provides a means to qualitatively compare the composition of different phases as a function of Bi content. An example of such a fit is shown in Figure 4.32, for $FePt_{0.7}Ni_{0.3}$ (+30%) annealed at 700°C for 30 minutes.

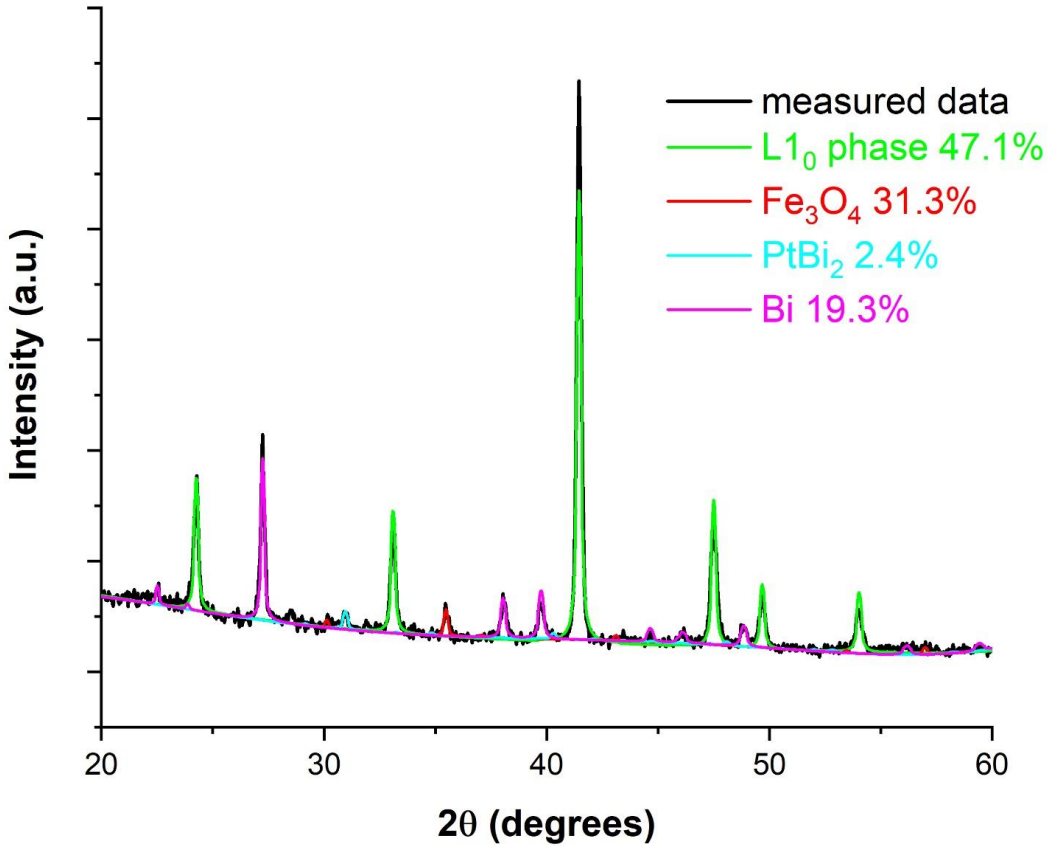

Figure 4.32: XRD pattern of $FePt_{0.7}Ni_{0.3}$ (+30% Bi) annealed at 700°C for 30 minutes, and a fit of four phases assumed to be present in the sample, along with their calculated percentage composition.

Table 4.4 summarizes the percentage composition of the different phases in all $FePt_{0.7}Ni_{0.3}$ (+z% Bi) annealed at 700°C for 30 minutes.

Table 4.4: Percentage compositions of various phases calculated from the XRD patterns of $FePt_{0.7}Ni_{0.3}$ (+*z*% Bi) annealed at 700°C for 30 minutes.

Sample	**$L1_0$ structure**	**Fe_3O_4**	**Bi**	**$PtBi_2$**
$FePt_{0.7}Ni_{0.3}$ (+10% Bi)	45.0%	49.5%	4.4%	1.1%
$FePt_{0.7}Ni_{0.3}$ (+20% Bi)	48.7%	36.9%	10.3%	4.2%
$FePt_{0.7}Ni_{0.3}$ (+30% Bi)	47.1%	31.3%	19.3%	2.4%

Table 4.4 shows that adding more Bi increases the amount of elemental Bi in the sample. The amount of $PtBi_2$ does not increase monotonically with Bi addition however. $FePt_{0.7}Ni_{0.3}$ (+20% Bi) has more $PtBi_2$ than $FePt_{0.7}Ni_{0.3}$ (+30% Bi). This trend is also seen from the XRD data in Figure 4.31 where more intense peaks reflect a higher percentage composition. Regarding Fe_3O_4, its percentage composition is observed to decrease when more Bi is present in the synthesis.

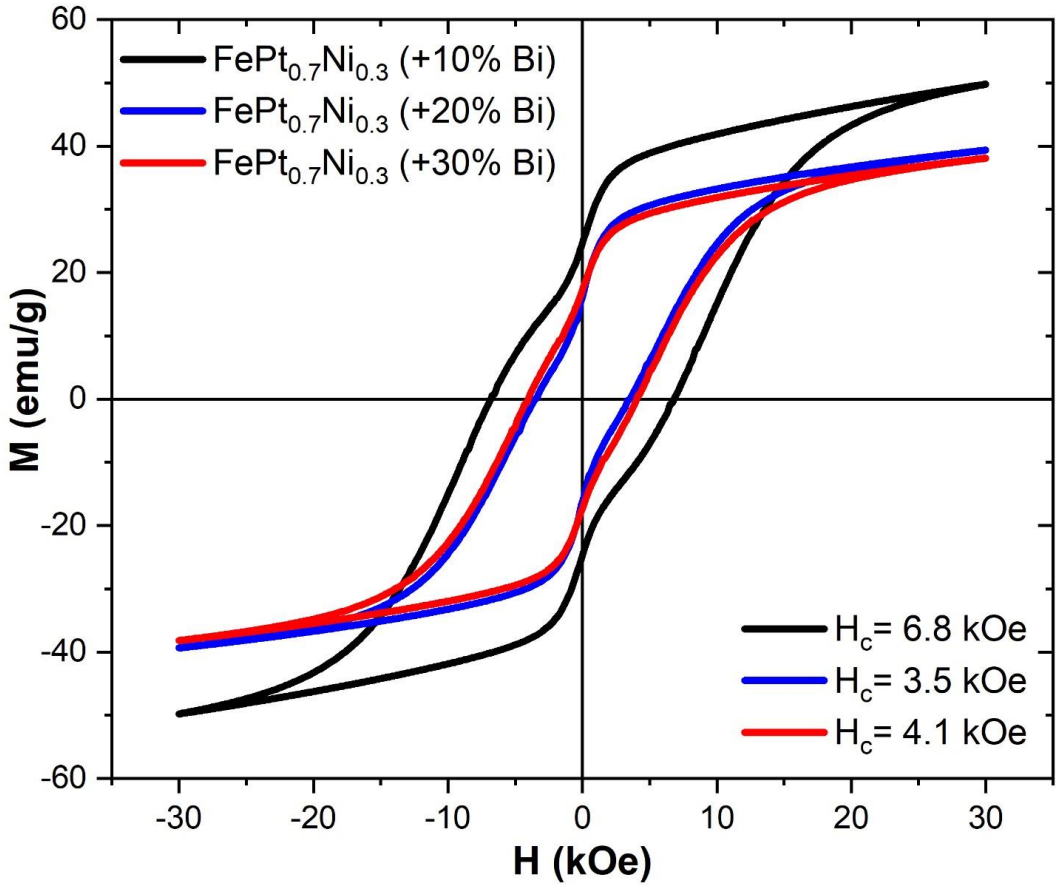

Figure 4.33: Room temperature hysteresis loops of $FePt_{0.7}Ni_{0.3}$ (+z % Bi) for $z =$ 10,20,30, annealed at 700°C for 30 minutes.

The introduction of soft phases due to the increased Bi content in the synthesis was also reflected in the shoulder observed in the hysteresis loops for the annealed samples taken at room temperature (Figure 4.33). Besides the irregular shape of the curves which is typical for mixtures of hard and soft magnetic materials, the coercivity of the samples also decreased for +20% and +30% Bi content. This also highlights the difficulty in determining the magnetization as the measured mass of the samples always include other phases such Fe_3O_4 and Bi related phases. Using less Bi (less than 10%)

may reduce the number of soft phases while retaining the desired hard magnetic properties.

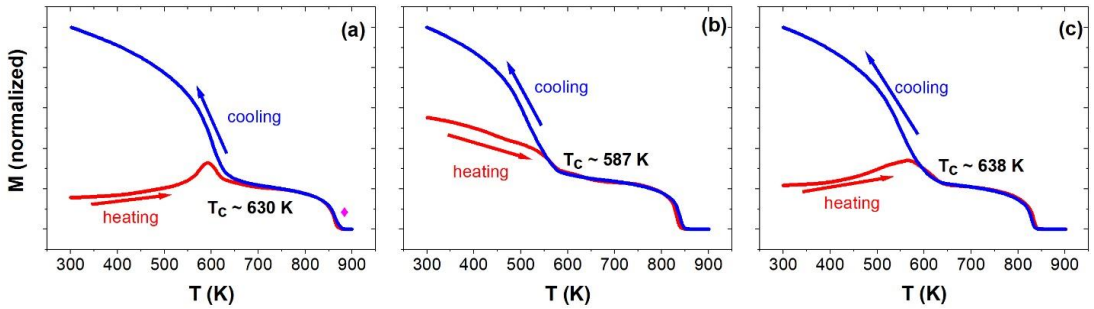

Figure 4.34: Thermomagnetic measurements at an applied field of 500 Oe on annealed nanoparticles of (a) $FePt_{0.7}Ni_{0.3}$ (+10% Bi), (b) $FePt_{0.7}Ni_{0.3}$ (+20% Bi) and (c) $FePt_{0.7}Ni_{0.3}$ (+30% Bi). The ♦ indicates the Fe_3O_4 phase.

Thermomagnetic measurements were performed on the annealed samples with different Bi content (Figure 4.34). The results show that the Curie temperature decreases by about 40 K when Bi is increased from 10% to 20% but remains about the same when Bi is 30%. Possibly, the abrupt decrease at the 20% Bi content could be related to the higher proportion of $PtBi_2$ phase. One of the main results of this study remains the fact that Bi addition to $FePt_{1-x}Ni_x$ decreases the Curie temperature significantly for certain Ni content. Future work will involve working with Bi content lower than 10%.

4.4 Structural and Magnetic Properties of Chemically Synthesized $CoPt_{1-x}Ni_x$

CoPt in the fct ($L1_0$) phase is stable and its magnetic properties make it potentially suitable for applications in ultrahigh magnetic storage [32–34]. As-

synthesized CoPt is usually in the chemically disordered fcc (A1) phase. Heat treatment is required to form the ordered $L1_0$ phase. Higher annealing temperatures have been reported to improve the coercivity [35,36]. However, high annealing temperatures may also lead to growth in grain sizes, lattice deformation and a reversal form the $L1_0$ phase to the disordered fcc phase [37–41]. One means of avoiding this difficulty in CoPt nanoparticles is to create core/shell structures with CoPt embedded in non-magnetic matrices [42].Third element addition, such as the introduction of Ag, B and C in CoPt, has also been explored [18,43,44]. In some cases, this lead to a significant decrease in ordering temperature and improvement in coercivity [18,44]. In this work, we investigate the effect of substituting Pt with Ni in CoPt to form $CoPt_{1-x}Ni_x$ and compare the structural and magnetic properties of these nanoparticles to $FePt_{1-x}Ni_x$.

$CoPt_{1-x}Ni_x$ nanoparticles were chemically synthesized using a similar procedure to that used to produce $FePt_{1-x}Ni_x$. In a three-neck flask, 0.25 mmol of cobalt(ii) acetylacetonate was mixed with pre-determined amounts of $Pt(acac)_2$ and $Ni(acac)_2$ to form compounds of the desired stoichiometric ratio. 1 mmol of 1,2-hexadecanediol was used as the reducing agent and 200 mg of palmitic acid as the surfactant. 20 ml of trioctylamine was used as the solvent for the reaction. The mixture was purged between 60°C and 80°C for 30 minutes under forming gas (5% H_2 – 95% Ar), and then heated to 330°C. The reaction ran for 1 hour at this temperature after which, the mixture was allowed to cool to room temperature, and the nanoparticles were washed and separated as before.

The first sample we produced was CoPt. This sample was annealed at 700°C for 1 hour also. The XRD data (Figure 4.35) shows that the as-made nanoparticles are in

the disordered fcc stage. After annealing, the $L1_0$ phase was formed, with a high degree of ordering, although the splitting of the (200) and (002) peaks are not complete.

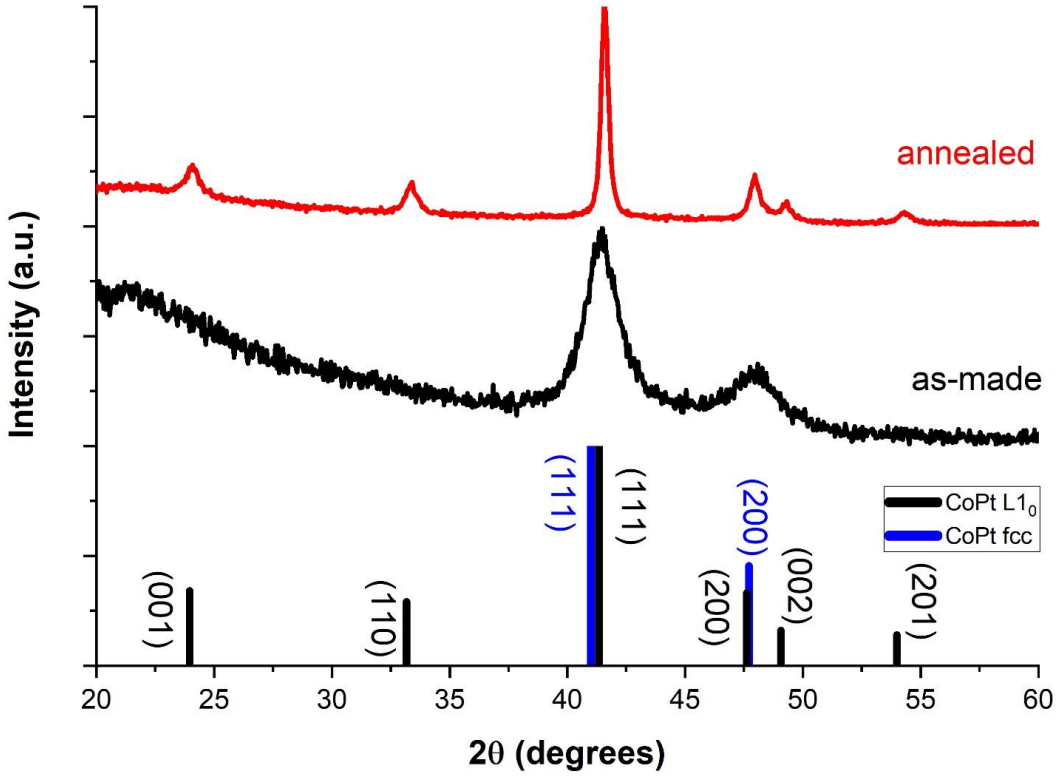

Figure 4.35: XRD data of as-synthesized CoPt nanoparticles and CoPt annealed at 700°C for 1 hour.

The room temperature hysteresis loops in Figure 4.36 also reflects the phase transformation from fcc to $L1_0$. The coercivity increases from 0.2 kOe for the as-made CoPt to 10 kOe for the annealed CoPt, thereby indicating that annealing is required to obtain the ferromagnetic state.

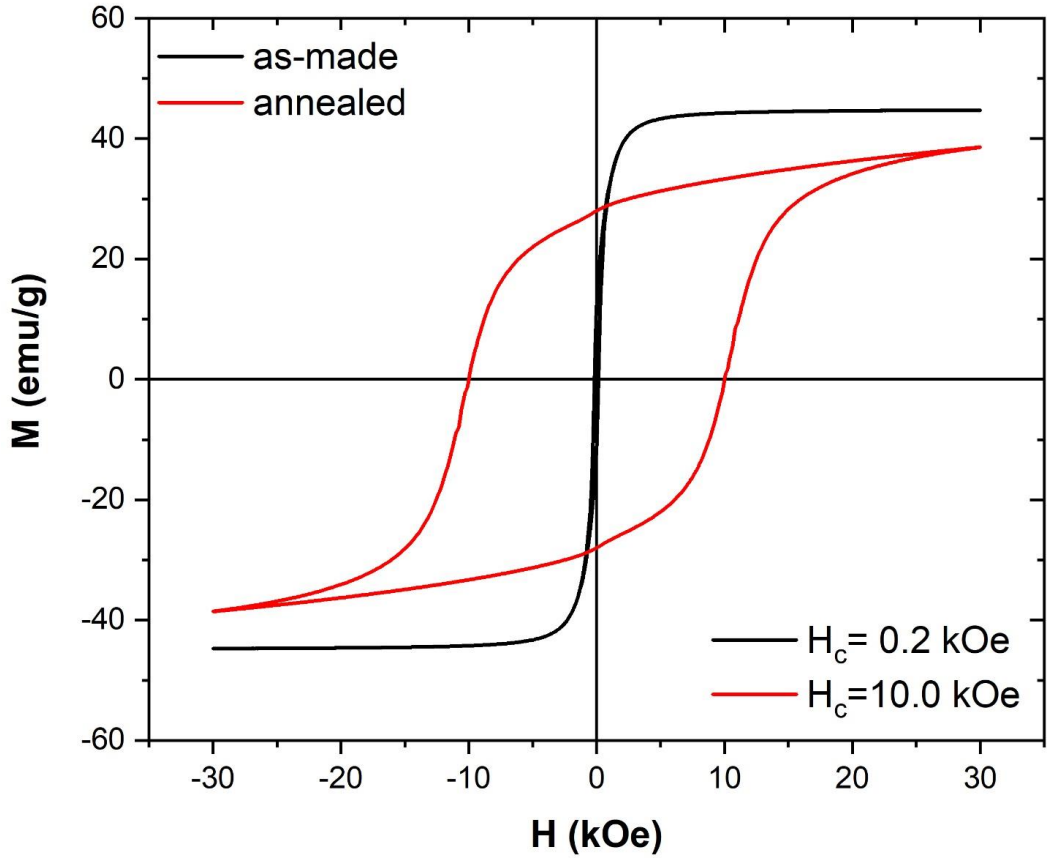

Figure 4.36: Room temperature hysteresis on as-synthesized CoPt and CoPt annealed at 700°C for 1 hour.

$CoPt_{0.8}Ni_{0.2}$ was prepared and annealed at 700°C for different time periods. The XRD data in Figure 4.37 for the as-made and annealed samples show that, in contrast to $FePt_{0.8}Ni_{0.2}$, the $L1_0$ phase is not fully formed in the heat treated samples, despite annealing for up to 16 hours.

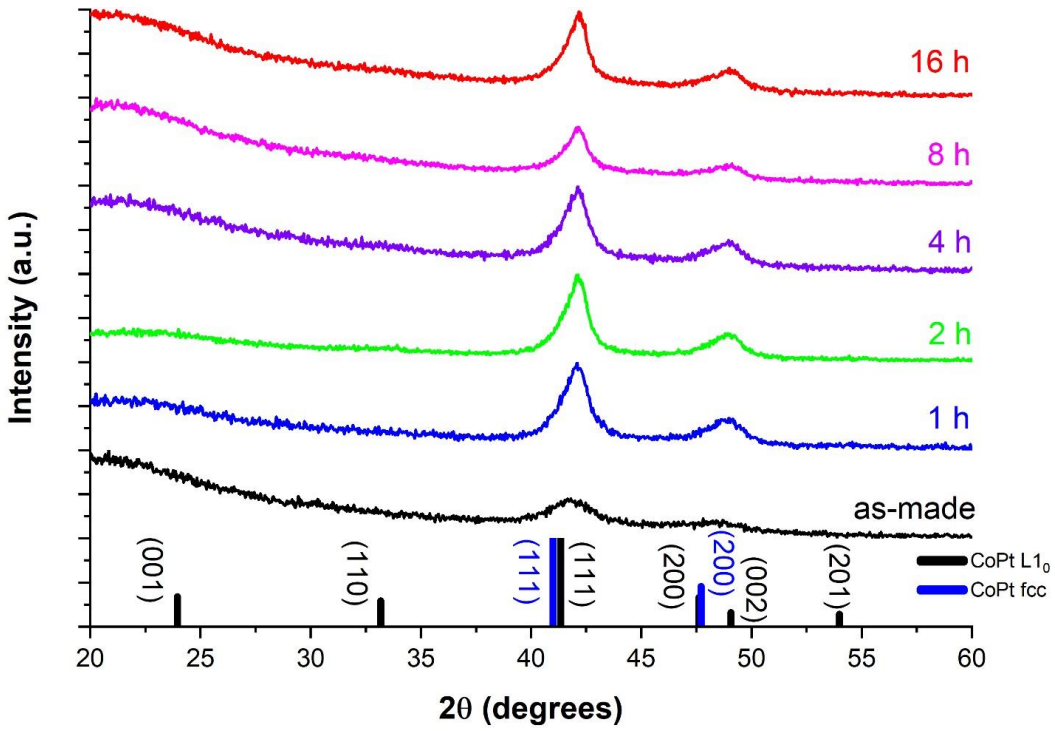

Figure 4.37: XRD data of as-synthesized $CoPt_{0.8}Ni_{0.2}$ and $CoPt_{0.8}Ni_{0.2}$ annealed at 700°C for times ranging from 1 hour to 16 hours.

The magnetization of the $CoPt_{0.8}Ni_{0.2}$ nanoparticles annealed at 700°C were also measured as a function of applied magnetic field at 300 K (Figure 4.38). The $CoPt_{0.8}Ni_{0.2}$ sample annealed for 1 hour has a much lower coercivity (0.12 kOe) compared to the CoPt sample annealed under the same conditions (10.0 kOe). Successively doubling the annealing time up to an annealing time of 16 hours caused the coercivity to increase and the magnetization at 3 T to decrease, however these changes are very small. Effectively, the addition of Ni into the CoPt lattice to produce $CoPt_{0.8}Ni_{0.2}$ greatly inhibits the formation of the $L1_0$ phase, which is in sharp contrast to what was observed in $FePt_{0.8}Ni_{0.2}$ nanoparticles.

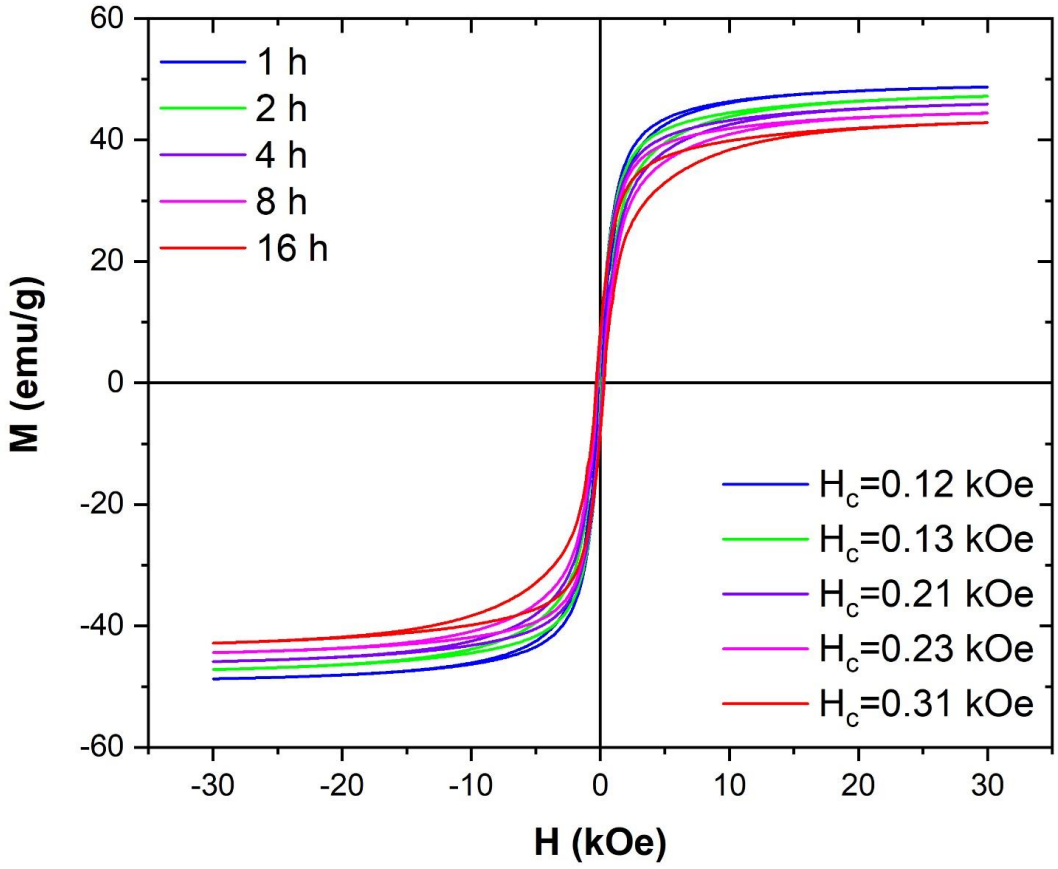

Figure 4.38: Room temperature hysteresis loops on $CoPt_{0.8}Ni_{0.2}$ nanoparticles annealed at 700°C for different durations.

To better understand any significant phase transformation that may occur as a result of heat treatment, we also annealed the $CoPt_{0.8}Ni_{0.2}$ nanoparticles at temperatures below and above 700°C, namely, at 600°C, 650°C and 800°C. The XRD data in Figure 4.39 show that the structure is again mostly cubic.

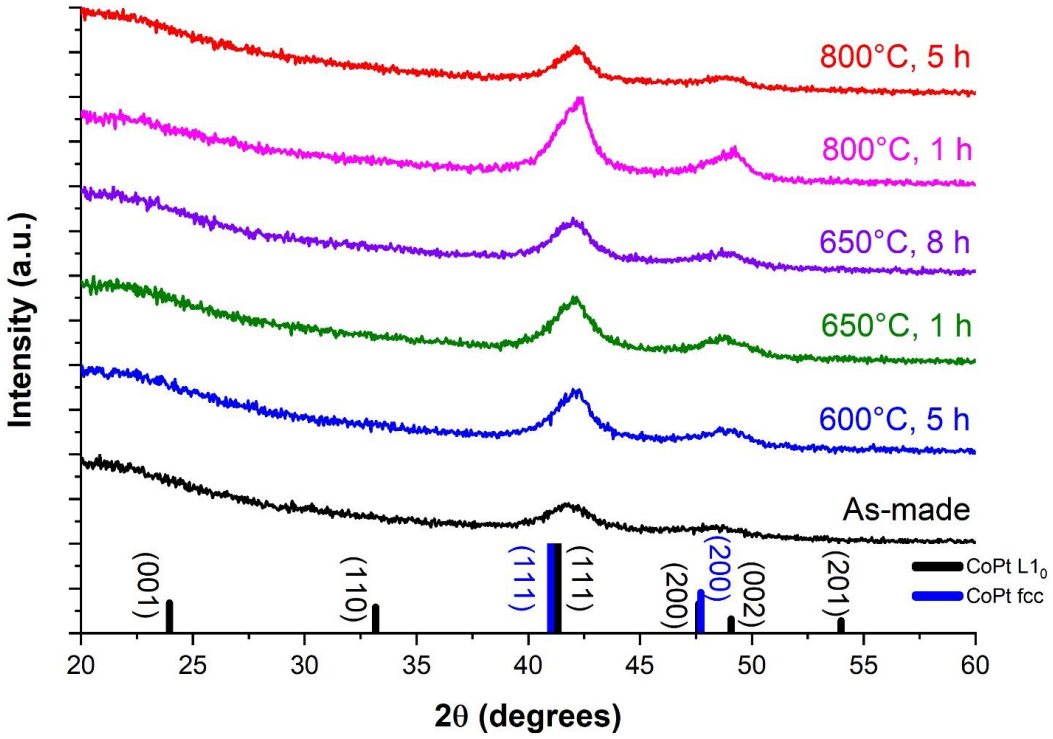

Figure 4.39: XRD data of as-synthesized $CoPt_{0.8}Ni_{0.2}$ and $CoPt_{0.8}Ni_{0.2}$ annealed under different conditions (listed on the graph).

The hysteresis loops of the annealed samples in Figure 4.40 shows that the coercivity of the $CoPt_{0.8}Ni_{0.2}$ samples annealed at the temperatures studied above are lower than those annealed at 700°C as seen from Figure 4.38. The highest coercivity in this part of the study was observed when the $CoPt_{0.8}Ni_{0.2}$ sample was annealed at 650°C for 8 hours (0.08 kOe). This is the closest the coercivity approached the coercivity of $CoPt_{0.8}Ni_{0.2}$ annealed at 700°C for 1 hour (0.12 kOe). The coercivity dropped down to approximately half this value when the as-made sample was heat treated at 800°C. The structural and magnetic data suggests a phase transformation towards the $L1_0$ state, occurring between 650°C and 800°C. However, the transformation to the $L1_0$ phase is

still slow in $CoPt_{0.8}Ni_{0.2}$ compared to what was observed in $FePt_{0.8}Ni_{0.2}$ as the (200) and (002) peaks are not separated yet in the XRD patterns.

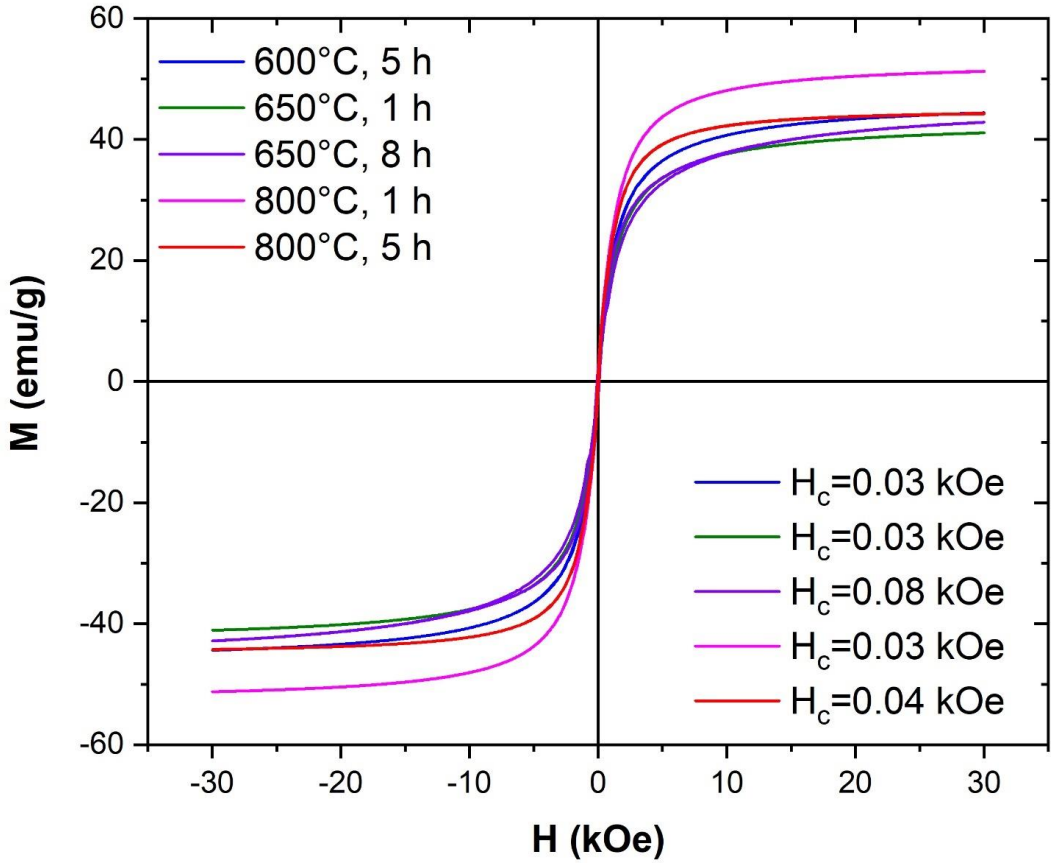

Figure 4.40: Room temperature hysteresis loops on annealed $CoPt_{0.8}Ni_{0.2}$. The annealing conditions are indicated in the figure.

Since substituting less Pt with Ni in $FePt_{1-x}Ni_x$ was found to produce more highly ordered structures, we performed the same procedure with $CoPt_{1-x}Ni_x$ by synthesizing

an alloy with $x = 0.1$. The XRD data of the as-made and annealed $CoPt_{0.9}Ni_{0.1}$ are shown in Figure 4.41.

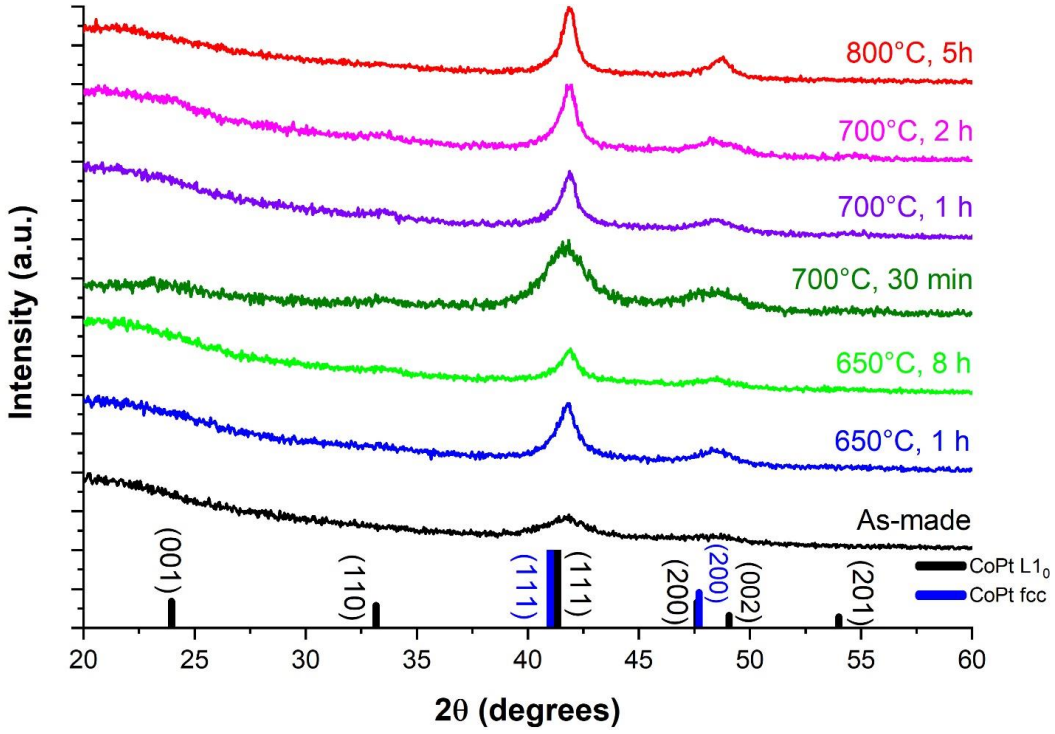

Figure 4.41: XRD data of as-synthesized $CoPt_{0.9}Ni_{0.1}$ and $CoPt_{0.9}Ni_{0.1}$ annealed under different conditions (listed on the graph).

For the samples annealed at 700°C, the emergence of the (001), (100) and (201) peaks indicates that the $L1_0$ is present to some extent. Like in the case of $FePt_{1-x}Ni_x$, using less Ni helps in the formation of a more ordered $CoPt_{1-x}Ni_x$ structures, after annealing under the appropriate conditions. The intensity of the superlattice peaks are considerably diminished when $CoPt_{0.9}Ni_{0.1}$ is annealed at 800°C. The studies on heat treating both $CoPt_{0.8}Ni_{0.2}$ and $CoPt_{0.9}Ni_{0.1}$ indicate that a phase transformation into the

$L1_0$ state is not enhanced by simply increasing the annealing temperature. Rather, the transformation, even if not complete, is favored by heat treatment at a temperature between 650°C and 800°C in $CoPt_{0.8}Ni_{0.2}$ and $CoPt_{0.9}Ni_{0.1}$. Room temperature hysteresis loops on the annealed $CoPt_{0.9}Ni_{0.1}$ also provides evidence of the increase in ordering in the samples annealed at 700°C, and the phase transformation towards a less ordered phase after annealing at 800°C (Figure 4.42).

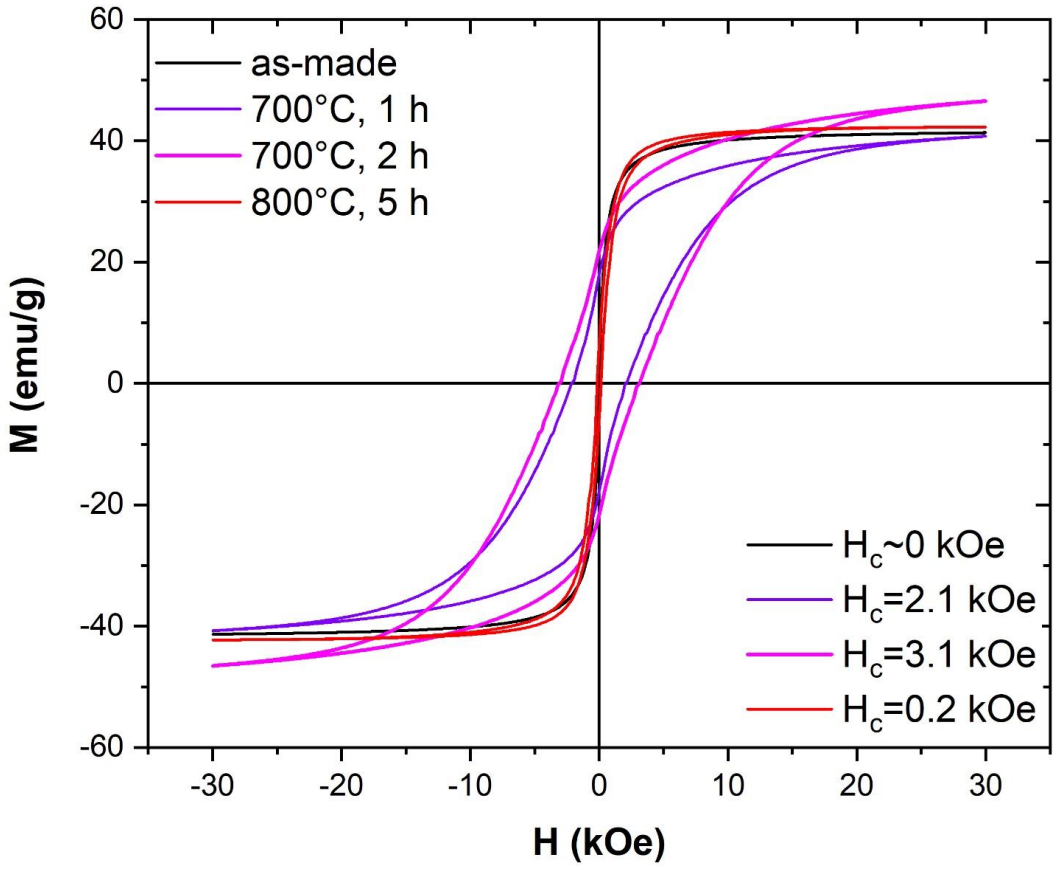

Figure 4.42: Room temperature hysteresis loops on as-synthesized and annealed $CoPt_{0.9}Ni_{0.1}$. The annealing conditions are listed in the figure.

Compared to the coercivities of $CoPt_{0.8}Ni_{0.2}$ annealed at 700°C for 1 hour (0.12 kOe) and 2 hours (0.13 kOe), the corresponding coercivities of $CoPt_{0.9}Ni_{0.1}$ are around 20 times higher. The coercivity significantly dropped for the sample annealed at 800°C for 5 hours, because of a phase transformation away from the ordered $L1_o$ phase.

From a practical standpoint, one primary interest in substituting Pt by Ni in applications such as magnetic data storage is to reduce cost by using appreciably lower amount of Pt than in the equiatomic binary CoPt structure, provided the alloy under study retains its hard magnetic properties. While it is possible that using even less Ni ($x < 0.1$) will bring the $CoPt_{1-x}Ni_x$ closer to the equiatomic CoPt in terms of magnetic properties, we attempted to obtain the $L1_0$ ordering by adding Bi to the $CoPt_{1-x}Ni_x$ structure instead. We synthesized $CoPt_{0.8}Ni_{0.2}$ (+10% Bi) using the same procedure for synthesizing $CoPt_{1-x}Ni_x$ with 0.025 mmol of bismuth(ii) acetate added to the reaction mixture. The XRD data for the as-made $CoPt_{0.8}Ni_{0.2}$ (+10% Bi) and $CoPt_{0.8}Ni_{0.2}$ (+10% Bi) annealed under different conditions are shown in Figure 4.43.

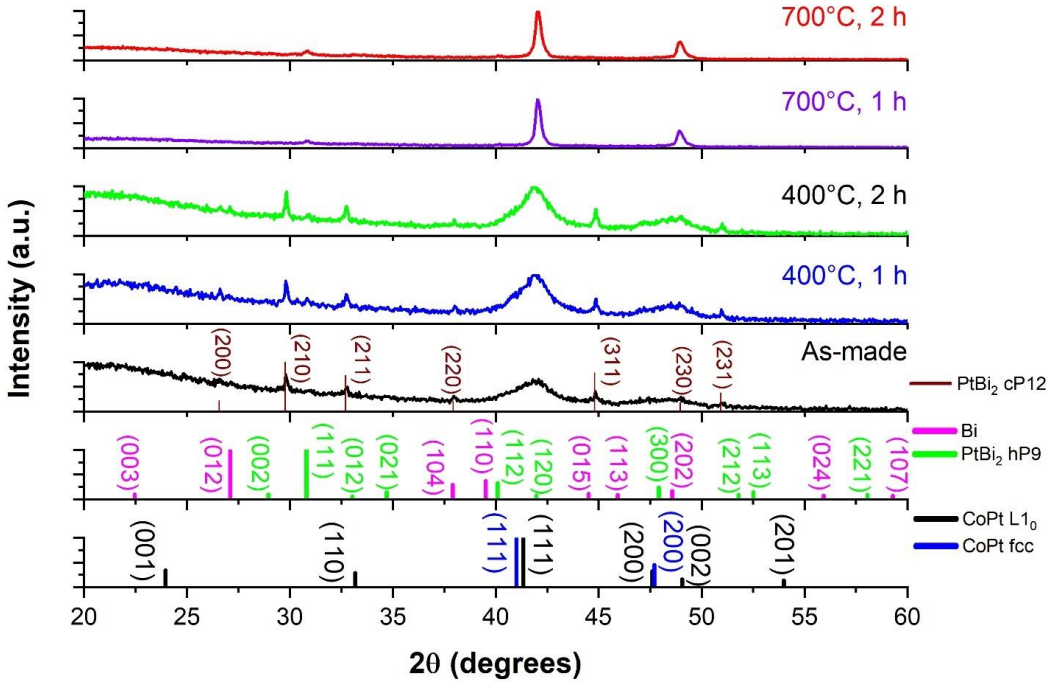

Figure 4.43: XRD data of as-synthesized $CoPt_{0.8}Ni_{0.2}$ (+10% Bi) and $CoPt_{0.8}Ni_{0.2}$ (+10% Bi) annealed under different conditions (listed on the graph).

When Bi is used in the synthesis, it introduces additional Bi-related phases as seen from the XRD data. The as-made nanoparticles contain predominantly the cubic phase of $PtBi_2$ (Pearson symbol cP12), in addition to elemental Bi and the hexagonal phase of $PtBi_2$ (hP9). These Bi-related phases are retained even after annealing the sample at 400°C for 1 hour and 2 hours. Annealing at 700°C for 1 hour and 2 hours suppresses the cubic phase of $PtBi_2$, whereas the hexagonal phase of $PtBi_2$ is present, as indicated by the presence of its (111) peaks in both samples. The particle size of the $CoPt_{0.8}Ni_{0.2}$ (+10% Bi) also increases when it is annealed at 700°C, shown by a sharpening of the (111) and (200) peaks. However, the absence of a clear splitting of

the (200) and (002) peaks show that Bi addition does not guarantee the $L1_0$ structure in $CoPt_{0.8}Ni_{0.2}$. The corresponding magnetic data are shown in Figure 4.44.

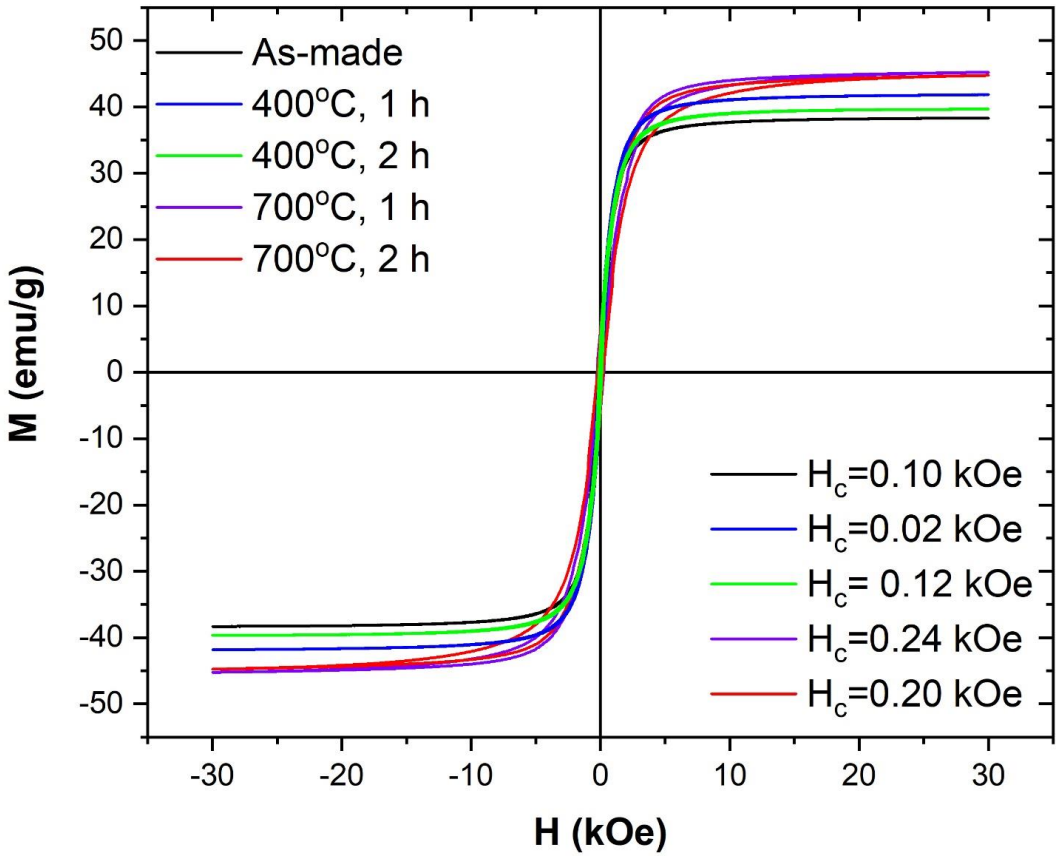

Figure 4.44: Room temperature hysteresis loops on as-synthesized and annealed $CoPt_{0.8}Ni_{0.2}$ (+10% Bi). The annealing conditions are listed in the figure.

A possible explanation for the non-monotonic change in coercivity is as follows: upon annealing as the as-made $CoPt_{0.8}Ni_{0.2}$ (+10% Bi) at 400°C for 1 hour, the increased formation of $PtBi_2$, indicated by a slight intensification of the $PtBi_2$ cP12 peaks, causes less Pt to be available in the Co-Pt-Ni structure leading to an overall decrease in

coercivity. Annealing at 400°C for 2 hours however promotes the ordering to the $L1_0$ phase, reflected by a rise in coercivity again. The onset of this transformation may be very slow at under these conditions though, and the amount of the Bi related phases does not change considerably from the sample annealed at 400°C for 1 hour, as seen from the XRD data. Annealing at 700°C however clearly shifts the transformation towards a more tetragonal structure, indicated by a shift of the (111) peak to the right, leading to a further increase in coercivity. More studies are required to work out the relative compositions of the different phases in the sample. However, one conclusion is that Bi addition to $CoPt_{1-x}Ni_x$ may increase the coercivity, for a range of Ni content that is yet to be determined. For example, comparing $CoPt_{0.8}Ni_{0.2}$ and $CoPt_{0.8}Ni_{0.2}$ (+10% Bi) annealed at 700°C for 1 hour, the coercivity increases from 0.12 kOe to 0.24 kOe.

4.5 Summary

- Pt substitution by Ni in FePt creates an fcc structure. Upon annealing at 700°C for different durations, the magnetically hard $L1_0$ ordered phase is obtained.
- The degree of ordering is higher at low Ni content. This is reflected both in the XRD pattern of the annealed samples and the higher coercivity of the samples with low Ni content.
- Bi addition to the Fe-Pt-Ni helps in producing a more ordered $L1_0$ phase in the annealed samples, even at higher Ni content.
- Bi is observed to introduce additional soft magnetic phases, causing a reduction in coercivity, in the annealed $FePt_{1-x}Ni_x$ samples, for $x = 0.2$ and 0.3. In the case of $x = 0.4$, the increased in ordering due to Bi addition produces an overall increase in coercivity.

- Bi addition also leads to a reduction in the Curie temperatures of the samples. Both increase in ordering and reduction in coercivity can be achieved by the addition of a small amount of Bi (+10%). It is possible that adding even less Bi could achieve the same results with the introduction of fewer soft phases. This will be subject of future studies.
- Substituting Pt with Ni in CoPt may produce the fully ordered $L1_0$ structure in $CoPt_{1-x}Ni_x$, however the amount of Ni needed to achieve this transformation may be significantly less than in the case of $FePt_{1-x}Ni_x$.
- Increasing the annealing temperature does not necessarily enhance the formation of the $L1_0$ phase. Our XRD and magnetic data suggest the optimum annealing temperature lie in the range of 650°C to 800°C for the sample compositions we studied.
- Adding Bi helps the transformation towards the $L1_0$ structure in $CoPt_{1-x}Ni_x$, however decreasing Ni towards achieving the same goal is more significant.
- In terms of hard magnetic properties obtained by the substitution of Pt with Ni, our studies show that ternary alloys of FePtNi are superior to those of CoPtNi.

REFERENCES

[1] D. Weller, A. Moser, L. Folks, M. E. Best, Wen Lee, M. F. Toney, M. Schwickert, J.- Thiele, and M. F. Doerner, *High K_u Materials Approach to 100 Gbits/in^2*, IEEE Trans. Magn. **36**, 10 (2000).

[2] Ivanov, O. A., L. V. Solina, and Demshina, *Determination of the Anisotropy Constant and Saturation Magnetisation and Magnetic Properties of Powders of an Iron-Platinum Alloy*, (n.d.).

[3] V. Nandwana, K. E. Elkins, and J. P. Liu, *Magnetic Hardening in Ultrafine FePt Nanoparticle Assembled Films*, Nanotechnology **16**, 2823 (2005).

[4] I. Zafiropoulou, V. Tzitzios, D. Petridis, E. Devlin, J. Fidler, S. Hoefinger, and D. Niarchos, *Optimized Synthesis and Annealing Conditions of $L1_0$ FePt Nanoparticles*, Nanotechnology **16**, 1603 (2005).

[5] V. K. Tzitzios, D. Petridis, I. Zafiropoulou, G. Hadjipanayis, and D. Niarchos, *Synthesis and Characterization of $L1_0$ FePt Nanoparticles from Pt–Fe_3O_4 Core-Shell Nanoparticles*, J. Magn. Magn. Mater. **294**, e95 (2005).

[6] M. Chen, J. P. Liu, and S. Sun, *One-Step Synthesis of FePt Nanoparticles with Tunable Size*, J. Am. Chem. Soc. **126**, 8394 (2004).

[7] C. Liu, X. Wu, T. Klemmer, N. Shukla, X. Yang, D. Weller, A. G. Roy, M. Tanase, and D. Laughlin, *Polyol Process Synthesis of Monodispersed FePt Nanoparticles*, J. Phys. Chem. B **108**, 6121 (2004).

[8] X. Teng and H. Yang, *Synthesis of Face-Centered Tetragonal FePt Nanoparticles and Granular Films from Pt@Fe_2O_3 Core−Shell Nanoparticles*, J. Am. Chem. Soc. **125**, 14559 (2003).

[9] K. E. Elkins, T. S. Vedantam, J. P. Liu, H. Zeng, S. Sun, Y. Ding, and Z. L. Wang, *Ultrafine FePt Nanoparticles Prepared by the Chemical Reduction Method*, Nano Lett. **3**, 1647 (2003).

[10] M. S. Wellons, W. H. Morris, Z. Gai, J. Shen, J. Bentley, J. E. Wittig, and C. M. Lukehart, *Direct Synthesis and Size Selection of Ferromagnetic FePt Nanoparticles*, Chem. Mater. **19**, 2483 (2007).

[11] W. Lei, Y. Yu, W. Yang, M. Feng, and H. Li, *A General Strategy for Synthesizing High-Coercivity $L1_0$-FePt Nanoparticles*, Nanoscale **9**, 12855 (2017).

[12] E. Kang, H. Jung, J.-G. Park, S. Kwon, J. Shim, H. Sai, U. Wiesner, J. K. Kim, and J. Lee, *Block Copolymer Directed One-Pot Simple Synthesis of $L1_0$-Phase FePt Nanoparticles inside Ordered Mesoporous Aluminosilicate/Carbon Composites*, ACS Nano **5**, 1018 (2011).

[13] O. Kitakami, Y. Shimada, K. Oikawa, H. Daimon, and K. Fukamichi, *Low-Temperature Ordering of $L1_0$–CoPt Thin Films Promoted by Sn, Pb, Sb, and Bi Additives*, Appl. Phys. Lett. **78**, 1104 (2001).

[14] Y. Xu, Z. G. Sun, Y. Qiang, and D. J. Sellmyer, *Preparation and Magnetic Properties of CoPt and CoPt:Ag Nanocluster Films*, J. Magn. Magn. Mater. **266**, 164 (2003).

[15] Y. Yang, K. K. M. Pandey, J. S. Chen, G. M. Chow, and J. F. Hu, *Chemical Ordering and Magnetic Properties of $L1_0$ CoPt–SiO_2 Nanocomposite*, J. Appl. Phys. **105**, 07B709 (2009).

[16] T. Huang, F. Wang, J. Guo, and X. Xu, *Effect of Cu Additive on the Structure and Magnetic Properties of $(CoPt)_{1-x}Cu_x$ films*, Rare Met. **28**, 14 (2009).

[17] V. Karanasos, I. Panagiotopoulos, D. Niarchos, H. Okumura, and G. C. Hadjipanayis, *CoPt:B Granular Thin Films for High Density Magnetic Recording Media*, J. Magn. Magn. Mater. **236**, 234 (2001).

[18] H. Yamaguchi, O. Kitakami, S. Okamoto, Y. Shimada, K. Oikawa, and K. Fukamichi, *Effects of B and C on the Ordering of $L1_0$-CoPt Thin Films*, Appl. Phys. Lett. **79**, 2001 (2001).

[19] Y. Yu, P. Mukherjee, Y. Tian, X.-Z. Li, J. E. Shield, and D. J. Sellmyer, *Direct Chemical Synthesis of $L1_0$-FePtAu Nanoparticles with High Coercivity*, Nanoscale **6**, 12050 (2014).

[20] L. H. Lewis, A. Mubarok, E. Poirier, N. Bordeaux, P. Manchanda, A. Kashyap, R. Skomski, J. Goldstein, F. E. Pinkerton, R. K. Mishra, R. C. K. Jr, and K. Barmak, *Inspired by Nature: Investigating Tetrataenite for Permanent Magnet Applications*, J. Phys. Condens. Matter **26**, 064213 (2014).

[21] J. I. Goldstein and J. M. Short, *Cooling Rates of 27 Iron and Stony-Iron Meteorites*, Geochim. Cosmochim. Acta **31**, 1001 (1967).

[22] J. F. Albertsen, J. M. Knudsen, N. O. Roy-Poulsen, and L. Vistisen, *Meteorites and Thermodynamic Equilibrium in f.c.c. Iron-Nickel Alloys (25-50% Ni)*, Phys. Scr. **22**, 171 (1980).

[23] A. Makino, P. Sharma, K. Sato, A. Takeuchi, Y. Zhang, and K. Takenaka, *Artificially Produced Rare-Earth Free Cosmic Magnet*, Sci. Rep. **5**, 1 (2015).

[24] H.-W. Yang, C.-M. Chung, and J. Y. Ding, *Effect of Ni Doping on the Structural and Magnetic Properties of FePt Nanoparticles*, J. Magn. Magn. Mater. **312**, 239 (2007).

[25] Y. K. Takahashi, T. Koyama, M. Ohnuma, T. Ohkubo, and K. Hono, *Size Dependence of Ordering in FePt Nanoparticles*, J. Appl. Phys. **95**, 2690 (2004).

[26] S. Yuasa, H. Miyajima, and Y. Otani, *Magneto-Volume and Tetragonal Elongation Effects on Magnetic Phase Transitions of Body-Centered Tetragonal $FeRh_{1-x}Pt_x$*, J. Phys. Soc. Jpn. **63**, 3129 (1994).

[27] J. W. Edington, *Electron Diffraction in the Electron Microscope*, in *Electron Diffraction in the Electron Microscope*, edited by J. W. Edington (Macmillan Education UK, London, 1975), pp. 1–77.

[28] A. Khajehnezhad and S. A. Sebt, *Order Parameter in $L1_0$ FePt Nanocrystals*, Trans. Indian Inst. Met. **67**, 903 (2014).

[29] S. Okamoto, N. Kikuchi, O. Kitakami, T. Miyazaki, Y. Shimada, and K. Fukamichi, *Chemical-Order-Dependent Magnetic Anisotropy and Exchange Stiffness Constant of FePt (001) Epitaxial Films*, Phys. Rev. B **66**, 024413 (2002).

[30] F. M. Abel, V. Tzitzios, E. Devlin, S. Alhassan, D. J. Sellmyer, and G. C. Hadjipanayis, *Enhancing the Ordering and Coercivity of $L1_0$ FePt Nanostructures with Bismuth Additives for Applications Ranging from Permanent Magnets to Catalysts*, ACS Appl. Nano Mater. **2**, 3146 (2019).

[31] W. Kraus and G. Nolze, *POWDER CELL– a Program for the Representation and Manipulation of Crystal Structures and Calculation of the Resulting X-Ray Powder Patterns*, J. Appl. Crystallogr. **29**, 301 (1996).

[32] M. Abes, M. V. Rastei, J. Venuat, A. Carvalho, S. Boukari, E. Beaurepaire, P. Panissod, A. Dinia, J. P. Bucher, and V. Pierron-Bohnes, *Magnetic Switching Field Distribution of Patterned CoPt Dots*, J. Appl. Phys. **105**, 113916 (2009).

[33] X. B. Liu and Z. Altounian, *Exchange Interaction in $L1_0$-Ordered FePt and CoPt from First-Principles*, J. Appl. Phys. **109**, 07B762 (2011).

[34] Y. Liu, Y. Yang, Y. Zhang, Y. Wang, X. Zhang, Y. Jiang, M. Wei, Y. Liu, X. Liu, and J. Yang, *A Facile Route to Synthesis of CoPt Magnetic Nanoparticles*, Mater. Res. Bull. **48**, 721 (2013).

[35] N. Sehdev, R. Medwal, and S. Annapoorni, *Enhanced Phase Stabilization of CoPt in the Presence of Ag*, J. Appl. Phys. **110**, 033901 (2011).

[36] M. Yu, Y. Liu, A. Moser, D. Weller, and D. J. Sellmyer, *Nanocomposite CoPt:C Films for Extremely High-Density Recording*, Appl. Phys. Lett. **75**, 3992 (1999).

[37] E. Ahmed, M. Takahashi, H. Iwasaki, and K.-I. Ohshima, *X-Ray Diffraction Study on the Thermal Properties of $CuMPt_6$ (M=3d Elements) Alloys*, J. Alloys Compd. **473**, 1 (2009).

[38] C. W. Hsu, S. K. Chen, W. M. Liao, F. T. Yuan, W. C. Chang, and J. L. Tsai, *Effect of Pt Underlayer on the Coercivity of FePt Sputtered Film*, J. Alloys Compd. **449**, 52 (2008).

[39] J. Dvorak, Y. U. Idzerda, S. B. Ogale, S. Shinde, T. Wu, T. Venkatesan, R. Godfrey, and R. Ramesh, *Are Strain-Induced Effects Truly Strain Induced? A Comprehensive Study of Strained LCMO Thin Films*, J. Appl. Phys. **97**, 10C102 (2005).

[40] L. Castaldi, K. Giannakopoulos, A. Travlos, D. Niarchos, S. Boukari, and E. Beaurepaire, *CoPt Nanoparticles Deposited by Electron Beam Evaporation*, J. Magn. Magn. Mater. **290–291**, 544 (2005).

[41] R. Tang, W. Zhang, and Y. Li, *Annealing Environment Effects on the Microstructure and Magnetic Properties of FePt–TiO_2 and CoPt–TiO_2 Nanocomposite Films*, J. Alloys Compd. **496**, 380 (2010).

[42] T. Seto, K. Koga, F. Takano, H. Akinaga, T. Orii, M. Hirasawa, and M. Murayama, *Synthesis of Magnetic CoPt/SiO_2 Core-Shell Nanoparticles*, J. Phys. Conf. Ser. **59**, 255 (2007).

[43] Y. Wang, X. Zhang, Y. Liu, Y. Jiang, Y. Zhang, and J. Yang, *Microstructure and Magnetic Properties of $L1_0$ CoPt Nanoparticles by Ag Addition*, J. Sol-Gel Sci. Technol. **70**, 528 (2014).

[44] H. Wang, S. X. Xue, F. J. Yang, H. B. Wang, X. Cao, J. A. Wang, Y. Gao, Z. B. Huang, C. P. Yang, W. Y. Cheung, S. P. Wong, Q. Li, and Z. Y. Li, *CoPt/Ag(Cu) Nanocomposite Films for Ultra-High Density Perpendicular Magnetic Recording Media*, Thin Solid Films **505**, 77 (2006).

Chapter 5

STRUCTURAL AND MAGNETIC PROPERTIES OF IODIDE-MEDIATED CHEMICALLY SYNTHESIZED $L1_2$ $FePt_3$ NANOPARTICLES

5.1 Introduction

The structural and magnetic properties of $Fe_{1-x}Pt_x$ nanoparticles are highly dependent on the composition *x*, which can be tailored to suit potential applications such as ultrahigh density storage media, biomedicine and catalysis [1–3]. The equilibrium Fe-Pt phase diagram shows 3 highly ordered phases: $L1_0$ FePt, $L1_2$ Fe_3Pt and $L1_2$ $FePt_3$ [4] (Figure 5.1). Because of the different crystal structures of the alloys being dependent on their Fe/Pt compositions, their magnetic properties are also different.

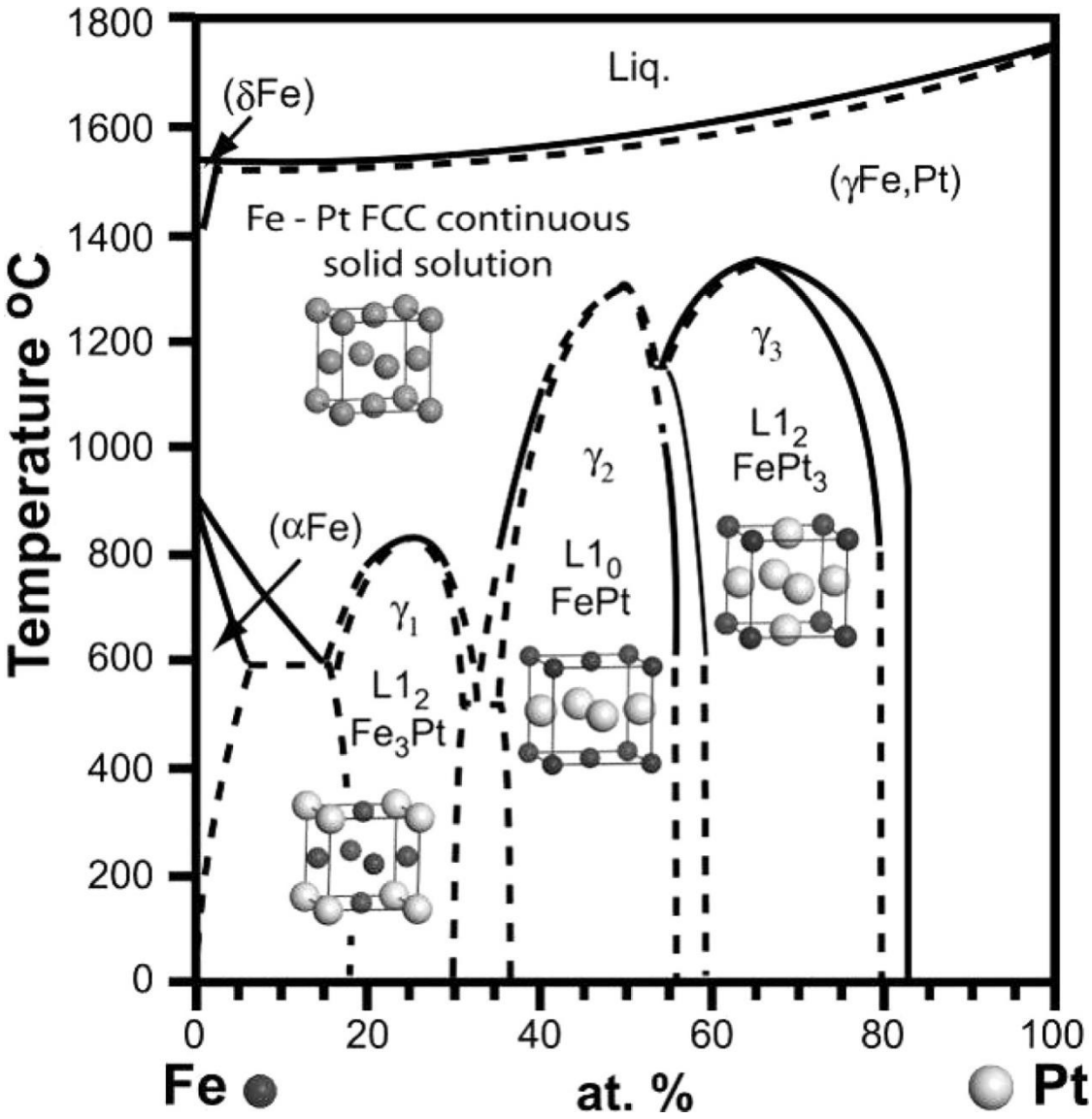

Figure 5.1: Fe-Pt phase diagram [4–6]. Dashed lines represent predicted values from reference [5].

$L1_2$ Fe_3Pt is ferromagnetic at room temperature and the $L1_0$ FePt alloy is a hard magnetic material [7]. $FePt_3$ is of particular interest. In the chemically disordered phase, $FePt_3$ is ferromagnetic (FM) with Fe moments of $2\mu_B$.The ordered $L1_2$ phase on the

other hand shows two coexisting antiferromagnetic (AFM) phases with T_{N1}~160 K and T_{N2}~120 K [4]. The phase with T_{N1}~160 K occurs when the Fe moments alternate in direction in the (110) plane. In slightly Fe-rich alloys, the Fe moments form alternating ferromagnetic sheets parallel to the (100) plane, with T_{N2}~120 K [8,9]. These two phases are depicted in Figure 5.2.

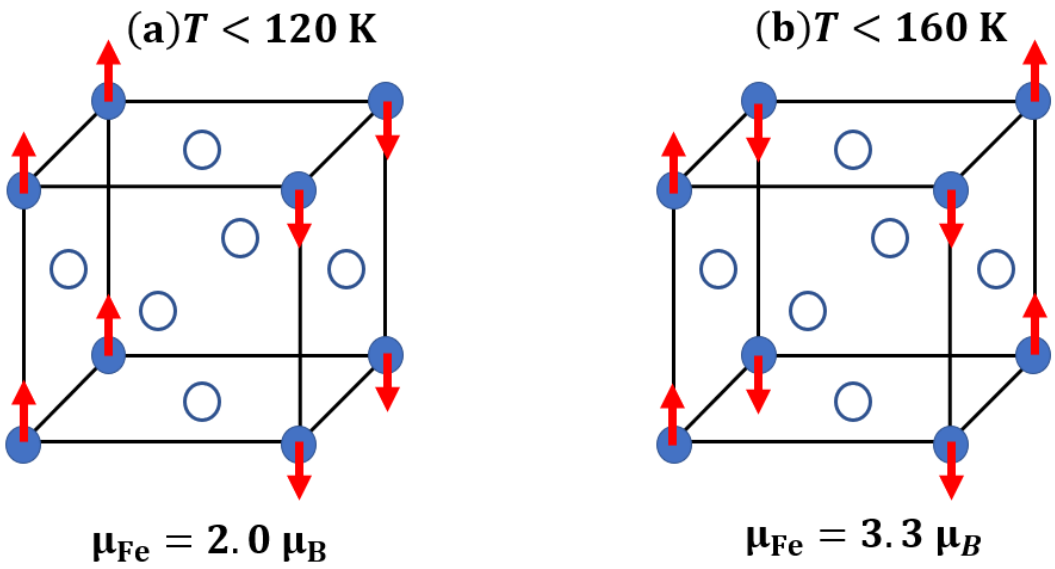

Figure 5.2: The magnetic structure of $FePt_3$ in both AFM phases. The blue spheres represent Fe atoms and the white spheres the Pt atoms. The moments carried by the Fe are also shown [10].

Most studies so far have been focused on equiatomic Fe-Pt with the highly anisotropic $L1_0$ structure [1–3,11–13]. Recently, $L1_0$ FePt nanoparticles have been chemically synthesized through a halide mediated route without requiring any post annealing heat treatment [14,15]. Strong bonds between Fe^{3+} and Pt^{2+} ions and the

halide ions facilitate the formation of FePt, through an energetically favorable way, thus leading to the formation of an ordered state.

In our experiments, we used elemental iodine to synthesize this phase, but our results showed that the $L1_2$ $FePt_3$ phase is obtained instead of the $L1_0$ phase. Previously, reported work on $FePt_3$ nanoparticles highlighted the antiferromagnetic to ferromagnetic transitions, which depend on the size and chemical ordering of the particles [4,10,16,17]. $FePt_3$ nanoparticles have also been shown to have an effective magnetic anisotropy energy density at least twice the value of the corresponding bulk values [16]. In our work, we study the structural and magnetic properties of the $FePt_3$ nanoparticles synthesized using iodine. We also report the effect of annealing at different temperatures on particle size, structure, degree of ordering and magnetic properties of the $FePt_3$ nanoparticles.

5.2 Chemical Syntheses Details

$L1_2$ $FePt_3$ nanoparticles were chemically synthesized by the co-reduction of iron and platinum-based precursors in the presence of elemental iodine. In a typical reaction, which we will denote as the standard reaction, 0.25 mmol of iron(iii) acetylacetonate ($Fe(acac)_3$), 0.25 mmol of ammonium tetracholoroplatinate(ii) ($(NH_4)_2PtCl_4$) and 1 mmol of 1,2-hexadecanediol were mixed in a three-neck flask in a mixture of 18 ml trioctylamine (TO) and 2 ml oleylamine (OAm). The mixture was purged under forming gas (5% H_2 – 95% Ar) for 30 minutes in the temperature range of 60 – 80^{o}C.

After 30 minutes, 250 mg of iodine was added to the mixture which was purged for an additional 30 minutes under forming gas. The mixture was then heated to obtain a reaction temperature in the range of 280°C – 300°C, which was at the threshold of

boiling of the mixture. Afterwards, the solution was cooled to room temperature, and the resulting solution was washed with ethanol and hexane. The black resulting powder was isolated from the solution magnetically before being dried in a desiccator at room temperature. The as-made nanoparticles were annealed at different temperatures from 300-700°C and for different durations by sealing them in quartz tubes using a rough pump and diffusion vacuum pump filled with forming gas (5% H_2 - 95% Ar) before subjecting them to heat treatment. The crystal structure of both the as-made and annealed nanoparticles was analyzed using X-ray diffraction (XRD), and their magnetic properties were measured using a vibrating sample magnetometer (Versalab VSM). The magnetic properties of some samples were also measured using a physical property measurement system (PPMS). The morphology of 2 samples was analyzed using a JEOL 3010 transmission electron microscope.

In this study, we performed several different reactions by varying the precursor composition, the TO/OAm solvent ratio, the amount of iodine and the reaction time as shown in Table 5.1.

Table 5.1: Details of the different reaction conditions.

Sample/reaction	Fe:Pt precursor ratio	TO/OAm solvent ratio	Iodine (mg)	Reaction time
A (standard)	1:1	18 ml / 2ml	250	1 h
B	1:1	10 ml / 10 ml	250	1 h
C	2:1	18 ml / 2ml	250	1 h
D	3:1	18 ml / 2ml	250	1 h
E	3:1	2 ml / 18 ml	250	3 h
F	1:1	18 ml / 2 ml	0	1 h
G	1:1	18 ml / 2 ml	500	1 h

5.3 Structural Analysis of $FePt_3$ Nanoparticles

Figure 5.3 shows the as-made XRD data of the nanoparticles produced in the reactions listed in Table 5.1.

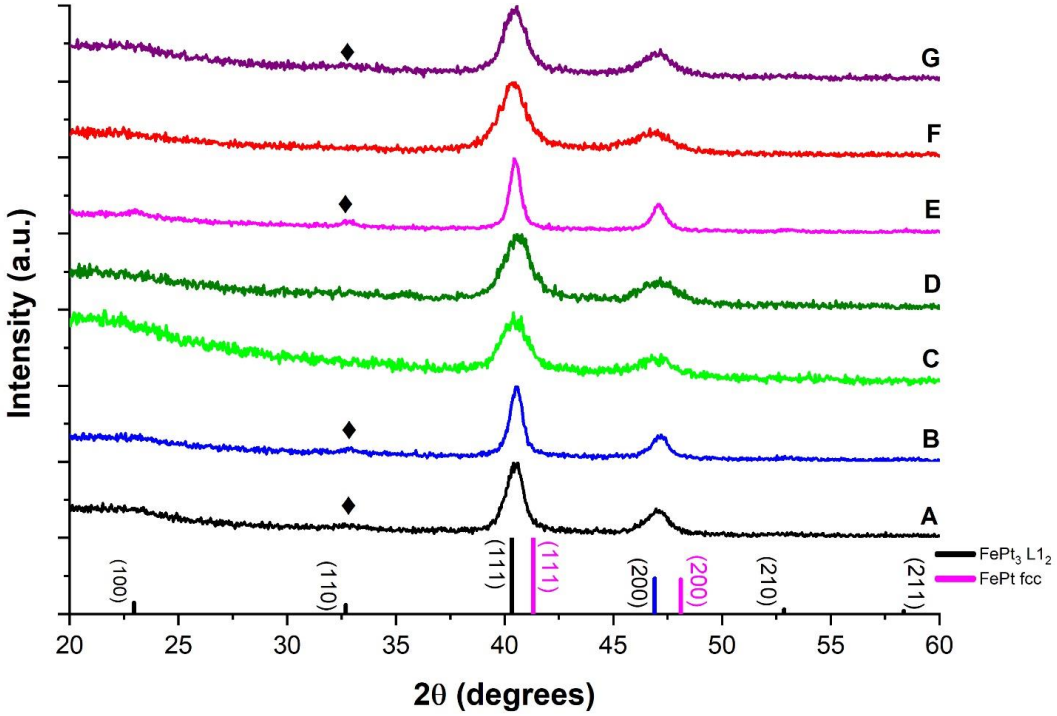

Figure 5.3: X-Ray diffraction patterns of as-made $FePt_3$ nanoparticles obtained from the reactions listed in Table 5.1. The visible (110) peaks from the $L1_2$ structure is denoted by ♦.

The as-synthesized nanoparticles mainly consist of $FePt_3$ in the disordered fcc structure. The fcc FePt is not present significantly to show in the XRD pattern. The nanoparticles produced from some of the reactions (A, B, E, G) also exhibit emerging (001) and (110) peaks. These reactions also have larger nanoparticles seen from a narrower (111) peak. No $L1_0$ phase was detected in the as-made and annealed nanoparticles, as indicated by the absence of resolved (002) and (200) peaks of the fct-FePt phase. This was confirmed by estimating the particle sizes using the Scherrer equation (Table 5.2). The lattice parameter a was calculated using the relationship between the lattice spacing and the Miller indices for a cubic lattice (Table 5.2):

$$\frac{1}{d^2} = \frac{h^2 + k^2 + l^2}{a^2} \tag{5.1}$$

Table 5.2 shows that the lattice parameters of each sample were close to the published lattice parameter of 0.3874 nm of $L1_2$ $FePt_3$ [18]. This however does not exclude the possibility of the presence of the $L1_0$ FePt and A1 FePt phase in our samples.

Table 5.2: Estimated particle size and lattice parameter of the as-synthesized $FePt_3$ nanoparticles.

Sample/reaction	**Calculated size (nm)**	***a*** **(nm)**
A	12	0.385
B	13	0.385
C	6	0.387
D	6	0.384
E	15	0.386
F	6	0.385
G	7	0.386

The nanoparticles from the different reactions were annealed at 700°C for 30 minutes. The sharpening of the peaks in the XRD data of the annealed samples (Figure 5.4) indicates an increase in particle size after annealing, as heat treatment promotes the transformation from the disordered fcc $FePt_3$ phase into the ordered $L1_2$ $FePt_3$ phase. Table 5.3 shows the particle sizes estimated using the Scherrer equation.

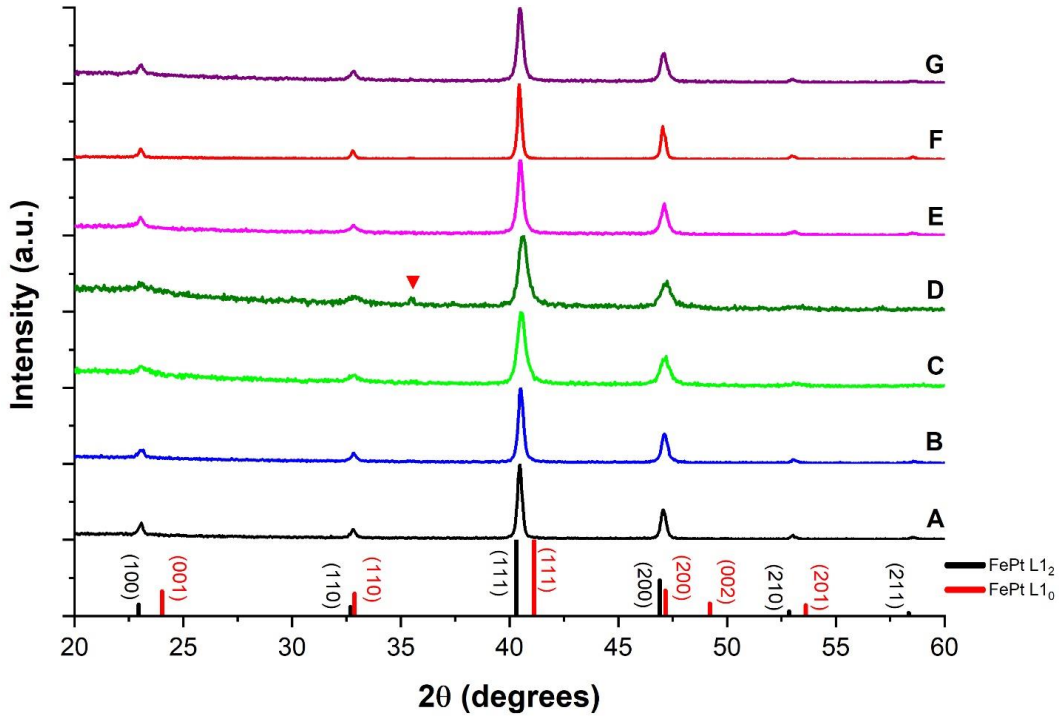

Figure 5.4: X-ray diffraction patterns of the annealed samples. The inverted triangle ▼ in graph D (3:1 Fe:Pt precursor ratio) corresponds to the (311) peak of Fe_3O_4.

No $L1_0$ phase was detected in the as-made and annealed nanoparticles, as indicated by the absence of resolved (002) and (200) peaks of the fct-FePt phase. Table 5.3 also shows that the calculated lattice parameter a was close to that of $L1_2$ $FePt_3$.

Table 5.3: Calculated sizes and lattice parameters for the samples annealed at 700°C for 30 minutes.

Sample/reaction	Calculated size (nm)	a (nm)
A (standard)	41	0.386
B	37	0.385
C	21	0.385
D	20	0.385
E	34	0.385
F	37	0.385
G	33	0.386

5.3.1 Effect of Annealing Temperature and Annealing Time on Structural Transformation

Nanoparticles from the standard reaction A were also annealed at 300°C, 400°C and 500°C for 30 minutes. The XRD data in Figure 5.5 shows that the increase in particle size, reflected by a sharpening of the XRD peaks, correlates with an increase in annealing temperature. All samples contain the ordered $L1_2$ ordered $FePt_3$ phase to varying degrees. No $L1_0$ phase is detectable from the XRD patterns of our samples.

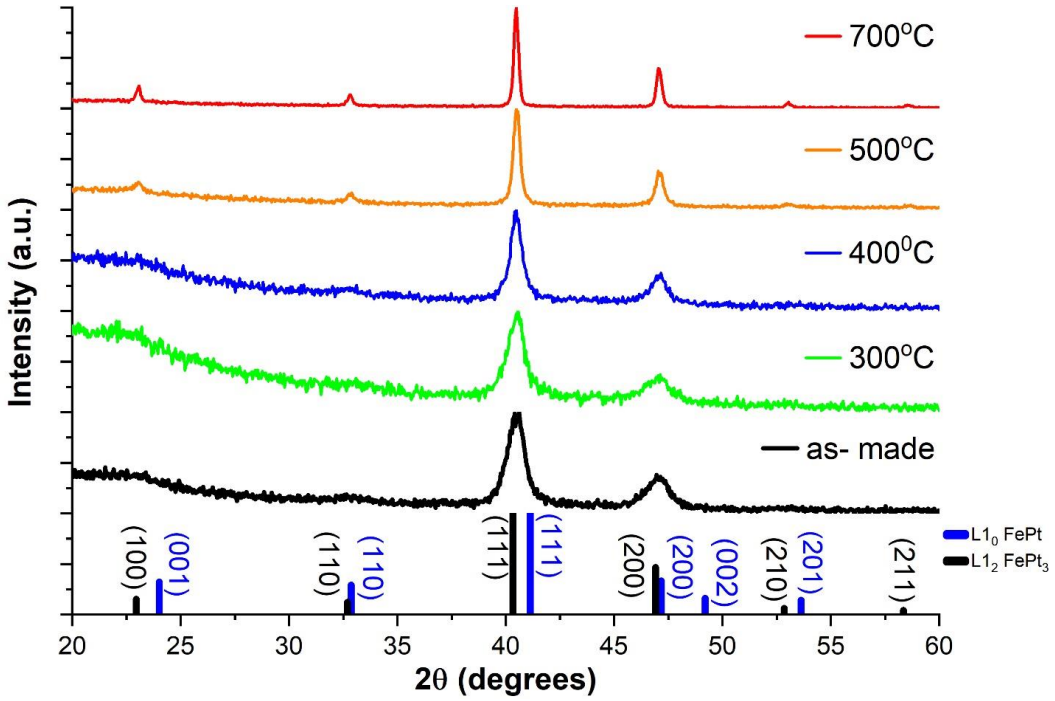

Figure 5.5: X-ray diffraction patterns of as-made and annealed nanoparticles obtained from the standard reaction A. All annealing times were 30 minutes.

The particle size was calculated using the Scherrer equation and the degree of ordering S was calculated for the different alloys to better quantify the structural transformation after annealing. The following expression is used for S [19].

$$S^2 = \frac{I_{110}/I_{111}}{I^O_{110}/I^O_{111}} \tag{5.2}$$

I_{110} and I_{111} are the measured peak intensities of the (110) and (111) peaks respectively in the XRD data, whereas I^O_{110} and I^O_{111} are the corresponding peak intensities of the fully ordered $L1_2$ $FePt_3$ phase. The increase in the degree of chemical ordering S with annealing temperature plotted in Figure 5.6 shows that higher annealing

temperatures enhance the transformation to the ordered $L1_2$ $FePt_3$ phase. The particle size is also found to increase with annealing temperature.

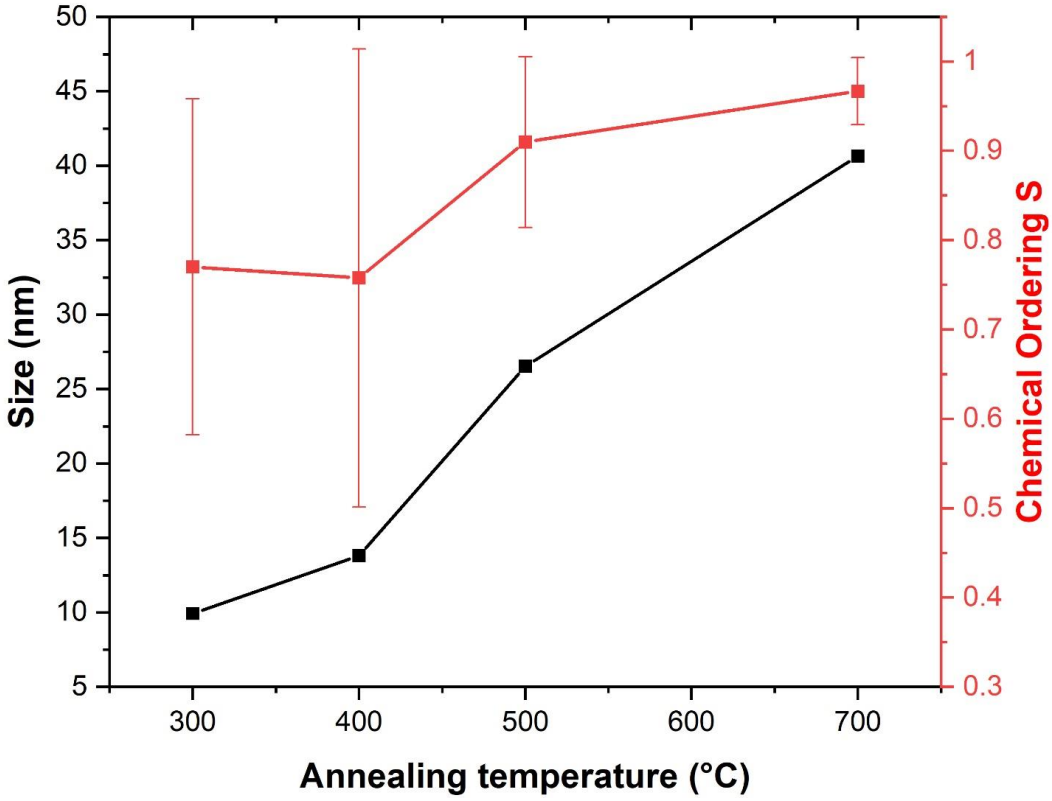

Figure 5.6: Calculated sizes and chemical ordering S as a function of annealing temperature. The different data points are connected to guide the eye. No error bars are placed on the size values as they are only estimates from the Scherrer equation.

We also annealed samples from the standard reaction at 700°C for longer durations. The XRD data of this study is shown in Figure 5.7 and the estimated sizes, lattice parameters a and order parameter in Table 5.4.

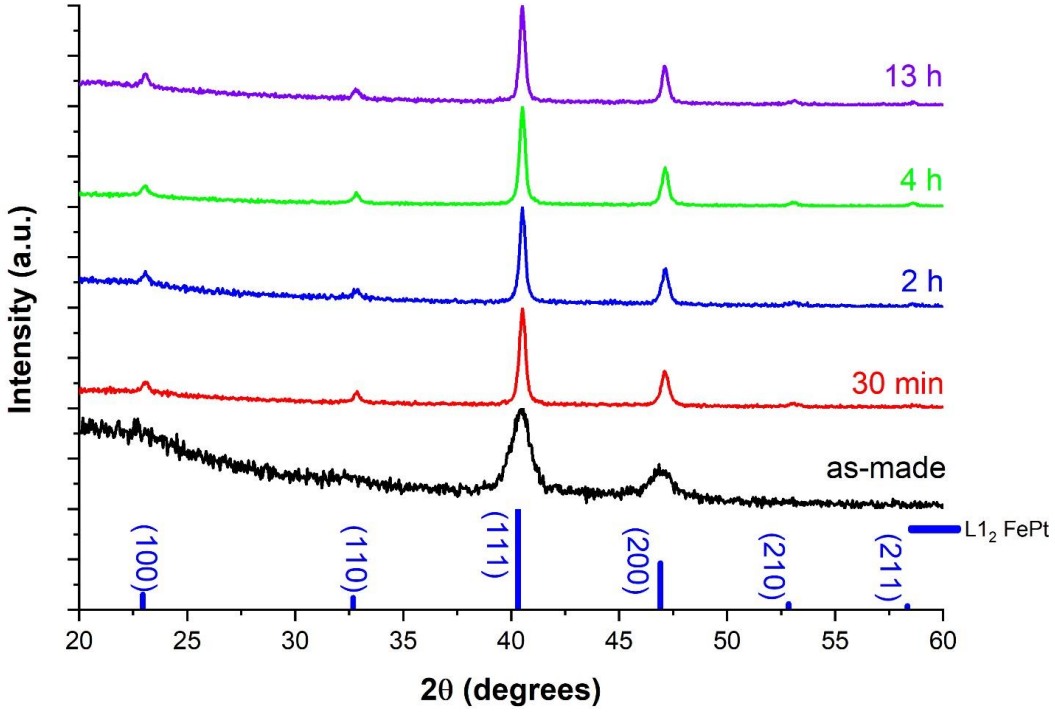

Figure 5.7: X-Ray diffraction patterns of as-synthesized and annealed nanoparticles from the standard reaction. The annealing temperature was 700°C.

Table 5.4: X-Ray diffraction patterns of as-synthesized and annealed nanoparticles from the standard reaction. The annealing temperature was 700°C.

Sample annealing condition	Estimated size (nm)	a (Å)	Degree of ordering
As-made	9	3.86	0.83
700°C, 30 minutes	29	3.85	0.99 ± 0.08
700°C, 2 hours	32	3.85	0.93 ± 0.13
700°C, 4 hours	32	3.85	0.97 ± 0.03
700°C, 13 hours	33	3.85	0.93 ± 0.09

Our results show that heat treatment of the nanoparticles at 700°C increases the $L1_2$ phase transformation though there is no significant change in the size and degree of annealing for annealing times of 2 hours or more. The main objective of increasing the annealing period at 700°C was to see if eventually a phase transformation to the $L1_0$ state occurs. The XRD data from Figure 5.7 shows that the structure remains in the $L1_2$ phase even after annealing for a period as long as 13 hours.

The structural transformation as a function of annealing time was also investigated in samples made from a different reaction (reaction B: 10 ml/10 ml TO/OAm solvent ratio).

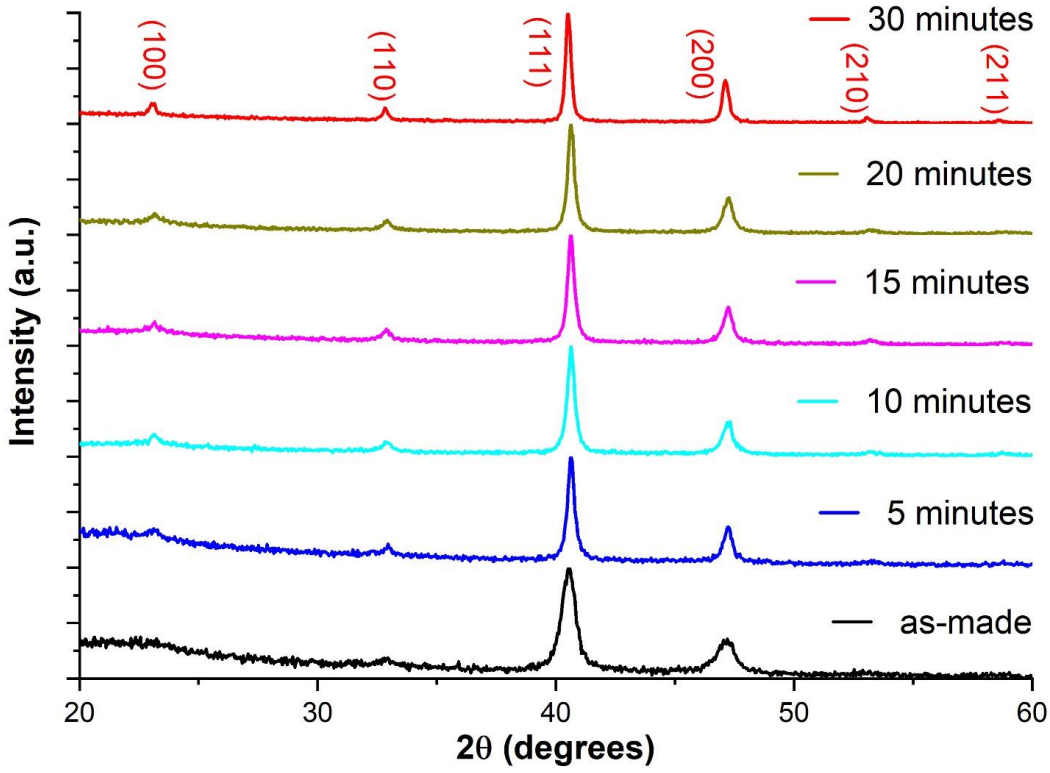

Figure 5.8: X-ray diffraction patterns of as-made nanoparticles (made in reaction B with 1:1 TO/OAm solvent ratio) and nanoparticles annealed at 700°C for different durations. Indexed peaks are those of $L1_2$ $FePt_3$.

The XRD data (Figure 5.8) shows that the $L1_2$ phase is produced even for low annealing durations at 700°C. The particle size and degree of chemical ordering *S* were determined as described before and plotted in Figure 5.9. In general, annealing for longer times produces larger nanoparticles. The chemical degree of ordering also increases, and the effect is more visible for longer annealing times.

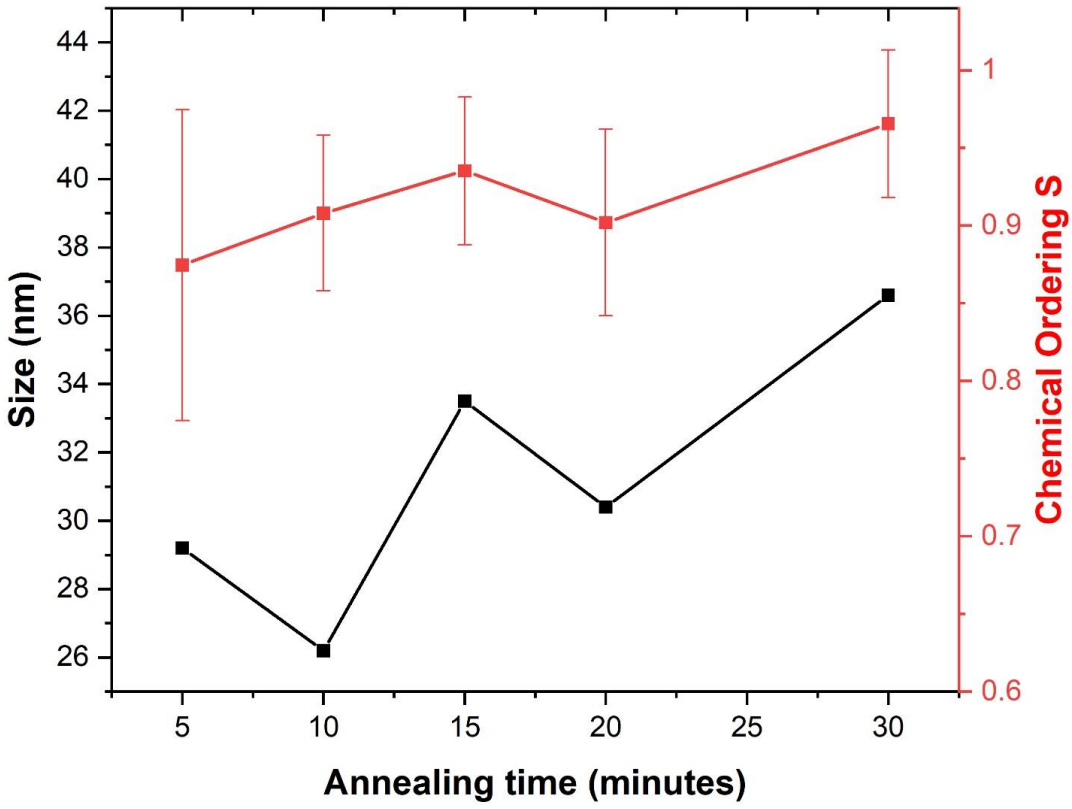

Figure 5.9: Calculated particle size and chemical ordering S as a function of annealing time at 700° C for reaction B. The different data points are connected to guide the eye.

5.3.2 Effect of Varying Fe:Pt Precursor Ratio in Synthesis

Reaction E was performed by using a 3:1 Fe:Pt precursor ratio, a 2 ml TO/18 ml OAm solvent ratio and a reaction time of 3 hours. A reaction temperature larger than 320°C was able to be achieved under these conditions, which was higher than the temperatures obtained in the other reactions. The XRD patterns in Figure 5.10 show that even when the amount of $Fe(acac)_3$ used was tripled, the $L1_0$ FePt phase did not form. This is in sharp contrast to previously reported work done where the stoichiometric ratio of Fe and Pt in Fe-Pt nanoparticles is controlled by varying the amounts of the Fe and Pt precursors used in the synthesis [20]. It may be possible that our choice of precursors combined with the presence of halide ions in the reaction mixture favor the formation of the $L1_2$ $FePt_3$ phase and may provide a pathway of guaranteeing the formation of the $L1_2$ $FePt_3$ phase with different size distributions. It is also likely that Pt precursor is reduced at a higher rate than the Fe precursor. A similar effect is observed in reactions C (2:1 Fe:Pt precursor ratio, 18 ml/2 ml TO:OAm ratio) and D (3:1 Fe:Pt precursor ratio, 18 ml/2 ml TO:OAm ratio). Doubling and tripling the Fe precursor amount still did not produce an alloy closer to the equiatomic composition. The XRD pattern of the annealed sample from reaction in Figure 5.4 also indicates a strong Fe_3O_4 peak, showing that the excess Fe used in the synthesis does not go into forming the Fe-Pt alloy.

Reaction E is also distinct from the other reactions we performed because it produced as-made nanoparticles containing a large amount of $L1_2$ $FePt_3$ nanoparticles with larger sizes, without the need of any post annealing to achieve these larger sizes and degrees of ordering, as seen in Figure 5.10. Annealing at 700°C for 30 minutes also increased the size as indicated by the sharper peaks in the XRD pattern of the annealed $FePt_3$ particles.

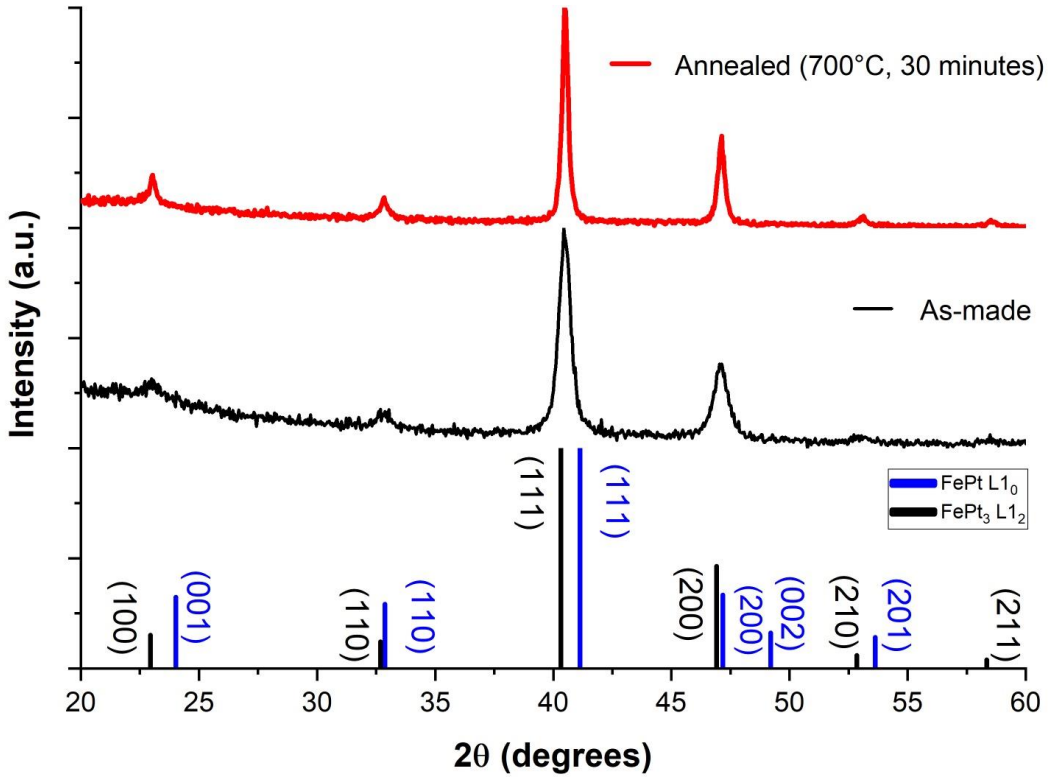

Figure 5.10: XRD pattern of as-made nanoparticles and nanoparticles annealed at 700°C for 30 minutes in a reaction where a 3:1 Fe:Pt precursor ratio and 2 ml/18 ml TO/OAm solvent ratio were used.

The ordered $L1_2$ $FePt_3$ content was estimated by fitting the XRD patterns of as-made and annealed nanoparticles using the software PowderCell [21]. The input phases were $L1_2$ $FePt_3$ and fcc FePt. An example of a fit is shown in Figure 5.11 for the as-made nanoparticles from reaction E.

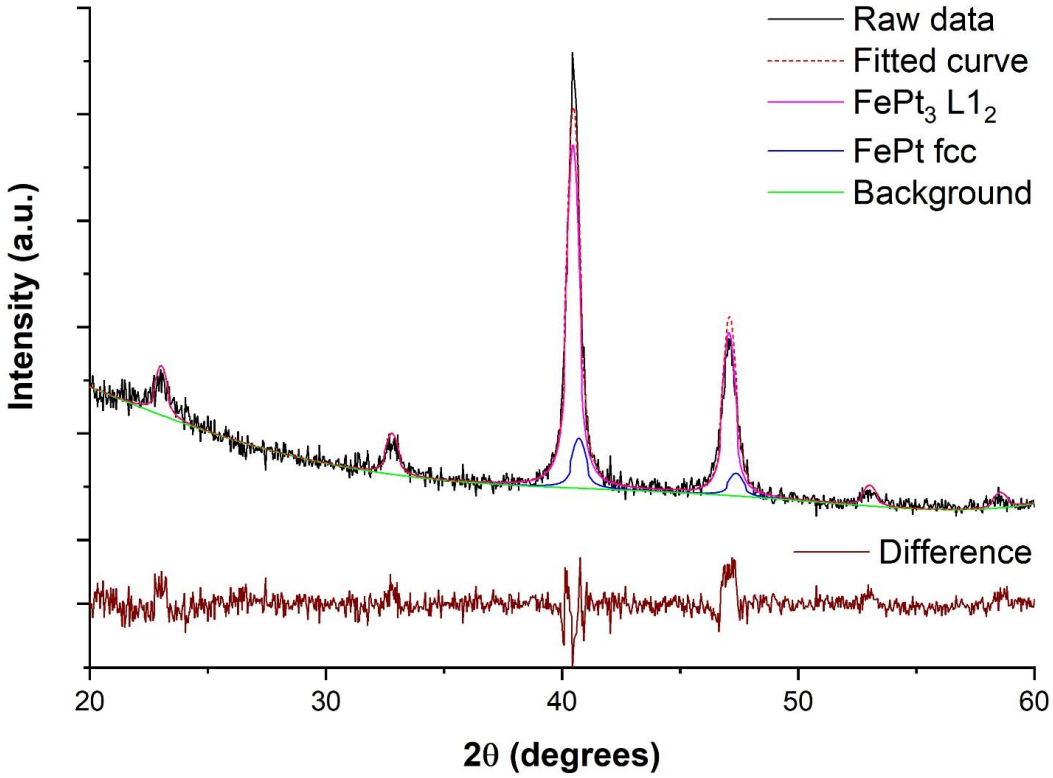

Figure 5.11: XRD fit of the as-synthesized data of nanoparticles obtained from reaction E. The difference between the raw (measured) data and the fitted curve is also shown.

Using this method, the $L1_2$ content in the as-synthesized sample was estimated to be 75.7%, and 24.3% fcc content for reaction E. Upon annealing, the estimated $L1_2$ content jumped to 100.0%. While the percent composition from the simulation are estimated, they show that reaction conditions for reaction E produce a significant amount of $L1_2$ $FePt_3$.

The sizes of the as-made nanoparticles and nanoparticles annealed at 700°C for 30 minutes from reaction E were compared to those from the standard reactions (Table 5.5).

Table 5.5: Comparison of as-made nanoparticles and nanoparticles at 700°C for 30 minutes from both standard reaction and reaction C (3:1 Fe/Pt precursor ratio, 2 ml/18 ml TO/OAm ratio).

Reaction	Sample	Estimated size (nm)	Degree of ordering
Standard reaction	As-made	9	0.83
Standard reaction	Annealed	41	0.96 ± 0.04
3:1 Fe/Pt ratio	As-made	15	0.86 ± 0.11
3:1 Fe/Pt ratio	Annealed	34	0.92 ± 0.06

The data confirms that larger as-made nanoparticles with a higher degree ordering are obtained in the modified reaction E, compared to the standard reaction. This result suggests the possibility of producing $L1_2$ $FePt_3$ as-made nanoparticles with a given size distribution and chemical ordering by adjusting the reaction parameters.

An additional synthesis was performed by modifying the standard reaction to use a solvent mixture of 19 ml paraffin oil and 1 ml oleylamine (OAm), keeping all other parameters the same (1:1 Fe:Pt precursor ratio, 1 mmol 1,2-hexadecadediol etc). The purpose of using paraffin oil was to guarantee that a reaction temperature as high as 330°C could be reached. In all reactions except reaction E, the reaction mixture reached the threshold of boiling in the range of 280°C – 300°C. In reaction E, the reaction temperature momentarily reached temperatures above 320°C before settling to a temperature around 315°C. A notable difference in reaction E from the other reactions described so far was that the solvent was consisted mostly of oleylamine. The as-made XRD data obtained from the synthesis using paraffin oil in Figure 5.12 shows a large amount of $L1_2$ $FePt_3$ in it, comparable to what is obtained in reaction E.

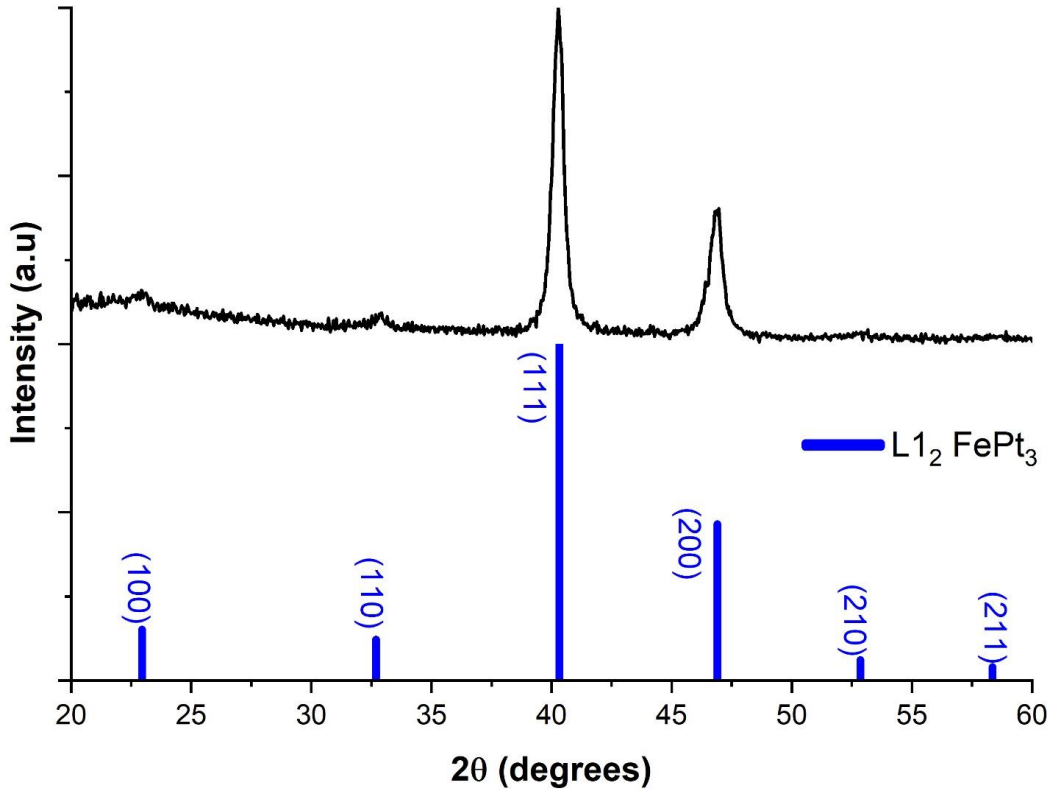

Figure 5.12: X-Ray diffraction pattern of as-synthesized nanoparticles obtained from the standard reaction modified to use a solvent mixture of 19 ml paraffin oil and 1 ml oleylamine.

Based on this observation, higher synthesis temperatures may be more suitable to directly produce $L1_2$ phase without any post annealing. A practical drawback of using paraffin oil and oleylamine as the main solvents is that it is harder to separate the nanoparticles and the yield is lower. A focus of future studies would be to find the optimum reaction conditions needed to produce monodisperse $L1_2$ nanoparticles directly in the as-made sample.

5.3.3 Effect of Using Iodine in Reaction on Structure

The effect of iodine in the formation of the $FePt_3$ phase was investigated by performing a reaction without the use of any iodine (reaction F). As it is already clear from Figure 5.4 that annealing produces the $L1_2$ $FePt_3$ phase in samples from all reactions that we studied, any significant effect of iodine in the structural transformation will be visible in the XRD data of the as-synthesized nanoparticles. Figure 5.13 shows such data for nanoparticles from the standard reaction A (with iodine), reaction F (no iodine) and reaction G (twice the amount of iodine).

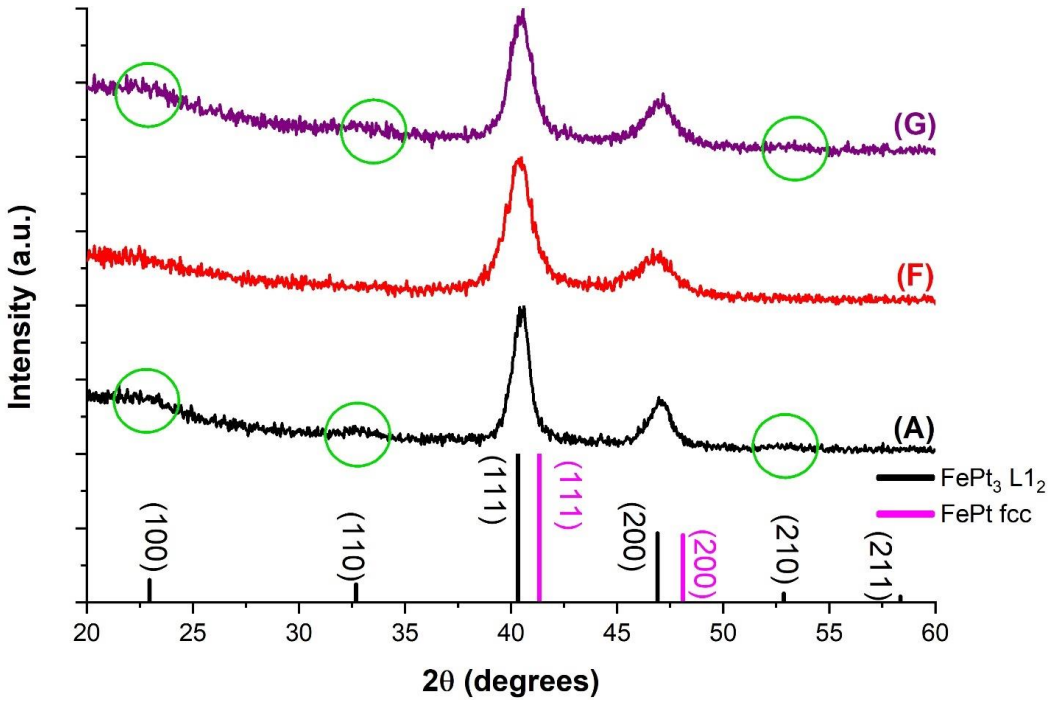

Figure 5.13: X-ray diffraction patterns of as-synthesized nanoparticles from reactions A (standard), F (no iodine) and G (double iodine). The less intense superlattice peaks in the XRD patterns of reactions A and G are encircled.

When no iodine is used, the (100) and (110) peaks from the $L1_2$ structure are absent or are too weak in intensity to be observed in the XRD pattern. In contrast, both as-made nanoparticles from the standard reaction and the reaction with twice the amount of iodine used exhibit emerging (100) and (110) peaks, indicating some $L1_2$ $FePt_3$ content in these samples. Their corresponding percentage composition of disordered fcc structure and ordered $L1_2$ structure was estimated computationally, using PowderCell as previously described for reaction E in the previous section (Table 5.6).

Table 5.6: Estimated content of $L1_2$ $FePt_3$ in as-synthesized samples from reactions A, F, and G.

Reaction	% $L1_2$ phase	% fcc phase
A (standard)	29.5%	70.5%
F (no iodine)	0.5%	99.5%
G (double iodine)	41.1%	58.9%

The results from the computations from Table 5.6 agree with the corresponding XRD data from Figure 5.13 regarding the effect of using iodine, namely; iodine enhances the formation of the $L1_2$ $FePt_3$ phase when used in the reaction. Additional work is required to investigate the effect of the amount of iodine used on the amount of $L1_2$ phase produced. However, as described in the previous section, producing as-made $L1_2$ $FePt_3$ nanoparticles is dependent on more than one reaction parameter, such as the precursor ratio and solvent ratio.

5.4 Thermomagnetic Measurements on Nanoparticles Made from The Standard Reaction

Thermomagnetic measurements were performed on samples produced from the standard reaction to further study any possible magnetic phase transformation. Below room temperature, the field-cooled (FC) and zero field-cooled (ZFC) curves for the as-made nanoparticles (Figure 5.14) diverge close to 300 K. The ZFC curve also peaks close to 280 K. Neither of these temperatures are close to the two Néel temperatures of the antiferromagnetic $FePt_3$ phase. We can conclude that the A1 fcc phase is present in the as-made nanoparticles with a Curie temperature higher than 300 K.

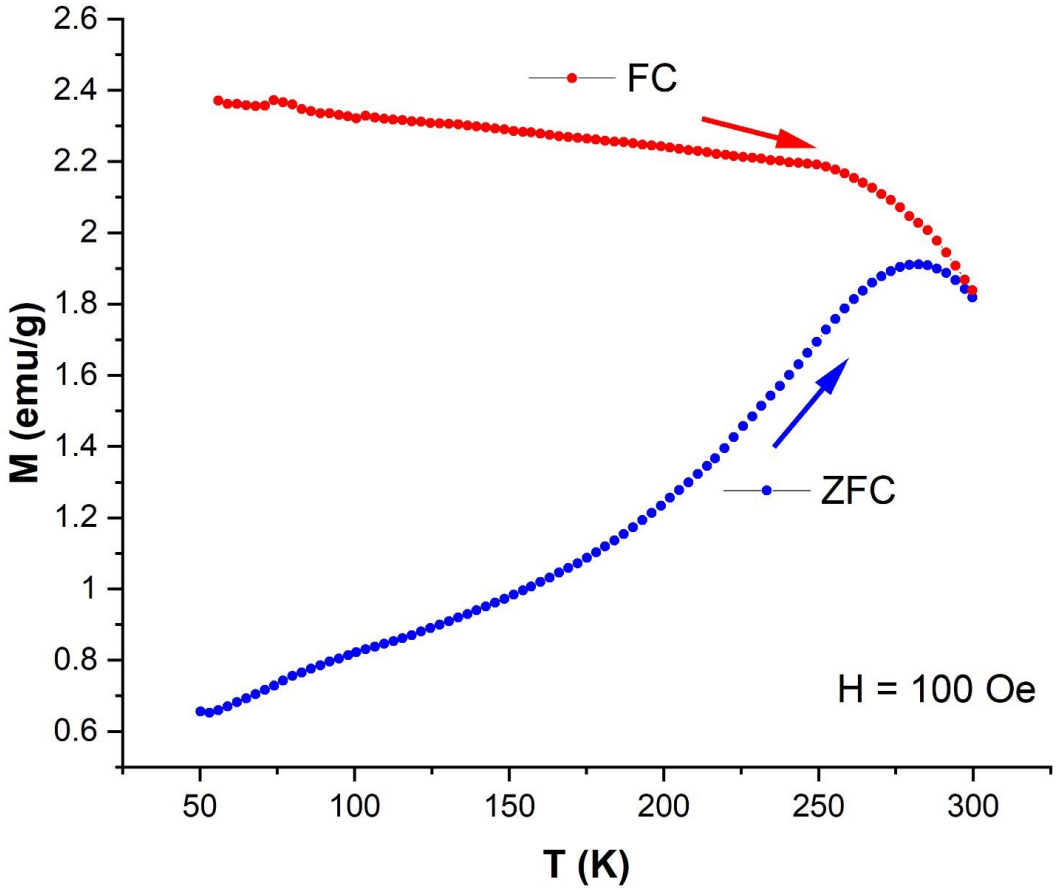

Figure 5.14: Field cooled (FC) and zero field cooled (ZFC) plots of magnetization versus temperature on the as-made nanoparticles from the standard reaction A, at an applied field of 100 Oe.

AC susceptibility measurements from physical property measurement system (PPMS) on the same samples also confirmed no phase transition below 300 K (Figure 5.15).

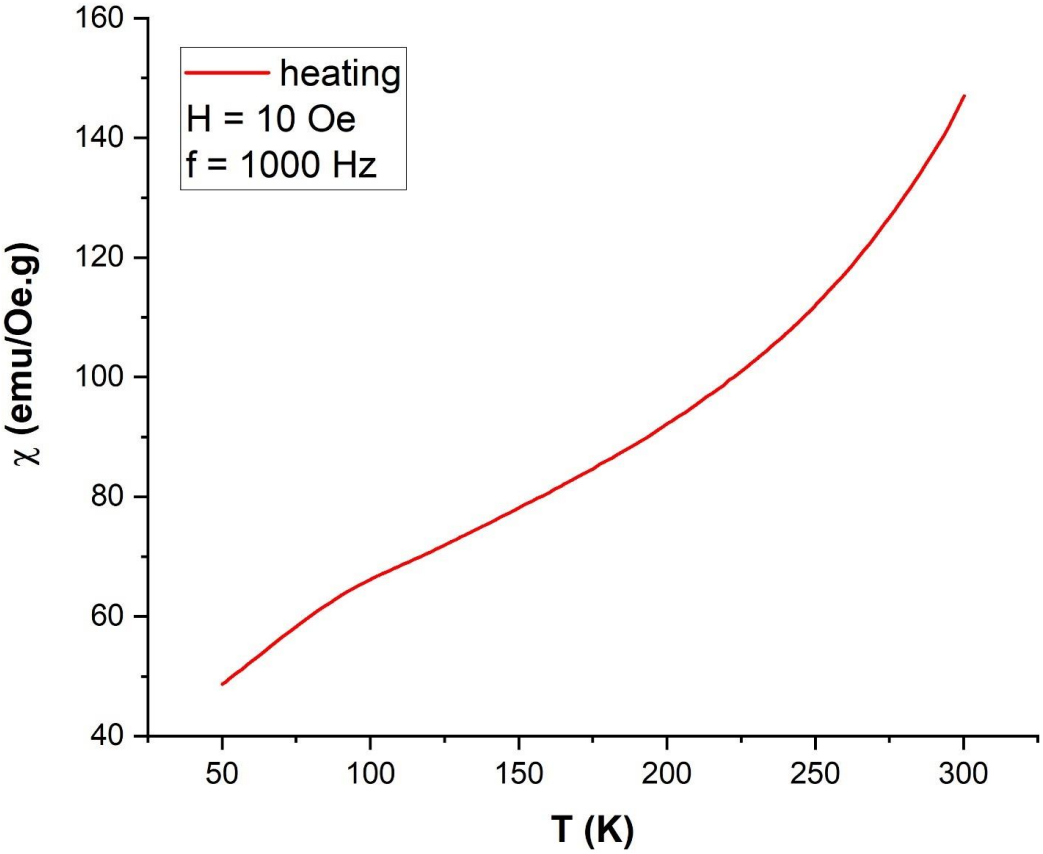

Figure 5.15: AC susceptibility measurement on as-made nanoparticles from standard reaction A.

Figure 5.16 shows magnetization versus temperature data in the range 300 K – 950 K.

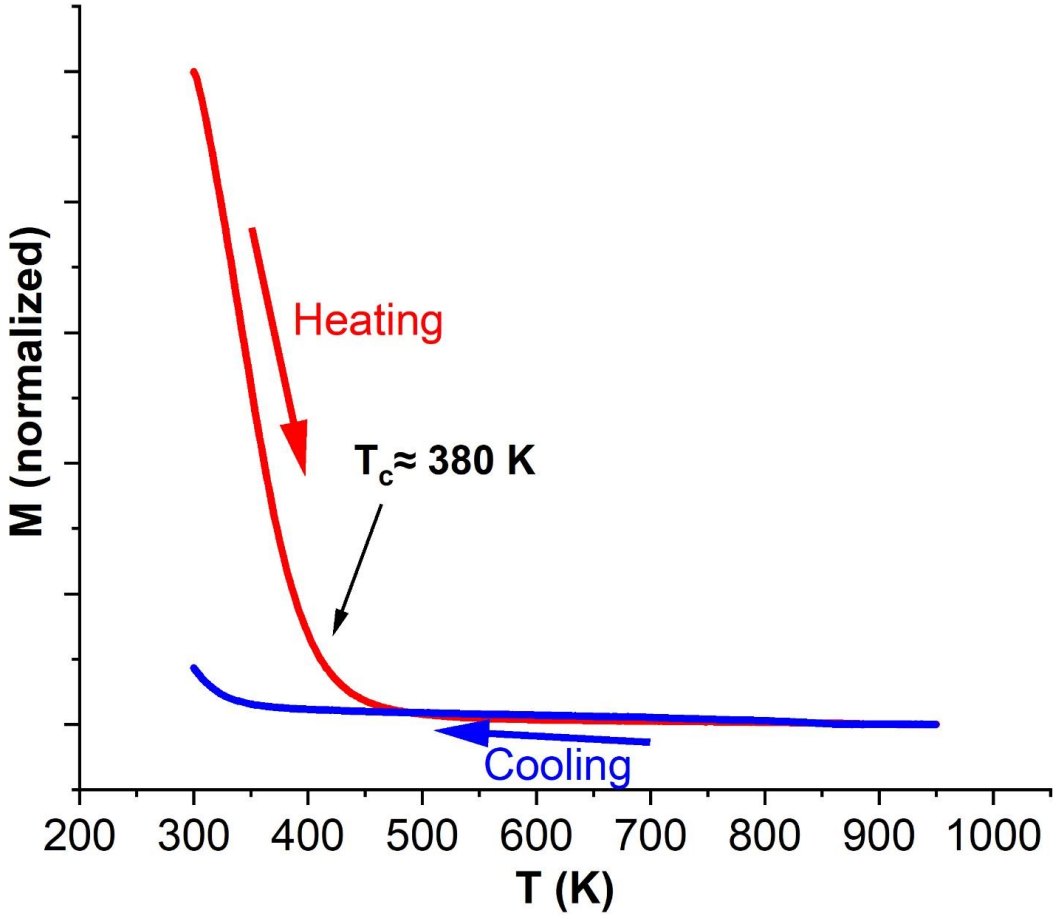

Figure 5.16: M vs T measurements on as-made nanoparticles from the standard reaction A at an applied field of 500 Oe.

The Curie temperature is determined as described in the previous chapter, from a plot the magnetization squared versus temperature. The data shows that the as-made particles have an fcc phase and are ferromagnetic with a Curie temperature of 380 K. M versus T data measurements on the nanoparticles annealed at 700°C for 30 minutes (Figure 5.17) reveal the appearance of a Curie temperature at 833 K. This Curie temperature is however not associated to an Fe-Pt phase, but instead due to a minority Fe_3O_4 phase which grows with heating to 950 K.

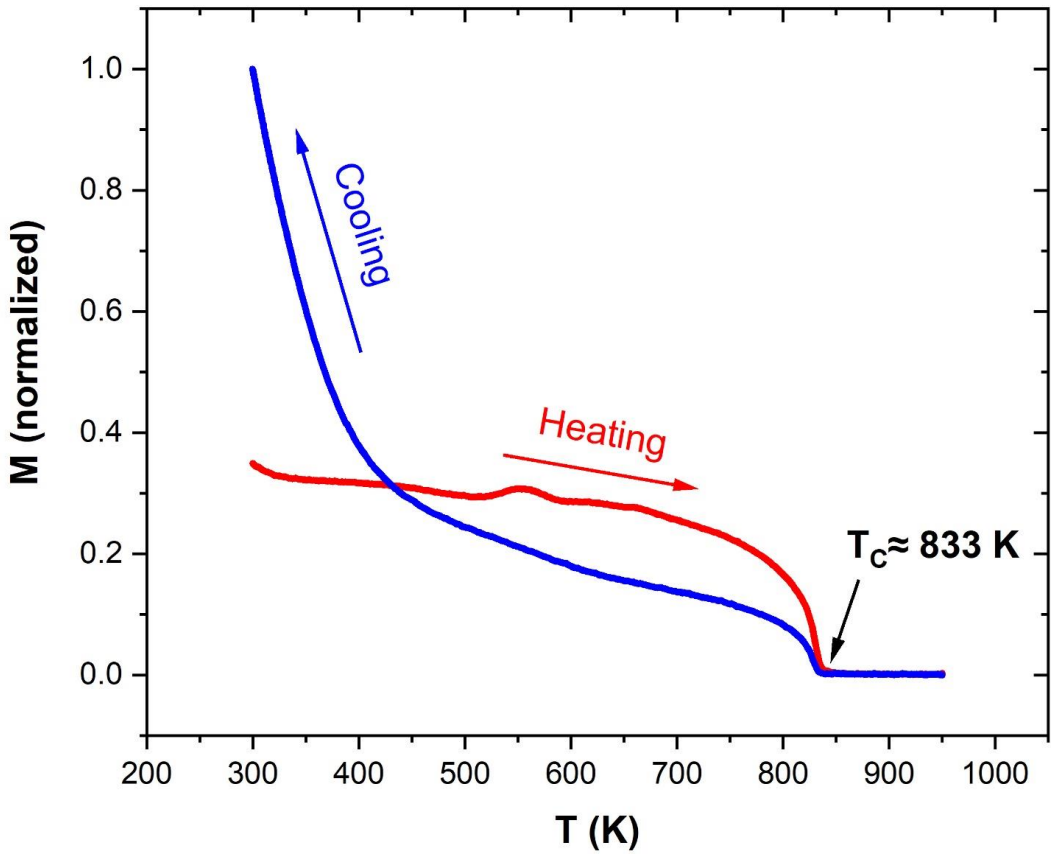

Figure 5.17: M vs T measurement at an applied field of 500 Oe on the nanoparticles from the standard reaction A which are annealed at 700°C for 30 minutes.

Thermomagnetic data on the annealed sample in the temperature range 50 K – 380 K plotted in Figure 5.18 reveal a mixture of two magnetic structures: a ferromagnetic phase with Curie temperature of about 297 K and an antiferromagnetic phase with a Néel temperature around 135 K.

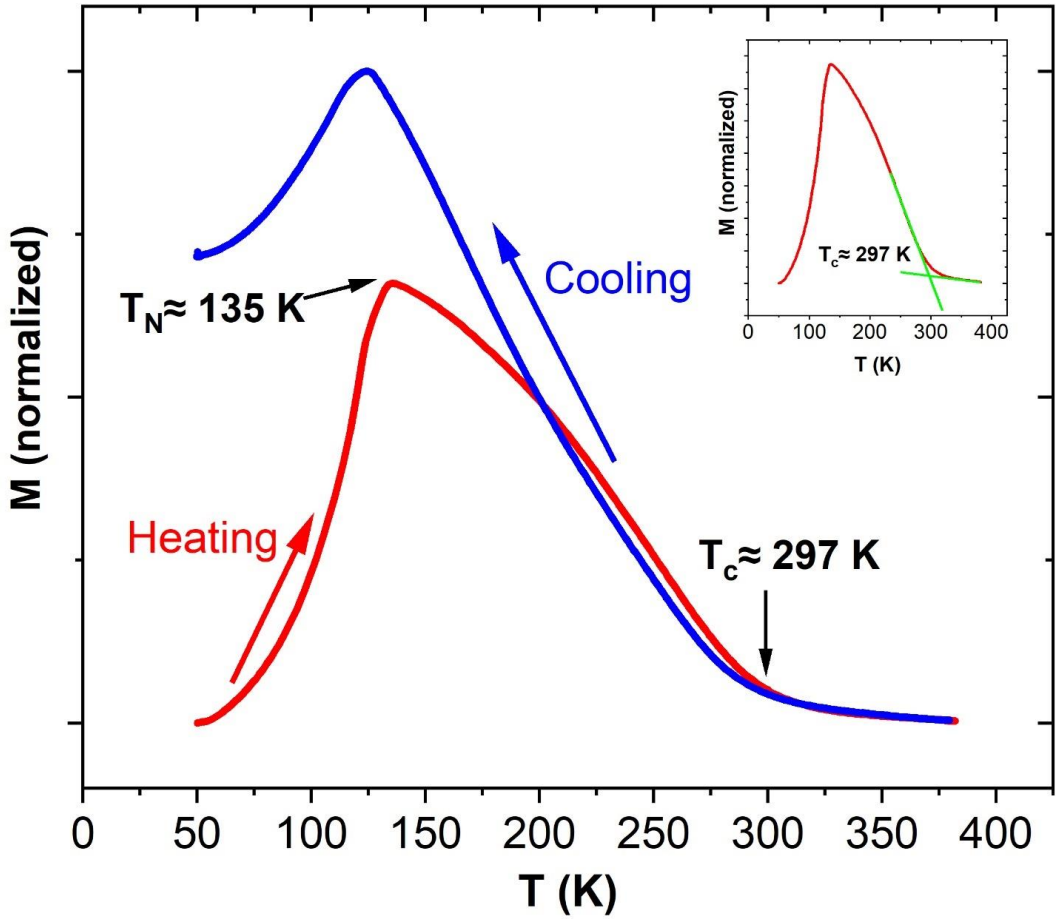

Figure 5.18: M vs T measurement on the nanoparticles from the standard reaction A annealed at 700°C for 30 minutes. The applied field was 500 Oe. The inset shows how T_c was determined from the graph.

A physical property measurement system (PPMS) was also used to carry out AC susceptibility measurements on the annealed sample. The AC susceptibility data confirms the transition temperature of about 135 K for the antiferromagnetic transition and another magnetic transition around 254 K (Figure 5.19). For comparison, a Curie temperature of 255 K has been observed by Margeat et al. [16] in chemically disordered

$FePt_3$ nanocubes, which is a much lower temperature than what is known for disordered $FePt_3$ bulk samples.

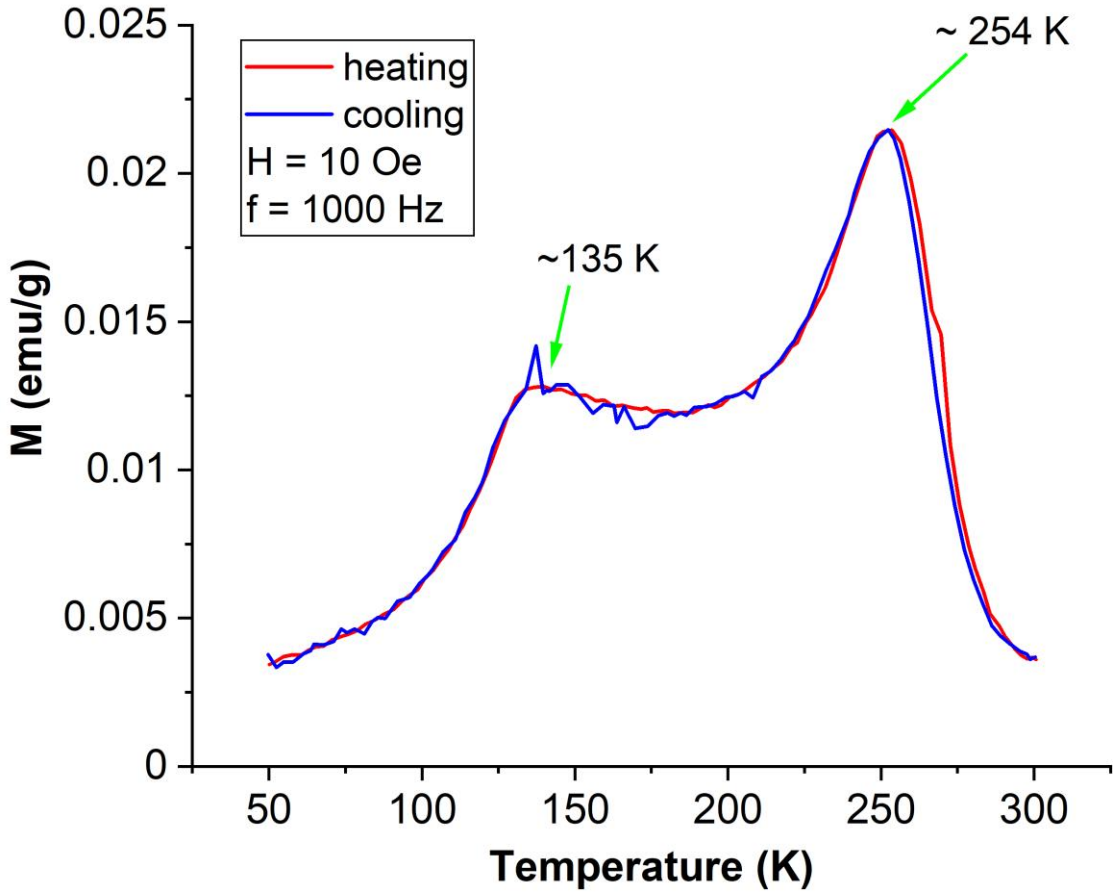

Figure 5.19: AC susceptibility measurement on sample annealed at 700°C for 30 minutes.

Figures 5.20 shows the M versus T data on the nanoparticles from the standard reaction annealed at 400°C and 500°C for 30 minutes. In both cases, the Curie temperatures fall outside the upper limit of the measurement range of 380 K. The Curie

temperature of both these samples are higher than the value of 297 K for the nanoparticles annealed at 700°C for the same duration, possibly due to a larger proportion of disordered $FePt_3$ phase in the samples annealed at 400°C and 500°C. The higher Curie temperatures in Figure 5.20 are consistent with the lower chemical ordering of these nanoparticles compared to the higher ordering obtained at an annealing temperature of 700°C (Figure 5.6). On the other hand, higher Néel temperatures of 233 K and 197 K are obtained for annealing temperatures of 400°C and 500°C respectively, compared to 135 K for an annealing temperature of 700°C. These measurements again indicate that a higher annealing temperature enhances the $L1_2$ ordering the $FePt_3$ nanoparticles for an annealing duration of 30 minutes.

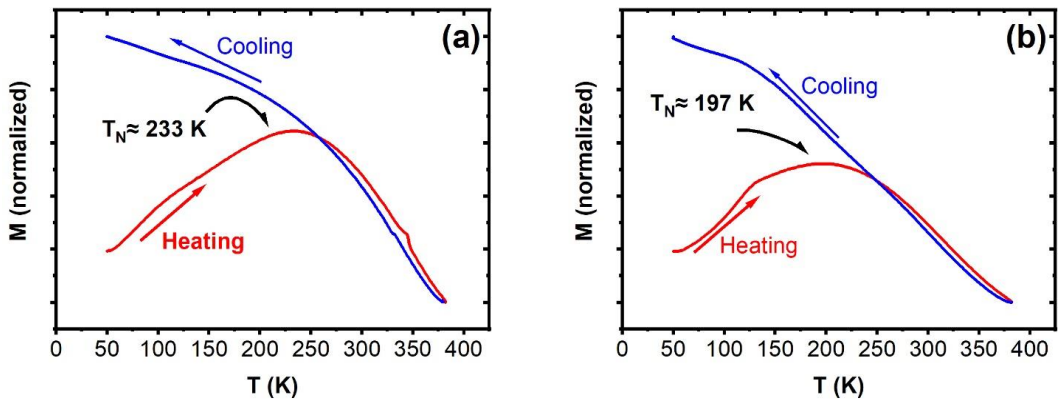

Figure 5.20: *M* vs *T* measurement at an applied field of 500 Oe on the nanoparticles from the standard reaction A annealed at (a) 400°C for 30 minutes and (b) 500°C for 30 minutes.

Magnetic moment versus temperature data were also taken for the samples annealed at 700°C for 2 hours, 4 hours and 13 hours at an applied field of 500 Oe in the temperature range 50 K – 400 K. Figure 5.21 shows the resulting data.

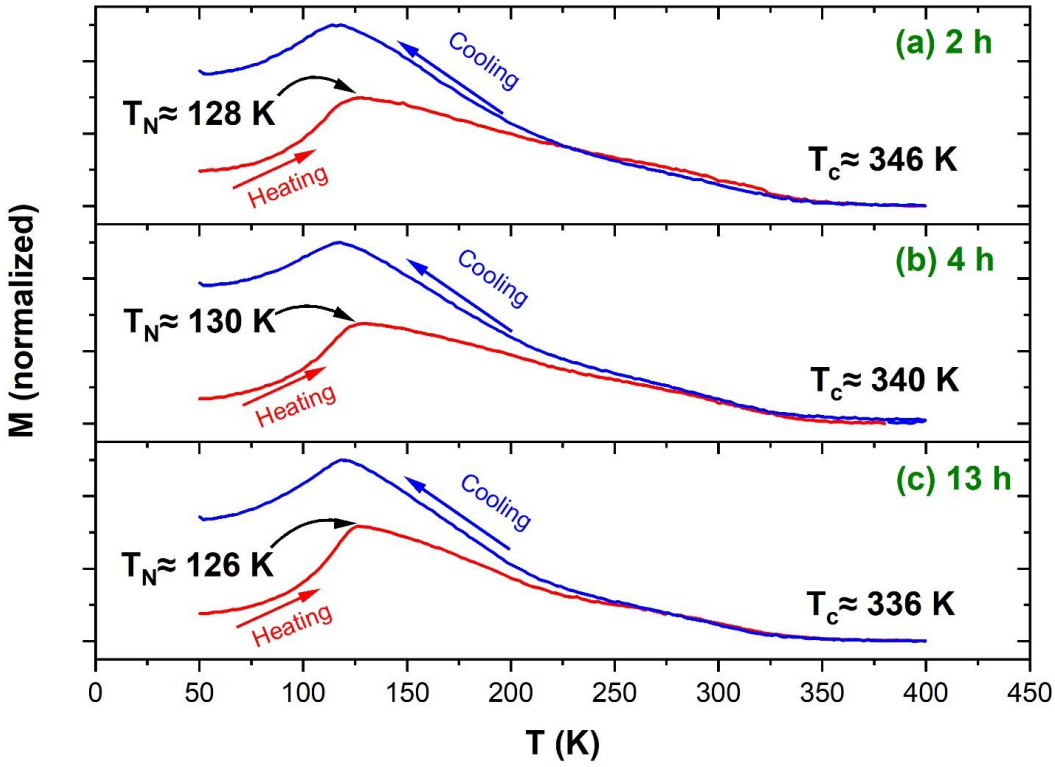

Figure 5.21: M vs T for nanoparticles from the standard reaction annealed at 700°C for 2 hours, 4 hours and 13 hours at an applied field of 500 Oe.

The Curie temperatures of the annealed $FePt_3$ nanoparticles range from 336 K to 346 K. For comparison, the Curie temperature of the as-made nanoparticles was found to be 380 K in Figure 5.17. The existence of a Curie temperature in the annealed samples indicates that the transformation to the $L1_2$ phase after annealing is only partial, and that there are some residual fcc phase present. There is no significant change in the Néel temperature with annealing duration. The data suggest that annealing for longer

periods at 700°C will not bring any significant change to the Curie temperatures or Néel temperatures. Future work in that area will consist of annealing at higher temperatures to attempt to suppress the ferromagnetic phase within the AFM matrix [17].

5.4.1 Thermomagnetic Study of Nanoparticles Synthesized Without Iodine

To further investigate the effect of using iodine in the $FePt_3$ synthesis, thermomagnetic measurements in the temperature range of 300 K – 950 K and AC susceptibility measurements in the temperature range of 50 K – 300 K were performed on the nanoparticles from reaction F, where no iodine was used (Figures 5.22 and 5.23).

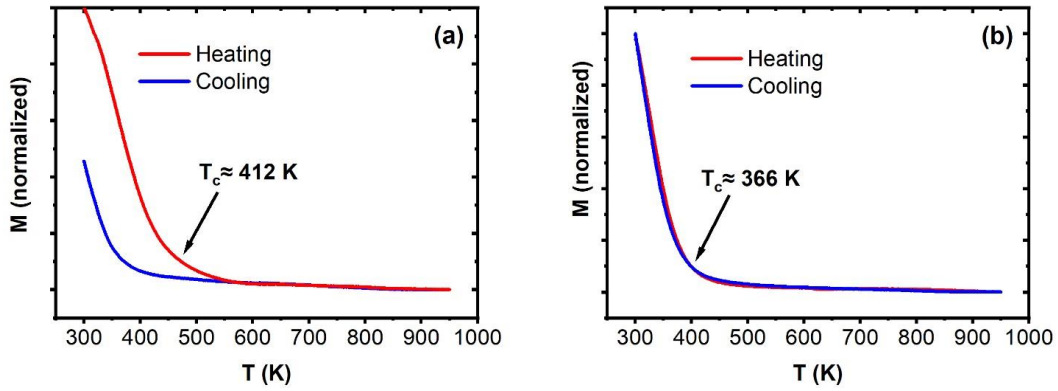

Figure 5.22: *M* vs *T* data at an applied field of 500 Oe for the nanoparticles synthesized without using iodine: (a) as-synthesized nanoparticles (b) nanoparticles annealed at 700°C for 30 minutes.

The as-made nanoparticles from reaction F (no iodine used) have a Curie temperature of 412 K, which is higher than the 380 K value of the as-made nanoparticles from the standard reaction. However, when they are heated to 950 K and then cooled to

room temperature, the observed Curie temperature is close to 380 K as for the particles made by the standard reaction. The lower Curie temperature obtained from the cooling curve is due to a structural transformation occurring during the heating part of the measurement. The annealed nanoparticles from reaction G have a Curie temperature of 366 K. In contrast, no Curie temperature was detected in this range of measurement temperature in the corresponding annealed nanoparticles from the standard reaction (Figure 5.18). The Curie temperature of 366 K could be associated to fcc (A1) FePt. It is also possible that the use of iodine affects the size distribution and morphology of the synthesized nanoparticles, which affect the Curie temperature. No Fe_3O_4 phase was detected in the annealed sample from reaction G.

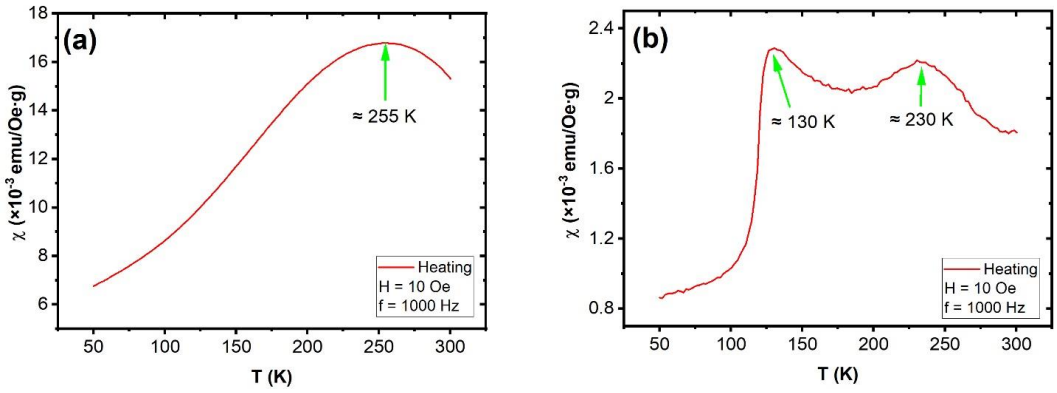

Figure 5.23: AC susceptibility measurements on the (a) as-made and (b) annealed nanoparticles (at 700°C for 30 minutes) from reaction G (no iodine used).

The AC susceptibility measurements in Figure 5.23 were carried out in the range of 50 K – 300 K on both samples. The peak in the as-made data in Figure 5.23(a) is similar to the one observed in Figure 5.19 and may be associated to the Curie

temperature of a disordered $FePt_3$ phase as suggested by Margeat *et al*. [16]. The annealed data in Figure 5.23(b) shows both a transition from the antiferromagnetic state at 130 K and another transition at 230 K. The transition at 130 K is expected since annealing the nanoparticles from all reactions produced the $L1_2$ $FePt_3$, as seen from the XRD pattern in Figure 5.4.

5.5 Hysteresis Loops Measurements

5.5.1 *M* vs *H* Measurements on Nanoparticles from The Standard Reaction

Magnetization as a function of applied field of the as-made and annealed nanoparticles from the standard reactions were measured at 50 K and 300 K (Figure 5.24).

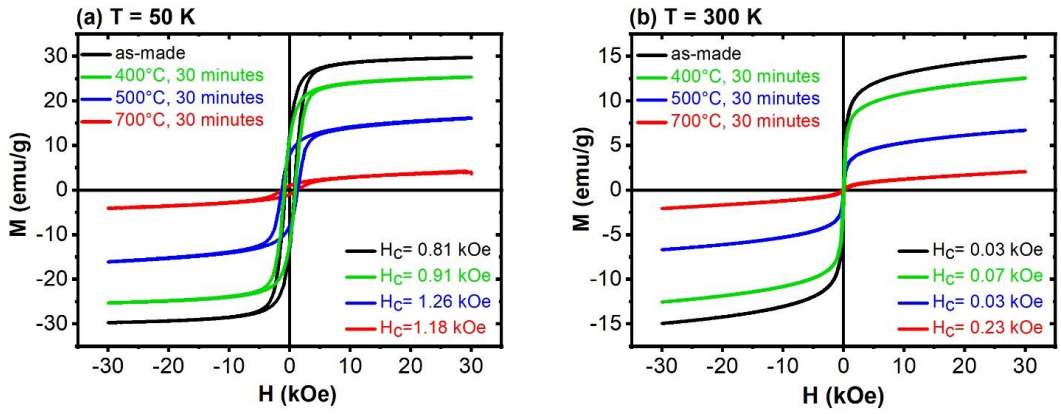

Figure 5.24: *M* vs *H* data on as-made and annealed nanoparticles from the standard reaction at (a) 50 K and (b) 300 K.

The hysteresis loops at 300 K and 50 K show that the magnetization decreases with increasing annealing temperature, because of the ferromagnetic to antiferromagnetic transition. A non-monotonic change in the coercivity with annealing temperature is observed which can be explained by the mixture of ferromagnetic and antiferromagnetic phases and to increased particle sizes at higher annealing temperatures. The coercivities of each sample are lower at 300 K compared to their corresponding values at 50 K as expected because of thermal effects. Both our XRD and magnetic data illustrate that annealing at 700°C for 30 minutes results in a very ordered $L1_2$ phase.

5.5.2 Hysteresis Loops of Nanoparticles from Reaction E

As described previously, we were able to obtain as-made $FePt_3$ nanoparticles with a higher ratio of ordered $L1_2$ phase to disordered fcc phase in reaction E (3:1 Fe/Pt precursor ratio, 2 ml/18 ml TO/OAm solvent ratio, 3 hour reaction), as seen from the XRD data in Figure 5.10, and the estimated degree of ordering in Table 5.5. The room temperature hysteresis loops of the as-made and annealed nanoparticles from reaction E are shown in Figure 5.25.

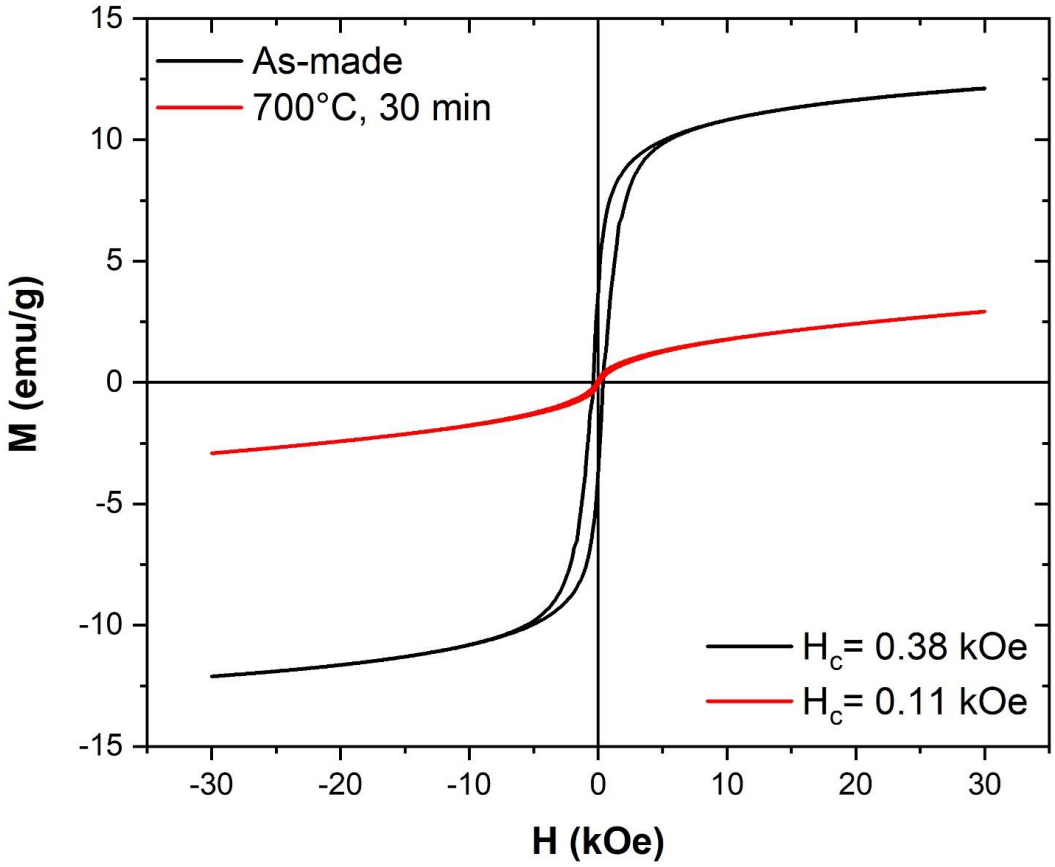

Figure 5.25: Room temperature hysteresis loops of as-made nanoparticles and nanoparticles annealed at 700°C for 30 minutes from reaction E.

Compared to the 300 K data from the standard reaction from Figure 5.24(b), we notice a larger coercivity for the as-made nanoparticles (0.38 kOe vs 0.03 kOe for the standard reaction) and a smaller one for the annealed nanoparticles (0.11 kOe vs 0.23 kOe for the standard reaction). Upon annealing, the transformation of the nanoparticles in the fcc structure into the $L1_2$ structure causes a drop in coercivity. A higher content of $L1_2$ $FePt_3$ in the annealed sample from reaction E compared to that from the standard reaction signifies more paramagnetic materials in that sample at room temperature.

5.5.3 Hysteresis Loops from Reaction F (No Iodine Used in The Synthesis)

The XRD data of the as-made nanoparticles from reaction F in Figure 5.13 indicate that iodine promotes the formation of the $L1_2$ $FePt_3$ phase in the as-made nanoparticles. We performed hysteresis loops measurements on the as-made nanoparticles from reaction F at temperatures of 50 K, 100 K, 200 K and 300 K (Figure 5.26).

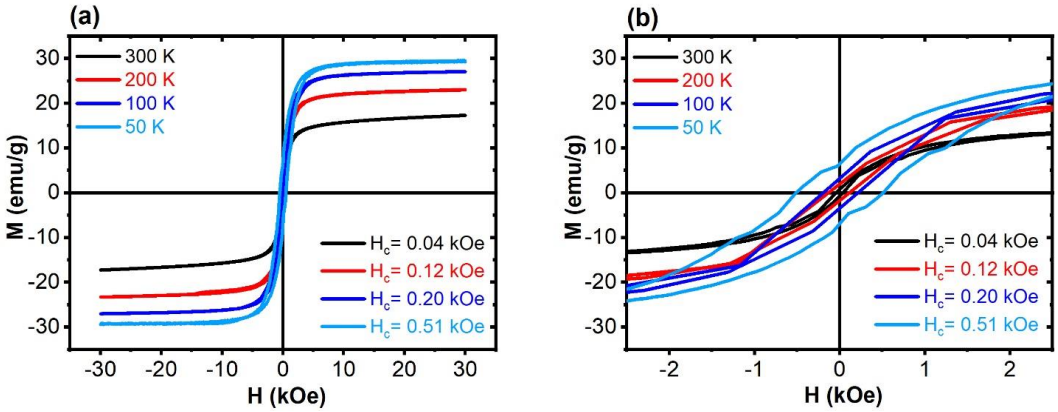

Figure 5.26: (a) *M* vs *H* data on the as-made nanoparticles from reaction F (no iodine used in synthesis) at different temperatures. (b) Zoomed in graph to show variation of coercivity.

The coercivity of the as-made nanoparticles from this reaction is 0.04 kOe at 300 K which is close to the value of 0.03 kOe at 300 K the as-made nanoparticles from the standard reaction. At 50 K, the coercivity of the as-made nanoparticles from this reaction is 0.51 kOe which is lower than the value of 0.81 kOe for the as-made nanoparticles from the standard reaction. The coercivity of the as-made nanoparticles decrease monotonically with increasing temperature because of the absence or very low

amount of $L1_2$ phase in it. As shown in Table 5.6, the content of the as-made nanoparticles from reaction F were estimated to be predominantly fcc in structure.

Figure 5.27 shows the hysteresis loops taken on the annealed nanoparticles (at 700°C for 30 minutes) from this reaction at 50 K, 100 K, 200 K and 300 K. As the XRD pattern in Figure 5.4 depicts, annealing caused the formation of the $L1_2$ $FePt_3$ phase. Therefore, the coercivity is observed to change non-monotonically from 50 K to 300 K due to mixture of ferromagnetic and antiferromagnetic phase. Compared to the nanoparticles from the standard reaction annealed under the same conditions, the coercivity of the nanoparticles are very similar at 300 K (0.25 kOe for reaction F compared to 0.23 kOe for the standard reaction A). At 50 K, there is a bigger difference in the coercivities of the nanoparticles from these 2 reactions: 0.81 kOe for reaction F compared to 1.18 kOe for the standard reaction A. The higher coercivity at 50 K of the nanoparticles from the standard reaction is due very likely to a higher amount of $L1_2$ $FePt_3$ phase in it. The coercivities at 50 K of the annealed nanoparticles from these 2 reactions suggest that when iodine is not used in the synthesis, annealing at 700°C for 30 minutes does not fully transform the as-made nanoparticles to the $L1_2$ phase. Possibly, a higher annealing temperature and/or longer annealing period may be required to achieve this effect, given that the as-made nanoparticles are almost entirely in the disordered fcc phase to begin with.

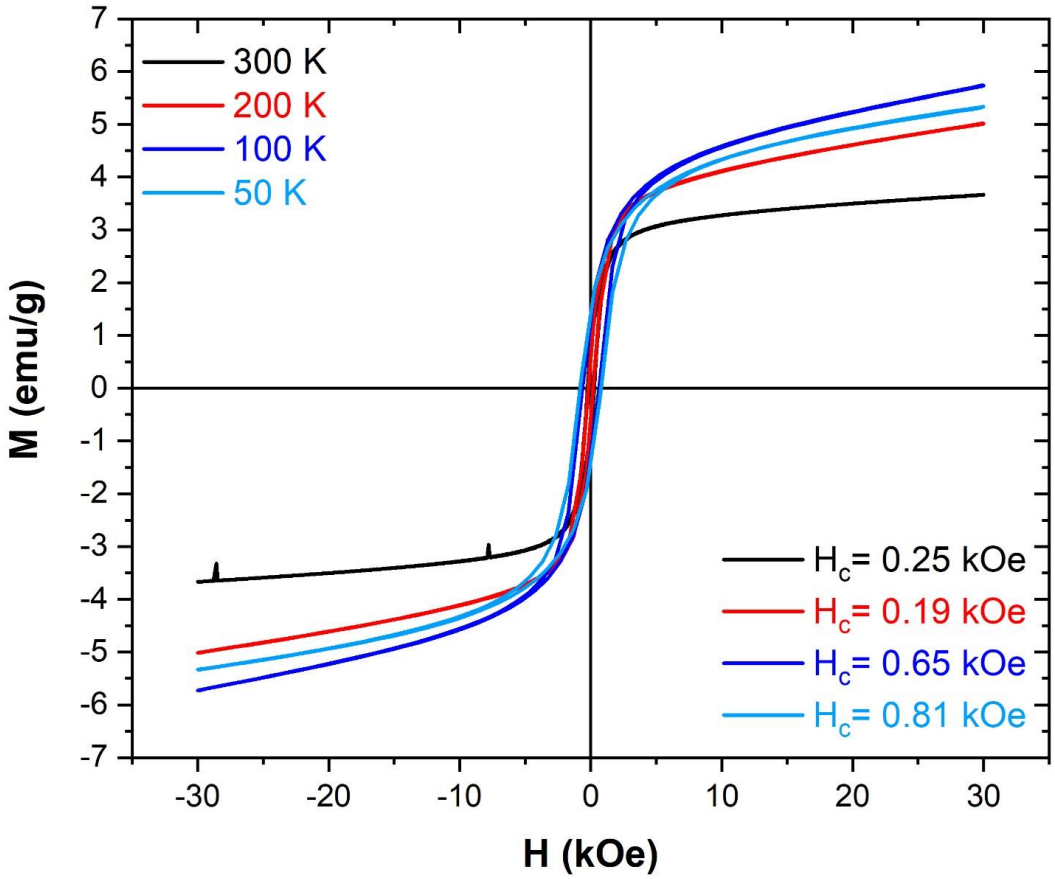

Figure 5.27: *M* vs *H* data on the nanoparticles from reaction F (no iodine used in synthesis) at different temperatures.

5.6 Summary

- Using $Fe(acac)_3$ and $(NH_2)_2PtCl_2$ as precursors, $FePt_3$ nanoparticles were synthesized. The $L1_2$ structure was obtained after heat treatment. No $L1_0$ FePt phase was obtained despite varying the precursor ratio.
- Annealing at higher temperatures improved the degree of ordering. Annealing for longer periods at 700°C also improved the $L1_2$ ordering. This is shown both by the XRD data, and thermomagnetic data which shows a Néel temperature in the annealed sample.

- The transformation to the $L1_2$ is not complete when the nanoparticles are annealed at 700°C for time periods up to 13 hours, based on our data, as seen by the presence of a Curie temperature in these samples. A higher annealing temperature may be required to produce samples with higher $L1_2$ $FePt_3$ content. This will be the subject of future investigations.
- By a suitable choice of solvent ratio, precursor ratio and reaction time, it was possible to increase the amount of $L1_2$ $FePt_3$ in the as-made nanoparticles. Modifying the reaction parameters to produce the $L1_2$ $FePt_3$ nanoparticles with a narrow size distribution with any post heat treatment will be a main subject of study.
- In general, annealing at higher temperatures increased the coercivity at 50 K and 300 K. Because of the mixture of ferromagnetic and antiferromagnetic nanoparticles, the change is not monotonic at 50 K.

REFERENCES

[1] S. Sun, *Recent Advances in Chemical Synthesis, Self-Assembly, and Applications of FePt Nanoparticles*, Adv. Mater. **18**, 393 (2006).

[2] K. Zhu, Y. Ju, J. Xu, Z. Yang, S. Gao, and Y. Hou, *Magnetic Nanomaterials: Chemical Design, Synthesis, and Potential Applications*, Acc. Chem. Res. **51**, 404 (2018).

[3] Y. Shi, M. Lin, X. Jiang, and S. Liang, *Recent Advances in FePt Nanoparticles for Biomedicine*, J. Nanomater. **2015**, (2015).

[4] A. T. Heitsch, D. C. Lee, and B. A. Korgel, *Antiferromagnetic Single Domain $L1_2$ $FePt_3$ Nanocrystals*, J. Phys. Chem. C **114**, 2512 (2010).

[5] W. G. Moffatt, *The Handbook of Binary Phase Diagrams* (19760000).

[6] T. Massalski, H. Okamoto, and P. Subramanian, *Binary Alloy Phase Diagrams ASM International*, Okamoto PR Subramanian Kacprzak–1996–852 P (1990).

[7] J. Lyubina, I. Opahle, K.-H. Müller, O. Gutfleisch, M. Richter, M. Wolf, and L. Schultz, *Magnetocrystalline Anisotropy in $L1_0$ FePt and Exchange Coupling in FePt/Fe_3Pt Nanocomposites*, J. Phys. Condens. Matter **17**, 4157 (2005).

[8] G. E. Bacon, J. Crangle, and W. Sucksmith, *Chemical and Magnetic Order in Platinum-Rich Pt + Fe Alloys*, Proc. R. Soc. Lond. Ser. Math. Phys. Sci. **272**, 387 (1963).

[9] D. Palaith, C. W. Kimball, R. S. Preston, and J. Crangle, *Magnetic Behavior of the Pt+Fe System Near Pt_3Fe*, Phys. Rev. **178**, 795 (1969).

[10] S. Maat, O. Hellwig, G. Zeltzer, E. E. Fullerton, G. J. Mankey, M. L. Crow, and J. L. Robertson, *Antiferromagnetic Structure of $FePt_3$ Films Studied by Neutron Scattering*, Phys. Rev. B **63**, 134426 (2001).

[11] Q. Li, L. Wu, G. Wu, D. Su, H. Lv, S. Zhang, W. Zhu, A. Casimir, H. Zhu, A. Mendoza-Garcia, and S. Sun, *New Approach to Fully Ordered Fct-FePt Nanoparticles for Much Enhanced Electrocatalysis in Acid*, Nano Lett. **15**, 2468 (2015).

[12] J. Kim, Y. Lee, and S. Sun, *Structurally Ordered FePt Nanoparticles and Their Enhanced Catalysis for Oxygen Reduction Reaction*, J. Am. Chem. Soc. **132**, 4996 (2010).

[13] F. M. Abel, V. Tzitzios, E. Devlin, S. Alhassan, D. J. Sellmyer, and G. C. Hadjipanayis, *Enhancing the Ordering and Coercivity of $L1_0$ FePt Nanostructures with Bismuth Additives for Applications Ranging from Permanent Magnets to Catalysts*, ACS Appl. Nano Mater. **2**, 3146 (2019).

[14] W. Lei, Y. Yu, W. Yang, M. Feng, and H. Li, *A General Strategy for Synthesizing High-Coercivity $L1_0$-FePt Nanoparticles*, Nanoscale **9**, 12855 (2017).

[15] W. Lei, J. Xu, Y. Yu, W. Yang, Y. Hou, and D. Chen, *Halide Ion-Mediated Synthesis of $L1_0$-FePt Nanoparticles with Tunable Magnetic Properties*, Nano Lett. **18**, 7839 (2018).

[16] O. Margeat, M. Tran, M. Spasova, and M. Farle, *Magnetism and Structure of Chemically Disordered $FePt_3$ Nanocubes*, Phys. Rev. B **75**, 134410 (2007).

[17] H. Min Song, W. Seop Kim, Y. Bok Lee, J. Hoon Hong, H. Gyu Lee, and N. Hwi Hur, *Chemically Ordered FePt 3 Nanoparticles Synthesized by a Bimetallic Precursor and Their Magnetic Transitions*, J. Mater. Chem. **19**, 3677 (2009).

[18] T. J. Klemmer, N. Shukla, C. Liu, X. W. Wu, E. B. Svedberg, O. Mryasov, R. W. Chantrell, D. Weller, M. Tanase, and D. E. Laughlin, *Structural Studies of $L1_0$ FePt Nanoparticles*, Appl. Phys. Lett. **81**, 2220 (2002).

[19] Y. K. Takahashi, T. Koyama, M. Ohnuma, T. Ohkubo, and K. Hono, *Size Dependence of Ordering in FePt Nanoparticles*, J. Appl. Phys. **95**, 2690 (2004).

[20] Y. Liu, Y. Jiang, X. Zhang, Y. Wang, Y. Zhang, H. Liu, H. Zhai, Y. Liu, J. Yang, and Y. Yan, *Structural and Magnetic Properties of the Ordered $FePt_3$, FePt and Fe_3Pt Nanoparticles*, J. Solid State Chem. **209**, 69 (2014).

[21] W. Kraus and G. Nolze, *POWDER CELL– a Program for the Representation and Manipulation of Crystal Structures and Calculation of the Resulting X-Ray Powder Patterns*, J. Appl. Crystallogr. **29**, 301 (1996).

Chapter 6

EFFECT ON STRUCTURAL TRANSFORMATION (FCC TO $L1_0$) ON THE MAGNETIC PROPERTIES OF FePt, CoPt AND $PtFe_{0.5}Co_{0.5}$

6.1 Introduction

The magnetic properties of hard magnetic materials such as FePt and CoPt depend strongly on their structure. These binary alloys exhibit hard magnetic properties when they are in the ordered face-centered tetragonal (fct/$L1_0$) structure. In the first part of this work, we discuss FePt and the formation of the $L1_0$ structure after heat treatment. FePt nanoparticles attract a lot of interest because of their many potential applications such as permanent magnets, high density recording media, biomedicine and catalysis [1–5]. In the fct state, FePt has a high magnetocrystalline anisotropy of about 70 Merg/cm^3 and high coercivity making it ideal for use in high recording media [6,7]. Various chemical techniques have been used to enhance the coercivity of $L1_0$ FePt, particles such as using halide intermediary [8,9] or using Bi additive [10]. Usually, the as-made particles have the fcc structure and low coercivity. In most cases, the simplest way to obtain the $L1_0$ structure after synthesis is by performing heat treatment under an inert environment above 550°C. The drawback of post annealing is the increase in grain size and sintering, leading to widening in size distribution and solubility of the nanoparticles, reducing their suitability in applications as catalysis. In this work, we study the onset of the $L1_0$ state in FePt nanoparticles after annealing them under various conditions. In particular, we studied the evolution of coercivity and anisotropy constant

with temperature of some of our samples at different stages of the fcc to fct transformation.

In the second part of this chapter, we discuss the properties of chemically synthesized CoPt nanoparticles. Chemical synthesis of CoPt nanoparticles have the general advantage of providing a better means of controlling the size distribution and morphology of the nanoparticles compared to other fabrication techniques [11,12]. The phase diagram of CoPt (Figure 6.1) shows that near the equiatomic composition, it can exist as either the disordered fcc (A1) structure or the ordered fct ($L1_0$) structure.

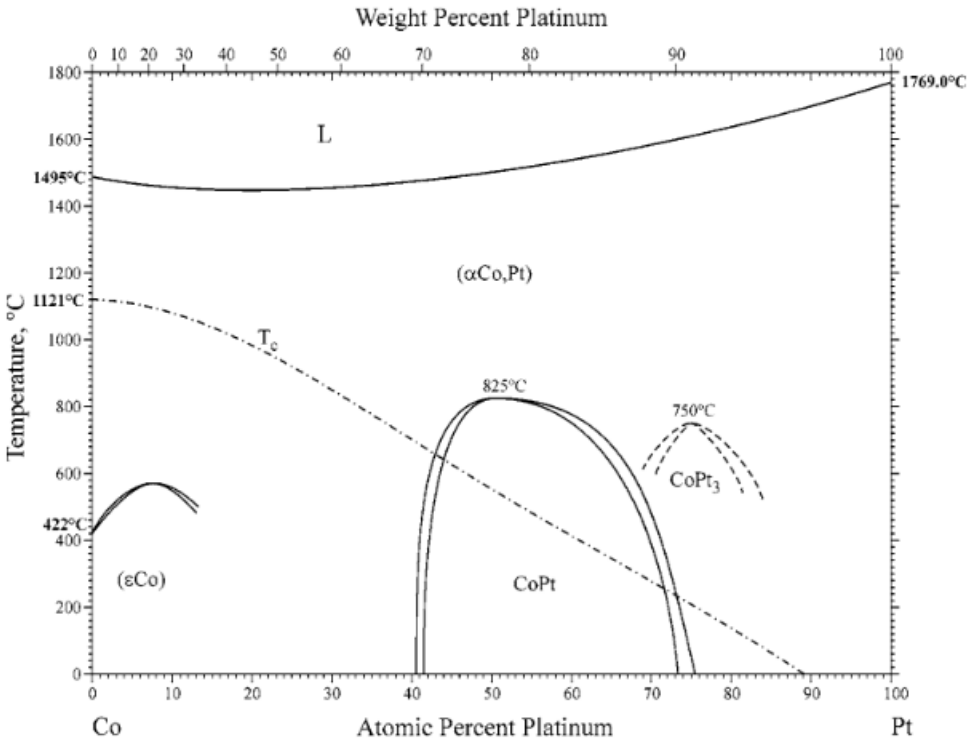

Figure 6.1: Equilibrium phase diagram of Co-Pt systems [13].

The phase diagram of bulk CoPt also shows that the $L1_0$ structure is stable below 825°C [14]. As-synthesized CoPt nanoparticles are usually in the fcc structure and require heat treatment above 600°C in inert environment to form the ordered fct structure [14,15]. CoPt nanoparticles are chemically stable and have a high magnetocrystalline anisotropy of the order of 4×10^7 erg/cm^3, making them suitable as a stable permanent magnetic material [16,17] and for applications in ultrahigh density magnetic recording [18]. In our work, we studied mainly the magnetic properties of CoPt which were annealed at 700°C for 4 hours and the evolution of its coercivity and anisotropy with temperature.

In the third part of this work, we study the nanoparticles of a ternary system of Pt-Fe-Co, namely $PtFe_{0.5}Co_{0.5}$ which were chemically synthesized. Pt-Fe-Co trimetallic alloys in the fct structure are of high interest as catalysts in oxygen-reduction reactions (ORR) [19–21]. Using a trimetallic alloy shows performance improvement in catalysis compared to using PtFe or Pt only [19]. To our knowledge, there is no known study focused on the magnetic properties of these alloys. We studied the evolution of the structure from fcc to fct of $PtFe_{0.5}Co_{0.5}$ upon annealing under various conditions, as well as its magnetic properties.

6.2 Development of Coercivity in FePt nanoparticles

6.2.1 FePt Nanoparticles Synthesis and Characterization

The chemical synthesis of FePt was carried out using iron(iii) acetylacetonate ($Fe(acac)_3$) and platinum(ii) acetylacetonate ($Pt(acac)_2$) as precusors. 1,2-hexadecanediol was used as the reducing agent. 0.25 mmol of $Fe(acac)_3$, 0.25 mmol of

$Pt(acac)_2$ and 1 mmol of 1,2-hexadecanediol were mixed in a solvent mixture consisting of 2 ml of oleic acid and 18 ml oleylamine in a three-neck flask setup. The reaction solution was purged under forming gas (5% H_2 – 95% Ar) for 1 hour at temperatures ranging from 60°C to 80°C. The temperature was then increased to 300°C and the reaction allowed to run for 1 hour, after which the solution was cooled to room temperature. The solution was washed in ethanol and hexane and then sonicated and dried to obtain the FePt nanoparticles.

The resulting black powder was then heat treated under forming gas at different temperatures for different durations. The structure of both as-synthesized and annealed nanoparticles were analyzed using X-Ray diffraction (XRD) and their magnetic properties were measured using a vibrating sample magnetometer (VSM).

6.2.2 Structural and Magnetic Properties of FePt Nanoalloys

From our previous studies of Fe-Pt-Ni alloy discussed in Chapter 4, we know from XRD measurements that FePt annealed at 700°C for 15 minutes transforms into the $L1_0$ structure. To study the transformation from the fcc to the $L1_0$ phase, FePt synthesized as described above was annealed at 500°C, 600°C, 700°C and 800°C for 1 hour. The XRD patterns of these samples are shown in Figure 6.2.

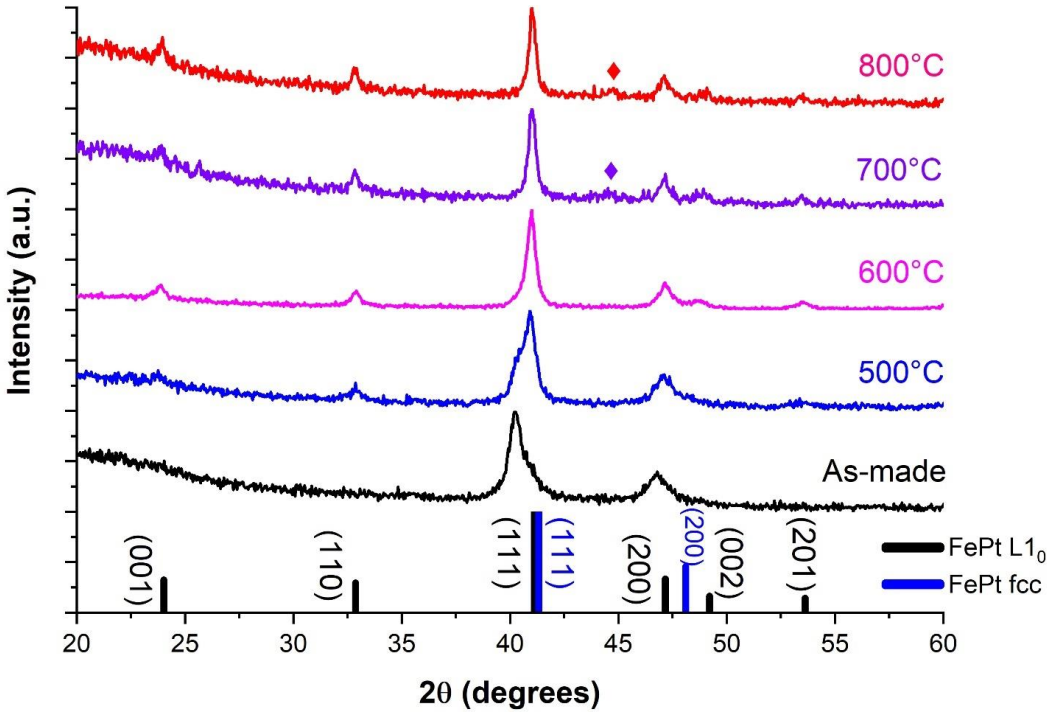

Figure 6.2: XRD data of as-synthesized FePt and FePt annealed for 1 hour at 500°C, 600°C, 700°C and 800°C. The ♦ at 2θ= 44.8° represents the (110) peak of α-Fe.

The XRD patterns reveal a few details in the structure evolution. Firstly, FePt produced in this reaction is not exactly equiatomic, but slightly rich in platinum, as indicated by a general shift of the (111) peaks towards a smaller angle, indicating a higher reduction of Pt ions compare to Fe ions during the chemical reactions. The as-synthesized structure is mostly fcc, however, upon annealing at 500°C for 1 hour, the presence of a growing $L1_0$ phase is visible, designated by the presence of the emerging (001) and (110) superlattice peaks and a shift of the main (111) peak towards a higher angle. The $L1_0$ phase is still not fully formed as the (002) and (200) peaks are not clearly resolved yet. The asymmetric shape of the (111) peak also shows that the sample annealed at 500°C is still a mixture of fcc and $L1_0$.

Increasing the annealing temperature to 600°C enhanced the formation of the fct structure, as indicated by a partial splitting of the (002) and (200) peaks. The transformation to $L1_0$ is more complete when the annealing temperature was increased to 700°C and 800°C. However, the emergence of α-Fe at these two annealing temperatures also becomes obvious from their XRD data. To verify this, an extended XRD of the FePt sample annealed at 700°C was taken from $2\theta = 20^0$ to $2\theta = 90^0$ (Figure 6.3). The resulting XRD pattern was compared to the XRD references of both $L1_0$ FePt and α-Fe [22,23]. The three peaks of α-Fe in this measurement range, ((110), (200), (211)) are found to be present in the XRD pattern in Figure 6.3.

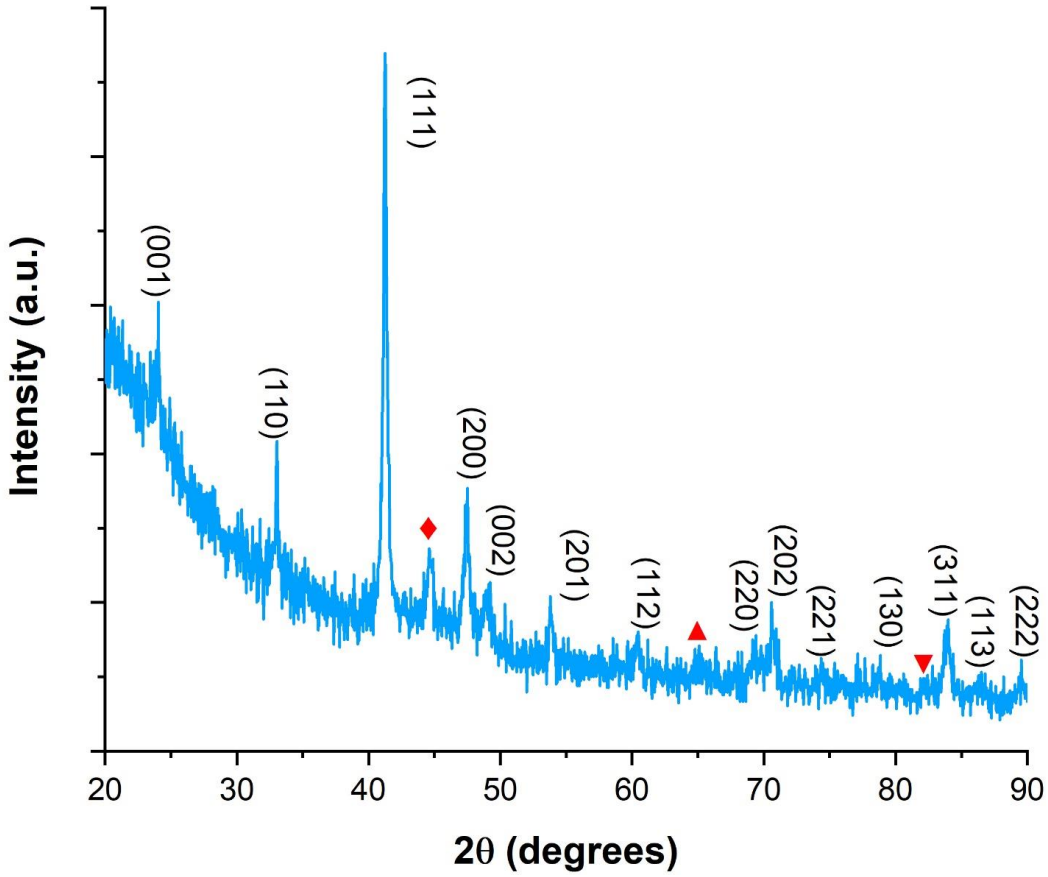

Figure 6.3: XRD pattern of FePt annealed at 700°C for 1 hour. The $L1_0$ peaks are indexed. The peaks of α-Fe labeled are by ♦ (110), ▲ (200) and ▼ (211).

A major difficulty in obtaining clearer XRD patterns for the samples annealed at higher temperatures is the increasing amount of sintering, making it harder to obtain fine powdered samples for the XRD measurements, resulting in noisier signals. Nevertheless, the XRD data of these samples show that in each case, the (111) peak has shifted towards a higher angle and is more symmetric; also the separation between the (200) and (002) peaks has increased, indicating a larger percentage of $L1_0$ phase in the samples.

The Scherrer equation was used to estimate of the variation of particle size with annealing temperature (Table 6.1).

Table 6.1: Estimated size found from the Scherrer equation.

Sample	**Estimated particle size (nm)**	**Estimated degree of ordering**
As-made	13	--
Annealed at 500°C for 1 hour	14	0.69
Annealed at 600°C for 1 hour	20	0.67
Annealed at 700°C for 1 hour	29	0.78
Annealed at 800°C for 1 hour	32	0.90

In general, the calculated particle size increases with annealing temperature. Because the sample annealed at 500°C for 1 hour is clearly a mix of both fcc and fct, resulting in a broad (111) peak, the Scherrer equation does not give an accurate estimation for the average particle size for nanoparticles annealed under this condition. However, the main (111) peak was deconvoluted into fcc and $L1_0$, and the width the $L1_0$ was used in the calculation to give a better estimate of the size. The order parameter was estimated using [24]

$$S^2 = \frac{\left(\frac{I_{001}}{I_{111}}\right)_{obs}}{\left(\frac{I_{001}}{I_{111}}\right)_{ref}} \tag{6.1}$$

where we used the ratio of the peak intensities in the observed XRD pattern after correcting for the background noise in the numerator. In the denominator, the reference ratio of peak intensities used is that of a fully ordered $L1_0$ FePt lattice.

Room temperature hysteresis loops of each sample reveals that the coercivity does not increase monotonically with annealing temperature (Figure 6.4).

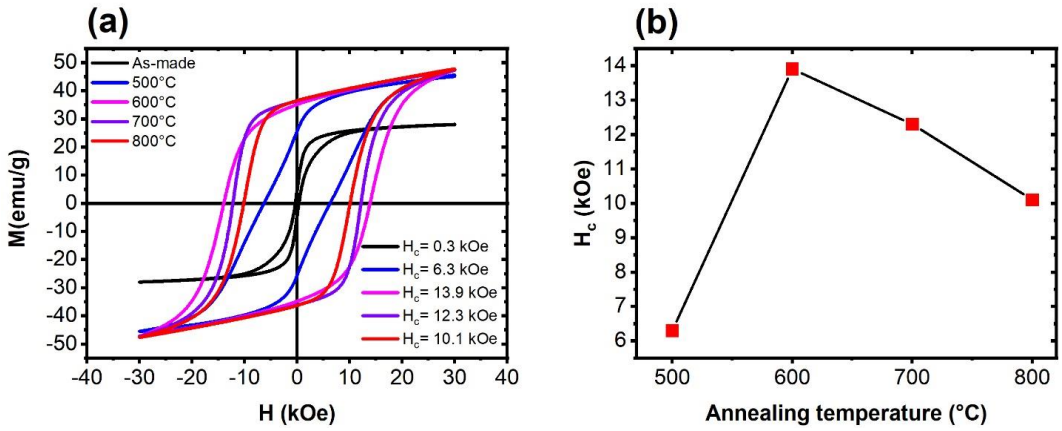

Figure 6.4: Room temperature hysteresis loops of the as-synthesized nanoparticles of FePt and FePt nanoparticles annealed at various temperatures for 1 hour and (b) variation of coercivity with annealing temperature.

In our case, the sample annealed at 600°C had the highest coercivity. The decrease in coercivity for the 700°C and 800°C sample may be explained by the emergence of α-Fe at room temperature. The decrease in coercivity in larger particles may also be due to increased polycrystalline structure, as intergranular exchange coupling leads to reduced magnetocrystalline anisotropy [25]. Thermomagnetic measurements were performed on the annealed samples to check for any correlation

with the hysteresis loops (Figure 6.5). An applied field of 1 T was used for all samples except the one annealed at 600°C, in which case, the applied field was 100 Oe.

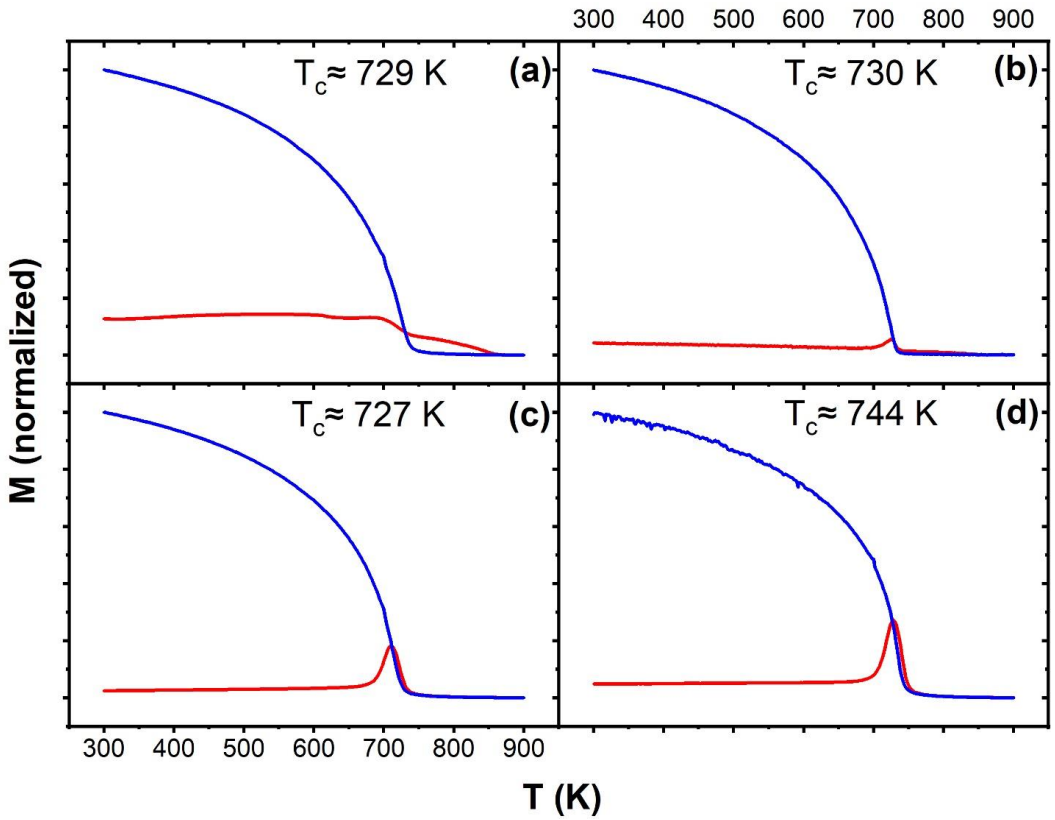

Figure 6.5: Thermomagnetic measurements on samples annealed at (a) 500°C, (b) 600°C, (c) 700°C and (d) 800°C for 1 hour. In each case, the red line represents the heating curve and the blue lines the cooling curve. All Curie temperatures in this chapter are determined as outlined in Chapter 4, from a plot of M^2 vs T.

The thermomagnetic data do not show any immediate correlations when comparing the Curie temperatures. The Hopkinson effect, the increase in magnetization near the Curie temperature, is observed to be bigger for the samples annealed at 600°C,

700°C and 800°C. The Hopkinson effect may be explained by a decrease in coercivity of these samples when the temperature increases. Eventually, the magnetic fields used in the thermomagnetic measurements becomes high enough to exceed the coercivity at the measurement temperature, causing an increase in the magnetization of the samples. As the temperature keeps on increasing, thermal effects become more important once again and the magnetization decreases once again with temperature. Hence, a peak in the magnetization is observed in heating curves of these three samples.

The effect of increasing the annealing time on coercivity was examined for one annealing temperature, 600°C (Figure 6.6.).

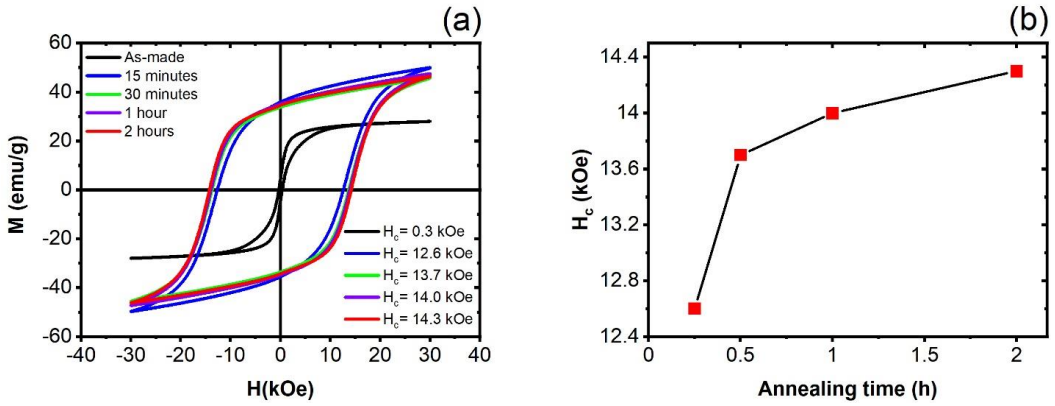

Figure 6.6: (a) Room temperature hysteresis loops of FePt annealed at 600°C for various times. (b) H_c versus annealing time.

Annealing the as-made sample causes an increase in the coercivity, because of the transformation from fcc to fct. Successively doubling the annealing time from 15 minutes up to 2 hours also caused the coercivity to increase monotonically, indicating the transformation is ongoing. The rate of increase on coercivity decreases with

increasing time. The main objective of this study is to show that the coercivity increases with annealing time. One preliminary conclusion of this is that the appearance of the α-Fe phase observed in the samples annealed at 700°C and 800°C depends on the annealing temperature rather than the annealing time and is favored by higher annealing temperatures.

We next investigated the fcc to fct ($L1_0$) phase transformation at an annealing temperature of 500°C by varying the duration of the heat treatment. We prepared samples annealed for up to 8 hours. The structural transformation was observed using XRD (Figure 6.7).

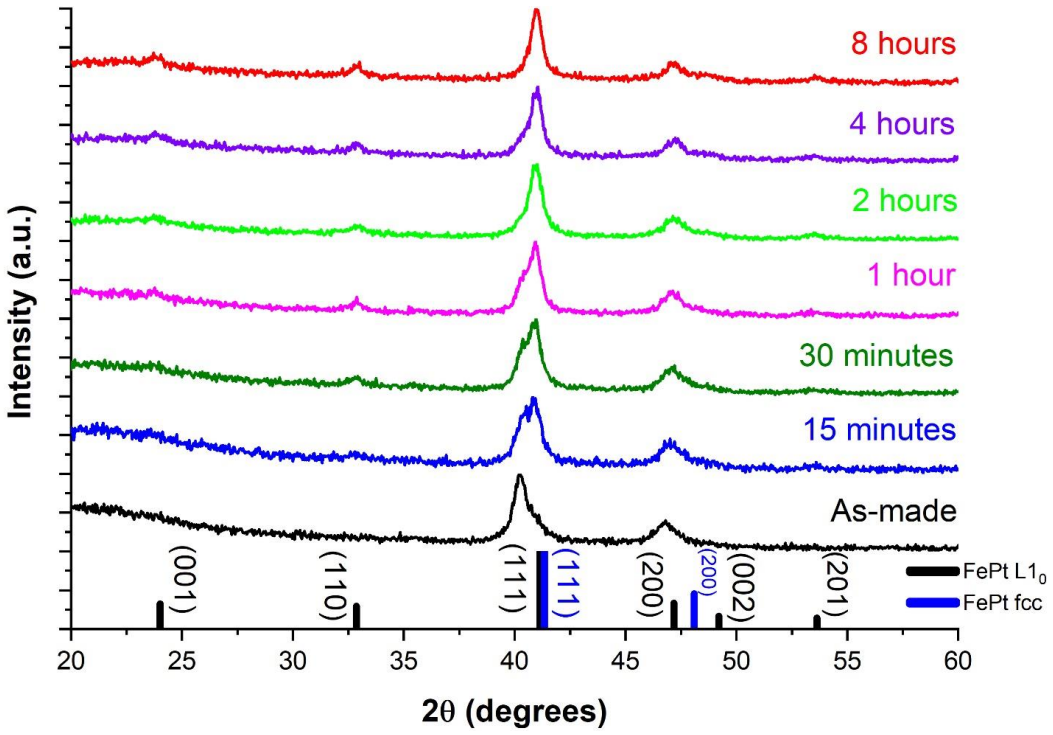

Figure 6.7: XRD data of FePt nanoparticles annealed at 500°C for various times. The as-made data is included for comparison.

Figure 6.7 shows that an annealing duration as little at 15 minutes is enough to start the onset of the phase transformation to the fct phase, from the observation of the (111) peak being split and shifted towards a higher angle. The transformation to the $L1_0$ structure increases with annealing duration. For annealing durations of 2 hours or more, a shoulder surfaces to the right of the (200) peak, which represents the onset of (002) peak, a consequence of a partial transformation to the fct phase. No complete splitting of these two peaks occurred even after heating the sample for 8 hours. This means that longer annealing periods and/or higher temperatures may be necessary to reach a fully ordered phase. The room temperature hysteresis loops in Figure 6.8 also confirms the phase transformation from fcc to fct.

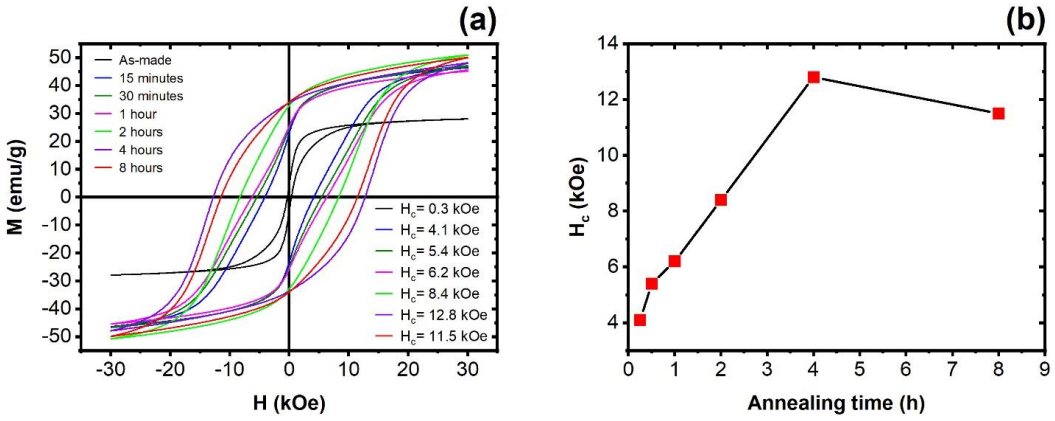

Figure 6.8: (a) Room temperature hysteresis loops of FePt annealed at 500°C for different periods. The as-synthesized data is included for comparison. (b) Plot of H_c versus annealing time.

In general, the coercivity increases with annealing time because of the increased ordering. The peak coercivity obtained was 12.8 kOe for an annealing time of 4 hours. For comparison, this is slightly higher than the coercivity of the sample annealed at 700°C for 1 hour (12.3 kOe). The decrease in coercivity to 11.5 kOe when the annealing

time is further doubled to 8 hours may be due to the increase in particle size and the introduction of a magnetically softer phase with lower coercivity, most likely α-Fe which was observed in the XRD data in Figure 6.2 for higher annealing temperatures. Both the XRD analysis and magnetic data of our FePt samples indicate that to obtain a magnetically hard compound, both annealing temperature and annealing time needs to be controlled.

6.2.3 Temperature Dependence of Coercivity, Saturation Magnetization and Anisotropy Constant in FePt

The variation of coercivity with temperature was studied for FePt nanoparticles annealed at 600°C for 1 hour (Figure 6.9). Hysteresis loops were measured at temperatures ranging from 50 K to 750 K which is above the Curie temperature of this sample.

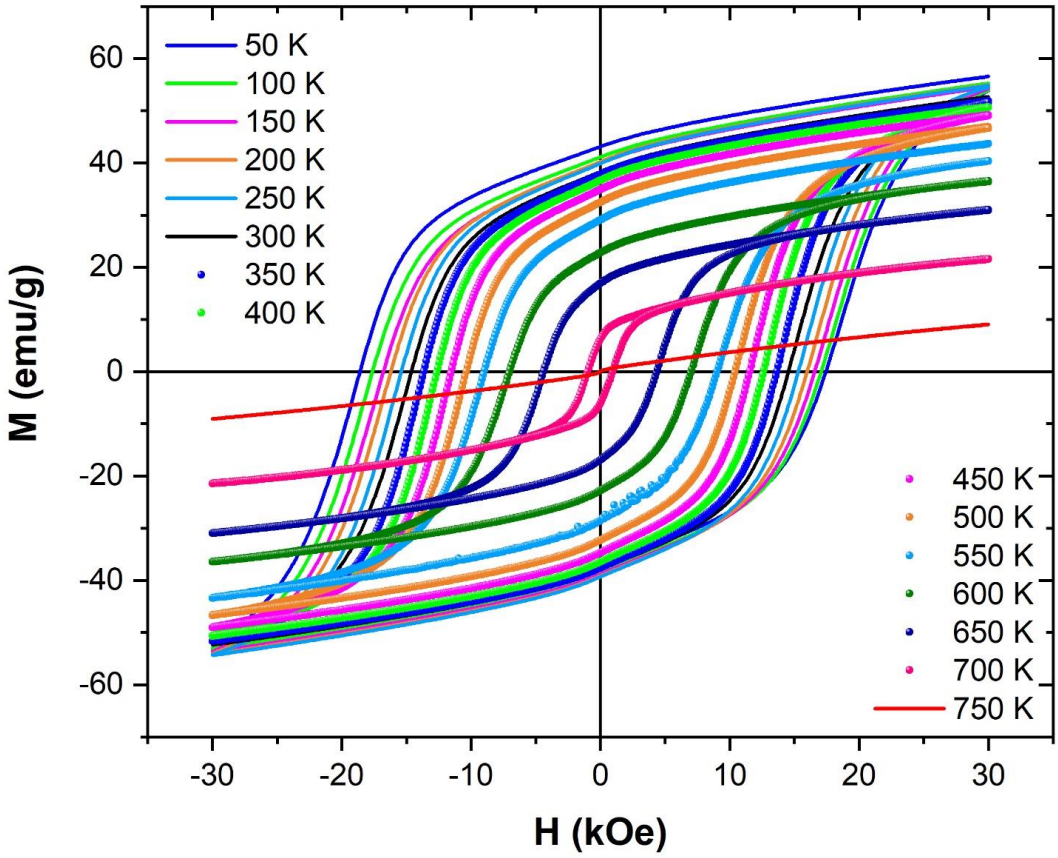

Figure 6.9: Hysteresis loops of FePt annealed at 600°C for 1 hour at different temperatures.

The same measurements were performed on the FePt nanoparticles annealed at 800°C for 1 hour (Figure 6.10).

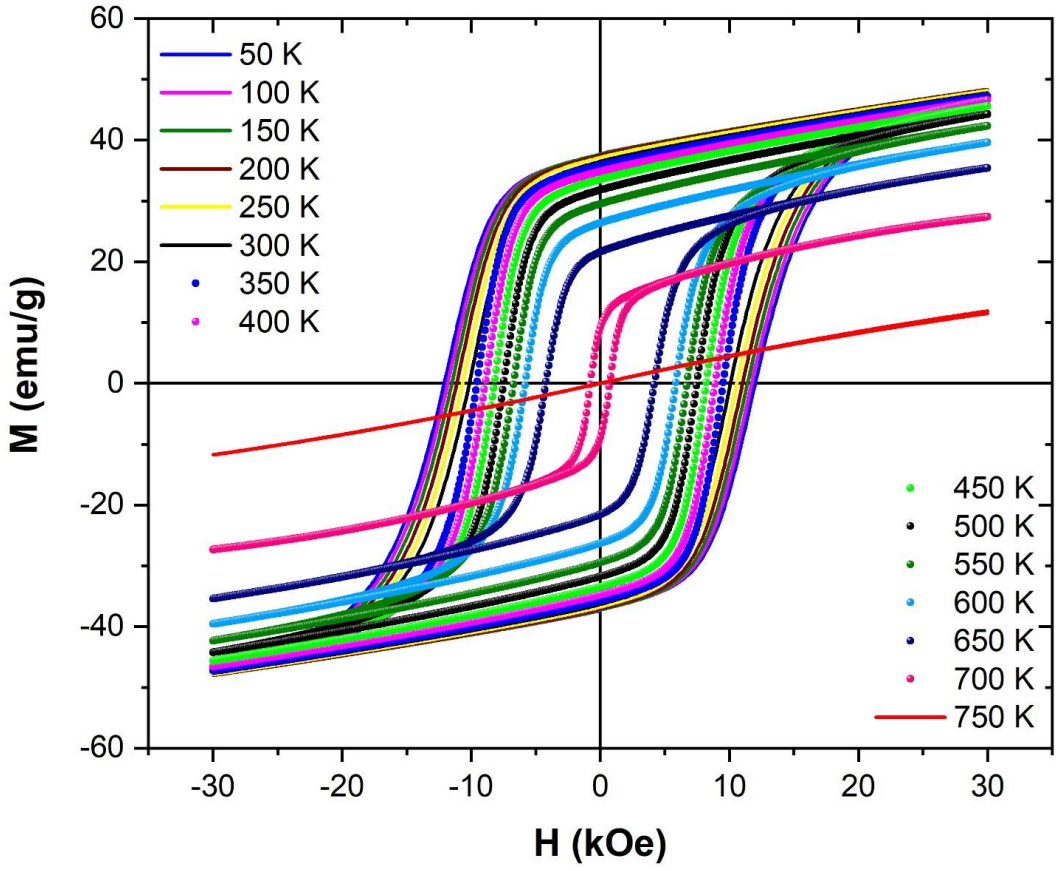

Figure 6.10: Hysteresis loops of FePt annealed at 800°C for 1 hour at different temperatures.

Using the law of approach to saturation, a plot of M vs $1/H^2$ was used to determine the anisotropy constant K_1 and the saturation magnetization M_s at each measurement temperature for both samples. The results of $H_C(T)$, $M_s(T)$ and $K_1(T)$ are shown in Figure 6.11. The errors in the estimates of K_1 and M_s is greater at low temperatures because the samples are further away from magnetic saturation. This is reflected more on $K_1(T)$ which shows nearly constant K_1.

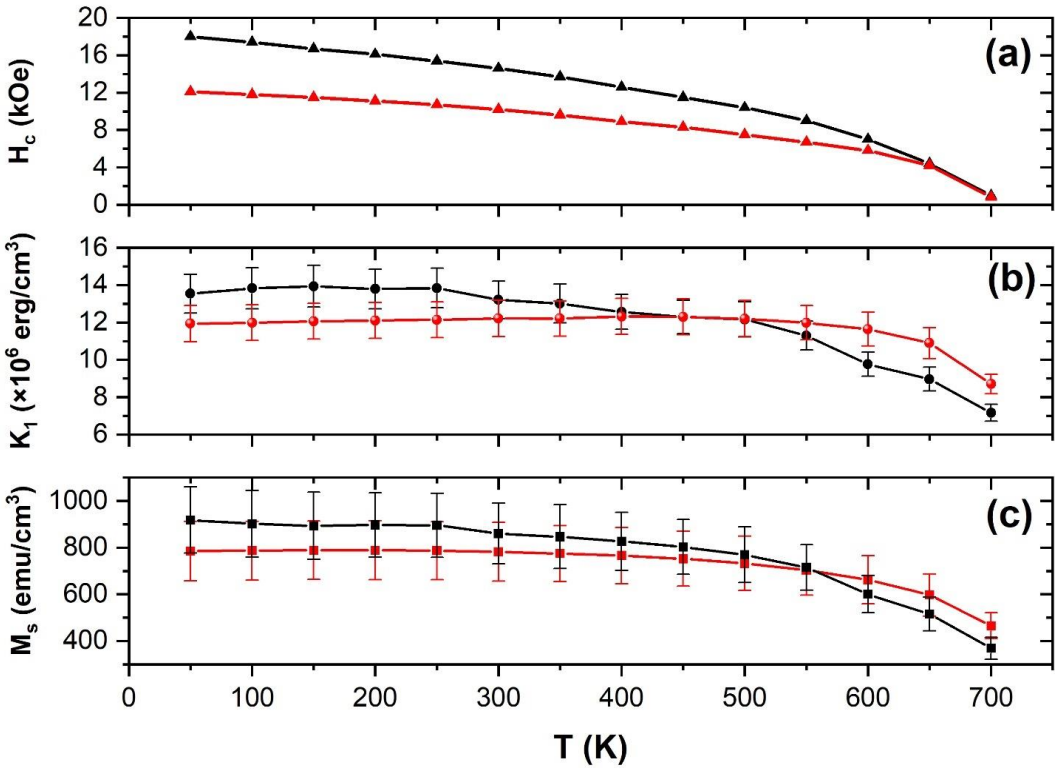

Figure 6.11: Plots of (a) H_c, (b) K_1 and (c) M_s versus temperature for FePt annealed at 600°C (black) and 800°C (red) for 1 hour. The solid lines are guides for the eye.

For measurement temperatures lower than 650 K, Figure 6.11(a) shows the coercivity of the FePt annealed at 800°C for 1 hour is lower than that of its counterpart annealed at 600°C, and the coercivities gets closer in value above 650 K. Above this temperature, the temperature gradient of coercivity dH_c/dT of both are very similar. In heat assisted magnetic recording (HAMR), the variation of coercivity of the $L1_0$ FePt nanoparticles near the Curie temperature is of critical importance. A high dH_c/dT would enhance the effective head field gradient and magnetic transition sharpness, as a shorter range of temperature is needed to initiate the data writing process [26].

Figure 6.11(b) shows that the anisotropy constant is bigger for the sample annealed at 600°C below 450 K. The anisotropy constant of the sample annealed at 800°C varies by very little around a value of 12 Merg/cm^3 before decreasing above 500 K. Figure 6.11(c) shows that the saturation magnetization of the sample annealed at 600°C is higher than the 800°C sample below 550 K because this sample has lower degree of ordering and it is closer to saturation.

We attempted to model our experimental data based on previous theoretical models. Recently, the magnetization of bulk $L1_0$ FePt have been shown to follow $m_e(T) = \left(1 - \frac{T}{T_c}\right)^{\beta}$, where the critical exponent $\beta = 0.366$ from the 3D Heisenberg model [27]. This exponent has been found to fit the variation of $m_e(T)$ at low temperatures obtained by Monte Carlo simulations for FePt nanoparticles of different sizes [28]. The anisotropy field H_K, which is proportional to K_1/M, is expected to follow the same scaling law as for the magnetization [29]:

$$H_K(T) = H_K(0)\left(1 - \frac{T}{T_C}\right)^{\gamma} \tag{6.2}$$

Critical exponent values ranging from 0.35 and 0.65 have been determined previously based on simulations [28,30]. One limitation in using our experimental data to determine the anisotropy constant using the law of approach to saturation is our instrument does not attain a high enough field to saturate our samples. Our model assumes a coercivity H_C proportional to K_1.

Figure 6.12 shows a plot of the fitted data for both FePt samples.

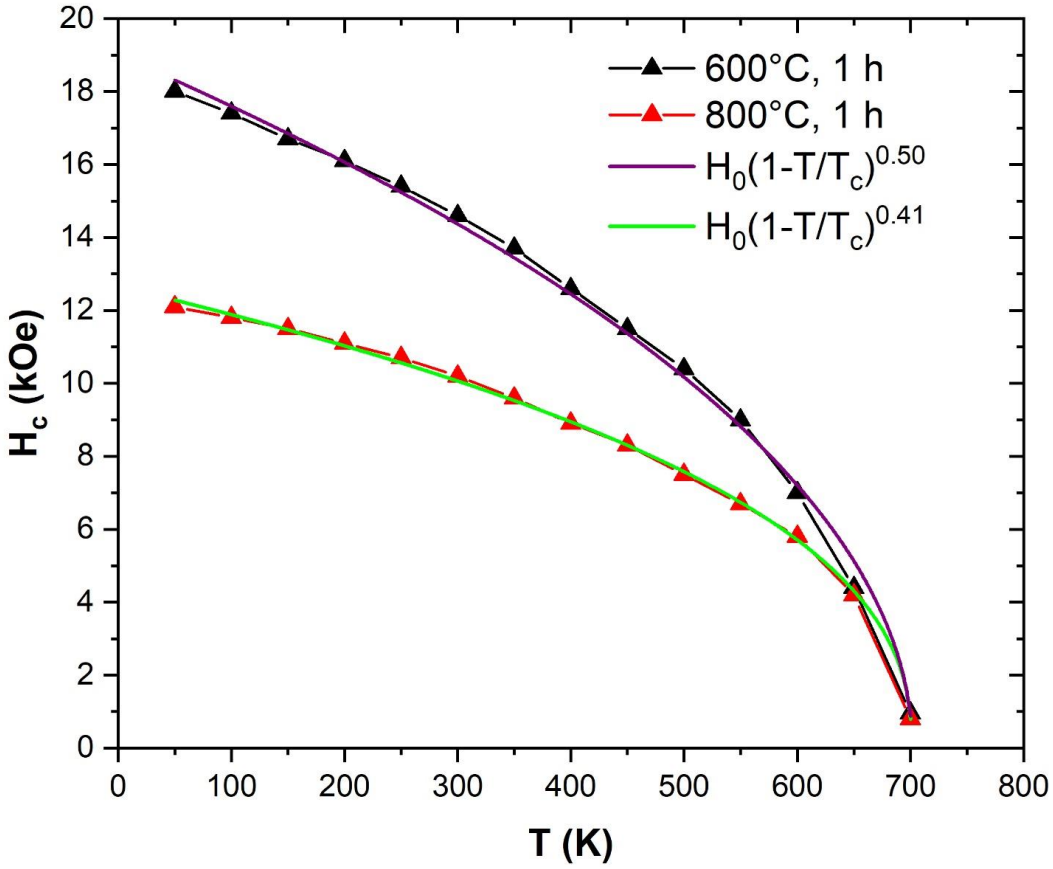

Figure 6.12: Experimental and fitted data of both annealed FePt samples.

From an application perspective, the variation of coercivity near the Curie temperatures of both samples indicate that they would have the same performance regarding the ease of recording data if the samples were used in magnetic storage. A larger exponent γ which indicates a stronger temperature dependence is desirable in heat assisted magnetic recording as this leads to a larger temperature gradient of coercivity dH_c/dT. Performing measurements at high field using a physical property measurement system (PPMS) and taking more measurements near the Curie temperature will be required to obtain more accurate values of the exponent from the model.

6.3 Development of Coercivity in CoPt Nanoparticles

We synthesized CoPt nanoparticles by the co-reduction of 0.25 mmol cobalt(ii) acetylacetonate ($Co(acac)_2$) and 0.25 mmol platinum(ii) acetylacetonate ($Pt(acac)_2$) in 20 ml of trioctylamine as solvent. 1 mmol of 1,2-hexadecanediol was used as the reducing agent and 200 mg of palmitic acid was use as the surfactant. The mixture was purged between 60°C and 80°C under forming gas (5% H_2 – 95% Ar). The reaction solution was heated to 330°C and the reaction continued for 1 hour. The solution was then cooled to room temperature and washed with ethanol and hexane and sonicated. The nanoparticles were separated magnetically from the solution and dried.

As-synthesized CoPt has primarily the disordered fcc stage. After heat treatment at 700°C for 4 hours, the $L1_0$ phase was produced in CoPt. Figure 6.13 shows the XRD pattern of our samples.

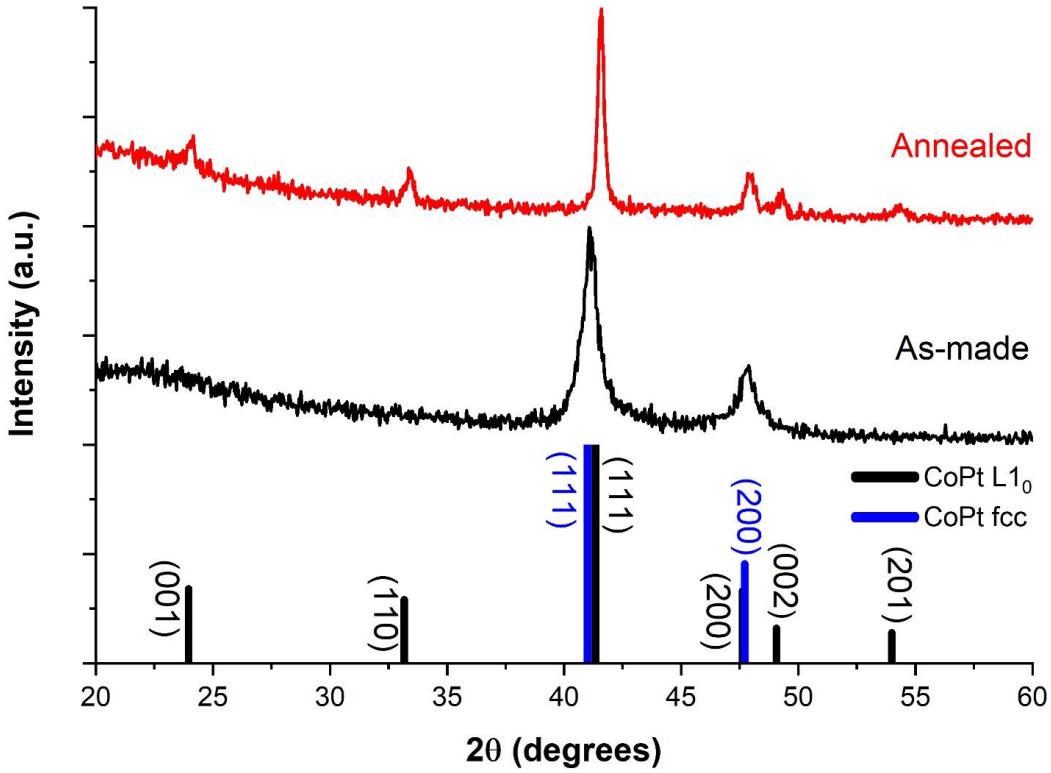

Figure 6.13: XRD pattern of as-synthesized CoPt and CoPt annealed at 700°C for 4 hours.

The XRD data in in Figure 6.13 confirms the disordered structure of the as-made CoPt nanoparticles. The annealed sample is in the ordered $L1_0$ phase, as seen from the splitting of the (002) and (200) peaks and the presence of the (001) superlattice reflections. Furthermore, the peaks of the XRD patterns of both as-synthesized and annealed CoPt nanoparticles were aligned with the reference data, showing that in each case, the nanoparticles were very close to be the equiatomic configuration. The transformation to the $L1_0$ structure was also confirmed by taking the room temperature hysteresis loops (Figure 6.14), which shows a significant increase in the coercivity after annealing.

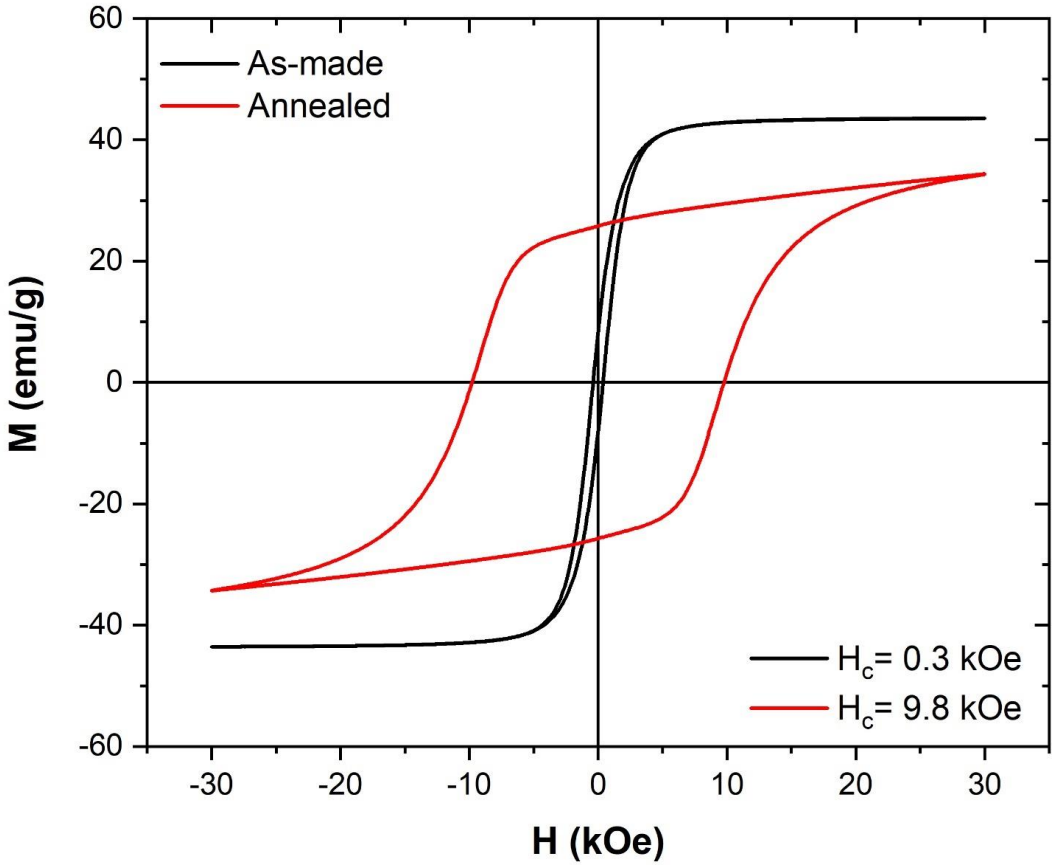

Figure 6.14: Room temperature hysteresis loops of as-synthesized CoPt and CoPt annealed at 700°C for 4 hours.

The shape of the loop of the annealed CoPt also shows that there are no soft phases in it. Its Curie temperature was found from thermomagnetic measurements to be 765 K (Figure 6.15).

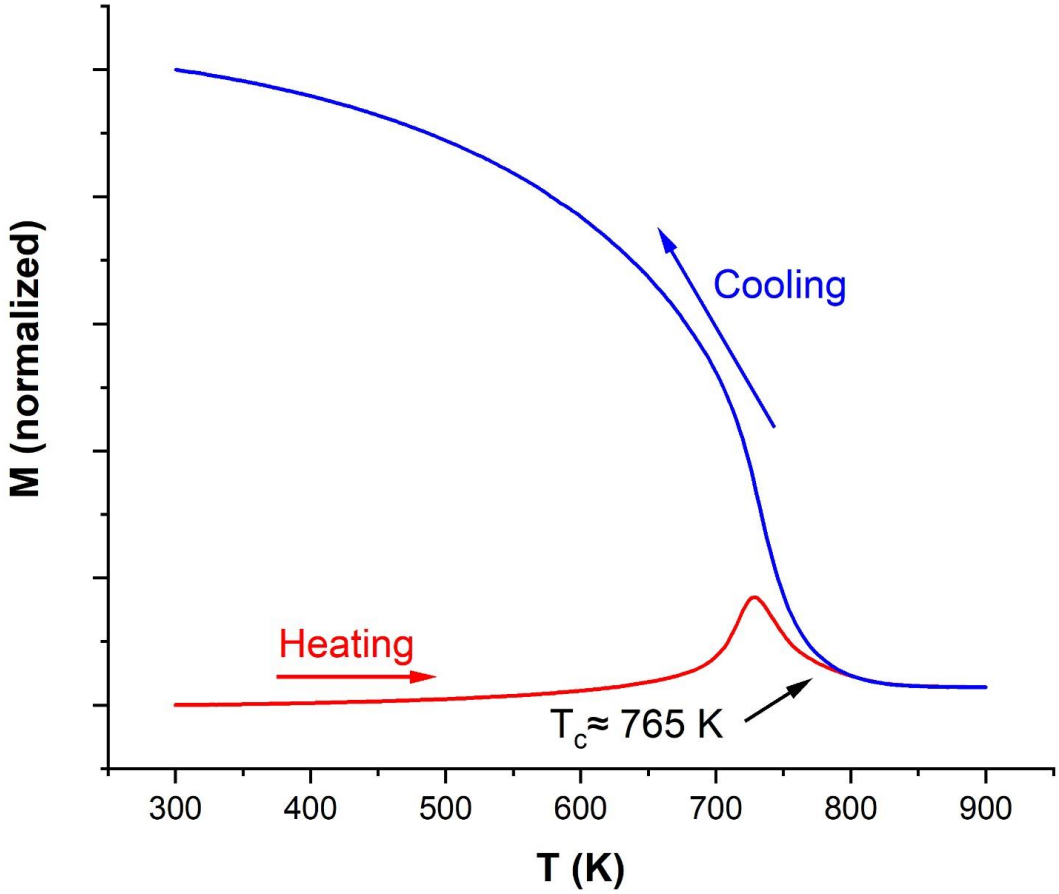

Figure 6.15: Magnetization as a function of temperature of CoPt annealed at 700°C for 4 hours at an applied field of 500 Oe.

The variation of coercivity, saturation magnetization and anisotropy constant with temperature were investigated by measuring the magnetization from 50 K up to 800 K, which is higher than the Curie temperature, in increments of 50 K (Figure 6.16). The high field $M(H)$ slope again suggests that the samples are far from saturation. Using the law of approach to saturation, plots of M vs $1/H^2$ were used to determine H_c, M_s and K_1 (Figure 6.17).

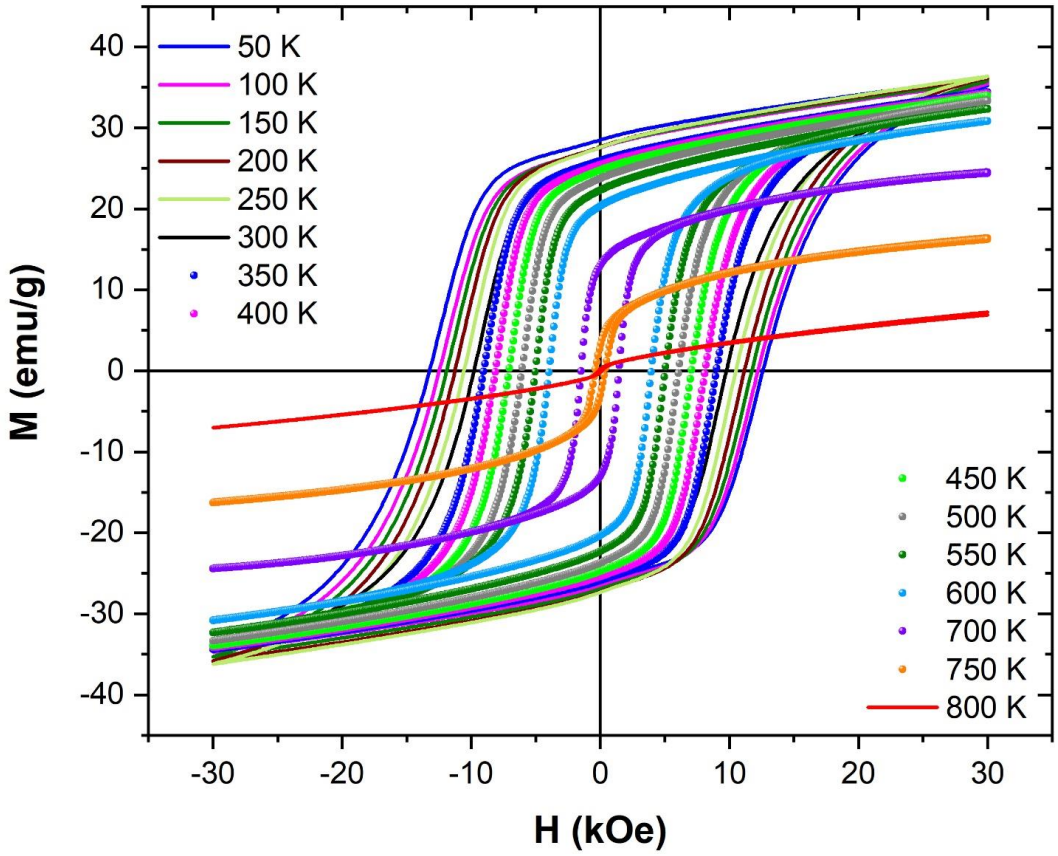

Figure 6.16: Hysteresis loops of CoPt annealed at 700°C for 4 hours at different temperatures.

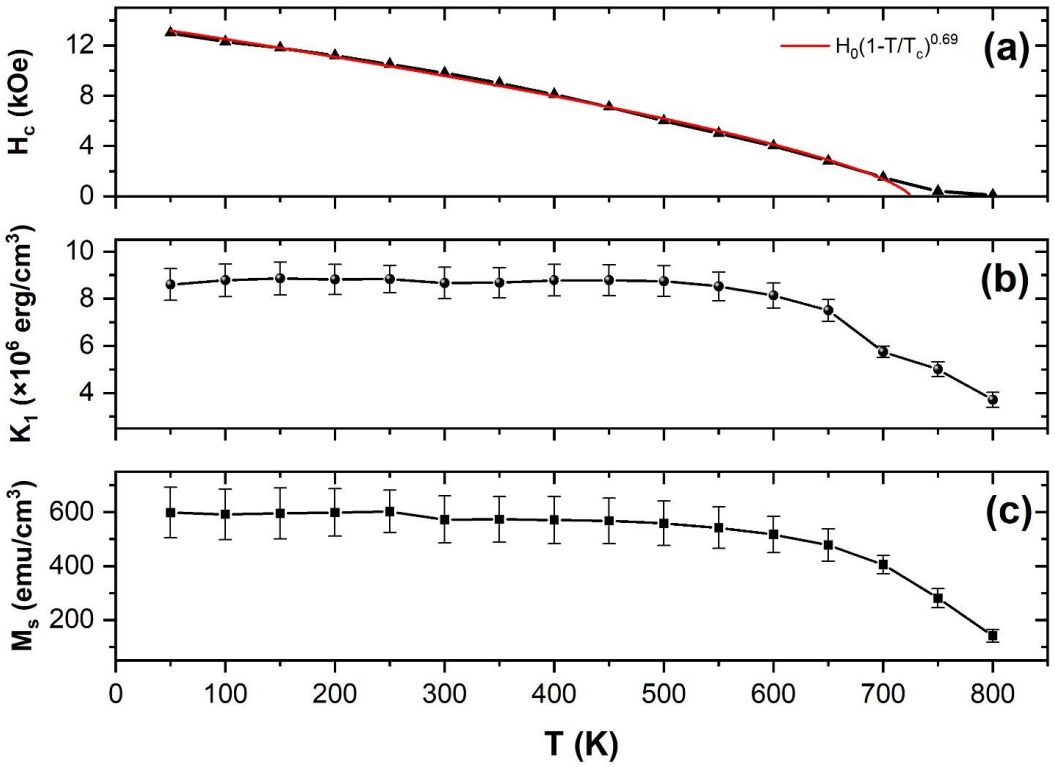

Figure 6.17: Plots of (a) H_c, (b) K_1 and (c) M_s versus temperature for CoPt annealed at 700°C for 4 hours. The solid lines are guides for the eye.

Figure 6.17(a) shows that that compared to the annealed FePt samples described before, the coercivity of the CoPt sample vary more smoothly with temperature, with a lower temperature gradient of coercivity dH_c/dT near the Curie temperature. The coercivity data was fitted with the scaling law used previously, with an exponent of 0.69 found. The fit deviates near the Curie temperature and provides an estimated value of 725±7 K for the Curie temperature. For better accuracy of the fit, more data points would be required closer to the Curie temperature.

Considering temperatures up to 600 K, we observe that K_1 and M_s do not vary much with temperature because their values are underestimated. Their values then

decrease at a higher rate above approximately 650 K. The values of H_c, K_1 and M_s obtained are generally lower than in the case of the annealed FePt samples in Figure 6.11. However, these values are still high, showing that the annealed CoPt still behaves as a hard magnetic material in a range of temperatures suitable for applications.

6.4 Study of The Evolution of Coercivity in $PtFe_{0.5}Co_{0.5}$ Nanoalloys

6.4.1 Structural Analysis $PtFe_{0.5}Co_{0.5}$ Nanoalloys

The procedure to synthesize FePt was modified to produce $PtFe_{0.5}Co_{0.5}$ nanoparticles, with $Co(acac)_2$ added to the reaction mixture as the precursor for Co. The quantities of the precursors were adjusted as follows to obtain the desired stoichiometric ratio: 0.25 mmol $Pt(acac)_2$, 0.125 mmol $Fe(acac)_3$ and 0.125 mmol $Co(acac)_2$. The nanoparticles obtained were annealed under different conditions in forming gas, and the XRD measurements performed on them (Figure 6.18).

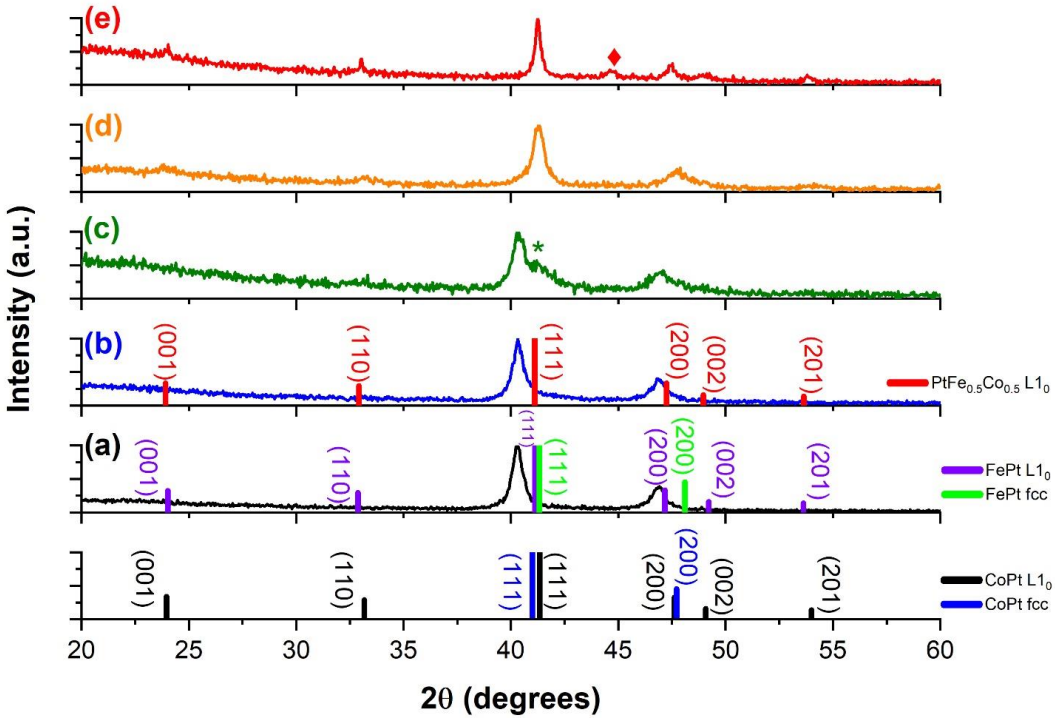

Figure 6.18: XRD patterns of $PtFe_{0.5}Co_{0.5}$ in the following states: (a) as-synthesized, and annealed at (b) 400°C for 30 minutes, (c) 400°C for 2 days, (d) 400°C for 1 week and (e) 700°C for 1 hour. The * in (c) indicates the (111) peak of $PtFe_{0.5}Co_{0.5}$ and the ♦ in (e) represents the (110) peak of α-Fe.

Table 6.2: Estimated size and degree of ordering of the $PtFe_{0.5}Co_{0.5}$ samples.

Sample annealing condition	**Estimated size (nm)**	**Estimated degree of ordering**
As-made	15	0.40
400°C, 30 minutes	13	0.31
400°C, 2 days	10	0.65
400°C, 1 week	13	0.68
700°C, 1 hour	42	0.84

Table 6.2 lists the estimated sizes and degree of ordering. Table 6.2 along with the XRD patterns in Figure 6.18 shows that the as-made nanoparticles as well as the nanoparticles annealed at 400°C for 30 minutes are cubic in structure, with an estimated low degree of ordering. Annealing at 400°C for 30 minutes does not show any clear onset of an $L1_0$ pattern, seen from an absence of split (200) and (002) peaks in Figure 6.18(b). The XRD pattern of the sample annealed at 400°C for 2 days shows a shoulder to the right of the (111) peak, which we attribute to the onset of the (111) peak of the $L1_0$ $PtFe_{0.5}Co_{0.5}$ (Figure 6.18(c)). Likewise, a shoulder on the (200) peak is attributed to the (002) peak of the $L1_0$ structure. The lower intensity shoulder on the main (111) peak means that the nanoparticles are mostly in the disordered phase and suggests that the transformation to the $L1_0$ phase is very slow at 400°C.

To verify this, we annealed one sample at 400°C for 1 week to see how far the $L1_0$ transformation reaches. Figure 6.18(d) shows that the main (111) peak is now shifted to a higher angle, matching the $L1_0$ reference XRD pattern. The presence of the superlattice (001) peak also confirms the ordering has increased. However, the transformation to the $L1_0$ phase is not complete as the (002) peak persists as a shoulder of the (200) peak instead of being fully separated from it. This result signifies that lengthy annealing at 400°C may not be sufficient to produce the ordered fct state and that higher annealing temperatures need to be explored.

The $PtFe_{0.5}Co_{0.5}$ nanoparticles were also annealed at 700°C for 1 hour. The XRD pattern of this sample (Figure 6.18(e)) shows that the $L1_0$ phase is obtained with a higher degree of ordering, since the (200) and (002) peaks are separated. Just like in the case of FePt annealed at temperatures of 700°C and higher (Figure 6.2), some α-Fe is

produced when the sample is annealed at 700°C. This means the annealed sample does not contain a significantly pure $PtFe_{0.5}Co_{0.5}$ phase when it annealed at 700°C.

We also compared the lattice parameters of the $PtFe_{0.5}Co_{0.5}$ annealed at 700°C for 1 hour with FePt annealed at 700°C for 1 hour and CoPt annealed at 700°C for 4 hours. All these samples have a high degree of $L1_0$ ordering, as seen from their respective XRD patterns, with estimated values of 0.78 for FePt, 0.96 for CoPt and 0.84 for $PtFe_{0.5}Co_{0.5}$. The lattice parameters were calculated using the 2θ values at the (200) and (002) peaks into the equation for plane separation of an fct structure:

$$\frac{1}{d_{hkl}} = \frac{h^2 + k^2}{a^2} + \frac{l^2}{c^2} \tag{6.1}$$

The plane separation was found from Bragg's equation $2d \sin\theta = \lambda$ where $\lambda = 1.5406$ Å for the Cu K_α radiation. Figure 6.19 shows the results.

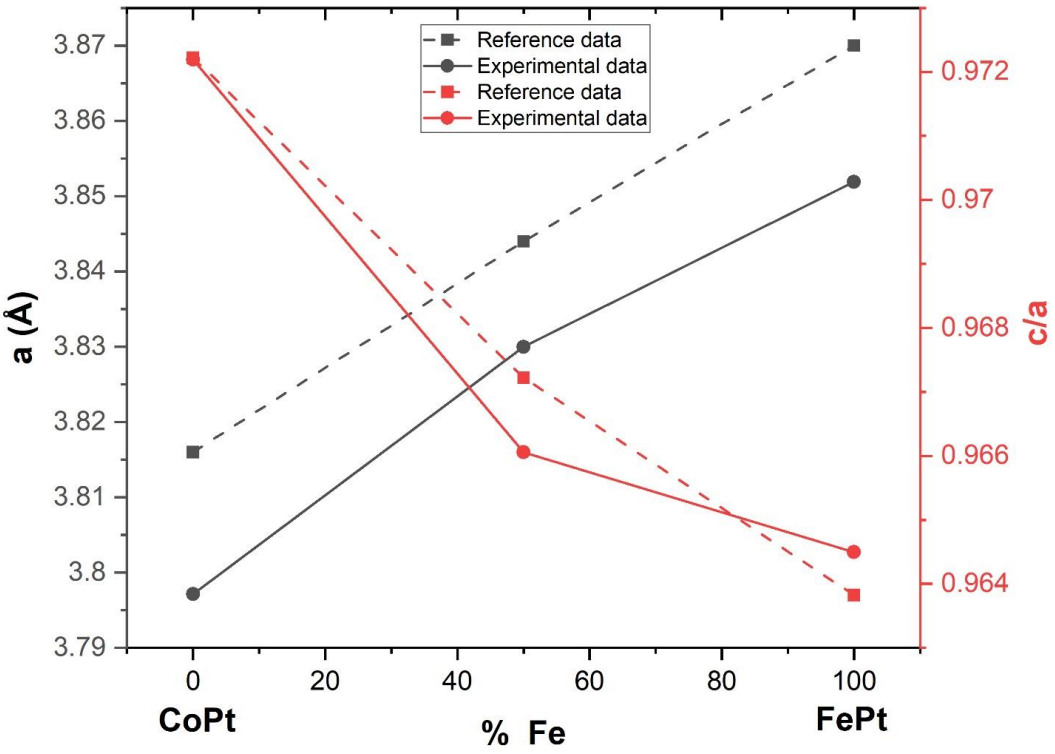

Figure 6.19: Plot of lattice parameter a and tetragonality c/a as a function of Fe content. The experimental results are compared to the reference data of CoPt, FePt and $PtFe_{0.5}Co_{0.5}$ [31–33].

The lattice parameter a and the c/a ratio of $PtFe_{0.5}Co_{0.5}$ are both smaller than their corresponding values calculated from their reference data. The smaller a means that the d spacing of this $PtFe_{0.5}Co_{0.5}$ is higher than its predicted value. It is hard to estimate the composition without EDX data, however, it appears that this sample is rich in platinum leading to a smaller d spacing.

6.4.2 Magnetic Properties of $PtFe_{0.5}Co_{0.5}$ Nanoalloys

Room temperature hysteresis loop measurements on the as-made and annealed $PtFe_{0.5}Co_{0.5}$ samples are shown in Figure 6.20.

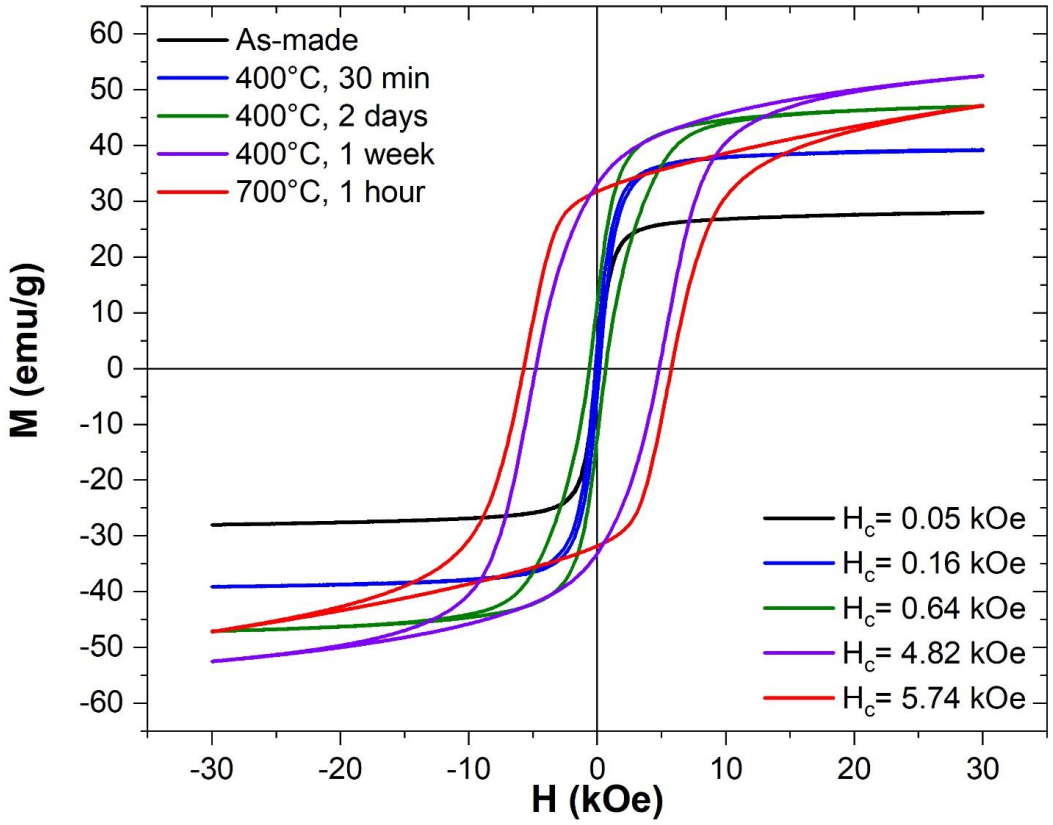

Figure 6.20: Room temperature hysteresis loops of as-synthesized $PtFe_{0.5}Co_{0.5}$ and $PtFe_{0.5}Co_{0.5}$ annealed under different conditions.

The magnetic behavior shown in Figure 6.20 further supports the phase transformation from fcc to fct deduced from the XRD data. Annealing increases the coercivity. The increase is relatively small when the sample is annealed at 400°C for 30 minutes ($H_c = 0.16$ kOe). When the sample has been heat treated at this temperature

for 2 days, the increase is four-fold ($H_c = 0.64$ kOe), further supporting an onset in the phase transformation to the fct phase. However, even that coercivity is relatively low, as that sample is still to a very large extent in the fcc phase. The samples annealed at 400°C for 1 week and 700°C for 1 hour show even more significant increases in H_c (4.82 kOe and 5.74 kOe respectively), in accordance with a larger shift towards the more ordered $L1_0$ phase. Our data suggests that the increase in coercivity is mostly due to chemical ordering than size. However, more work is needed to study the size of the nanoparticles, such as using TEM.

So far, our results show that heat treatment at temperature as high as 700°C produces the $L1_0$ phase, with the additional effect of α-Fe emerging in the structure. Regarding the stage when the $L1_0$ state is fully formed which avoids the emergence of α-Fe in the structure, a lower annealing temperature of 400°C is not sufficient form a fully ordered phase, even with a long annealing period. Future work will consist of trying out annealing temperatures in the range of 450°C to 650°C.

It is also interesting to note that the coercivity of $PtFe_{0.5}Co_{0.5}$ annealed 700°C for 1 hour ($H_c = 5.74$ kOe) is significantly smaller than that of FePt and CoPt annealed under the same conditions ($H_c = 12.3$ kOe for FePt from Figure 6.4 and 10.0 kOe for CoPt from Figure 4.36). Our preliminary data shows that $PtFe_{0.5}Co_{0.5}$ does not have the same hard magnetic behavior that a mixture of equiatomic CoPt and FePt would have. Because of the difficulty in estimating the density of the $PtFe_{0.5}Co_{0.5}$, we did not use the law of approach to saturation to calculate its anisotropy constant. However, our data suggests that the $PtFe_{0.5}Co_{0.5}$ sample has lower anisotropy than the FePt and CoPt sample.

Thermomagnetic measurements were performed on most of the Pt-Fe-Co samples (Figure 6.21).

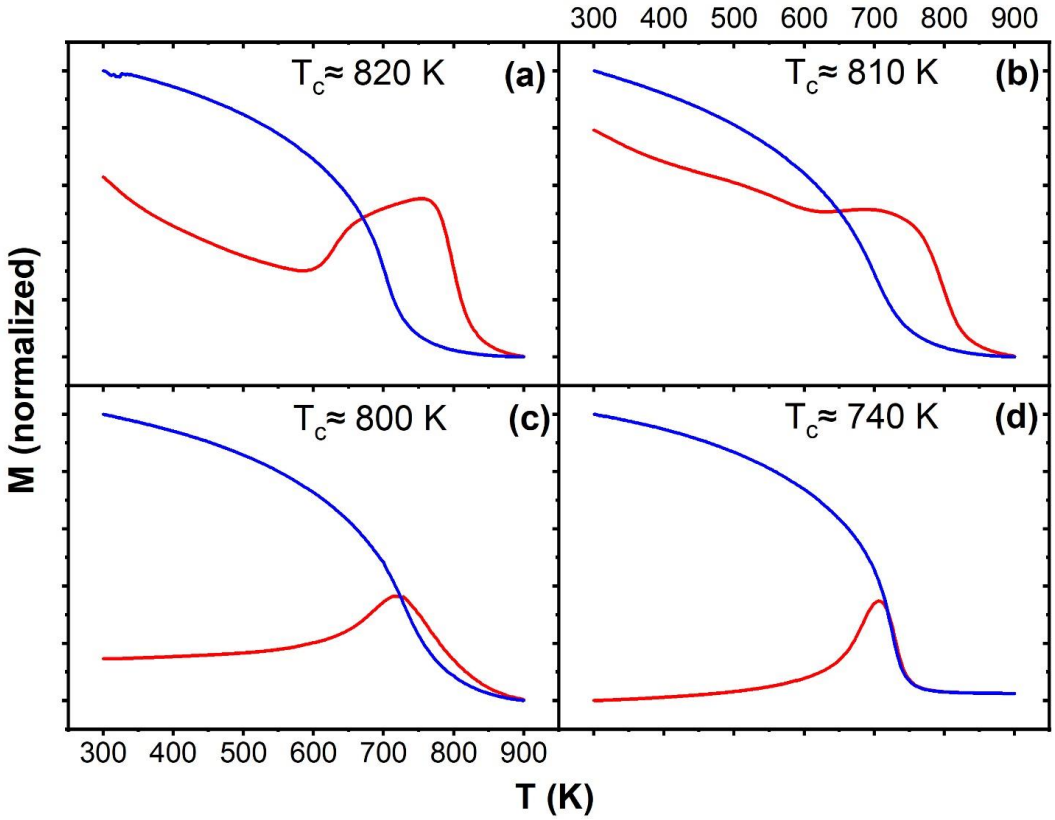

Figure 6.21: Thermomagnetic measurements on the following $PtFe_{0.5}Co_{0.5}$: (a) as-synthesized, (b) annealed at 400°C for 30 minutes, (c) annealed at 400°C for 1 week and (d) annealed at 700°C for 1 hour. In each case, the red line represents the heating curve and the blue lines the cooling curve. All measurements were done at an applied field of 1 T. T_C was obtained from a plot of M^2 versus T as detailed before.

The heating curves in Figures 6.21(a) (as-made) and Figure 6.21(b) (annealed at 400°C for 30 minutes) show some irregular behavior which are due to some ordering or

phase transformation occurring during the measurement. This behavior is smaller in Figure 6.21(b) indicating a slightly more ordered structure.

The sample annealed at 400°C for 2 weeks has an even lower Curie temperature. The shape of its heating curve in Figure 6.21(c) shows that it is made up on one phase only. Figure 6.21(d) shows a sharper decrease in Curie temperature (down to 740 K) for the sample annealed at 700°C for 1 hour. Our results indicate that increased ordering may result in a decrease in Curie temperature in our samples. Note that the presence of α-Fe will not appear in Figure 6.21(d) as its Curie temperature (1043 K) falls outside the range of measurement temperatures [34].

The evolution of coercivity with measurement temperature was studied in $PtFe_{0.5}Co_{0.5}$ annealed at 400°C for 1 week. Hysteresis loops measurements were taken at temperatures ranging from 50 K to 750 K. The results are shown in Figure 6.22.

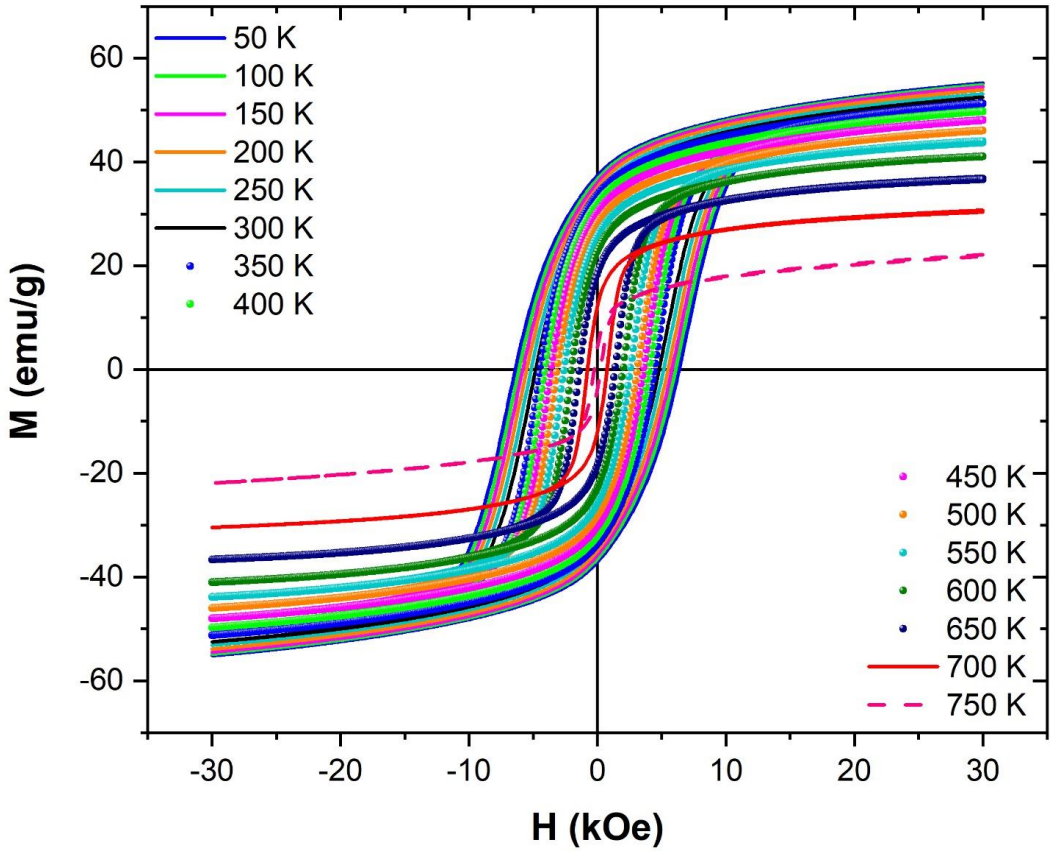

Figure 6.22: Hysteresis loops of $PtFe_{0.5}Co_{0.5}$ annealed at 400°C for 1 week at different temperatures.

Due to the difficulty in this case to find the volume of the unit cell from our XRD data alone, we did not find the anisotropy constant and saturation magnetization (in emu/cm^3) of this sample at the different measurement temperatures shown in Figure 6.22. The variation of its coercivity with measurement temperature is shown in Figure 6.23.

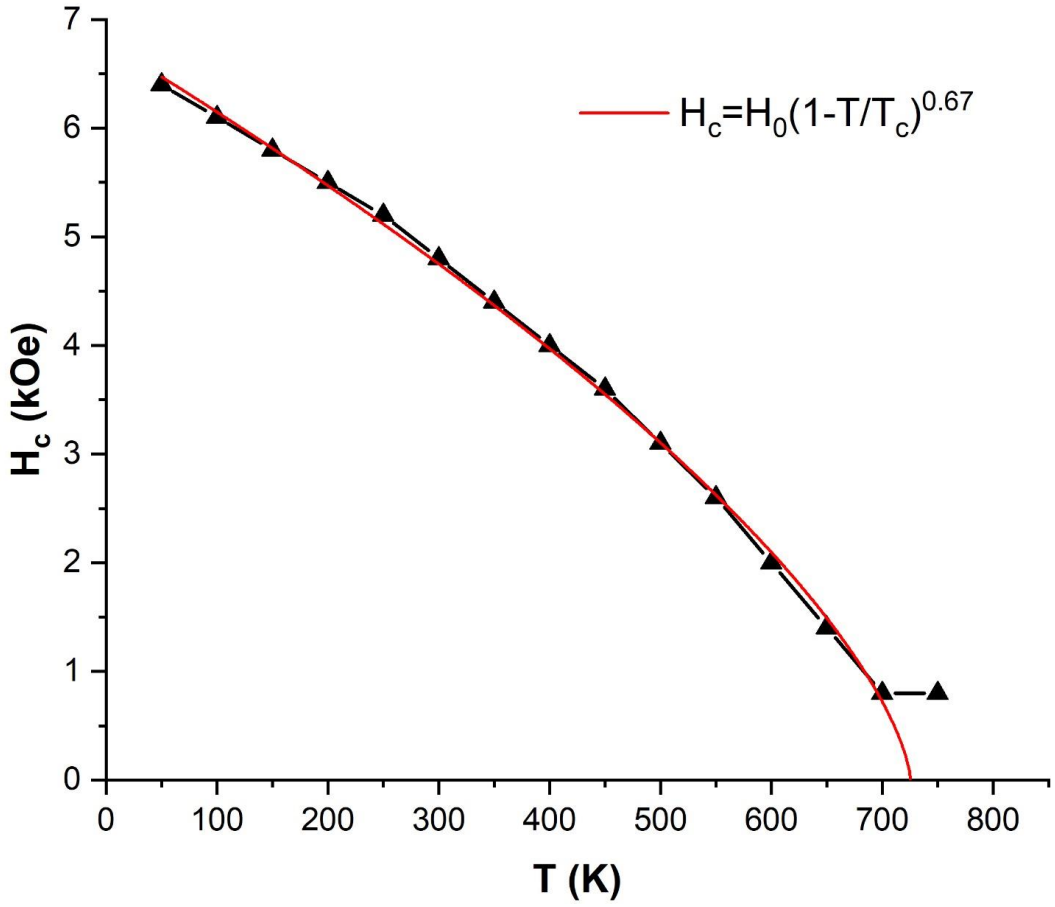

Figure 6.23: Plot of coercivity versus temperature of $PtFe_{0.5}Co_{0.5}$ annealed at 400°C for 2 weeks. The solid lines are guides for the eye. The fitted data is also shown.

For the same measurement temperatures, the coercivity of this sample is smaller than that of FePt annealed at 700°C and 800°C for 1 hour (Figure 6.11(a)) and CoPt annealed at 700°C for 4 hours (Figure 6.17(a)), as anticipated as the FePt and CoPt are at a complete stage of their $L1_0$ phase transformation, unlike this $PtFe_{0.5}Co_{0.5}$ sample. Close to the Curie temperature, the magnitude of the temperature gradient of coercivity dH_c/dT does not increase significantly from its value at lower temperatures. The $PtFe_{0.5}Co_{0.5}$ sample annealed at 400°C for 1 week may be considered to be magnetically

hard near room temperature, although CoPt and FePt are expected to have superior magnetic properties. Its main purpose was to study the phase transformation from fcc to $L1_0$ structure at an intermediate stage. We also fitted the $H_C(T)$ data using $H_C(T) = H(0)\left(1 - \frac{T}{T_C}\right)^{\gamma}$. The Curie temperature from the fit is 726±18 K. This deviation from the observed Curie temperature of 800 K is very likely since, being a mixture of phases, we cannot approximate H_C to be equal to the anisotropy field closer to the Curie temperature. The model would be better applied to a sample with a higher degree of ordering.

6.5 Summary

- FePt nanoparticles were synthesized using the procedure described. Annealing at temperatures of 500°C and above for 1 hour sets off the transformation to the $L1_0$ structure.
- The formation of the $L1_0$ state is improved at higher annealing temperatures. However, α-Fe emerges at 700°C and above. In the temperature range studied, the optimum temperature was 600°C when a structure with a high degree of ordering was obtained. Both XRD data and magnetic measurements confirmed this. A decrease in coercivity of FePt nanoparticles annealed above 600°C may also be due to reduced magnetocrystalline anisotropy from increased polycrystalline structure. In general, the size and degree of ordering increased with annealing temperature.
- The magnetic properties of FePt annealed at 600°C and 800°C were studied as a function of temperature. Both samples show high K_1, M_s and H_C below T_c and a high dH_c/dT close to T_c.
- The coercivity dependence with temperature data of the above FePt nanoparticles was modelled based on the anisotropy field being scaled as

$\left(1-\frac{T}{T_C}\right)^{\gamma}$. One limitation in its application to our experimental data was the use of the law of approach of saturation for hysteresis loops taken at low fields (maximum of 3 Tesla). We still obtained values of the exponent γ found within the range of those simulated in other published work.

- The chemical reaction used to produce CoPt is effective at producing single phase CoPt which is nearly equiatomic or close to being equiatomic. CoPt annealed at 700°C for 4 hours has a high coercivity of 9.8 kOe.
- H_c, K_1 and M_s of the annealed CoPt were studied as a function of temperature and were typical of a hard magnetic material. Compared to the annealed FePt samples, the variation of H_c with temperature was more linear, with a lower dH_c/dT close to the Curie temperature.
- $PtFe_{0.5}Co_{0.5}$ was also studied. Annealing it at 700°C for 1 hour produced the fct structure, with α-Fe present. Future work in this area will also include controlling the precursor ratio in the reaction to better control the composition of the nanoparticles.
- Annealing at a lower temperature of 400°C starts the transformation to the fct structure. The transformation is very slow. The optimum temperature for producing the largest coercivity is between 400°C and 700°C and needs to be investigated.
- In terms of magnetic properties, compared to FePt and CoPt, $PtFe_{0.5}Co_{0.5}$ is less magnetically hard, as evidenced by the lower coercivity of its annealed samples in general.
- The coercivity of the sample annealed at 400°C for 1 week was also found to change more in a linear fashion with temperature compared to the annealed FePt samples studied.

REFERENCES

[1] S. Sun, *Recent Advances in Chemical Synthesis, Self-Assembly, and Applications of FePt Nanoparticles*, Adv. Mater. **18**, 393 (2006).

[2] K. Zhu, Y. Ju, J. Xu, Z. Yang, S. Gao, and Y. Hou, *Magnetic Nanomaterials: Chemical Design, Synthesis, and Potential Applications*, Acc. Chem. Res. **51**, 404 (2018).

[3] Q. Li, L. Wu, G. Wu, D. Su, H. Lv, S. Zhang, W. Zhu, A. Casimir, H. Zhu, A. Mendoza-Garcia, and S. Sun, *New Approach to Fully Ordered Fct-FePt Nanoparticles for Much Enhanced Electrocatalysis in Acid*, Nano Lett. **15**, 2468 (2015).

[4] J. Kim, Y. Lee, and S. Sun, *Structurally Ordered FePt Nanoparticles and Their Enhanced Catalysis for Oxygen Reduction Reaction*, J. Am. Chem. Soc. **132**, 4996 (2010).

[5] Y. Shi, M. Lin, X. Jiang, and S. Liang, *Recent Advances in FePt Nanoparticles for Biomedicine*, J. Nanomater. **2015**, (2015).

[6] D. Weller, G. Parker, O. Mosendz, A. Lyberatos, D. Mitin, N. Y. Safonova, and M. Albrecht, *Review Article: FePt Heat Assisted Magnetic Recording Media*, J. Vac. Sci. Technol. B **34**, 060801 (2016).

[7] Y. Dong, F. Liu, W. Yang, J. Zhu, J. Yu, and Y. Hou, *Layer-by-Layer Assembly of $L1_0$-FePt Nanoparticles with Significant Perpendicular Magnetic Anisotropy*, CrystEngComm **16**, 9430 (1393).

[8] W. Lei, J. Xu, Y. Yu, W. Yang, Y. Hou, and D. Chen, *Halide Ion-Mediated Synthesis of $L1_0$-FePt Nanoparticles with Tunable Magnetic Properties*, Nano Lett. **18**, 7839 (2018).

[9] W. Lei, Y. Yu, W. Yang, M. Feng, and H. Li, *A General Strategy for Synthesizing High-Coercivity $L1_0$-FePt Nanoparticles*, Nanoscale **9**, 12855 (2017).

[10] F. M. Abel, V. Tzitzios, E. Devlin, S. Alhassan, D. J. Sellmyer, and G. C. Hadjipanayis, *Enhancing the Ordering and Coercivity of L10 FePt Nanostructures with Bismuth Additives for Applications Ranging from Permanent Magnets to Catalysts*, ACS Appl. Nano Mater. **2**, 3146 (2019).

[11] Y. Wang and H. Yang, *Synthesis of CoPt Nanorods in Ionic Liquids*, J. Am. Chem. Soc. **127**, 5316 (2005).

[12] D. Kaya, I. Adanur, M. Akyol, F. Karadag, and A. Ekicibil, *Synthesis of Monodisperse CoPt Nanoparticles: Structural and Magnetic Properties*, J. Mol. Struct. **1224**, 128999 (2021).

[13] H. Okamoto, *Co-Pt (Cobalt-Platinum)*, J. Phase Equilibria **22**, 591 (2001).

[14] V. Tzitzios, D. Niarchos, M. Gjoka, N. Boukos, and D. Petridis, *Synthesis and Characterization of 3D CoPt Nanostructures*, J. Am. Chem. Soc. **127**, 13756 (2005).

[15] Y. J. Zhang, Y. T. Yang, Y. Liu, Y. X. Wang, L. L. Yang, M. B. Wei, H. G. Fan, H. J. Zhai, X. Y. Liu, Y. Q. Liu, N. N. Yang, Y. H. Wu, and J. H. Yang, *A Novel Approach to the Synthesis of CoPt Magnetic Nanoparticles*, J. Phys. Appl. Phys. **44**, 295003 (2011).

[16] J. A. Christodoulides, Y. Zhang, G. C. Hadjipanayis, and C. Fountzoulas, *CoPt and FePt Nanoparticles for High Density Recording Media*, IEEE Trans. Magn. **36**, 2333 (2000).

[17] A. Dannenberg, M. E. Gruner, A. Hucht, and P. Entel, *Surface Energies of Stoichiometric FePt and CoPt Alloys and Their Implications for Nanoparticle Morphologies*, Phys. Rev. B **80**, 245438 (2009).

[18] D. Weller and M. F. Doerner, *Extremely High-Density Longitudinal Magnetic Recording Media*, Annu. Rev. Mater. Sci. **30**, 611 (2000).

[19] B. Arumugam, B. A. Kakade, T. Tamaki, M. Arao, H. Imai, and T. Yamaguchi, *Enhanced Activity and Durability for the Electroreduction of Oxygen at a Chemically Ordered Intermetallic PtFeCo Catalyst*, RSC Adv. **4**, 27510 (2014).

[20] Y. Zhou, X. Cheng, C. H. Yen, C. M. Wai, C. Wang, J. Yang, and Y. Lin, *Synthesis of an Excellent Electrocatalyst for Oxygen Reduction Reaction with Supercritical Fluid: Graphene Cellular Monolith with Ultrafine and Highly Dispersive Multimetallic Nanoparticles*, J. Power Sources **347**, 69 (2017).

[21] H. Wang, K. Zhang, J. Qiu, J. Wu, J. Shao, H. Wang, Y. Zhang, J. Han, Y. Zhang, and L. Yan, *Ternary PtFeCo Alloys on Graphene with High Electrocatalytic Activities for Methanol Oxidation*, Nanoscale **12**, 9824 (2020).

[22] *Materials Data on FePt by Materials Project*, https://doi.org/10.17188/1198813.

[23] *Materials Data on Fe by Materials Project*, https://doi.org/10.17188/1189317.

[24] Y. K. Takahashi, T. Koyama, M. Ohnuma, T. Ohkubo, and K. Hono, *Size Dependence of Ordering in FePt Nanoparticles*, J. Appl. Phys. **95**, 2690 (2004).

[25] G. Herzer, *Grain Size Dependence of Coercivity and Permeability in Nanocrystalline Ferromagnets*, IEEE Trans. Magn. **26**, 1397 (1990).

[26] T. Rausch, J. A. Bain, D. D. Stancil, and T. E. Schlesinger, *Thermal Williams-Comstock Model for Predicting Transition Lengths in a Heat-Assisted Magnetic Recording System*, IEEE Trans. Magn. **40**, 137 (2004).

[27] J. Waters, D. Kramer, T. J. Sluckin, and O. Hovorka, *Resolving Anomalies in the Critical Exponents of FePt Using Finite-Size Scaling in Magnetic Fields*, Phys. Rev. Appl. **11**, (2019).

[28] A. Lyberatos, D. Weller, and G. J. Parker, *Finite Size Effects in $L1_0$-FePt Nanoparticles*, J. Appl. Phys. **114**, 233904 (2013).

[29] A. Lyberatos, *Anisotropy Field and Dynamic Coercivity of $L1_0$ FePt Nanoparticles Close to the Curie Temperature*, Phys. B Condens. Matter **576**, 411741 (2020).

[30] R. H. Victora and P.-W. Huang, *Simulation of Heat-Assisted Magnetic Recording Using Renormalized Media Cells*, IEEE Trans. Magn. **49**, 751 (2013).

[31] C. Leroux, M. C. Cadeville, V. Pierron-Bohnes, G. Inden, and F. Hinz, *Comparative Investigation of Structural and Transport Properties of $L1_0$ NiPt and CoPt Phases; the Role of Magnetism*, J. Phys. F Met. Phys. **18**, 2033 (1988).

[32] S. Yuasa, H. Miyajima, and Y. Otani, *Magneto-Volume and Tetragonal Elongation Effects on Magnetic Phase Transitions of Body-Centered Tetragonal $FeRh_{1-x}Pt_x$*, J. Phys. Soc. Jpn. **63**, 3129 (1994).

[33] J. C. Woolley and B. Bates, *Ordering in CoPt—FePt Alloys*, J. Common Met. **1**, 382 (1959).

[34] *ASM Handbook, Volume 03 - Alloy Phase Diagrams - Knovel*, https://app.knovel.com/web/toc.v/cid:kpASMHVAP1/viewerType:toc/.

Chapter 7

CONCLUSIONS AND FUTURE WORK

In this work, we presented the chemical synthesis of magnetically hard FePt, CoPt and their ternary alloys made with Ni and Bi. The structure of the nanoparticles produced were characterized using X-ray diffraction (XRD) and their morphology was studied using transmission electron microscopy (TEM). The magnetic properties were measured with magnetometry using a vibrating sample magnetometer (VSM) and a physical properties measurement system (PPMS).

In the first part, Pt was substituted by Ni to form $FePt_{1-x}Ni_x$ for $x = 0.2, 0.3, 0.4$. The as-made particles have the disordered fcc structure. Heat treatment of the samples at 700°C for durations as short as 15 minutes can produce the $L1_0$ structure, but the transformation occurred more readily at lower Ni content. In general, annealing for longer periods improved the degree of ordering in the $L1_0$ structure. The phase transformation from fcc to the $L1_0$ phase was also reflected in the magnetic measurement data: the coercivity increased for nanoparticles annealed for longer periods and was lower for higher Ni content. This work shows that Ni may be used as a viable partial replacement for Pt in applications, which would bring down the cost in applications.

We also investigated the effect of Bi addition to $FePt_{1-x}Ni_x$ for $x = 0.2,0.3,0.4$. After annealing at 700°C, the $L1_0$ structure was formed for all values of x studied. The XRD data of the samples annealed at 700°C showed that Bi addition increased the

degree of ordering of the annealed samples. However, Bi also formed secondary soft phases resulting in lower coercivities for Ni content lower than $x = 0.3$. Thermomagnetic data also revealed that Bi addition decreased the Curie temperature. For example, the Curie temperature of $FePt_{0.7}Ni_{0.3}$ and $FePt_{0.7}Ni_{0.3}$ (+10% Bi) annealed at 700°C for 30 minutes are 720 K and 630 K respectively. The decrease in Curie temperature could possibly be due to an increase in the degree of ordering with Bi and/or a change in Fe-Pt-Ni stoichiometry because of the Bi-Pt phases formed. A potential application of this is in heat assisted magnetic recording (HAMR), which would benefit from a lower operating temperature to read/write data to magnetic storage media. The effect of using various amounts of Bi in the Fe-Pt-Ni alloys synthesis was also investigated. The results of this study suggest that a small amount of Bi ($\leq 10\%$) may be sufficient to cause the increased degree of ordering.

Ni substitution of Pt in CoPt to form $CoPt_{1-x}Ni_x$ was also explored. Ni substitution has a different effect on the structural and magnetic properties in $CoPt_{1-x}Ni_x$ compared to $FePt_{1-x}Ni_x$. Despite using Ni contents as low as $x = 0.1$, and later adding Bi to the synthesis, no $L1_0$ structure was formed in the $CoPt_{1-x}Ni_x$ nanoparticles. The nanoparticles produced remained predominantly in the disordered fcc structure, even after annealing for long periods at temperatures ranging from 600°C to 800°C. The low ordering was consistent with the coercivities of $CoPt_{1-x}Ni_x$ being significantly lower of that of the binary CoPt nanoparticles. Our results show that Ni substitution of Pt in the CoPt lattice does not form the $L1_0$ structure like other substitutions like Ag, B and C. Future work on ternary alloys of FePt and CoPt may involve the following: (a) use a smaller amount of Ni substitution, (b) use a smaller amount of Bi (<10%) to optimize

the balance between ordering and coercivity, and (c) explore other third element additions.

In the next part of this work, we attempted to directly synthesize $L1_0$ FePt using an iodine-mediated route. However, our synthesis procedure yielded a mixture of $FePt_3$ in the fcc and $L1_2$ structure. The as-made nanoparticles have predominantly the fcc structure with a Curie temperature of 380 K. This structure is transformed to a mixture of $L1_2$ $FePt_3$ and another ferromagnetic phase with a Curie temperature of 297 K upon annealing at 700°C for 30 minutes. The $L1_2$ structure shows an antiferromagnetic transition at 135 K. Structural data analysis shows that a significant effect of using iodine in the synthesis is that it facilitates the formation of the $L1_2$ structure in the as-made sample. By a suitable choice of reaction conditions which were different from those of the standard reaction, as-synthesized nanoparticles with a higher degree of $L1_2$ ordering could be formed. An area of high interest for future work is finding the reaction conditions that will produce monodisperse $FePt_3$ $L1_2$ particles in the as-made sample, without the need for any post-annealing to form the ordered $L1_2$ structure.

In the final part of this work, we explored the phase transformation from fcc to $L1_0$ structure in FePt and $PtFe_{0.5}Co_{0.5}$ at different annealing temperatures and the effect of the phase transformation on the magnetic properties. Two FePt samples were annealed at 600°C and 800°C for 1 hour, resulting into these two samples being at different stages of the $L1_0$ transformation. The temperature dependence of their coercivities and anisotropy were investigated and compared to the corresponding values for CoPt in the $L1_0$ structure with a high degree of ordering. Compared to the FePt samples, the CoPt sample had a higher rate of decrease of coercivity with temperature and lower magnetocrystalline anisotropy. To better fit our FePt data and compare them

with existing models, it may be desirable in future work to use higher fields to obtain hysteresis loops with magnetization close to saturation at various temperatures, as well as more hysteresis loops closer to the Curie temperature. Using higher measurement fields would allow for a more accurate estimation of the saturation magnetization and anisotropy constant from the law of approach to saturation and enable us to accurately determine the anisotropy field. Plots of anisotropy field versus temperature instead of coercivity versus temperature would also fit the model more accurately and allow for direct comparisons with published simulated data for FePt nanoparticles. The particle size and degree of ordering of FePt nanoparticles were higher for larger annealing temperatures, when annealed for 1 hour. However, the coercivity did not change monotonically with annealing temperature. Fitting of the $H_C(T)$ to a scaling model of $H_C(T) = H_C(0)\left(1 - \frac{T}{T_C}\right)^{\gamma}$ gave values of γ in the range of 0.41 to 0.50.

The phase evolution of $PtFe_{0.5}Co_{0.5}$ resulting from different annealing conditions was also studied. As-synthesized $PtFe_{0.5}Co_{0.5}$ nanoparticles are in the disordered fcc structure. Annealing $PtFe_{0.5}Co_{0.5}$ at 700°C for 1 hour produced the $L1_0$ structure. A more gradual phase transformation to the $L1_0$ structure could be seen more readily by annealing the $PtFe_{0.5}Co_{0.5}$ sample at 400°C for 30 minutes, 2 days and 1 week. The transformation to the $L1_0$ state is slow at 400°C, requiring two days of heat treatment to show a mixture of fcc and $L1_0$ phase in XRD data of the $PtFe_{0.5}Co_{0.5}$ sample. After one week of annealing, the nanoparticles are partially in the $L1_0$ state with a much more reduced amount of the fcc phases. The preliminary results indicate annealing temperatures higher than 400°C is required to produce a fully ordered $L1_0$ structure in $PtFe_{0.5}Co_{0.5}$. More work, including a microstructure study, is required to compare the behavior of $PtFe_{0.5}Co_{0.5}$ to that of FePt and CoPt.